Investigation into Alternative Devices for Joint Load Transfer in Jointed Concrete Pavement

by

James Mann

A thesis

presented to the University of Waterloo

in fulfillment of the

thesis requirement for the degree of

Master of Applied Science

in

Civil Engineering

Waterloo, Ontario, Canada, 2013

Author’s Declaration

I hereby declare that I am the sole author of this thesis. This a true copy of the thesis, including any required final revisions, as accepted by my examiners. I understand that my thesis may be made electronically available to the public.

James Mann

Abstract

Conventional construction of Jointed Plain Concrete Pavements (JPCP) in Canada consists of placing a round steel epoxy-coated dowel at the mid height of the pavement. Steel dowels reduce stepping at the joint to improve comfort and reduce the stress concentration on the support layer beneath the pavement. Most importantly they transfer load and are commonly referred to as load transfer devices. Problems with dowel bar deterioration, including corrosion causes the slab joint to lock and cause stress concentrations as the slab expands and or contracts and curls due to thermal and shrinkage straining occurring in the concrete. In this research, alternative joint load transfer devices are presented and compared to conventional steel dowels. Four device alternatives are developed and evaluated: a Glass Fibre Reinforced Polymer (GFRP) I-beam placed directly on the base material; GFRP tapered plates; a continuous horizontal V device; and a continuous horizontal pipe device both placed directly on the support layer. The two devices that are continuous run the length of the joint similar to a shear key.

The GFRP tapered plate and I-beam, as well as conventional steel dowels, were analyzed in a wheel path sized three dimensional finite element model for wheel loading and static loading applied to either side of the joint. An experimental testing program was developed to test joint load transfer capabilities of each device when subjected to a static wheel load applied to either side of the joint. The GFRP tapered plates and I-beams were shown to transfer load based on the results from the wheel path finite element model and experimental testing program. The differential joint deflection, stress concentrations and plastic straining occurring in the concrete is not reduced with either the tapered plate or I-beam compared to a dowel under wheel loading. In addition, a similar plastic straining area identified in the finite element models were noticed as an area of damage in the experimental testing program.

All of the devices developed are analyzed in a quarter slab three dimensional finite element model with shrinkage and thermal strains as well as wheel loading applied to the slab to simulate service loading. A detailed investigation into the stress distribution around the devices and the differential deflection at the joint through the service loading applied is presented in this paper. Similarly to the wheel path investigation the stress concentration in the tapered plate and I-beams are greater than conventional dowels and also have greater differential deflection occurring at the joint. Both the continuous Horizontal V and Horizontal Pipe device reduce stress and plastic straining in the concrete during the service load analysis compared to dowels. During daytime wheel loading the differential deflection in the joint is the lowest with no noticeable stepping occurring at the joint with the Horizontal V device; however is greater than conventional steel dowels under nighttime wheel load application. The differential deflection with the Horizontal Pipe during day and night straining and wheel loading is similar to conventional steel dowels.

Acknowledgements

I would like to express many thanks for the help I received on this research from supervisor Prof. Jeffrey West (Civil Engineering Department at the University of Waterloo). He supported me and helped guide me through my research. I would also like to thank Cyril Levy for his previous research and finite element model development completed under Jeffrey West at the University of Waterloo. I would like to thank Prof. Robert Gracie for insight into three dimensional finite element modeling and Prof. Giovanni Cascante for guidance in base support selection for laboratory testing. I would also like to thank the second and third readers of my thesis Prof. Susan Tighe and Brian Tolson.

I would like to thank Richard Morrison, Doug Hirst, and Rob Sluban for their help in preparing forms, placing concrete, and preparing equipment for experimental work in the laboratory and recommendations during the development of the experimental program. Other graduate students who helped me cast to ensure the placement of concrete in the slabs as well as making cylinders went as smoothly as possible.

I would like to thank my family for their support through my thesis development. I would like to thank my parents for their support. I would like to thank my brothers for encouraging me and being interested in my progress which always kept me on track.

Finally I would like to express my thanks to the Cement Association of Canada and the Ontario Student Assistance Program for their financial support throughout my thesis development.

Table of Contents

List of Tables

List of Figures

1.0 Introduction

1.1 Problem Statement

Rigid pavements consist of a concrete slab placed either on base/subbase or directly on the subgrade. The stiff concrete slab disperses the wheel load to the granular base using beam action. Rigid pavements are commonly used for high volume/high load applications as well as areas where the subgrade is poor and a rigid pavement is more efficient than a flexible pavement. There are four main types of rigid pavements: Jointed Plain Concrete Pavement (JPCP); Jointed Reinforced Concrete Pavements (JRCP); Continuously Reinforced Concrete Pavements (CRCP); and prestressed/post-tensioned. In Canada, the most common type of rigid pavement used is JPCP because of the relatively low cost of installation compared to the other types as well as the thermal behaviour of concrete in the Canadian climate. Generally the pavement is constructed with joints at a maximum spacing of 4.5m (Transportation Association of Canada, 2013).

JPCP can either include a mechanical device for joint load transfer or not. If a joint is included the concrete interlock at the joint is used to provide load transfer. Rigid pavements that were constructed without joint load transfer were shown to require rehabilitation earlier than those containing mechanical devices such as dowel bars.

Ideally, a joint load transfer device in JPCP will allow the concrete to expand and contract during shrinkage and thermal cycles and transfer traffic loads across the joint. Thermal and shrinkage loading of the slab causes the concrete to expand and contract in three directions and also causes curling of the slab due to strain gradients that occur due to heat transfer through the slab for thermal strains and evaporation of water for shrinkage. Joint load transfer devices need to allow movement along the length of the pavement due to seasonal temperature changes causing expansion and contraction of the slab. Perpendicular to the joint the movements of the each slab section should be similar about the middle of the slab due to shrinkage and thermal straining and this movement should be restrained to avoid slight differential movement through straining cycles.

Smooth round steel dowels are the most common joint load transfer device used in rigid pavements. Generally the dowels are inserted into the slab during paving using either a dowel bar

inserter (which is installed at the back of the paver) or placed on top of the base prior to paving in wire baskets. Perfectly aligned conventional steel dowels provide restraint vertically across the joint and perpendicular to the joint while allowing the expansion and contraction of the slabs at the joint location. Both of these types of installations lead to the possibility of misalignment of the dowel bars in the concrete. Levy (2010) and Leong (2006) both found when the dowel bars are skewed, the joint is not able to function properly as the misaligned dowel bar locks the joint (restrains the expansion and contraction along the length of the slab) causing joint distress/failure. High concentrations of stress at the dowel concrete interface may cause the concrete to fail around the dowel (Levy, 2010). The damaged concrete may affect the joint behaviour as the damaged concrete around the device is less stiff locally at the dowel which affects stepping (Porter et al., 2001) at the joint or can cause extensive damage to the slab itself (Prabhu et al., 2006). Horizontal and vertical misplacement of dowel bars does not cause as much concrete distress around the joint but affects the amount of load transferred across the joint (Levy, 2010).

Steel is also susceptible to corrosion, although epoxy-coating is typically applied to avoid corrosion of the device. Corrosion of the bar reduces the load carrying capacity of the device which will affect the joint load transfer as the effective area of the device is reduced as the bar corrodes. Secondly, the corrosion causes a volumetric change to the dowel that increases the resistance of relative movement between the dowel and concrete (Cairns et al., 2007).

Research into the complex nature of joints including the effects of misalignment, shrinkage, thermal cycles, and wheel loads is ongoing. It is possible to predict the effects of these variables using lab testing as well as analytical studies using computer analysis. The complex nature of the loading and distribution of loads through the slab, joints and base layers, make a 3D finite element analysis necessary to properly analyze the pavement.

Dowel bars restrain movement vertically and perpendicular to the slab while allowing movement along the length of the slab as desired when they are perfectly aligned; however, dowel bars are prone to misalignment and premature distress and deterioration. There has been some research into the development of other alternatives that may increase the life of the joints including other materials, shapes and sizes for the devices. Developing a device to increase the life of the joint has focused mainly on device shape to decrease concrete stress levels and using alternative

materials to increase the life of the device itself. Alternative devices are required to reduce stresses, minimize the effects of misalignment (or probability of misalignment), and reduce/eliminate durability problems in the device itself.

1.2 Research Scope and Objectives

The overall objective of the current study is to develop and study alternatives to smooth round steel dowels to transfer loads in JPCP by evaluating the performance of dowels, identifying possible alternatives to dowels and comparing the alternatives to dowels using analytical and laboratory testing.

The study is directed at development of an analytical model of the slab behaviour because it is not practical to test the slabs experimentally under service conditions. Experimental testing will be used to supplement the analytical data for device comparison and compare the actual behaviour of the devices. The objectives of the study are to:

- Identify other alternatives that have already been implemented as joint load transfer devices and examine their behaviour;
- Develop alternative joint load transfer devices that could improve on current devices;
- Develop three-dimensional finite element model that can be used to compare the ability of the devices to transfer load under perfect alignment conditions;
- Develop a three-dimensional finite element model to compare the viable devices subjected to service conditions including shrinkage, thermal and traffic loadings;
- Compare the results of the analytical studies of joint load transfer devices to dowels;
- Confirm results of analytical study comparison of the joint load transfer devices by testing the devices in an experimental setting;
- Provide recommendation for future use.

1.3 Research Methodology

The research methodology that was used is presented in Figure 1-1. A literature review was completed to investigate existing load transfer devices, joint behavior and concrete pavement finite element models. The research gathered in the literature review was used as a basis to determine alternative designs and criteria for the load transfer devices. Based on previous finite

element models of concrete pavements investigated in the literature, material models for use in the finite element model were developed. The initial finite element model was generated for dowel bars and used to create the geometry for the wheel path model. Based on the development of the finite element model device alternatives were determined. Two different types of devices were developed which were continuous and discrete devices (defined in Chapter 3.0). The discrete devices were evaluated using finite element analysis in a wheel load model, then experimentally tested under wheel loading and finally analyzed under service loading conditions. The continuous devices were only analyzed using the finite element service load analysis.

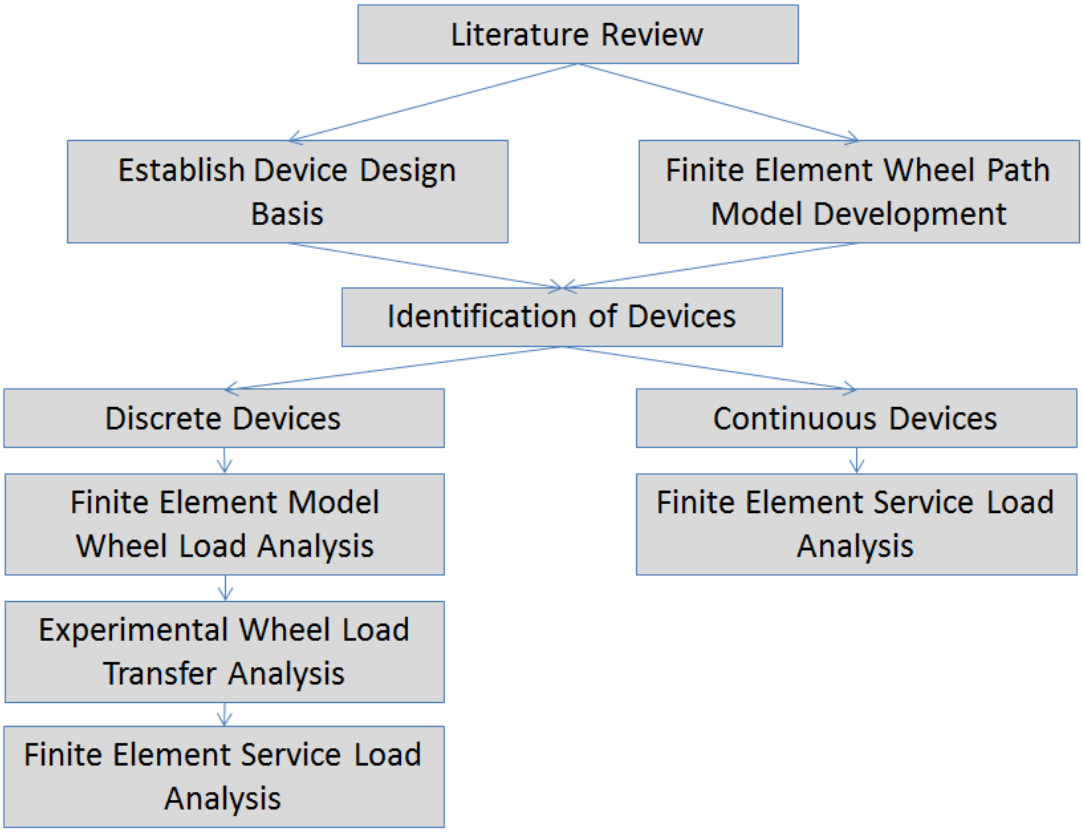

Figure 1-1 – Research Flow Chart

1.4 Thesis Layout

The thesis is organized as follows:

- Chapter Two provides a review of the literature relating to the current state of practice of concrete pavements, concrete pavement distresses, dowel bar load transfer theory,

alternative load transfer devices that have been reported, and previous experimental testing of concrete pavement joint load transfer ability;

- Chapter Three presents design criteria for alternative device design criteria and describes the device alternatives proposed and evaluation methods;
- Chapter Four presents the three dimensional model development, including the material models/parameters used for the finite element analysis evaluation;
- Chapter Five presents the results from the wheel path finite element model slab for the different alternatives;
- Chapter Six presents the experimental testing program as well as the results from the experimental study;
- Chapter Seven presents the results from the service load study comparison of the devices;
- Chapter Eight presents the conclusions and recommendations from the current study.

2.0 Literature Review

This chapter reviews the behaviour and problems associated with dowels bars and then details existing joint load transfer alternatives. The literature review is divided into four sections. The first section focuses on conventional steel dowel bar fundamentals and identifies features that can result in failure at the joint prior to the life of the pavement. The next two sections present alternatives to conventional steel dowel bars that have been used in restoration, slab on grade and paving applications for joint load transfer. Following the review of alternative dowel bars, a review of analysis and testing procedures for dowel bars is presented.

2.1 Joint Load Transfer Current State of Practice and Problems

2.1.1 Rigid Pavement Structure

A rigid pavement consists of a concrete slab placed on a base and subbase layer which typically consists of an unbound layer. In Ontario, a treated (ie. either asphalt or cement) bound layer is also often used and is commonly referred to as an Open Graded Drainage Layer (OGDL) (Transportation Association of Canada, 2013). Concrete is placed in lane sections using a slip form paver. There are two types of joints in rigid pavements: longitudinal and transverse. The transverse joints are placed at 4.5m to accommodate strains and cracking due to daily and seasonal thermal expansion and contraction, as well as shrinkage. These joints are sawcut. Longitudinal joints are typically between lanes and use tie bars to prevent slabs from separating. Figure 2-1 presents the general arrangement of the pavement structure.

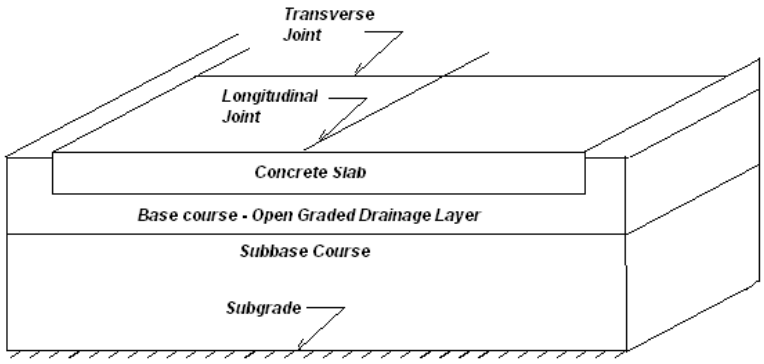

Figure 2-1 – General pavement arrangement

Beneath the concrete layer there is a base and subbase layer. The base and subbase layers provide drainage, frost protection, and a level and desired grade for the slab. The base and subbase layers also provide further load spreading to the subgrade below (the load distributes out in two directions reducing the maximum bearing stress on the surface as the depth increases).

2.1.2 Conventional Round Steel Dowel Bar Description

Conventional dowel bars are round epoxy-coated steel smooth dowels placed perpendicular to the joint to provide load transfer. The spacing of the dowel bars depends on the loading and the thickness of the concrete slab. Load is transferred through shear force on the dowel bar from one side of the joint to the other. The force is distributed to the concrete through bearing stress above and below the dowel bar on either side of the joint. Typical bar sizes used for dowels in concrete pavements are 30-35 mm diameter bars, and are spaced at 300 mm (Porter et al., 2001). Figure 2-2 presents the layout of the dowel bars in JPCP. The dowel is placed at the mid depth of the slab and the joint is sawcut to a depth of one third the slab depth (Transportation Association of Canada, 2013).

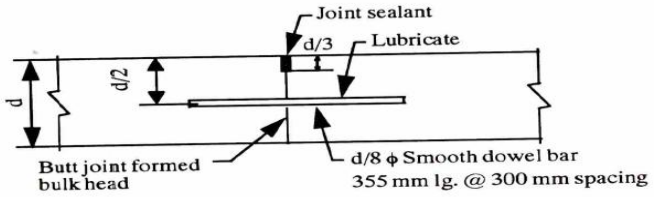

Figure 2-2 – Typical details for JPCP Dowel Bar Location (Transportation Association of Canada, 2013)

2.1.3 Dowel Bar Joint Load Transfer Theory

In order to design a new load transfer mechanism, a review of wheel load transfer theory was completed. The review will be used to form design equations to determine preliminary sizes of the new devices. This review will also help in understanding the distribution of load at the joint.

A dowel bar is designed to transfer a portion of a wheel load from the loaded slab to an adjacent slab. Transferring load from one slab to another reduces the subgrade stresses at the joint interface and minimizes “stepping” (differential deflection of the adjacent sides of the joint) of

the slab as the wheel load crosses the joint. The following equations were presented by Porter et al., (2001) to estimate the load transfer in dowel bars. Theoretical modeling of deflection at the joint is based on the Timoshenko and Lessels beam on an elastic foundation (Timoshenko & Lessels, 1925) presented in Equation (2-1).

$$y_o = \frac{d^4y}{dx^4} EI = -ky \tag{2-1}$$

Where:

$\beta = \sqrt[4]{\frac{bK_o}{4EI}}$ = relative stiffness of the dowel bar encased in concrete (mm^{-1})

y_o = deflection at the face of the joint

K_o = Modulus of Dowel Support (N/mm^3)

b = dowel bar width (mm)

E = Modulus of elasticity of the dowel bar (MPa)

I = Moment of Inertia of the dowel bar (mm^4)

P_t = Load transferred through the dowel bar (N)

z = joint width (mm)

Friberg (1938)simplified Equation (2-1) for a beam of semi-infinite length where deflection (y_o) is described by Equation (2-2) (Porter et al., 2001).

$$y_o = \frac{P_t(2 + \beta z)}{4\beta^3 EI} \tag{2-2}$$

The total differential deflection of a joint (Δ) or "stepping" consists of the deflection at the face of the joint, the slope, shear deflection and flexural deflection of the dowel bar (presented in Equation (2-3) and Figure 2-3.

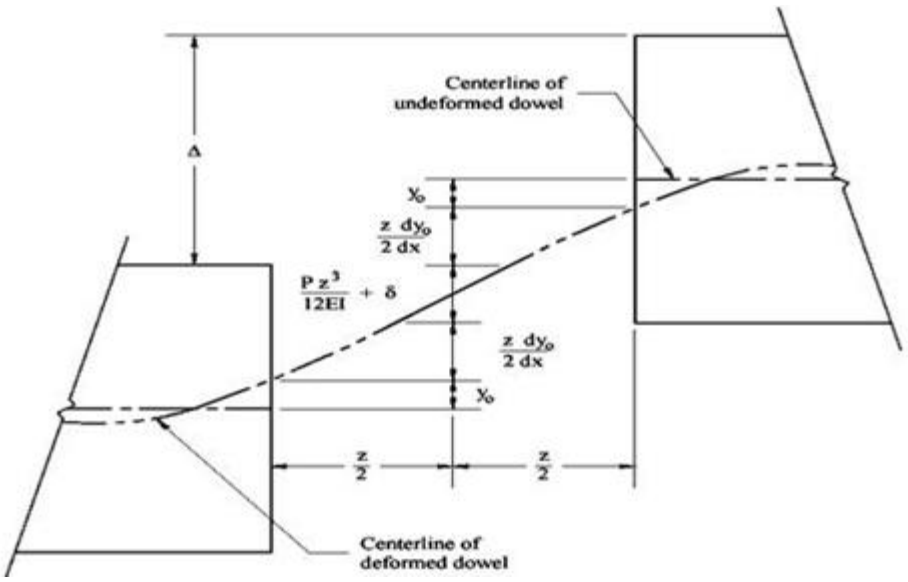

Figure 2-3 – Differential Deflection at joint components (Porter et al., 2001)

$$\Delta = 2y_o + z\left(\frac{dy_o}{dx}\right) + \delta + \frac{Ptz^3}{12EI} \quad (2\text{-}3)$$

Where:

$\delta = \frac{\lambda P_t Z}{AG}$ = Shear deflection

$\lambda =$ = form factor equal to 10/9 for solid circular sections and ellipses

A = cross-sectional area of the dowel bar (in^2)

G = Shear Modulus (psi)

For a small joint width it can be assumed that the flexural deflection and deflection due to the slope of the dowel bar can be assumed to be zero and Equation (2-3)simplifies to Equation(2-4) (Porter et al., 2001).

$$\Delta = 2y_o + \delta \quad (2\text{-}4)$$

The bearing stresses experienced by the concrete (σ_b) can be calculated based on the deflection at the joint face according to Equation (2-5) (Porter et al., 2001).

$$\sigma_b = K_o y_o \quad (2\text{-}5)$$

The elasticity theory and simplified formulas presented above give an estimate for the differential deflection and concrete bearing stress at the joint interface. These simplified equations will be used to develop design options similar to dowels. A more rigorous approach

such as finite element modeling is required to investigate the local stress concentrations developed or the behaviour of the pavement under shrinkage and thermal strains.

2.1.4 Dowel Bar Misalignment

A review of dowel bar misalignment problems was completed in order to understand the problems associated with dowel bars and to identify which elements of the design of dowels should be improved upon in the current study.

Dowel bar misalignment has caused problems in concrete pavements including problems with joint locking. Misaligned dowels restrain the joint from opening and the restraint causes high localized stresses. These high local stress concentrations cause damage to the concrete which will reduce the life of the joint. Damaged areas of concrete also produce lower stiffness which will affect the load transfer and stepping at a joint. Dowel bars can be misaligned in two ways: a skew and a translational misalignment. A translational misalignment occurs when the entire dowel is offset from the central plane of the joint. Skew misalignments occur when the dowel bar axes are offset from the pavement axes. Both types of misalignment are presented in Figure 2-4.

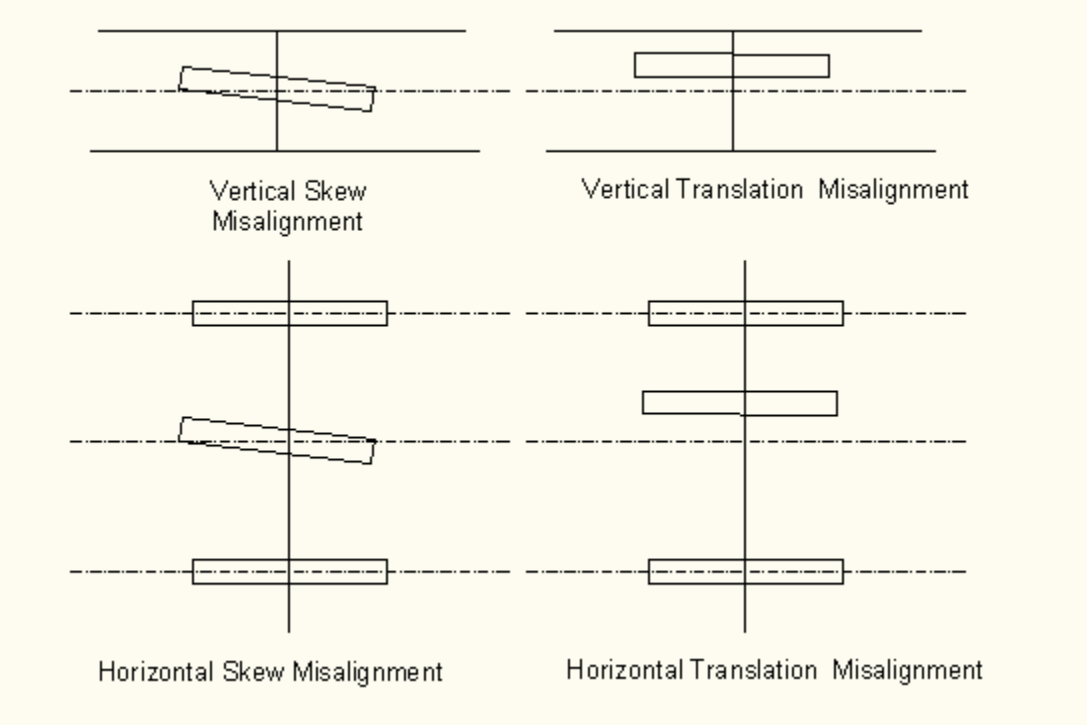

Figure 2-4 – Types of dowel bar misalignment

Dowel bars can be placed with a misalignment in a number of ways. Some of the factors that will affect the alignment of basket assemblies (where the dowels are placed in wire baskets on the base before paving) are: basket rigidity, placement of basket on base, concrete placement, and location of sawcut with respect to the dowel baskets. Factors that affect dowel bar misalignment when dowel bar inserters are used include: operation of the dowel bar inserter, vibration after placement, and location of sawcut relative to dowel location. The effect misalignment will have on a slab will also depend on straining in the slab which will depend on the climate, shrinkage in the concrete, and spacing of the joints as all of these will affect the amount of joint opening required.

The misalignment of dowel bars in both translation and skew misalignment have an effect on the load transfer at the joint. Vertical translation horizontal and vertical skew can cause spalling at the joint. Horizontal and vertical skew misalignment can cause cracking of the concrete.

Prabhu et al. (2006) presents the results from a two phase project that investigated the effects of skew misalignments on joint opening behaviour. The study focused on determining the force required to pull slabs apart with different magnitudes of skew misalignment. The first phase of the project included modeling misalignments using finite element analysis to determine the joint opening behaviour of joints with single and multiple dowel bars. Linear elastic material properties were used with contact interface elements used to model the dowel pavement interaction. A pseudo change in dowel temperature was used to develop the initial contact pressure between the dowel and the concrete pavement. The finite element models were used to develop the experimental procedures for the second phase of the report. The second phase of the project consisted of experimental testing and analysis of dowel bar misalignments, finite element development and validation of the localized stresses. Finite element analysis was completed using ABAQUS.

The study used two analytical cases to compare to the experimental results. The first analytical model used the idealized material and pull out data and the second used measure material and friction coefficients. The study also investigated one, three and five dowel bar models.

For the single aligned dowel bar, the idealized and the measured analytical cases were almost identical because the perfectly aligned dowel does not develop large pressures at the contact

interface which will be affected by measured frictional values. The perfectly aligned case was found to only debond and no further damage occurred in the concrete in the analytical model. The experimental results were very similar to the analytical results.

A vertically skewed dowel bar, out of skew by 1/18 of radius of the dowel bar, the restraint due to the skew caused compressive and tensile plastic strains but did not cause significant crushing or cracking. The analytical cases both were able to predict the results but a noticeable increase in accuracy with the measured values input was noted.

The single horizontally skewed dowel bar model with a single dowel bar skewed 1/18 of a radius caused restraint that produced significant cracking and crushing of the concrete in both analytical models. The results of the single bar analysis completed by Parabhu et al., (2007) suggest that horizontal skew is worse than vertical skew in terms of potential concrete distress.

The two dowel bar model with perfect alignment did not experience damage just debonding similar to the single bar model (Prabhu et al., 2007). The experimental results did not compare as similarly as with the single bar model but still show similar behaviour. The two analytical cases for the two bar misaligned model were bounding the experimental values. When both dowels are misaligned in the two bar investigation, plastic damage in compression and tension is predicted but no excessive damage (Prabhu et al., 2007).. With a single dowel bar misaligned in a two dowel bar arrangement plastic damage but not excessive plastic damage was predicted (Prabhu et al., 2007). Finally a specimen with alternative skews was compared, and this specimen was predicted to have excessive compressive and tensile damage occurring (Prabhu et al., 2007). The vertically misaligned study of two bar models showed that non-uniform vertical skew is the worst type of vertical misalignment in terms of concrete damage (Prabhu et al., 2007).

Prabhu et al., (2007) show that horizontally misaligned non-uniform skew alignment causes the most severe damage. All of the horizontal bars caused excessive compressive damage and tensile damage to the concrete adjacent the misaligned dowels. Horizontal and vertical misalignment for joint opening was shown in the current study to affect the damage occurring at the joint as it opens in that the larger joint opening required the more damage occurs. As the displacement increases if restraint to movement occurs the force/stress to restrain more movement will

increase which results in stress increase until failures occur locally which will allow some movement and cause damage and reduces stiffness in the concrete (Prabhu et al., 2007).

Prabhu et al., (2007) predict the joint opening behaviour of concrete pavements using 3D finite-element models. As the misalignment magnitude increases the material distress and damage occurred at smaller joint openings. The study also found that horizontal misalignment is generally more detrimental than vertical misalignments for concrete damage and the distribution for horizontal misalignment (uniform, non-uniform or alternate) has a small influence when compared to the magnitude of misalignment for pull out tests.

Davids et al., (2007) completed a study of the horizontal misalignment of joints when the slab is modeled using a finite element model. The finite element analysis of the misaligned joints found that the amount of shear transferred across the joint did not vary significantly, but that the joint mislocation did increase the peak shears in the device.

An analytical study on the influence of misalignment was completed by Levy (2010) investigating the various effects of different misalignments in dowel bars exposed to shrinkage, thermal loads, and wheel loads. The investigation found that when the dowels were misplaced vertically upward in the slab 25 mm, there was a large increase in the plastic strain in the concrete around the dowel. The dowel also attracted more load when it was misplaced vertically upwards in the slab. A vertically skewed bar was determined to initiate plastic strains more quickly in the concrete around the joint and increase the force in the bar. A vertically skewed bar will still transfer load at the joint and did not appear to affect the load transfer in the analytical study completed. The load transfer efficiency in the model was found to be better with a misaligned case which the author suggested was due to a mechanical advantage where the unloaded slab was pried upward as the load was applied (Levy, 2010).

Leong et al., (2006) completed experimental testing and finite element analysis of dowel bar pull-out with various misalignments. The finite element model was completed using a three dimensional explicit analysis consisting of two slabs 200 mm thick, 900 mm wide and 1000 mm long connected by three dowels. Loads were applied using velocities to simulate the imposed displacement on the slab similar to opening caused by uniform slab expansion and contraction. Three different types of misalignment were investigated in the study completed by Leong et al.,

(2006) which were a single misaligned bar (middle of the three bars), all three bars misaligned similarly, and oppositely misaligned bars. In the single misaligned dowel bar case, both horizontal and vertical misalignments up to 30 mm were investigated. The results showed that there was little difference between the estimated pull-out force for the vertical and horizontal misalignments. The pullout force required to open the joint 14 mm increased by approximately 1 kN for a 5 mm increase in misalignment up to 20 mm. Between 20 and 25 mm an approximate 4 kN increase occurred. With the single bar misaligned 25 mm the stress in the concrete reached 3 MPa for the both horizontal and vertical misaligned cases. The finite element model with three misaligned dowel bars suggested that with 5 mm increase in misalignment the pullout force required increased by 5kN. Three dowel bars misaligned caused an increase in pullout force of 10 kN between 20 and 25 mm of misalignment. Misalignment of all three dowels by 25 mm caused stress concentrations that would suggest cracking occurring around the dowels. The opposite misalignment case consisted of misaligning the two outer dowels in one direction and the middle bar in the opposite direction. The opposite misalignment pullout investigation completed by Leong, et al., (2006) model predicted that cracking would occur at misalignment of 25 mm. The pullout force required almost doubled in with opposite misalignment between 20 mm and 25 mm. Leong, et al., (2006) concluded that with misalignments up to 20 mm cracking should not occur but at 25 mm or greater cracking will have occurred. The study completed by Leong, et al., (2006) did not take into account the effect of thermal or shrinkage gradients which may change the relationship between vertical and horizontal misalignments as well as reduce the allowable misalignment tolerance established as further restraint will be caused due to curling.

Vertically misaligned skewed behaviour is investigated in the current study only in wheel load transfer analysis at the joint with the wheel path model with quasi-static reversed loading applied. The loading is later described in Chapter Five.

2.1.5 Concrete Deterioration at Joints

Bearing stress is developed at the interface between the dowel bar and the concrete. Concrete can become damaged if the bearing stress exceeds the maximum bearing stress limit of the material. Under repetitive high stress loadings, a void will begin to form at the interface between the concrete and dowel bar. The void will allow additional deflection that reduces the efficiency of

the dowel to transfer loads across the joint and puts additional load in the subgrade which can lead to differential settlement of the slabs (Porter et al., 2001).

The most effective way to transfer load and avoid concrete deterioration is to ensure that there are no voids between the device and concrete in the vertical direction and no restraint from the device on the concrete in the horizontal direction. Since the horizontal sides of the device are not considered in transferring loads, it would be ideal to have the sides free from the concrete and the top and bottom of the device to be in constant contact with the device and be free of voids. The voids allow deflection to occur before the interface between the dowel and concrete become in contact (Schrader, 1991).

Davids et al., (2007) used a computer simulation to determine the effects of voids that may develop around a dowel bar after concrete has deteriorated around the joint. The efficiency of the joint was influenced by varying the joint void conditions and it was found that a parabolic void of 0.2 mm around this location may reduce joint load transfer by as much as 73%.

Joint voids were not investigated in the current study. Future research should consider the effect of voids on the performance of the devices proposed. The chance of forming voids with the device geometry is considered in the current study and the method of placement for the devices will be suggested based on avoiding the formation of voids based on the review of the literature completed.

2.1.6 Field Performance of Conventional JPCP

Early construction of JPCP did not include dowel bars or any other joint load transfer devices at the joint. JPCP that were constructed without load transfer devices and exposed to high truck volume experience stepping failures and joint problems, shortening the life of the pavement. A number of concrete pavements without load transfer devices have been rehabilitated to provide load transfer and reduce stepping. A review of JPCP case studies of slabs constructed with and without conventional dowels is completed in this section.

On four repair sections that were originally constructed without load transfer devices Chen et al (2008) found the dowel bar retrofit application was found to improve the behaviour of the

pavement that previously did not have any load transfer devices installed. Each of the repair sections was investigated to determine how effective the repair was.

A section of highway in Texas, Jefferson SH-73, included repairs using grouting under the slab to restore the base support and putting an overlay on the surface. The repairs that included dowel bars or were full depth repairs performed better than the ones without dowel bar retrofit. Sections that were retrofitted with dowel bars were found to only have minor reflective cracking. The areas that were not retrofitted with dowel bars experienced severe reflective cracking in the overlay. The load transfer was two to three times better at joints that were retrofitted with dowel bars (Chen et al., 2008).

Another Texas highway, US59, was originally constructed without a subbase or dowel bars, and only 15 years after construction in 1990, the pavement already required rehabilitation. The original design was created using a slab thickening at the joint locations. In this design, the base was prepared with steps at the joint locations and a thicker 350 mm concrete layer was used at the joint locations compared to a 200 mm slab. Slab thickening at joint locations was not found to be an adequate way to avoid load transfer devices in jointed plain concrete pavements. Rehabilitation was completed on the section by inserting dowel bar sockets and grouting the dowels into place. On US59, some of the dowel bar retrofit was found to not provide a large improvement in faulting and rider quality shortly after being repaired. A core was taken to determine the possible reasons for the dowels not functioning, and a void in the grout around the dowel was found to be the problem for the dowel not functioning properly (Chen et al., 2008). The void would not be a problem in newly constructed pavements as small grout openings do not exist. The void does indicate the importance that alternative device designs proposed in this study should be able to be placed and not create voids in the concrete around the device as this problem has been shown to reduce the effectiveness of dowel bars.

Interstate highway US69 was constructed without load transfer devices. The pavement load transfer efficiency was 33% (the author noted this may be artificially higher because the readings were taken in the winter) before rehabilitation was completed (Chen et al., 2008). The addition of dowel bars completed in the rehabilitation increased the load transfer efficiency by approximately 30% (Chen et al., 2008).

Deerfoot Trail in Calgary Alberta has an approximately 12 km long JPCP section that was constructed around 1980 (Falls, 2006). The JPCP transverse joints were skew sawn joints randomly cut at an average spacing of 4.9 m and was assumed to have smooth dowels at the transverse joints providing load transfer (Falls, 2006). The pavement has lasted beyond its service life in 2003 and was expected to last 14 years longer than the service life without major rehabilitation (Falls, 2006), showing that properly constructed concrete pavements with conventional dowels last as long as expected.

A 5.5 km section of Highway 427 from QEW to the 401 Interchange in the city of Toronto was constructed in 1968 using JPCP with dowel bars. At the time of a study completed by Tighe (2005) the pavement was still performing well beyond the 30 year life of the pavement without major rehabilitation. Joint failures and stepping were both noted as major surface distresses that were observed on the section of concrete pavement (Tighe, 2005). This suggests that joint load transfer devices do function but are one of the first areas in the pavement to require rehabilitation and a need for an alternative device.

Grant McConachie Way, a 4.4 km road near Vancouver, British Columbia, was constructed in 1967 originally with load transfer devices and a continuous wire mesh mat (Falls, 2006). In 1987, a distress survey for the road way found less than 0.1% of the road had high severity cracking or spalling occurring and 5% had corner breaks. A joint rehabilitation was completed in 1987, and the pavement is still in good condition. (Falls, 2006) The road has sections with different traffic distribution including one that has more truck traffic, but there does not appear to be a difference in the performance of the sections. (Falls, 2006)

The city of Winnipeg and province of Manitoba have used concrete pavements for decades, and pavements constructed before the 1970s had 9 m joint spacing typically without joint load transfer devices included (Shalaby, 2005). The past performance of concrete pavements in Winnipeg has led to changes in the design of JPCP used in Winnipeg. A study on Provincial Trunk Highway 75 in Manitoba investigated the behaviour of different sections of highway with and without dowels. The load transfer efficiency at the dowelled joints was found to be greater than at joints without dowels based on survey data for up to 11 years of service (Shalaby, 2005). Increased width of the lane also increased the load transfer efficiency of the joint (Shalaby, 2005). The Kenaston Boulevard (Route 90) is a major link road in Winnipeg that was re-

constructed in 1995 incorporating advances in joint design (Shalaby, 2005). Typical joint spacing in this section was a maximum spacing of 4 m and transverse smooth round dowels were included to provide load transfer. A survey of the road in 2002 showed that the road was still in good condition after seven years in service (Shalaby, 2005). This suggests that based on the experience in Winnipeg load transfer devices have been shown to improve the pavement life.

2.2 New Construction Load Transfer Devices

The following devices have been used or proposed as alternatives to dowel bars for use as load transfer devices in new concrete pavements.

2.2.1 Elliptical Steel Dowels

Elliptical steel dowels are placed with the larger ellipse dimension in the horizontal direction to increase the bearing area of the contact surface between the dowel and concrete used for wheel load transfer. The increased projected area of the top and bottom of the bar provide a larger bearing surface for the transfer of load from the dowel bar to the concrete, reducing the bearing stress in the concrete (Porter et al., 2001).

Porter et al., (2001) completed tests using round and elliptical dowels and measured the bearing stresses in the concrete for both. Two sizes of round dowels and three elliptical dowels were compared. The tests found that the large elliptical dowels that had an 18 percent increase in cross-sectional area when compared to a 1-1/2" circular dowel had a 26 percent reduction in bearing stresses. The 1-1/2" dowel, which has a 44 percent increase in cross-sectional area compared to a 1-1/4" dowel only produced a 25 percent reduction in bearing stress. The medium sized elliptical dowels had approximately the same bearing stress in the concrete when compared to a 1-1/2" round dowel. The stiffness of the round dowels was higher when compared to the elliptical dowels causing a small variation in the deflection of the slabs.

Elliptical steel dowels can reduce the bearing stresses on concrete. However they do not address the problems associated with dowel bar misalignment and deterioration of the dowel bar itself as they are still steel dowels. Due to the shape of elliptical steel dowels they also present a new misalignment problem associated with the non-symmetrical shape of the dowel and if they were

placed with the opposite axis bearing on the concrete an increase in bearing stress will be encountered at the dowel-concrete interface (Porter et al., 2006).

2.2.2 Alternative Materials for Dowel

GFRP dowels and stainless steel dowels have been used to eliminate the problems associated with joint locking caused by corrosion. The durability of GFRP in concrete is a concern but was out of the scope of this study.

Porter and Pierson (2007) demonstrated that stainless steel dowels had lower differential deflection when compared to epoxy-coated steel dowels. Stainless steel has a lower stiffness than epoxy-coated steel but deflected less in the tests. This observation was attributed to softness of the epoxy coating. The stainless steel dowels were found to provide adequate load transfer compared to epoxy-coated steel dowels.

Eddie et al. (2001) completed tests on two types of GFRP dowels and compared them to epoxy-coated, steel dowels. The test program consisted of testing 12 slabs with two dowels placed in the slab. The slabs were tested on a crushed limestone base, as well as a weak support consisting of steel springs. The shear strengths of the dowels were also tested in double shear tests. The tests on the slabs included monotonic loading to failure and cyclic loading to 1 million cycles. After laboratory tests were completed, the GFRP dowels were implemented in a field application in the city of Winnipeg, Manitoba. The research concluded that 38 mm GFRP dowels could perform similar to 32 mm epoxy-coated steel dowels even though the GFRP dowels have lower shear strength. Under dynamic impact field testing the three GFRP dowels exhibited higher joint deflections. These conclusions do account for the long-term performance of GFRP dowels.

Porter and Pierson (2007) found that GFRP dowels have a lower stiffness compared to steel dowels and that a GFRP dowel will have more joint deflection compared to steel dowels. The GFRP dowels were found to be adequate at transferring the load and keeping the stress concentrations below the allowable limits.

Direct shear tests completed to determine the modulus of dowel support using Friberg's equations found lower values for elliptical GFRP dowels than steel. The lower modulus of dowel support was explained as being based on the material properties (Porter et al., 2006). Although

material properties of the dowel are included in the deflection at the face of the joint, the modulus of dowel support is still slightly dependent on the dowel properties as well as the shape.

Based on the literature review completed, GFRP and stainless steel have been proposed and tested as alternative dowel bar materials. Research on GFRP and stainless steel applications have been limited to conventional dowel bars and elliptical dowel bars. GFRP extruded shapes were not considered as joint load transfer devices in previous research. It could be possible to apply different shapes and configurations of extruded GFRP shapes to address other issues associated with joint distress. The design of alternatives using GFRP should take into account the composite material properties. There are two parts in the GFRP structure: a fibre and a polymer. The polymer and fibres are placed in layers and the fibres generally run in one direction, although not exclusively. The fibres in GFRP materials are stronger than the polymers and hence the strength and stiffness characteristics of GFRP materials in the two directions tend to vary depending on the arrangement of the fibres. The shear strength of GFRP materials is low in comparison to steel. GFRP composites are most effective in plane stress applications and changing the arrangement of fibres can alter the strength properties of the material (Qiao et al., 1996).

2.2.3 Dowel Bar Shape Alternatives

In order to decrease the bearing stress in the concrete at the dowel-concrete interface and reduce joint locking due to misalignment, a number of shape alternatives have been used. A number of the joint load transfer devices alternatives presented in this Chapter have been used in industrial slab on grade applications as joint load transfer devices, but not in highway applications where the concrete slab is placed using a paver.

Square dowels consist of square steel dowel bar to increase the bearings area of the device and hence reduce the concrete bearing stresses above and below the dowel (APCA, 2008). Rectangular dowels further increase the bearing area of the dowel-concrete interface. Both devices are effective at reducing the bearing stresses on the concrete but still have difficulties addressing the problems with dowel bar misalignment. Compressible material and high density plastic was attempted as a possible way to offset the problems associated with dowel bar misalignment with some success (APCA, 2008).

Acrylonitrile-butadiene styrene (ABS) plastic clips were attached to square and rectangular dowels to allow some horizontal movement parallel to the joint. Compressible material that allows the horizontal movements was contained within the ABS sleeve along the sides of the dowel, presented in Figure 2-5.

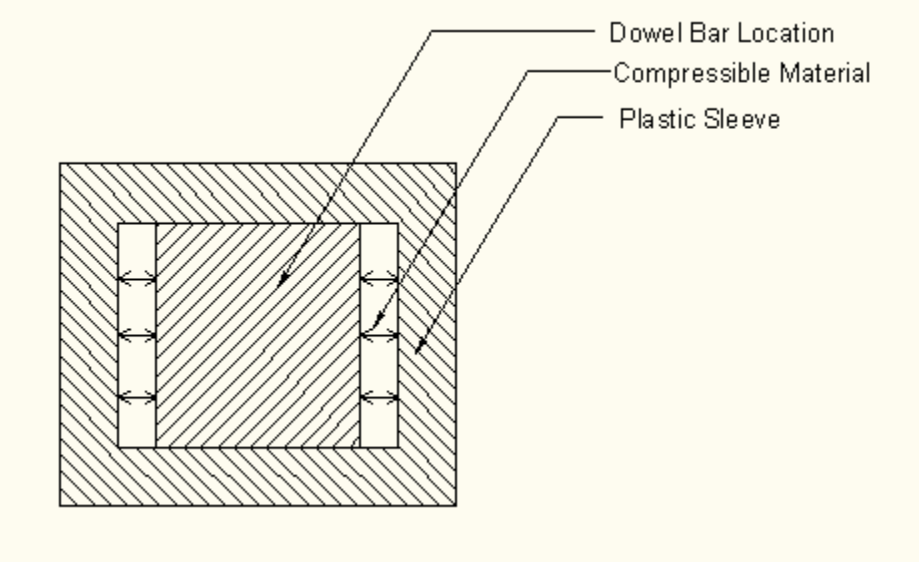

Figure 2-5 – Rectangular dowel bar with ABS sleeve and compressible material cross section

The compressible material at the sides of the dowel was used to allow the dowels to move within the ABS sleeve as depicted with the arrows in Figure 2-5. The ABS transfers the vertical load to the device. The ABS clips and dowels can be put into the slab using baskets similar to with round dowels (Schrader, 1991). The clip provides other advantages as noted by Schrader (1991), such as avoiding exposing the dowel to a corrosive environment since the ABS clip protects the dowel from dirt and contact with the concrete directly.

It was noted by Parkes (2007) that although square and rectangular dowels with clips have an advantage compared to round dowels, they were not being used in industrial slab on grade applications or pavements. One of the reasons noted for the lack of usage of square dowels was the installed cost of square dowels is almost twice that of round dowels for slab on grade application due to the additional labour to install devices in the formwork. In a paving application the devices would not be placed in formwork and it is assumed that the additional cost of rectangular devices would be avoided.

Diamond plate dowels were created to increase the bearing area near the joint where majority of the load transfer occurs. In slab on grade construction, diamond plate dowels were capable of transferring the load with a larger spacing compared to conventional steel dowels due to the large bearing area at the joint. Diamond plate dowels allow the thermal joint openings to occur because the void around the diamond created during construction and after shrinkage strains have occurred in the concrete is larger than the device itself (APCA, 2008). An ABS clip similar to the one used with rectangular and square dowels can also be used to ensure a void exists around the diamond plate dowel. Typical applications of diamond dowels have been limited to thinner slabs as only certain sizes of diamond dowels exist.

Fricks and Parkes (2002) noted that in constructing slabs on grade with diamond plate dowels it was more difficult to misalign the diamond plate dowels compared to round steel dowels. The ABS clip around the diamond plate dowels were easy to apply to the formwork and fewer repairs were required after completing the work in a formed application.

Diamond dowels have been installed in slabs on grade using formwork and are installed on the formwork, not in baskets or using a dowel bar inserter. Misalignment problems with diamond plate dowels may be more prevalent using a different installation method since the saw cut could cause a misalignment problem and so could skew misalignments of the diamond plate dowel.

A tapered plate dowel is larger at one end compared to the other end. The tapered effect of the device is intended to increase the bearing area at the joint and allow the concrete to shrink and create voids around the sides of the device which allow horizontal movement parallel to the joint. This type of device has been installed in baskets in paving applications (APCA, 2008).

2.3 Retrofit Load Transfer Devices

Slabs constructed without load transfer devices have been retrofitted to provide load transfer at the joint. The following devices are a number of different devices used in slab rehabilitation projects. Many of these devices were not found to transfer load effectively but are still reviewed as part of the current study to determine possible alternatives and comment on why the device does not function as expected.

2.3.1 Georgia Split Pipe Device

The Georgia split pipe device consists of two halves of a 100mm diameter pipe that are epoxied to a concrete core hole on either side of the joint. Plates rest on the top and bottom of the pipe halves epoxied to the concrete and are attached with four bolts. The top and bottom plate along with the four bolts transfer the load across the joint to either half of the pipe. The epoxy bond then transfers the load to the concrete slab. Thermal movement occurs through the slippage of the top and bottom plates resting on the split pipes (Figure 2-6**).**

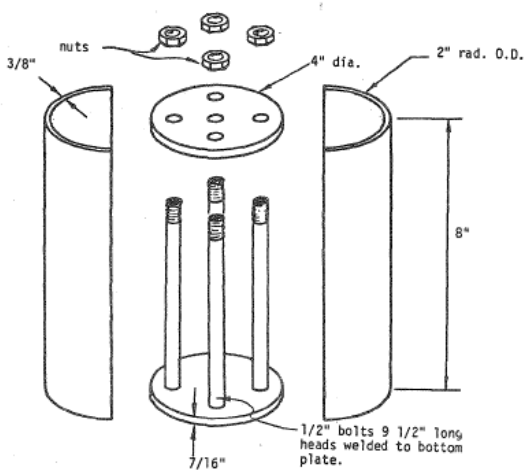

Figure 2-6 - Georgia split pipe device (Gulden and Brown, 1985)

Gulden and Brown (1985) found that the device did not adequately transfer load across the joint based on visual inspections of the installed devices in the field. Avoiding the use of an epoxy or concrete bond to the device by adding mechanical transfer of load could increase the load transfer ability of the device; however; due to the complex nature of constructing, and installing the device in conjunction with the poor results found in field application, no modifications are suggested to alter the device for use in new construction.

2.3.2 Figure Eight Device

The figure eight device is a cylindrical piece of metal with indents forming the shape of an eight. The figure eight device was epoxied inside a core hole and the epoxy was used to bond the device to the concrete. The force is transferred across the joint in the steel pipe itself. The transfer from the device to the concrete is through the bond of the epoxy. The indentations

forming the figure eight shape (aligned parallel to the joint) allow the thermal movements to occur (Figure 2-7).

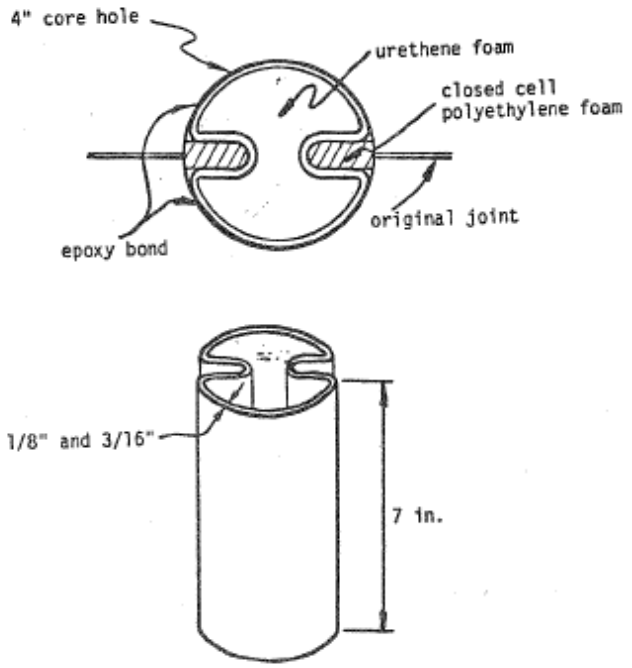

Figure 2-7 - Figure Eight Device (Gulden & Brown, 1985)

Gulden and Brown (1985) found the figure eight device failed to provide adequate joint load transfer based on maximum differential deflections between the loaded and unloaded slab corners. Reiter et al., (1988) also found that the figure eight device did not reduce faulting when compared to an unreinforced joint based on visual inspections and measured faulting.

Similar to the Georgia Split Pipe Device the Figure Eight Device relied on an epoxy bond between the device and the concrete to provide load transfer. Alterations in new construction to make a mechanical load transfer between the device and the slab could be completed but due to the tight tolerances for placement and difficulty of installation in the field, no modifications are suggested to the figure eight device.

2.3.3 V Load Transfer Device

A V load transfer device consists of a steel plate bent into the shape of a ‘V’ placed across a joint in two core holes (Figure 2-8). The tip of the V is aligned with the joint and urethane foam is

placed inside the ‘V’. The bond between the steel plate and the concrete provides the joint load transfer and the urethane foam filled ‘V’ shape allows thermal movements in the longitudinal direction of the slab (Reiter et al., 1988).

Gulden and Brown (1985) found that V load transfer devices did not adequately transfer the load across the joint based on the maximum differential deflection of the slab corners. The V device does not appear to have adequate load transfer abilities and may have alignment problems similar to dowel bars and will not be investigated further in the current research.

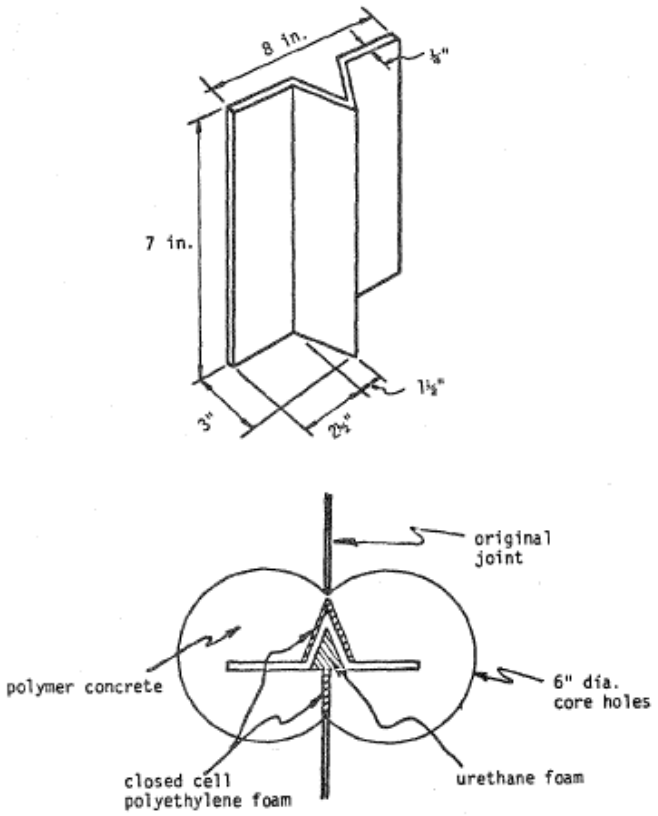

Figure 2-8 – V Load Transfer Device (Gulden & Brown, 1985)

2.3.4 Double V Load Transfer Device

A double V load transfer device is similar to a V load transfer device but uses two pieces of steel bent into the shape of a ‘V’ located back to back in one core and urethane foam between the steel plates (Figure 2-9) (Reiter et al., 1988).

Reiter et al., (1988) completed a restoration using double V load transfer devices and found that the device did not reduce the faulting across the joints. Reiter et al., (1988) observed that the double V device faild due to insufficient bond between the concrete and the device.

Gulden and Brown (1985) found that most of the double V devices nstalled were capable of transferring the load across joints and reducing joint deflection, and did not restrict the horizontal movement of the slabs. They recommended in the study that four devices be installed per lane width (two located near each wheel path).

Double V devices would be difficult to install in a new paving operation and would still have tight tolerances for alignment problems similar to dowels. The device also relies on concrete steel bond to transfer load, and does not provide mechanical transfer of the load across the joint. Due to the varying results found with double V devices and lack of advantages it is not recommended as an alternative to dowel bars for use in pavements.

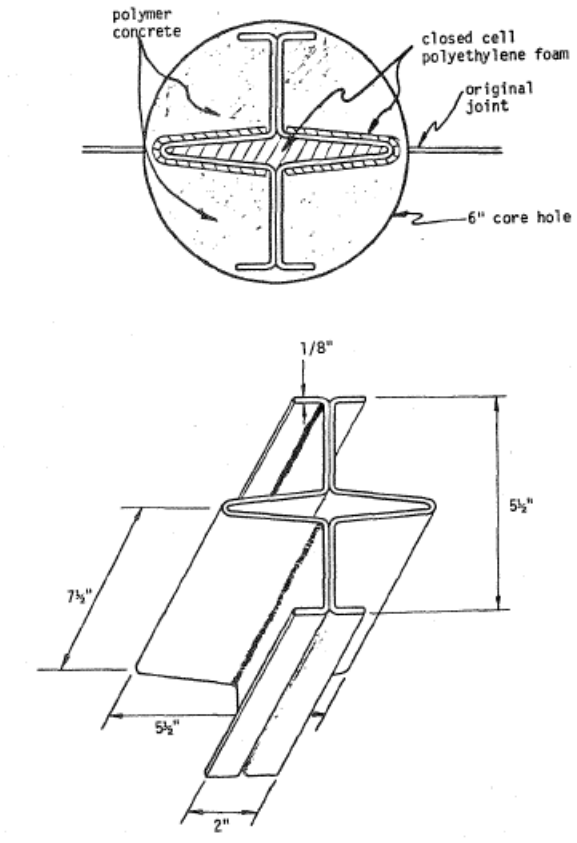

Figure 2-9– Double V Load Transfer Device (Gulden & Brown, 1985)

2.3.5 Miniature I-beam Load Transfer Device

A miniature I-beam load transfer device was used in restoration applications and consists of placing miniature I-beams across the joint similar to a dowel bar to transfer loads. The I-beam transfers load across the joint and also allows thermal movements to occur along the length of the beam.

Reiter et al., (1988) found that the miniature I-beam devices did not reduce faulting across the joint. None of the devices failed in the testing, although some of the backfill material had been dislodged. The I-beam application was completed in a restoration application and relied on the bond of new and old concrete to transfer load to the slabs as pockets were cut to place the devices at the joint. This device is similar to dowels and presents the similar problems associated with a dowel for misalignment, although it eliminates the vertical skew misalignment since the I-beam can be placed directly on the base layer, eliminating the vertical skew and translation misalignment problems. If the device is placed in a new slab, the load transfer would not be based on the bonded surface between new and existing concrete which could increase the load transfer ability of the device.

2.4 Summary of Alternative Devices

Based on the review of the literature for alternative devices used in both new and existing JPCP, Table 2-1 presents a summary of the alternative new construction devices and perceived advantages and disadvantages of each. Modified tapered plate dowels and miniature I-beams will be investigated further in the current research based on the previous behavior of these devices and the perceived advantages and disadvantages.

Table 2-1 - Summary of Previous New Construction Alternative Joint Load Transfer Devices

Device/Design Modification Description	Advantages	Disadvantages
Elliptical Steel Dowels	• Elliptical shape increases the bearing area at the joint	• Introduces a new misalignment plane
Elliptical GFRP Dowels	• GFRP material will eliminate problems associated with steel corrosion Elliptical shape increases the bearing area at the joint	• Introduces a new misalignment plane Long term durability of GFRP in concrete exposed to moisture
Square Steel Dowels in an ABS Sleeve	• Dowel is placed in an ABS Sleeve with a compressible material that allows dowel bar movement perpendicular to wheel load reducing misalignment effects	• Problems with Vertical misalignment still exist Expensive
Steel Diamond Plate Dowels Steel Tapered Plate Dowels	• Increased area at face of joint decreases bearing stress • Decreased area away from joint reduces chance of stress concentration due to misalignment	• Have not used in a paving application • Introduce a new misalignment plane
Stainless Steel Dowels	• Reduces differential deflection compared to epoxy dowels	• Expensive

2.5 Finite Element Modeling of Concrete Pavements

Due to the complex nature of the loading, materials, and material interactions in concrete pavements, finite element analysis is often used to investigate various aspects of the behaviour of the pavement. Application specific finite element analysis programs have been developed to analyze pavement behaviour depending on the size, spacing, and type of dowel with varying loads and material properties as inputs. General purpose finite element programs have also been used to study the behaviour of concrete pavements and dowelled joints. This Chapter presents a review of 3D finite element models of concrete pavements.

Figure 2-10 - Summary of Previous Retrofit Alternative Joint Load Transfer Devices

Device/Design Modification Description	Advantages	Disadvantages
Georgia Split Pipe Device	• Reduces effects of misalignment by allowing free movement of the slabs with nothing pultruding into the concrete adjacent to the joint or any piece continuous across the joint.	• Does not provide mechanical load transfer and relies on epoxy or aggregate interlock to transfer load • Expensive complex device
Figure Eight Device V Load Transfer Device Double V Load Transfer Device	• Reduces effects of misalignment with nothing pultruding into the concrete adjacent to the joint.	• Does not provide mechanical load transfer and relies on epoxy or aggregate interlock to transfer load Expansion plane requires alignment Load transfer device needs to extend and contract to allow slab movements
Miniature I-beam Load Transfer Device	• Eliminates vertical misalignment by being placed directly on base layer	• Previous rehabilitation with steel I-beams was not successful; however this relied on a bonded surface between new and existing concrete surfaces

2.6 Finite Element Modeling of Concrete Pavements

Due to the complex nature of the loading, materials, and material interactions in concrete pavements, finite element analysis is often used to investigate various aspects of the behaviour of the pavement. Application specific finite element analysis programs have been developed to analyze pavement behaviour depending on the size, spacing, and type of dowel with varying loads and material properties as inputs. General purpose finite element programs have also been used to study the behaviour of concrete pavements and dowelled joints. This Chapter presents a review of 3D finite element models of concrete pavements.

2.6.1 Element Selection

Finite element analysis is completed by dividing a large volume into small "elements" which are generally simple shapes such as triangles, squares, cubes, etc., depending on the nature of the problem. The element shapes are represented by a number of nodes that are connected using lines. Nodes are located at corners of the shape as well as other places of interest such as the middle of edges between corners or faces. The equations of the lines connecting the nodes, as well as the nodes themselves, are used to model shape geometry and locations at which calculations are completed. Generally, the fewer nodes and lower degree of line equations will lower the accuracy of the output.

Davids, (2007) modeled the slab, as well as the base layers, using twenty node quadratic hexahedral elements. These are solid elements that have a node located at each corner of the element as well as at the mid-points. Shoukry et al., (2000), Levy (2010), and Prabhu et al., (2007) modeled the slab using eight node linear brick elements which are rectangular solid elements with nodes located at each corner. The 8-noded elements can be used in contact, non-linear, and plastic analyses, making them ideal for modeling the slab and joint since contact exists between the concrete and the dowel as well as between the slab and the pavement base.

2.6.2 Concrete Properties

Concrete behaves quite differently in uniaxial compression and tension. Under low stress levels in compression and tension, the material behaviour is close to linear elastic. The compressive strength is much higher than the tensile strength of the material as well. Beyond the proportional limit concrete behaves nonlinearly and local concentrations of stress in a concrete pavement may cause non linear material behaviour in localized areas. It is important to capture the effects of such non-linearity near the joint and the effects on overall pavement behaviour. Using a linear elastic material model may be able to model the overall slab behaviour, but the local effects at the joint being studied will not be captured adequately. A brief discussion on the uniaxial behaviour of concrete under compressive and tensile loading is included in the literature review. Further discussion of the specific triaxial and three dimensional material model properties of concrete is included in the finite element model development (Chapter 4.0).

Suggested values for the concrete compressive properties are presented in detail by the CEB – FIP Model Code (Comite Euro-International Du Beton, 1991). The code suggests different material properties based on the characteristic compressive strength of the concrete, defined as f_{ck}, with tests taken after 28 days. The mean strength (f_{cm}) is assumed to be 8 MPa higher than the characteristic compressive strength. Moduli of elasticity are derived based on the compressive strengths as well. The tangent modulus of elasticity (E_{ci}) is defined in the CEB-FIP Model Code according to Equation (2-6).

$$E_{ci} = 21500\left(\frac{f_{cm}}{10}\right)^{\frac{1}{3}} \tag{2-6}$$

Where:

The modulus of elasticity for an elastic analysis suggested in the CEB-FIP Model code is a reduced modulus equal to 85% of the value calculated using Equation (2-6).

The secant modulus is based on the assumed mean strength (8 MPa greater than the characteristic strength) and strain at the mean compressive strength (0.0022). Equation (2-7) presents the secant modulus according to the CEB-FIP Model Code.

$$E_{c1} = \frac{f_{cm}}{0.0022} \tag{2-7}$$

Table 2-2 presents the CEB-FIP Model Code suggested values for concrete based on a 30 MPa compressive strength and normal density concrete.

The assumed limit of compression strain is given in Table 2-2 as suggested by CEB-FIP Model Code (30 MPa compressive strength assumed); however it has no significance in the material and is only used to limit the validity of Equation (2-8). Using the calculated compressive concrete properties in Table 2-2, equations are established to represent the stress-strain relationship of the concrete in two segments. The first equation for the concrete compressive strength is valid until a CEB-FIB Model code recommended limit of 0.0037 and is presented in Equation (2-8).

Table 2-2 –Compressive Concrete Properties suggested by CEB-FIP Model Code (30 MPa compressive strength assumed)

Description	Value
f_{ck}, Compressive Strength	30 MPa
f_{cm}, Mean Compressive Strength	38 MPa
E_{ci} (Tangent Modulus)	33550 MPa
E_c (0.85 E_{ci} linear concrete material is used)	28520 MPa
E_{cl} (Secant Modulus from origin to peak)	17500 MPa
ε_{cl} Assumed Strain at Max Mean Compressive Strength	0.0022
$\varepsilon_{c,lim}$, Limit of compressive strain	
ν (Poisson's Ratio of Concrete)	0.1-0.2

$$\sigma_c = \frac{\frac{E_{ci}}{E_{c1}}\frac{\varepsilon_c}{\varepsilon_{c1}} - \left(\frac{\varepsilon_c}{\varepsilon_{c1}}\right)^2}{1 + \left(\frac{E_{ci}}{E_{c1}} - 2\right)\frac{\varepsilon_c}{\varepsilon_{c1}}} f_{cm} \qquad for \ \ |\varepsilon_c| < |\varepsilon_{c,lim}| \tag{2-8}$$

Equation (2-9) is used to represent the remainder of the compressive strength curve. Figure 2-11 presents the compressive stress-strain curve for 30 MPa concrete using the assumptions given in the CEB-FIP Model Code 1990.

$$\sigma_c = -\left[\left(\frac{1}{\varepsilon_{c,lim}/\varepsilon_{c1}}\xi - \frac{2}{(\varepsilon_{c,lim}/\varepsilon_{c1})^2}\right)\left(\frac{\varepsilon_c}{\varepsilon_{c1}}\right)^2 + \left(\frac{4}{\varepsilon_{c,lim}/\varepsilon_{c1}} - \xi\right)\frac{\varepsilon_c}{\varepsilon_{c1}}\right]^{-1} f_{cm} \tag{2-9}$$

Where:

$$\xi = \frac{4\left[\left(\frac{\varepsilon_{c,lim}}{\varepsilon_{c1}}\right)^2\left(\frac{E_{ci}}{E_{c1}} - 2\right) + 2\frac{\varepsilon_{c,lim}}{\varepsilon_{c1}} - \frac{E_{ci}}{E_{c1}}\right]}{\left[\frac{\varepsilon_{c,lim}}{\varepsilon_{c1}}\left(\frac{E_{ci}}{E_{c1}} - 2\right) + 1\right]^2}$$

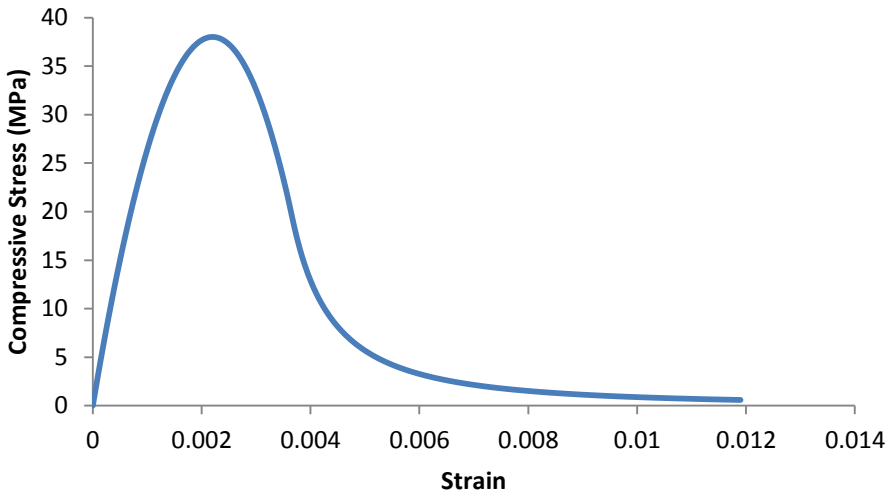

Figure 2-11 – Compressive Behaviour of Unreinforced Concrete based on CEB-FIP Model Code

Under uniaxial compressive unloading the CEB-FIP Model Code suggests using the tangent modulus of elasticity until cracking has occurred.

Based on the compressive strength properties of concrete, the CEB-FIP Model code predicts uniaxial tensile behaviour. The tensile behaviour can initially be represented using stress-strain relationships. After cracking occurs, an alternative method should be used. The strength of concrete in tension is much lower than compression. The minimum, mean and maximum tensile strengths are suggested according to Equations (2-10) to (2-12) respectively in the CEB-FIP Model Code.

$$f_{ctk,min} = f_{ctko,min}\left(\frac{f_{ck}}{f_{cko}}\right)^{\frac{2}{3}} \quad (2\text{-}10)$$

$$f_{ctm} = f_{ctko,m}\left(\frac{f_{ck}}{f_{cko}}\right)^{\frac{2}{3}} \quad (2\text{-}11)$$

$$f_{ctk,max} = f_{ctko,max}\left(\frac{f_{ck}}{f_{cko}}\right)^{\frac{2}{3}} \quad (2\text{-}12)$$

Where:

$f_{cko} = 10MPa$

$f_{ctko,min} = 0.95MPa$

$f_{ctko,m} = 1.4\ MPa$

$f_{ctko,max} = 1.85\ MPa$

In the elastic range for uniaxial tensile behaviour of concrete the CEB-FIP Model Code suggests using the initial compressive tangent modulus of elasticity presented in Equation (2-6). This relationship is assumed to be valid until 90% of the mean tensile strength of the concrete. After 90% of the mean tensile strength of the concrete has been reached the relationship between concrete tensile stress and strain can be represented using Equation (2-13). Figure 2-12 presents the behaviour of 30 MPa concrete under uniaxial tensile loads.

$$\sigma_{ct} = f_{ctm} - \frac{0.1 f_{ctm}}{0.00015 - 0.9 f_{ctm}/E_{ci}}(0.00015 - \varepsilon_{ct}) \qquad (2\text{-}13)$$

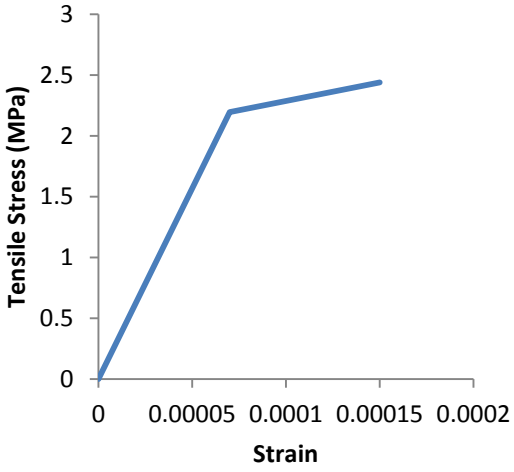

Figure 2-12 – Tensile stress-strain relationship of concrete to cracking (Comite Euro-International Du Beton, 1991)

The CEB-FIP Model code suggests using a bilinear stress-crack opening relationship for cracked sections. The stress-crack opening behaviour is based on the fracture energy of concrete, (G_f), which is the energy required to propogate a tensile crack of unit area. The fracture energy of concrete can be estimated using Equation (2-14). The value G_{Fo} is the base value of fracture energy and dependent on the aggregate size (as does the fracture energy). The CEB-FIP Model Code suggests a value of 0.030 Nmm/mm^2 for 16 mm maximum aggregate size and 0.058 Nmm/mm^2 for 32 mm maximum aggregate size.

$$G_f = G_{Fo}(f_{cm}/f_{cmo})^{0.7} \quad (2\text{-}14)$$

where:

$f_{cmo} = 10\ MPa$

The stress crack opening behaviour of concrete under uniaxial tensile loading can be represented using Equations (2-15) and (2-16). Figure 2-13 presents the tensile stress and crack opening behaviour of 30 MPa cracked concrete using Equations (2-15) and (2-16).

$$\sigma_{ct} = f_{ctm}\left(1 - 0.85\frac{w}{w_1}\right) for\ 0.15f_{ctm} \le \sigma_{ct} \le f_{ctm} \quad (2\text{-}15)$$

$$\sigma_{ct} = \frac{0.15f_{ctm}}{w_c - w_1}(w_c - w)\ for\ 0 \le \sigma_{ct} \le 0.15\ f_{ctm} \quad (2\text{-}16)$$

where:

$w_1 = 2\frac{G_f}{f_{ctm}} - 0.15w_c$, crack opening for $\sigma_{ck} = 0.15f_{ctm}$

$w_c = \alpha_F \frac{G_F}{f_{ctm}}$ is crack opening for $\sigma_{ct} = 0$

w = is the crack opening (mm)

α_F = coefficent depending on maximum aggregate size, 7 for 16mm and 5 for 32mm

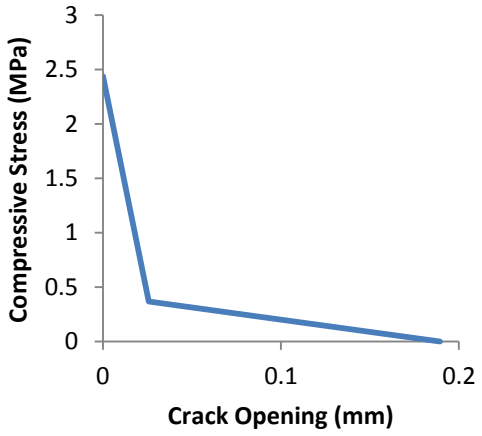

Figure 2-13 – Tensile stress-crack relationship of cracked concrete (Comite Euro-International Du Beton, 1991)

The minimum, mean and maximum tensile strengths, as well as the fracture energy and the tensile tangent modulus for 30 MPa concrete, are presented in Table 2-3.

Table 2-3 – Tensile Concrete Properties suggested by CEB-FIP Model Code (30 MPa compressive strength assumed)

Description	Value	
$f_{ctko,min}$, Minimum Tensile Strength	1.98	MPa
f_{ctm}, Mean Tensile Strength	2.91	MPa
$f_{ctko,max}$, Maximum Tensile Strength	3.85	MPa
G_F Fracture Energy required to propagate a tensile crack of unit area	0.095	N mm/mm^2
E_{ci} (Tangent Modulus)	33550	MPa

As mentioned previously the strength of concrete in tension is much lower than the compressive strength and the initial compressive tangent modulus is used to relate tensile stress and strain which is the same as compressive stress-strain behaviour.

The nonlinear behaviour of concrete in compression can be described in terms of an elastic region, a microcracking region where the material is nonlinear, and a localized failure region (Chen & Han, 2007). Under uniaxial loading, the concrete material is considered elastic until 30% of the failure strength. At this level, microcracking between the mortar and the aggregates occurs and grows causing a nonlinear material response up to about 75% of the ultimate compressive strength. At this point, localized damage begins to occur as the cracks are no longer stable, a progressive failure of the material occurs.

The nonlinear behaviour of concrete in tension can also be described as having the same three states: elastic, nonlinear and localized damage. The elastic stage occurs up to about 60% to 80% of the ultimate failure strength in tension. Under uniaxial tension loading, the microcracks begin propagate faster and the stable cracking phase is much shorter. The low tensile strength of the mortar is the reason for the brittle tensile behaviour of concrete (Chen & Han, 2007).

The behaviour of concrete is also dependent on the rate at which loads are applied and the temperature of the material. For the purpose of the current study, the effects of the rate of loading and the temperature on material stress-strain response were not considered.

Levy (2010) modeled the concrete using the concrete damaged plasticity model in ABAQUS. The model assumed 30 MPa concrete with an elastic modulus of 22 500 MPa, a Poisson's ratio of 0.18, and a coefficient of thermal expansion of 1.1E-005 per ^{o}C. The plastic properties that

were assumed for the concrete model were a based on ABAQUS recommended values (variables are explained in depth in Chapter 4.0). Prabhu et al., (2007) utilized the same model in ABAQUS as Levy (2010); however, the assumed compressive strength of the concrete was 24 MPa. For modeling tensile stress crack opening behaviour Prabhu et al., (2007) used a fracture energy value of 0.056 Nmm/mm^2 and Levy (2010) used a value of 0.18 N mm/mm^2.

2.6.3 Pavement Base and Foundation Properties

The concrete pavement slab is supported by the pavement base and subbase layers and by the subgrade. The layers provide continuous support to the concrete slab, and can be modeled in a number of different ways. A review of other base, subbase and subgrade models for concrete pavements is included below to determine how to model these layers. The review was limited to existing models and does not include a detailed material investigation. The detailed material behaviour of the pavement base and subgrade below are not of specific interest in the current study; however, the material properties must be able to simulate the stress distribution through the pavement base layers to properly simulate the concrete slab response. The interaction between the base and concrete slab is discussed later in this Chapter.

The model used by Davids (2007) assumed an asphalt treated base as a solid linear elastic material with a Young's Modulus of 3500 MPa, a Poisson's ratio of 0.2 and a density of 2000 kg/m^3. The vertical support to the base was assumed to be a dense liquid foundation with a modulus of subgrade reaction of 0.03 MPa/mm (Davids, 2007).

Shoukry et al., (2000) modeled the base and subbase as linear elastic materials. The base layer was assumed to have a Young's Modulus of 3.2 MPa and the subbase was assumed to be 3.09 MPa. The base layer has a Poisson's ratio of 0.40 and the subgrade is 0.45 in the model. The densities for the base and subgrade in this model are 2240 kg/m^3 and 2080 kg/m^3 respectively. These material models were back calculated based on tests conducted using falling weight defelctometer data from a section of highway in West Virginia.

Levy (2010) modeled the base and subbase as isotropic materials. The base was modeled using a Young's Modulus of 207 MPa the subbase was had modulus of 103 MPa. Both of the materials were assumed to have a Poisson's ratio of 0.3 and density of 2100 kg/m^3.

Repair projects were completed in Texas, and cores from the subbase and base material at various rehabilitation sites were gathered and tested. Eight cores were taken from SH73 and the subbase and subgrade moduli were found to be approximately 80.3 MPa and 55.3 MPa at service conditions, Chen and Han (Chen & Han, 2007) noted that ideal values would be 345 MPa and 103 MPa. US59 in Texas did not have a subbase and consisted of a slab placed directly onto a subgrade. The subgrade was found to have a modulus ranging from 76 to 227 MPa with an average of 146 MPa.

Based on the literature review completed of pavement base material properties and foundation support, it was concluded that a linear elastic material should be sufficient to model the behaviour of the slab and joint for the current study. The values for the modulus of elasticity varied from study to study as would be expected since the materials will vary based a number of factors. To assess the load transfer ability of a device it would be important to know how the slab behaves under a range of assumed base stiffnesses. More deflection of the base under the same loading (lower stiffness) will allow the slab to deflect more and increase the stress in the slabs.

2.6.4 Steel Properties

Shoukry (2000) model steel as a linear elastic material with a Young's Modulus of 205,000 MPa, a Poisson's ratio of 0.3 and a density of 7780 kg/m^3. Levy (2010) uses a linear elastic isotropic material with a Young's Modulus of 200,000 MPa.

2.6.5 Slab Dowel Interaction

The interface between the slab and device is able to move relative to one another; however load is also transferred at this interface and both of these effects should be captured in modeling of the interface. A review of different alternatives for modeling the slab-dowel interface as well as the interaction and methods to determine the values at the interface was completed.

Davids (2007) modeled the slab dowel interaction using a number of springs between the slab and the dowel with spring properties based on either the dowel support modulus or the dowel looseness. The dowel bars were modeled as flexural elements in the EverFE2.2 program. The interaction using springs does not consider the nonlinear behaviour of the interaction caused by slippage after dowel is moving. This approach would be efficient for modeling purposes and may

provide a more efficient model of the slab for design. It is difficult to determine the modulus of dowel support for nonconventional shapes and arrangements and the spring properties were based on these values. Alternatively modeling the interface using a contact surface with a frictional coefficient to account for the effects of slippage has also been used by others including Levy (2010).

Pull out testing of dowels to determine the frictional properties at the dowel-concrete interface was completed by Shoukry et al., (2003). The tests were completed on prisms measuring approximately 250 mm long, 300 mm wide and 275 mm deep, with 32 mm and 37.5 mm dowels. To determine the frictional coefficient between the concrete and the dowel from tests, the normal force (f_{clamp}) at the interface must be determined since the coefficient of friction is equal to Equation (2-17).

$$\mu = \frac{f_{pull}}{f_{clamp}} \tag{2-17}$$

To determine the clamping force Shoukry et al., (2003) considered the prism to be a thick-walled axes-symmetrical cylinder with an internal radius of a (at the dowel interface), external radius b, (at the edge of the specimen) and an internal pressure, p. The prism was assumed to have an outer diameter of 250 mm. The assumed stress distribution in the cylinder is shown in Figure 2-14. The equilibrium of radial (σ_r) and tangential (σ_θ) stresses at radius r shown in Figure 2-14 can be represented using Equation (2-18).

$$\frac{d\sigma_r}{dr} - \frac{\sigma_\theta - \sigma_r}{\sigma_r} = 0 \tag{2-18}$$

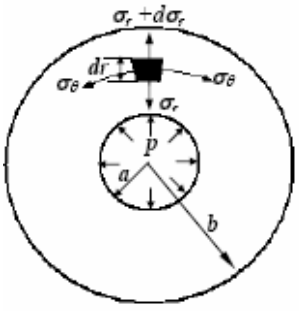

Figure 2-14 - Radial stress distribution in an axes-symmetrical thick wall cylinder (Shoukry et al., 2003)

Calculating the pressure at the dowel concrete interface and multiplying it by the projected area was completed by Shoukry et al., (2003) and Equation (2-19) predicts the clamping force.

$$f_{clamp} = pA \tag{2-19}$$

Using the relationships presented, values were obtained for 32 and 37.5 mm dowel bars that were uncoated, coated with silicone, and coated with a Tectyl (605) coating by Shoukry et al., (2003) and Table 2-4 presents the various values obtained. Prabhu et al., (2007) noted that typically values assumed for a greased dowel would have a friction coefficient of 0.0 and ungreased dowel would have a coefficient of friction of 0.3.

Table 2-4 – Experimental Dowel-Concrete Frictional Coefficients (Shoukry et al., 2003)

	Friction Coefficient	
	37.5mm Diameter	32mm Diameter
Uncoated dowel bar	0.3433	0.3837
Silicone coated dowel bar	0.0820	0.0926
Tectyl coated dowel bar	0.0986	0.0763

Shoukry et al., (2003) created an analytical pull-out model to determine the effects of applying the different frictional values to the dowel bars. The contact surface between the slab and dowel was modeled assuming hard normal contact with coulomb friction. Using the measured coefficients of friction of 0.076 and 0.384 presented in Table 2-4, Shoukry et al., (2003). did not find a reduction in mid-slab stresses with the different coatings at the slab interface when curling and temperature change is applied; however, it was noted by Shoukry et al., (2003) that under other straining situations possible for the slabs the frictional value may have more effect (2003) and the assumed values).

Levy (2010) and Prabhu et al., (2007) modeled the slab-dowel interface as a hard contact surface with the measured coefficients presented above in Table 2-4 and a shear stress limit of 2.1 MPa. The shear stress limit is the limit of the stress which the friction coefficient will be valid for and slipping will begin to occur (Shoukry et al., 2003). There was nothing included to account for chemical bond which is generally considered to not affect the long term performance or service behaviour of the concrete slab since it will be broken during early age shrinkage.

2.6.6 Slab Base Interaction

The slab and base will slide across each other under thermal and shrinkage movements occurring in the concrete. The interaction between the concrete slab and the base layer will affect the behaviour of the concrete under straining as friction will resist some free movement of the slab. A review of previous modeling methods for the slab base interaction is included below to determine an appropriate method to model this interaction for the current study.

Davids et al., (2007) modeled the interaction between the slab and the supporting material using a contact surface. The interaction between the slab and the base horizontally (for shear transfer) is modeled using a 16 noded quadratic element that is assumed to have no thickness. The shear transfer is modeled as having a non-linear behaviour with a constant stiffness until a peak value at which time the bond is broken and deforms without stress transfer.

Shoukry et al., (2000) modeled the slab base interaction using a coefficient of friction of 1.5 and the interaction allowed for the slab to lift off of the base. Shoukry et al., (2000) noted that the lift off will vary depending on the thermal gradient being applied, as well as the wheel load location and magnitude.

Rufino et al., (2006) gathered data from Denver International Airport pavement that was constructed with strain gauges at the top and bottom of the concrete, as well as deflection gauges in the concrete and base layers. The separation between the slab and the base was compared as part of the research as well. The slab deflection comparisons to the base were compared to temperatures to determine how the slab behaved under different temperature differentials. At longitudinal tie joints, the temperature differential did not seem to have an effect on the deflection of the slab relative to the base as the two remained in contact. The author attributed this to the two surfaces staying in contact during daily thermal cycling at longitudinal tie joints. At the corners of slabs and at transverse joints, the negative temperature differential was found have greater separation between the slab and base layers. The data collected at the interior of the slab showed that positive temperature differential caused separation between the slab and the base layers. The greatest differential deflection between the base and slab layers was found under negative temperature gradients at the corners of the slabs. The slab and base may not be in contact even under wheel load as presented by Rufino et al., (2006) and having a interaction

between the slab and base that allows separation will be important for analysis of alternative devices behaviour to thermal loading.

Levy (2010) modeled the slab base interaction using a contact surface with a frictional coefficient of 0.965 and an initial elastic slip of 0.475 mm. The elastic slip is the elastic displacement that is assumed to occur between the slab and base before the slip occurs. The base and subbase layers were assumed to be tied to each other in the model used by Levy (2010).

Based on the review completed, the surface between the slab and base should be modeled with a friction interaction between the pavement and base, the base and subbase layers can be tied as there is a decreased modulus of elasticity in the subbase layer but no distinct layer interaction.

2.6.7 Thermal Strains

Two different types of thermal strains are typical in a concrete pavement slab: thermal gradient strains and uniform thermal strains. Thermal gradient strains are due to daily temperature changes and cause curling of the slab. Uniform thermal strains occur due to seasonal temperature changes that cause the entire slab to expand or contract evenly. Slab curling caused by thermal stress gradients creates stress concentrations at the dowel bar locations (as the dowels act to restrain the slab from moving). The restraint and resulting stress concentrations caused by the dowels and alternatives is of interest for comparison of alternative joint load transfer designs.

Upwards curling on the slab occurs at night when the top of the slab cools and contracts. During the daytime the top of the slab heats and causes downward curling. General upward and downward curling is presented in Figure 2-15.

Figure 2-15 - Downward and Upwards curling of the Slab

Testing of rigid pavements completed by Sargand and Figueroa (2010) estimated linear gradients of temperature through the pavement based on a temperature reading taken at the top and bottom

of the slab and determined the different values of linear temperature gradient through the slab. The linear gradients ranged from about -0.054 to 0.065 ^{o}C/mm depending on the time of the day and year in early aged concrete. Sargand and Figueroa (2010) noted that the early age of the concrete means some hydration will still be occurring and an additional amount of heating will occur in the slab sections during this time.

Siddique et al., (2005) collected thermal data for a slab section on Interstate 70 that was constructed in 2003. The pavement section was constructed of a 300 mm concrete slab placed on a 100 mm portland cement-treated base and 150 mm of lime treated subbase. Temperature information was collected for the slab at the top surface and 75 mm increments to the bottom surface of the slab. The daily temperature variation at the bottom of the slab (approximately 4^{o}C) is lower than at the top of the slab where the temperature varies by about 18^{o}C in the thermal data collected on Interstate 70 (Siddique et al., 2005). The slab section instrumented with thermal data on Interstate 70 had 5 m spacing between joints. To assess the curling of the slab, Siddique et al., (2005) used an aluminum frame placed on steel pins and an extensometer measured the top surface of the slab.

Based on the data collected by Siddique et al., (2005) it can be seen that the middle of the slab to the outside of the slab increases and decreases causing upward curling of about 0.64 mm and downward of 0.13 mm. This upward and downward curling is not necessarily exact as the data is upward and downward curling from the first reference point at which point there could have been an upward or downward curling occurring at this reference point.

Finite element modeling completed by Siddique et al., (2005) input the thermal gradient as a linear distribution. Altering the linear temperature distribution does not have a linear effect on upward or downward curling. The profiles are also different depending on whether the distribution is upward or downward due to the interaction with the ground and dowel bars at the joint. In order to determine the behaviour of the alternatives, a night and day thermal profile should be used to estimate the upward and downward curling.

Levy (2010) input both day and night thermal profiles to estimate upwards and downwards slab curling. The equations used by Levy (2010) were based on thermal profiles gathered by Jeong

and Zollinger. Equations (2-20) and (2-21) present the daytime and nighttime temperature profiles used by Levy (2010).

$$T_{day}(y) = 5 + 0.076y - 1.6 \times 10^{-4}y^2 \quad (2\text{-}20)$$

$$T_{night}(y) = 2 - 1.28 \times 10^{-4}y^2 \quad (2\text{-}21)$$

Based on the review of thermal profiles for concrete pavement slabs, it was decided to use the nonlinear thermal gradient reported by Levy (2010) for both upward and downward curling to investigate the effectiveness of the alternative joint load transfer devices when subject to thermal variations in the current study.

2.6.8 Creep and Shrinkage Strains

Concrete shrinkage is defined as the contraction of concrete under constant ambient temperatures through drying and hardening (MacGregor & Bartlett, 2000). The primary type of shrinkage is drying shrinkage, which is due to evaporation of the adsorbed water in the gel pores in the hydrated cement. Exposed exterior surfaces will shrink at a rate more quickly than the interior surfaces, causing tensile stress to develop at the exposed exterior surfaces. A concrete pavement slab is exposed at the top surface and is placed directly on the base layer below. For analytical modeling of shrinkage strains it is important to capture the effects of nonlinear shrinkage strain through the depth of the slab including the effects of exposure at the top and bottom of the concrete slab.

Relative humidity, composition of the concrete, and the size of member will all affect the amount that concrete will shrink due to drying. Relative humidities below 40% will have the largest shrinkage strain. The drier air allows more adsorbed water to exit the concrete and hence more shrinkage strain. The shrinkage occurs in the cement paste component of the concrete not the aggregate; therefore, the shrinkage will depend on the volume of paste in a concrete compared to overall volume of concrete. Aggregate type affects the amount of shrinkage because the aggregates resist the shrinkage, and the aggregate modulus of elasticity will determine the resistance of the aggregates to volume changes. The water-cement ratio is related to the porosity of the hydrated cement and the amount of water present in the gel and capillary pores, and hence the amount of shrinkage occurring as the water exits the concrete. For larger members, the rate of evaporation from the interior portion of the concrete is reduced thereby reducing the overall

shrinkage. All of these factors will affect the shrinkage in a concrete pavement slab. Although reducing the shrinkage in concrete would be an effective way to reduce stress at the joint (caused by permanent shrinkage curling), it was not be investigated in detail in the current study because this study is focused on developing alternative devices that reduce restraint at the joint. The curling due to thermal effects would still assumed to occur and alternative devices would be beneficial even if the effects of shrinkage were reduced through control of the above factors.

Testing of concrete specimens 300 x 300 x 150 mm with five surfaces sealed using wax was completed by Kim et al., (1998) to investigate the effects of shrinkage. The top 300 x 300 mm surface was not sealed to force water to flow out of the concrete in one direction. Strain gauges were installed at 20 mm, 50 mm, 80 mm , and 120 mm depths from the exposed surface in the study. The specimens were moist cured for 7 days and then held in a constant temperature of 20 ± 1^{o}C and a constant humidity of $68 \pm 2\%$. Strain measurements decreased as the depth from the exposed surface increased.

Kim et al., (1998) presented strain data with depth for both 28 MPa and 44 MPa concrete mixtures with 65% and 40% water cement ratios, respectively. The data reported by Kim et al., (1998) show that the strain profile due to shrinkage is nonlinear with respect to depth, and that an uneven shrinkage strain profile will exist. The shrinkage profile proposed by CEB-FIP Manual can also be observed to underestimate the strains at in the top half of the slab and overestimate the strains in the bottom half of the slab. The nonlinear shrinkage strain gradient on the slab will cause a curling that should be captured in the shrinkage straining that is applied to the analytical model of the concrete slab.

Based on the experimental results Kim et al., (1998) suggested the use of Equation (2-22) to represent the shrinkage strain with respect to depth in a concrete slab.

$$\varepsilon_{sh}(y,t) = ae^{b\lambda} \qquad (2\text{-}22)$$

Where:

$\lambda = {}^{y}/_{\sqrt{t}}$ (Boltzmann Variable)

$a, b =$ Regression coefficients

Based on Equation (2-22)Kim et al., (1998) found values of 353 x10^{-6} and -415.4 for a and b, respectively, for the 28 MPa mix, and 238 x10^{-6} and -426.1 for the 44 MPa mix with regression coefficients of 0.95 for both.

Levy (2010) modeled the shrinkage strains in the concrete pavement based on the ACI 209 recommended values. The values were calculated at three distinct depths, and a modified version of Equation (2-22) was used to define the shrinkage profile as shown in Equation (2-23).

$$\varepsilon_{sh}(y) = a + e^{\lambda y} \quad (2\text{-}23)$$

The shrinkage profile used by Levy (2010) also eliminates the time variable included in the Kim et al., (1998) shrinkage profile since it is shrinkage strain profile which was assumed to have almost occurred after a year. The constants used for Equation (2-22) by Levy (2010) were: a=24.55, b=0.4465, and λ =0.0269.

Numerous researchers, including Davids et al., (2005) and Levy (2010), suggested that it would be possible to input shrinkage strains into a model by determining the temperature gradient that would result in the estimated shrinkage strains. This is an efficient way to input the strains from shrinkage into a computational model for a static analysis.

2.6.9 Wheel Loading

A pavement slab will encounter a number of different combinations of wheel loads which will vary in weight, tire rolling friction, arrangement of applied loads based on axle locations and the speed at which the traffic is moving. A wide range of wheel load applications could be applied to the slab in order to assess the behaviour of the slab under applied wheel loads. A review on existing wheel load models was completed to determine alternatives and variables that will affect the wheel loading on the slab.

Shoukry et al., (2007) modeled a moving wheel load with a nonlinear explicit solver to model the wheel load. A moving load based on a tandem axle was used in the current study. The load was applied as a 160 kN tandem with the load applied at four locations to represent the moving load. In this model a frictional coefficient for the rolling wheel is 0.02 and the speed for the load was assumed to be 112 km/h.

Levy (2010) modeled the wheel load by applying a static load using a pressure on the top surface of the concrete slab over an area equal to the wheel. The wheel load was applied directly at the joint location on one side of the joint.

The CAN/CSA S6-06–The Canadian Highway Bridge Design Code has a model truck that is used for the structural design of bridges. The highest wheel load on the truck is an 87.5 kN wheel load that is applied over an area of 250mmx 600mm. Increments of this load will be used to model the slab behaviour as it is the largest wheel load used in the Canadian Highway Bridge Design Code.

2.7 Previous Laboratory Experiments

In order to compare alternative device designs, it will be necessary to test the devices in an experimental setting. A review was completed of previous experiments to investigate alternatives used in the past to evaluate dowels and alternative devices. In order to assess alternative designs an experimental testing program will be implemented. The experimental testing program will be focused on wheel load transfer and will not be used to investigate the thermal or shrinkage loading. The review of experimental testing arrangements used previously was limited to load transfer experimental test setups.

Porter et al., (2001) used a modified AASHTO T253 direct shear test to test the load carrying capacity of elliptical GFRP dowels and conventional dowels. The test setup does not involve a granular base, nor does it use the spring reaction of the base layer. The test setup consists of three slabs segments with the joints between the devices being equal (Figure 2-16).

The AASHTO T253 tests eliminate the need for a complicated test frame by using simple statics to test the devices in direct shear. A load is applied to the middle slab and the deflections are measured. In the modified version of AASHTO T253 used by Porter et al., (2001) uses point loads applied 75mm from the joint on each slab. The original AASHTO T253 test used a uniform load along the middle beam which induced a bending moment into the center slab. The modification used by Porter et al., (2001) also involved clamping the ends of the two outside sections to resist rotation.

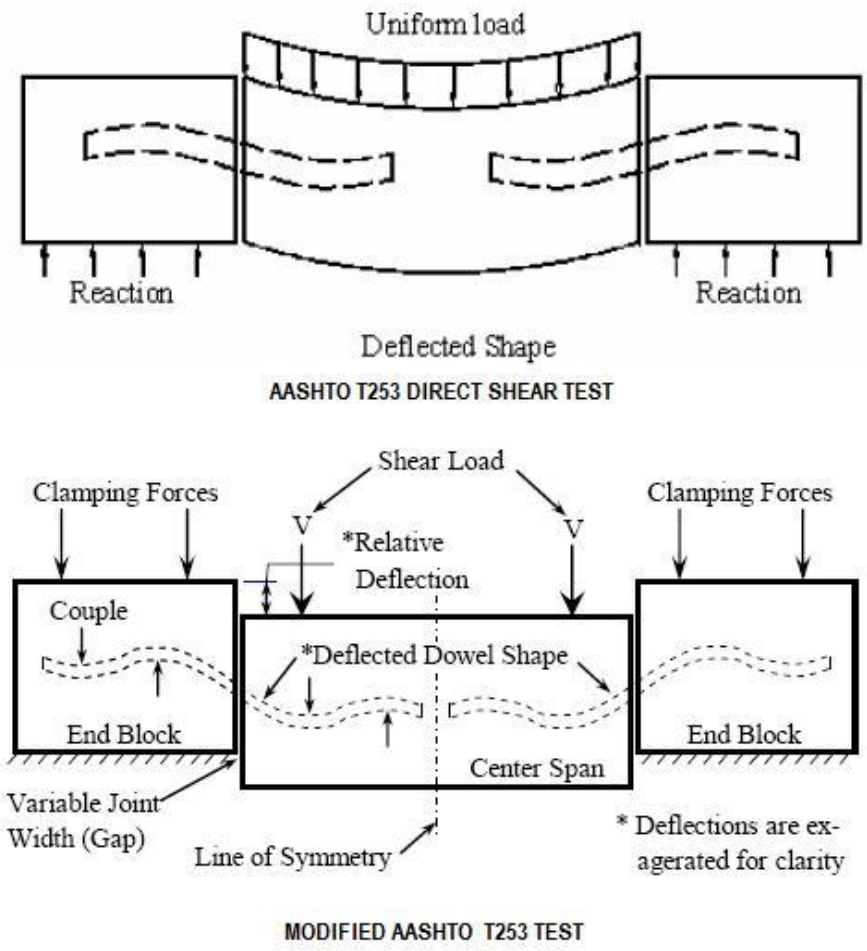

Figure 2-16 – AASHTO T253 and Modified AASHTO T253 Tests (Porter et al., 2006)

Based on Timoshenko beam theory and Friberg's expression for elastic foundation theory on a semi-infinite length, the modulus of dowel support can be found. Using a plot of all the calculated K_o values for a specific load (2000 lb) and dowel shape, it is possible to estimate the modulus of dowel support for different designs.

Porter et al., (2001) conducted Modified AASHTO T253 testing of dowel bars and alternative dowel bars and found the joint width to affect the modulus of dowel support using Friberg's dowel deflection calculations. The effects of the joint width were partially due to the rotation that occurred in the middle slab of the experiment that caused the slabs to come into contact in some of the experiments. When the slabs come into contact with one another, a force occurs between the two slabs causing friction between the slabs along the joint interface. The joints that were

3.125 mm and 12.7 mm had similar values for the modulus of dowel support using the modified T253 test (Porter et al., 2006).

In order to estimate the amount of bearing stresses in the concrete and the stresses in the dowel bars, it is possible to instrument the dowels with strain gauges and use theory to calculate the stresses. Although this has been used in other research (Porter et al., 2006) it does not seem to be ideal for alternative devices because if the device differs in shape and behaviour significantly from a dowel bar the assumptions used to develop the equations may not be valid.

Eddie et al., (2001) used two different experimental setups that were made to simulate joint load transfer at the joint on two different base materials. The purpose of the research was to compare alternative dowel designs, specifically oval GFRP dowels. One of the base support conditions consisted of a weak bed of springs with an equivalent spring stiffness of 3.6MN/m^3. The second base was a stiff soil and was made of crushed limestone 300 mm thick placed in three equal lifts. Plate tests were used to determine the stiffness of the limestone material, and the average stiffness of the base was estimated to be 122 MN/m^2. The dimensions of the slab were 610 mm x 2040 mm and the experimental testing frame is presented in Figure 2-17.

The 610mm slab width ensured that no load spreading occured as the load is applied over a 600mm width. Preventing load spreading through the slab will ensure that the loads in the test are larger than the actual loads that would be encountered in service conditions as some horizontal load spreading along the joint would occur. Although this will not capture the actual behaviour of the pavement slab joint it will make it easier to isolate the effects of the devices without more complex load spreading and will estimate an upper-bound for the stress and damage in the concrete around the joint as well as for stepping of the devices. This is also a manageable size for lab testing as it can be easily implemented in a testing frame.

The dowel bars and GFRP dowels were also tested and compared in a double shear test as well prior to slab testing. Epoxy-coated steel dowels were found to have an ultimate shear strength of 570 MPa. Two different GFRP dowels were tested in the experimental program: Glasform and FiberDowels. The ultimate shear strengths found for Glasform and FiberDowels were 150 MPa and 107 MPa, respectively (Eddie et al., 2001).

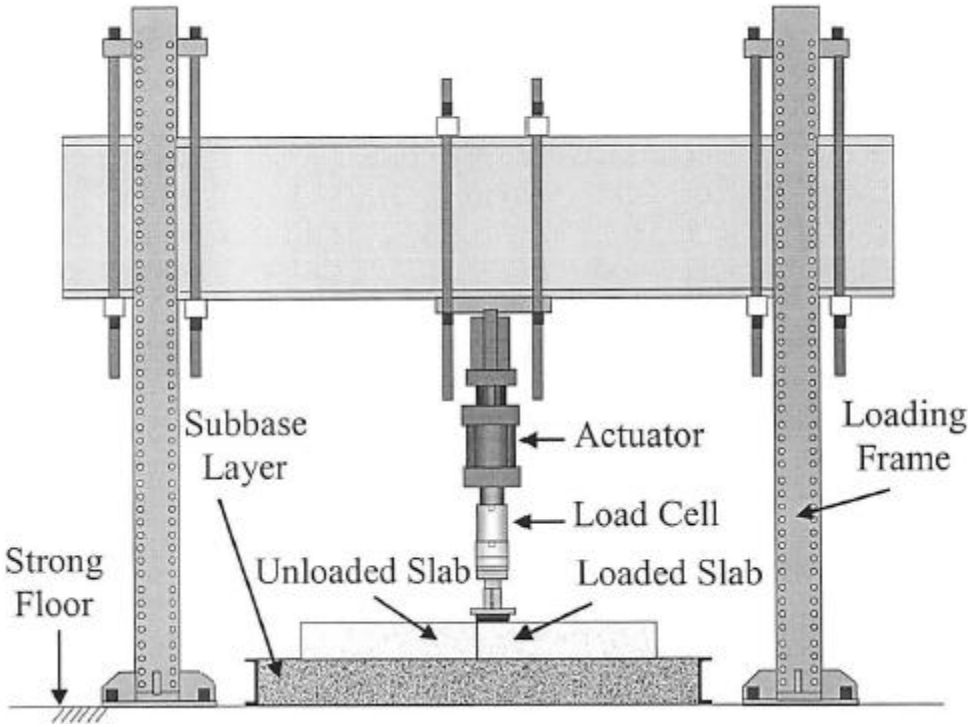

Figure 2-17 – Testing Frame/Setup Used by Eddie et al., (2001)

The first phase of the slab testing by Eddie et al., (2001) used the weak spring support layer and was intended to represent a worst case for base support that would be expected in the field. A single load was applied to failure during this phase of the test. The steel dowel test was stopped at a load of 114 kN excessive deformation had occurred. Side sway of the springs was also noted during the testing. At a load of 100 kN, the steel dowels had about 16 mm of differential joint deflection. The FiberDowels were also loaded in the first phase to a load of 114kN before excessive deflection and side sway of the devices cause the test to be stopped. At 100 kN a differential deflection of about 12 mm was observed with the FiberDowels. Glassform dowels were tested to 135 kN before excessive deflection and side sway caused the test to be stopped. A differential deflection of about 8 mm was observed at a load of 105 kN. As the load was increased during the testing, the back end of the slab was noticed to lift off the base support layer.

The second phase of testing by Eddie et al., (2001) used a stiffer crushed limestone base and applied loads to failure of the devices. The steel dowel device failed at a load of 350 kN beyond the end of dowel 400 mm from the joint on the loaded side of the slab and similarly on the

unloaded side at 500 kN. The FiberDowel was sheared off at a load of 540 kN during this phase of testing. A second test of the FiberDowel behaved similarly to the steel dowel specimen where cracks occurred on either end of the dowel after locking of the joint occurred. The first test completed on the Glassform Dowel caused a crushing failure of the concrete beneath the location of the load plate at a load of 500 kN ,but the dowels were not damaged. The second Glassform Dowel tested by Eddie et al., (2001) had cracking occur on either side of the dowel (loaded end then unloaded end), and was followed by crushing in the loading zone at failure.

The third phase of the testing completed by Eddie et al., (2001) involved cyclic loading of the slabs on the stiff limestone base. The load was cycled between 20kN and 130kN with monotonic tests to 130kN being taken at certain intervals (100, 1000, 10000, 100000, 300000, 600000, and 1000000 cycles). The steel dowels did not show signs of damage occurring to the concrete during the cyclic service load testing. As the cycles increased, the maximum displacement at the joint decreased and slab uplift at the ends of the slab became more consistent on either end of the slab. The FiberDowel was found to have similar cyclic loading results as the steel dowel, with the exception of a small crack occurring at the end of the test. Similarly the Glassform dowel also had very similar results to the steel dowel with no noticeable damage noted by Eddie et al., (2001).

Based on the testing setup used by Eddie et al., (2001) it is possible to obtain valuable experimental behaviour information about the slab in a realistic setting. Their research showed that using a bed of springs can provide a consistent stiffness across the entire base of the slab and also collect information on the load distribution in the slab easily. However, obtaining springs that would behave similar to the actual stiffness of pavement structures would not be economical. Eddie et al. (2001) noted using such a low stiffness (approximately 3% of that expected in a pavement structure) can act as a lower bound support condition, and it can provide an effective way to compare the devices with a easily repeatable testing setup. The thin granular base can also be used to provide a stiff base support; however, it is less repeatable as the base needs to be prepared each time and the compaction may vary from test to test.

Based on the review completed to adequately compare the device behaviour in a concrete pavement slab it would be important to have support layers and simulate a consistent support as a direct shear test will only capture the shear behaviour of the device itself. It is important when

comparing device alternatives to investigate the joint load transfer efficiency as well as the effect of based layers on the behaviour of the device. In this study a consistent base support will be provided in experimental testing to compare devices to capture more than the shear behaviour of the devices.

2.8 Summary of Literature Review

The review of the literature completed identified that load transfer devices are required in concrete pavements to avoid joint stepping and increase comfort. JPCP without load transfer devices have required rehabilitation prior to the service life of the pavement. Conventional load transfer at joints is provided using round steel dowels that reduce stepping but introduce stress concentrations adjacent the devices and introduce misalignment tolerances. Steel used in dowels corrodes in service causing further problems with joint locking. Due to the tight misalignment tolerances and material degradation alternative joint load transfer devices should be investigated.

A review of previous devices investigated showed that other alternatives have been used in the past that have attempted to address dowel bar misalignment and corrosion problems. A number of rehabilitation projects included devices designed to avoid misalignment problems and allow free movement at the joint but without mechanical load transfer at the concrete device interface but were found to be unsuccessful at reducing stepping. GFRP materials have been investigated as substitutions for round dowels but do not address misalignment issues in conventional dowels. Misalignment problems have been addressed in industrial floor slabs using steel diamond and tapered plate dowels but have not been investigated using alternative materials to reduce corrosion. Steel I-beams were found to behave poorly in rehabilitation; however, relying on existing and new concrete bonded surfaces to transfer load. The use of I-beams, tapered plates and GFRP material substitutions will all be investigated in this study.

Conventional dowel bar theory can be used to estimate the deflection and stress at the joint for wheel loading; however, involves multi-variable constants and does not capture the effects of misalignment, shrinkage or thermal straining. Previous investigations have suggested the use of three dimensional finite element analysis to assess the behavior of a concrete slab with nonlinear material properties and contact surfaces. Models have previously been developed successfully previously to assess the effects of shrinkage, thermal, and wheel loading on a JPCP with

traditional dowels. The models previously developed for conventional dowels will be used as a basis for the model development used to compare alternative designs investigated in this study.

Investigations of alternative devices and conventional dowels have been completed in both field and experimental settings. Based on the review of the literature, load transfer testing of conventional dowels and alternatives has been completed using static and cyclic wheel loading applied to one side of the slab or direct shear tests. A direct shear test does not replicate the load transfer occurring at the joint adequately as the effect constant base support is not captured. A static wheel load applied to one side of the joint provides more information about the behaviour of the joint as continuous support is provided; however, due to the nature of the load transfer stress reversals occur as the load is moved from one side of the joint to the other and will not be captured when the load is only applied one side of the joint.

3.0 Load Transfer Device Development

Alternative joint load transfer device concepts were developed in this research program based on a review of literature and engineering materials and mechanics. This chapter presents the device criteria that were used to develop the device concepts, describes alternative device concepts proposed, presents preliminary sizing of devices and design calculations for devices, describes the method of further evaluation that was used on the devices and qualitatively describes the perceived benefits or drawbacks of the different concepts and compares them to dowels as well as one another. Based on a qualitative analysis of the devices, the most promising devices were chosen for further evaluation using finite element analysis for joint load transfer performance and behaviour under shrinkage and thermal loading.

Several design approaches were considered to determine an alternative joint load transfer device. The first type of device is placed at discrete locations along the length of the joint and is aligned perpendicular to the joint (and parallel to traffic), similar to conventional dowels. The first type of devices will be referred to as "Discrete Devices" for the remainder of this thesis. The second type of device is designed to extend the entire width of the joint, and has much different load transfer mechanics than conventional dowel bars. The second type of devices will be referred to as "Continuous Devices" for the remainder of this thesis. Discrete devices will be presented first followed by the continuous devices.

3.1 General Device Criteria

In order to determine alternative device designs, a set of device design criteria was developed. This section presents the general device design criteria used when developing alternative concepts. These general criteria focus on the function of the joint and purpose of the device itself.

Ideally, a load transfer device would transfer half of the wheel load from one side of the joint to the other as the wheel crosses the joint to distribute the load to the base layer similarly to the remainder of the slab. High stress concentrations occur in the concrete slab and in the base layer below the joint at the discontinuity caused by the joint in the pavement slab. This will include

ensuring that the concrete around the device has tolerable stress concentrations that will not cause the concrete to crack and fail at these high stress locations under repetitive load application. The effects of cyclic loading on damaged concrete areas worsen the ability of the device to transfer load. Alternative device concepts should limit stress in the concrete to an acceptable range when transferring wheel loads to avoid extensive concrete damage (limits for plastic strain in concrete for finite element analysis is discussed later in Chapter 5.0).

The load transfer ability of the devices is also measured by the amount of differential deflection or stepping that occurs at the joint. As a wheel crosses the joint location differential deflection at the slab causes rider discomfort. Alternative device concepts should limit the stepping at the joint when transferring wheel loads.

Shrinkage strains on the slab cause large strain gradients on the slab as the concrete hardens. The shrinkage profile causes upward curling of the slab. As the shrinkage strains are applied to the slab, alternative device concepts should maintain acceptable limits of plastic strain in the concrete and not cause stepping in the slab at the joint.

Temperature cycles experienced by the slab cause concrete to expand and contract based on the day-to-day and season-to-season variation. Also thermal strain gradients through the slab due to the differential temperatures at the top and bottom of the slab must be accommodated by the devices. The alternative device concepts must limit stepping due to thermal strain gradients causing slab curling, and should also limit concrete plastic strains to an acceptable limit when thermal strain gradients are applied to the slab.

The method of placement and ease of construction will also be considered in development of the alternative device concepts. Alternative device concepts should alleviate misalignment conditions that could result in premature deterioration in an actual paving application. A general discussion of the misalignment tolerances and possible misalignments will be discussed for each of the devices.

In summary, the criteria used to select the devices in this research were: load transfer efficiency, concrete plastic limits, concrete stress concentrations, qualitative analysis of construction method and tolerances, and maximum base reaction stress.

3.2 Discrete Devices

Discrete devices are alternative device concepts that are assumed to behave similarly to dowel bars to transfer load at the slab. Generally, the devices are intended to improve on dowels with regards to possible restraint of joint movement. A discussion of the device properties, including the benefits of the device for misalignment as well as cost and constructability, are presented in this Chapter.

The proposed discrete devices were intended to combine previous steel dowel development and link it to other conventional round and elliptical dowel development using GFRP as an alternative to steel. Using the assumption that all the discrete devices will behave similarly to dowel bars, the proposed discrete devices were compared using the conventional dowel bar equations presented earlier (Section 2.1.2). The method of analysis using conventional dowel bar equations was adapted from the research on steel plate dowels by Walker et al., (1998). The detailed calculations for each device design can be found in APPENDIX A – Design Calculations for Discrete Devices using Dowel Bar .

The design equations require material properties for the device for elastic and shear modulus. An elastic modulus of 200,000 MPa and shear modulus of 77,000 MPa were assumed for steel dowel bars. The elastic modulus for the GFRP was adopted from manufacturer's product literature as 19,310 MPa and a shear modulus of 3,100 MPa. A range of modulus of dowel support values were used similarly to Walker et al., (1998) since these will vary depending on the behaviour of all the components below the device including the concrete-device interface and the base support provided below. Specific assumptions about the devices used in the calculations are justified in the following sections.

A number of device concepts were considered, although only the devices that were deemed to be promising based on a qualitative analysis are presented herein. Further joint load transfer comparisons using a wheel path finite element model are presented in Chapter 5.0.

3.2.1 GFRP I-beam

GFRP I-beam load transfer device would use a GFRP I-beam placed across the joint on the base layer to provide joint load transfer as shown in Figure 3-1. The device would be placed prior to

concrete placement, and it would avoid the use of dowel baskets or inserters. Advantages of using this type of GFRP device would be ease of placement due to the light shape, and being able to place them directly on the base layers and avoid vertical skew and misplacement misalignments. Previous research on I-beam joint load transfer devices has been limited to joint restoration. Furthermore, GFRP devices have not been considered.

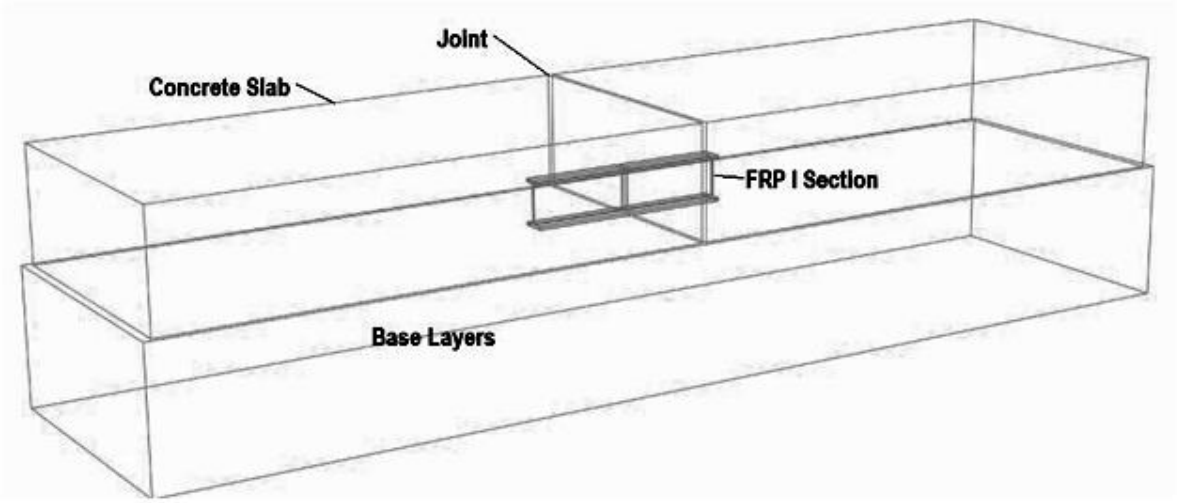

Figure 3-1 - GFRP I-beam Device: General Arrangement

The size of GFRP I-beams considered was limited by what was readily available. A 100 mm deep with 50 mm wide flanges with a section thickness of 6.4 mm (GFRP I 100x50x6.4) was selected and found to be comparable to conventional round dowels using conventional dowel bar equations. Three different spacings were assumed with the GFRP I-beam 300 mm, 600 mm and 900 mm. Devices were compared against conventional round steel dowels at a 300 mm spacing for 25 mm, 32 mm, and 38 mm diameters. Figure 3-2 and Figure 3-3 present the comparisons of the GFRP I-beam with the conventional dowels in terms of concrete bearing stress and differential joint deflection as a function of modulus of dowel support, $K_{o.}$ These figures were generated using Equations (2-1) through (2-5). The entire section modulus of the GFRP I-beam was assumed as well as the entire cross sectional area of the device at the joint for moment and shear deflection calculations. Conventional dowel bar theory assumes the device is located at the mid-height of the slab, however, the GFRP I-beam is placed directly on the base and will be

offset from the mid-height of the slab. No alterations were made to the estimations due to the placement of the GFRP I-beam compared to slab mid-height.

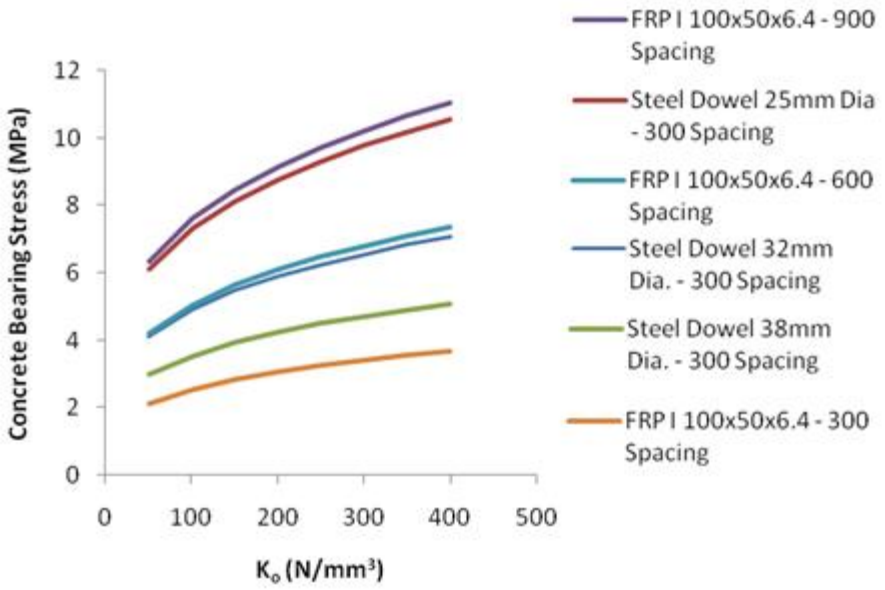

Figure 3-2 – GFRP I-beam 100x50x6.4 Development - Bearing Stress Predictions

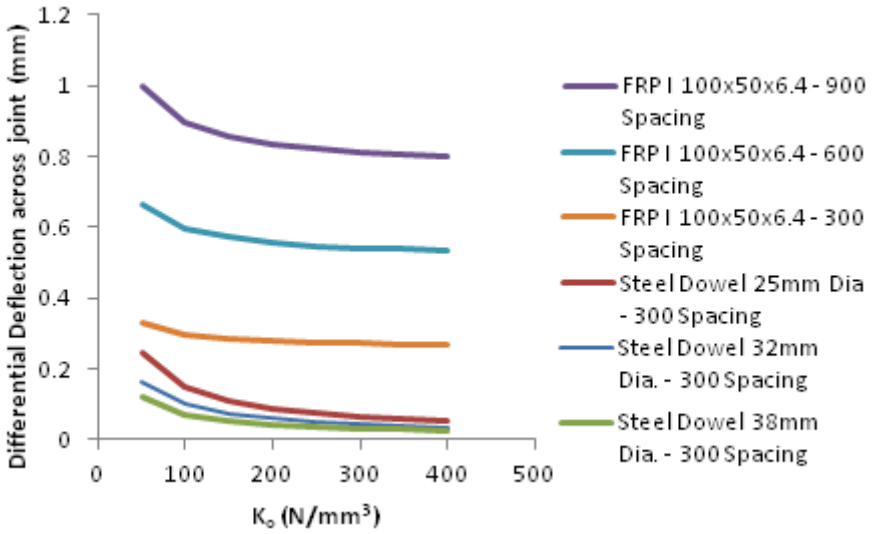

Figure 3-3 - GFRP I-beam 100x50x6.4 Development - Differential Joint Deflection Predictions

The 100x50x6.4 GFRP I-beam at a 300 mm spacing is predicted to reduce the bearing stress at the joint by approximately 1 MPa in comparison to the 38 mm diameter steel dowel. The 100x50x6.4 GFRP I-beam at a spacing of 600 mm behaves very similarly in bearing stress

predictions to a 32 mm dowel at 300 mm spacing. However, the predicted joint deflection is increased for the GFRP devices in comparison to the dowels. All of the differential deflection predictions are below 1 mm. Based on the predicted preliminary analysis of the 100x50x6.4 GFRP I-beam, a spacing of 300 mm could behave similarly to steel dowels while also lowering the bearing stress. Although there is an increased differential deflection, it is assumed that some differential deflection is allowable and maintaining a differential deflection below 1mm was assumed to be satisfactory for preliminary analysis completed in this research only. A more in depth analysis of joint deflection will be completed in Chapter 5.0.

Based on the preliminary analysis of the available GFRP I-beam a 100x50x6.4mm GFRP I-beam will be selected for further investigation. In an attempt to reduce the number of devices to reduce cost, a spacing of 600 mm was selected for modeling using joint load transfer analysis. This section and spacing provide a reasonable compromise between reduced bearing stress and increased differential deflection.

3.2.2 Tapered GFRP Plate dowels

Steel plate dowels have been recently investigated as load transfer devices for paving applications where joints are sawcut and misalignment misplacement of the sawcut is a concern. The progression through different shapes of plate dowels for industrial floor slab applications has included square dowels, rectangular plate dowels, diamond plate dowels, and tapered plate dowels. Based on the previous progression toward the tapered plate dowel the similarities between the general layout of conventional steel dowels and the tapered plate dowel (as shown in Figure 3-4) tapered plate dowels using GFRP as an alternative material were selected for investigation.

The assumed benefit of the GFRP tapered plate is that the general arrangement of the device allows the smaller end of the plate to release easily and not lock when misaligned to a greater tolerance than conventional round steel dowels. The reduced misalignment tolerance is the primary advantage in comparison to conventional steel dowels. The devices are still located at discrete locations and generally restrain the slab from shrinkage and thermal gradients that cause slab curling. This restraint causes high stress in the concrete around the device causing cracking and failure near the joint.

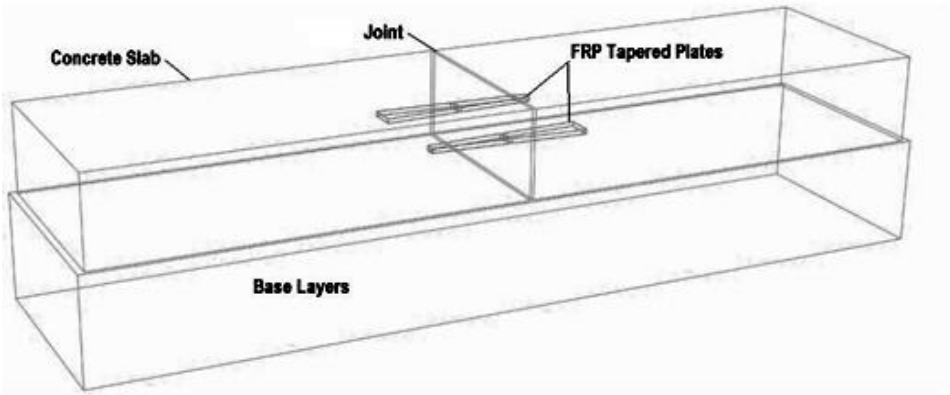

Figure 3-4 – GFRP Tapered Plate General Arrangement (Wheel Path Section Shown)

Three different GFRP Tapered plate arrangements are presented in Figure 3-5 and Figure 3-6. The first section is 75 mm at the wider end of the dowel, tapered evenly from both sides to 25 mm at the narrow end of the dowel. Two different plate thicknesses of 19 mm and 12.5 mm were used with this first section (GFRP Plate 75x25x12.5 and GFRP Plate 75x25x19mm. A spacing of 300 mm was assumed for the plate dowels since they will behave similarly to conventional dowels and method of placement will be similar. A second, wider, GFRP I-beam was used at a 600 mm spacing (GFRP Plate 125x75x12.5).

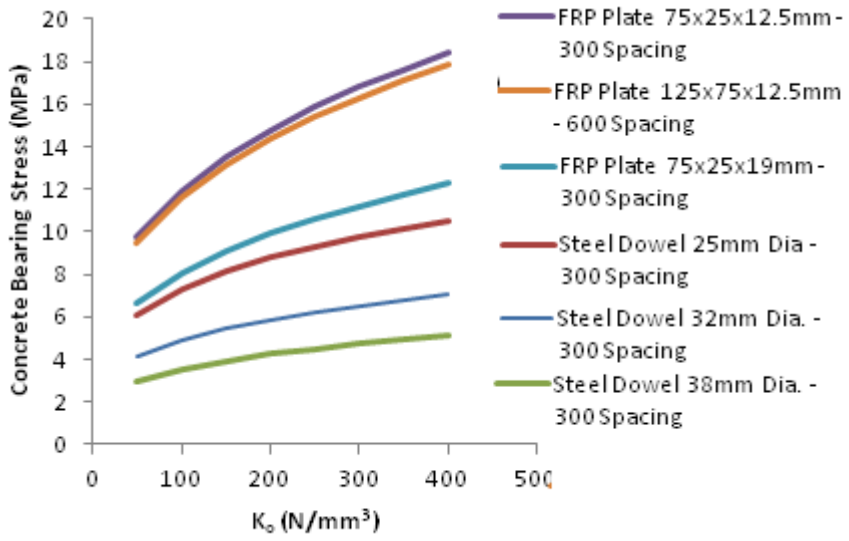

Figure 3-5 - GFRP Tapered plate Development – Bearing Stress Predictions

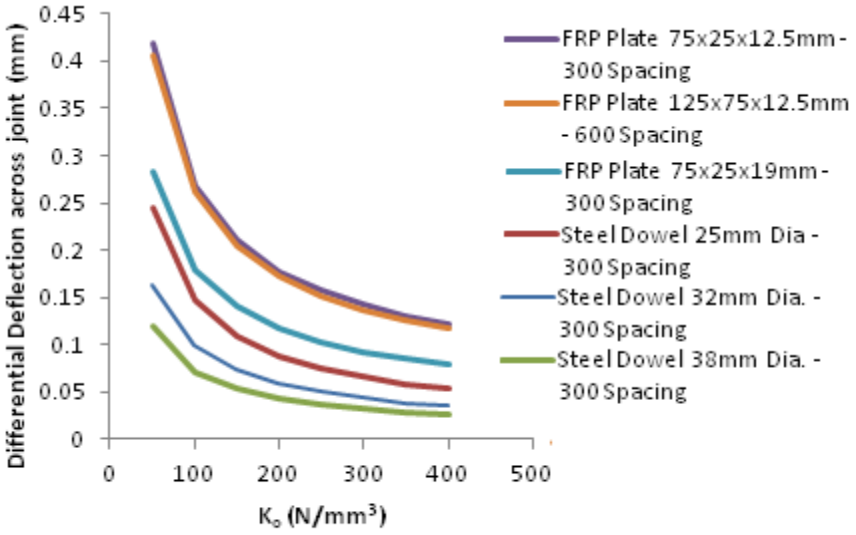

Figure 3-6 – GFRP Tapered plate Development – Differential Joint Deflection Predictions

All three sections proposed for Tapered plate dowels increase the assumed bearing stress in the concrete. The GFRP Plate 75x19x19 mm performed the best with the lowest bearing stress in the concrete. The GFRP thickness was not increased further to try and reduce the bearing stress further, as the reduction from 12.5 mm to 19 mm thickness reduced the predicted bearing stress by only 4MPa. Furthermore, plate thickness larger than 12.5 mm is not readily available.

The GFRP plate dowels performed very similarly to conventional dowels in differential deflection across the joint. All of the arrangements of GFRP tapered plates limited differential deflection at the joint to less than 1 mm. Due to the availability of material for testing purposes, a GFRP Plate 75x25x12.5 mm was selected for further investigation since it performed similar to dowels and provided a reasonable compromise on material use while maintaining bearing and differential deflection limits.

3.3 Continuous Devices

Continuous devices were developed in an attempt to allow the joint to function in a more effective manner. The devices run the entire width of the slab and are placed on the base material. The use of a weaker material and the introduction of the discontinuity prior to the casting of the concrete are assumed to form a weak plane in the concrete in the same way that a

saw cut does, thus creating a location for a planned crack to form. Continuous devices are also aimed at reducing the stresses developed near the joint during shrinkage and thermal strain gradients causing curling, while allowing an efficient means of load transfer continuously across the length of the joint. The assumed load transfer at the joint is through concrete device bearing surfaces at the joint interface created by the device. It is assumed that these concepts will reduce tensile stress locations at the dowel interface as well as reduce the stress at the device concrete interface by increasing the area of joint load transfer. The general benefits and function of the devices are described in this Section.

Although continuous joint devices are also designed with the thought that it could be possible to eliminate the need for saw cutting and is thought to be an advantage of the devices, this aspect will not be investigated in the current study.

The development of the continuous devices considered several shapes. They are concept devices and were analyzed using the quarter slab model developed later in Chapter 7.0. The analysis was intended to show proof of concept with a service loading of shrinkage and thermal strains as well as wheel loading. Ultimate load transfer analysis was not completed due to time constraints.

3.3.1 Continuous Horizontal V Device

The continuous horizontal V device uses a V-shaped section placed along the entire length of the joint across the slab width. Load transfer is intended to occur across the crack by using the slab interlock provided by the formed slab edges on either side of the device as shown in Figure 3-7.

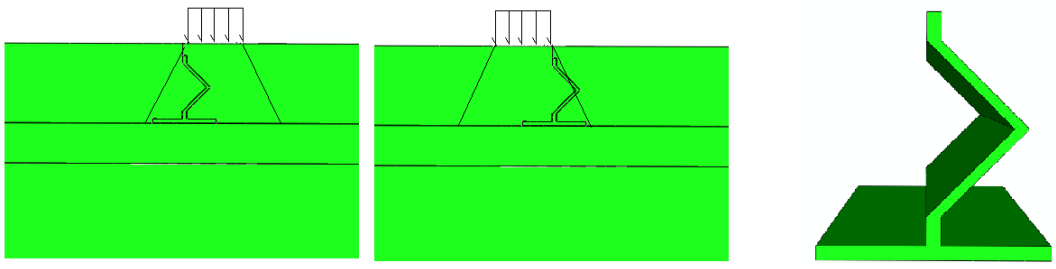

Figure 3-7 – Horizontal V Device

The angle of the V was chosen to avoid acute angles and to ensure that concrete placement should not be a problem. In order for the device to work, there must be adequate consolidation of

concrete around the joint and voids at the joint interface must be avoided. The device is intended to transfer load at the joint in a manner similar to the distribution assumed away from the joint, with the spread of load occurring at an angle of about 45 degrees through the slab. The plastic V shape is assumed to act as a point of weakness in the concrete and will be able to initiate the crack locations due to shrinkage. The concrete at the joint will be formed into a horizontal V, and will work similar to a shear key. As can be seen in Figure 3-7, the assumed load transfer when the load is on the right side of the joint is the bearing of the concrete on the device on the top leg of the horizontal V to the concrete beneath. When the load is on the left side of the joint, the load is transferred through the bottom leg of the horizontal V.

In the first model, no crack was assumed above the device. When the shrinkage load was first applied, the strains above the device become high and close to the cracking limit in tension above the device. Modeling the slab without a crack was completed only to identify tensile stress concentrations during shrinkage to identify the most likely zones for cracking to occur and is presented in Figure 3-8. The Von Mises stress in the quarter slab model with a joint is presented later in Chapter 7.0.

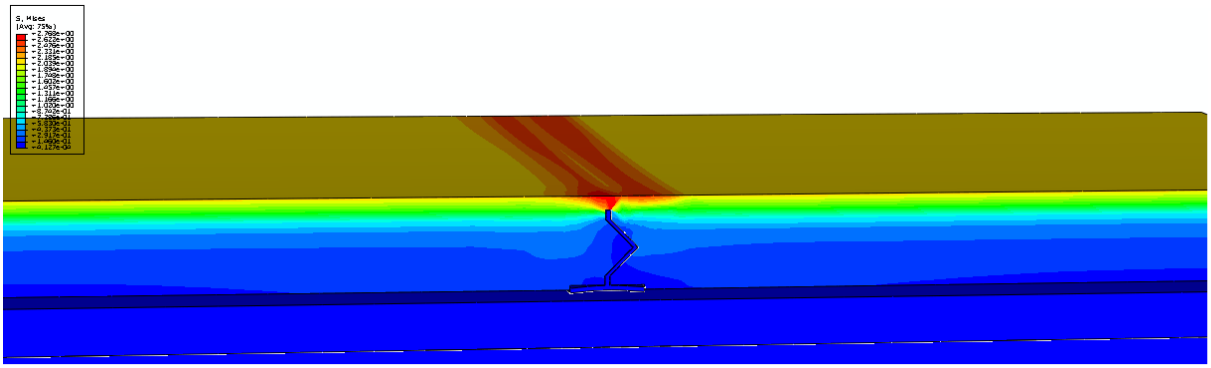

Figure 3-8 – Horizontal V Mises Stresses during Shrinkage step for crack formation

The analysis completed on the model was to demonstrate the concept and to investigate the possibility of creating cracking above the device without the use of a sawcut. A single application of shrinkage was applied, and as the concrete strains became plastic above the device the analysis was stopped. The highest Von Mises stresses located above the joint ranged from about 2.4 MPa to 2.75 MPa tension which is in the range for tension cracking. It appears that

natural shrinkage would create cracking in the intended location, as presented in Figure 3-8. However, the natural cracking due to shrinkage may cause uneven cracking on the top surface, which may lead to damage to the surface of the concrete due to random cracking. Similar problems exist when sawcuts are made too late after the concrete has been placed and shrinkage cracks begin to form. Also, it appears that the cracking may occur on either side of the device from the high tensile zone above this area and extend away from the device face based on the high stress concentrations occurring away from the above the top of the device.

The V shape and compressible material of the device will allow a natural keyed joint. The weaker compressible material in the device itself is planned to allow for the movement required to relieve curling strains due to thermal and shrinkage while still maintaining a constant load transfer surface. The device should also maintain an even surface across the top of the slab and reduce faulting during thermal and shrinkage strains.

The continuous horizontal V device will be investigated further using the quarter slab model for shrinkage, thermal and wheel loading in Chapter 7.0.

3.3.2 Continuous Italic L Device

The continuous italic L device is similar to the horizontal V device, and consists of a compressible material, possibly plastic, that looks similar in shape to an italic L in that the vertical leg extends at a 60 degree angle from the base as shown in Figure 3-9. The angle was chosen to provide load transfer across the joint, but also to keep the size of the device down to ensure that concrete would be placed evenly and without voids around the device. At the bottom of the device, the first portion of the leg is still extended up from the bottom at 90^{o} to reduce possible cracking out of the corner of the device and to improve the ability to place and consolidate the concrete. The italic L device is intended to reduce the locking at the joint by planning a crack formation to allow a slip surface.

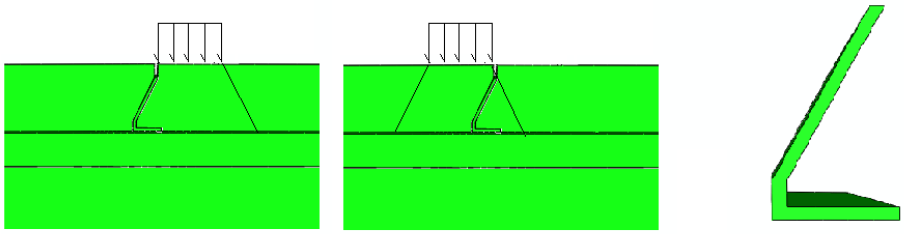

Figure 3-9 – Italic L Device

The italic L device is assumed to create a crack that will extend off the end of the device to the top of the slab during the initial shrinkage of the slab. It would be able to transfer load similar to the V device by using the assumed load distribution through the slab to the base. Figure 3-9 illustrates how the load is assumed to be transferred through the slab at the joint to the base layer. When the wheel is on the right hand side of the joint the load is assumed to follow the concrete along the inside of the device similar to the natural path through the slab. As the load passes to the other side of the device it is assumed that the concrete bearing on the device bears directly across the device to the concrete on the other side of the device.

The slab was initially analyzed with a quarter slab model without a crack above the device. The concrete stress above the device was above the cracking strength of concrete in the location planned and high tensile stresses in the concrete were isolated near the joint location. It is difficult to determine if the crack would still form in this location. It was also determined that the device may cause too much restraint to curling, or may not adequately transfer load at the joint depending on different angles of the device leg. Higher angles are better at transferring load; however, they restrain the slab more and vice versa. The italic L device is not studied further in this research based on the preliminary review.

3.3.3 Continuous Horizontal Pipe Device

The continuous horizontal pipe device was proposed in an attempt to provide load transfer across the joint through a pipe set at the middle of the slab, as shown in Figure 3-10. The pipe is also assumed to provide less restraint to shrinkage strains (and also thermal strains) that cause curling of the slab, as either slab will be able to rotate about the device while still maintaining a level driving surface at the top of the slab. The pipe is a 150 mm in diameter, and is placed on a stand

that has legs that extend above and below the pipe to ensure a discontinuity and weakness in the slab to create a crack. The horizontal pipe device is also assumed to be a compressible material to allow for some movement. Depending on the maximum stress in the pipe portion of the device an alternative (stronger) material may be required for the pipe portion, but alternative materials will not be investigated in this study.

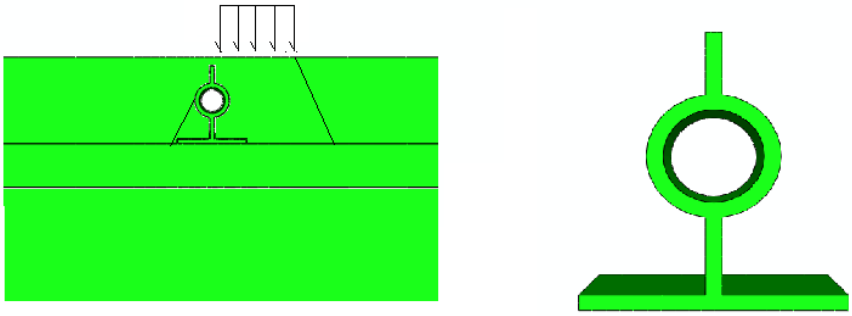

Figure 3-10 – Horizontal Pipe Device

The device transfers load across the joint through the pipe and bears on the concrete on the other side of the joint. The load transfer is similar to the remainder of the slab as the device will bear on the concrete on either side of the joint. If the joint is not sawcut, the application of the shrinkage load produces tensile stress in the concrete above the device that exceed the cracking strength of the concrete. These high tensile zones where plastic damage was occurring were isolated to above the device suggesting cracking should occur above the device. The horizontal pipe device will be analyzed under service conditions with a joint extending from the top leg of the device in the concrete in Chapter 7.0 (assuming either a sawcut or natural cracking has occurred during shrinkage).

3.3.4 Foundation Pipe Device

The foundation pipe device consists of a pipe being placed with half the pipe above grade and half below grade at the joint location. Extending from the top of the pipe is a straight piece of plastic that would be used to create the crack location as can be seen in Figure 3-11. The pipe would be a 200 mm diameter ABS pipe section. The section also includes two pieces that extend up from the top of the device in order to provide a location for the crack to occur. Two pieces were chosen in the current study to provide also for a place to allow drainage at the joint to occur. Use of the device as drainage at the joint was not investigated in this study although it is

thought that reducing water ingress at the joint location could reduce subgrade failure which has shown to increase faulting and reduce load transfer efficiency at the joint. These benefits are not considered.

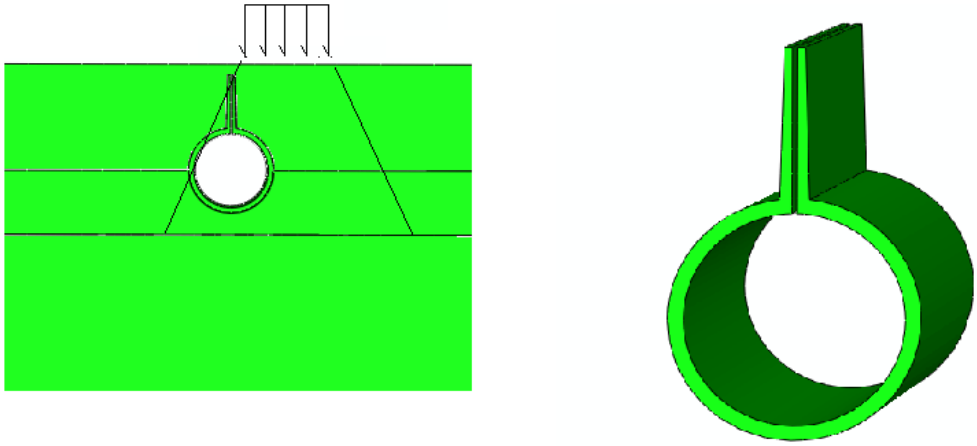

Figure 3-11 – Foundation Pipe Device

The pipe section was chosen to account for the effects of shrinkage and thermal gradients since it would allow a natural surface from which the slab could curl away and towards the device. The device itself is then intended to transfer the load through deeper to the subgrade at a larger area below. The faulting at the joint, however, is dependent in this case on the strength of the pipe device itself and the base material below as the device is not necessarily restrained from settling into the base material. Once the contact is lost between the opposite side of the joint and the device due to settling that may occur the device does not provide load transfer to the opposite side of the slab. Based on the rational analysis of the load transfer mechanism it was determined the device would not reduce faulting at the joint and would therefore not be a promising device and was not investigated further.

3.4 Summary of Device Development

Concept development and preliminary analysis of continuous and discrete joint load transfer devices were presented in this Chapter. Continuous devices generally run the full width of the joint whereas discrete devices are placed at discrete locations along the joint width.

The basis of design for the devices including the perceived advantages and disadvantages is presented in Table 3-1.

Table 3-1 – Device Development Summary Comparison

Device Description	Perceived Advantages	Perceived Disadvantages
GFRP I-beam	• Eliminates vertical misalignment by being placed directly on base material • Construction would be similar to conventional dowels and should be easy to implement	• Introduces a new misalignment plane Still creates stress concentrations at device locations under load transfer
GFRP Tapered Plate	• Reduces horizontal misalignment tolerance with tapered shape Construction would be similar to conventional dowels and should be easy to implement GFRP Material reduces corrosion problems	• Introduces a new misalignment plane • Creates stress concentrations at device locations under load transfer
Continuous Horizontal V Device	• Eliminates stress concentrations at the device concrete interface by providing a continuous load transfer surface • Eliminates horizontal misalignment by running continuously along the joint length • Could be used as a joint forming device • Eliminates vertical misalignment by being placed directly on the base material • Material would not corrode	• May not provide as effective of load transfer as traditional dowels Cracking may occur adjacent to the device causing failure
Continuous Italic L Device		• Does not provide adequate load transfer when the load is on the leave side of the joint • Cracking may occur adjacent to the device causing failure
Continuous Horizontal Pipe Device		• May not provide as effective of load transfer as traditional dowels • Cracking may occur adjacent to the device causing failure
Continuous Foundation Pipe Device		• Does not provide adequate load transfer when the load is on the leave side of the joint • Cracking may occur adjacent to the device causing failure

The discrete devices that were proposed in this Chapter include the GFRP I-beam and GFRP tapered plate section. Both the GFRP I-beam and GFRP tapered plate sections were determined to be capable of transferring wheel load at the joint comparably well to dowels based on analysis using conventional dowel bar theory equations for joint deflection and concrete bearing stresses. Each of the GFRP I-beam and GFRP tapered plate dowels were investigated further in this study. The discrete devices are compared to conventional round steel dowels, in Chapter 5.0, using finite element analysis to investigate wheel load transfer on a wheel path model. In Chapter 6.0, discrete devices are compared to conventional round steel dowels using experimental testing on a wheel path model. Finally, in Chapter 7.0, the discrete devices are compared to conventional round steel dowel bars using quarter slab finite element models with service loading applied.

The continuous devices that were proposed in this Section include the horizontal V device, the italic L device, horizontal pipe device, and foundation pipe device. Based on the rational analysis completed on the continuous devices, the horizontal V and horizontal pipe devices were investigated further. The continuous devices are analyzed and compared to conventional round steel dowels, in Chapter 7.0, using quarter slab finite element models with service loading applied.

4.0 Finite Element Model Development

Finite element modeling of the pavement structure was used to investigate the behaviour of the joints and to compare the alternative load transfer devices. As discussed previously, two different model geometries were developed for the comparison of the devices. The finite element model is also a continuation of work previously completed at the University of Waterloo by both Leong, et al., (2006) Levy (2010), and various material and loading inputs were based on this model. The shrinkage and thermal strains and material inputs were reevaluated previously in the Literature Review (Chapter Two), and further details are provided in this Chapter.

Four different model geometries were used in the finite analysis study: a wheel path model, and full slab, half-slab and quarter slab models. The wheel path model was used to investigate the joint load transfer of discrete devices as described in Chapter 5.0. During the development of the wheel path model, larger model geometries of a full and half slab were also used, and the global response of the joint was investigated with dowels to compare the effects of the size of slab section as well as boundary conditions in developing the wheel path model geometry. Detailed comparisons of the larger models to the wheel path model are described in Chapter 5.0. The full and half slab models were used to investigate the joint load transfer of conventional dowels in more depth, and to study the effects of load transfer and restraint in other directions not captured in the wheel path model. These comparisons are also presented in Chapter 5.0.

The second model used to compare the devices is a quarter slab model. The quarter slab model is an efficient model of full slab behaviour when subjected to shrinkage, thermal and wheel loading. The quarter slab model was used to investigate the service loading of all the devices (both continuous and discrete) that proved to be promising based on preliminary analysis. The loading on the quarter slab model consisted of shrinkage and thermal strain gradients, as well as wheel loading applied at the joint. The service load analysis using the quarter slab model is described in Chapter 7.0.

The materials used in the study consist of subbase, base, concrete, steel, GFRP, as well as a compressible material that was assumed to be a plastic. The material properties, as well as the general load and strain application, are explained in this Chapter. Detailed geometries and

boundary conditions of the wheel path and quarter slab models are discussed in Chapter 5.0 and 7.0.

4.1 Material Properties

The required material properties were based on the material models that are available in ABAQUS. Specific input values were chosen based on previous finite element modeling of pavements reported in the literature and performed at the University of Waterloo, as well as using the recommendations from the ABAQUS manual.

4.1.1 Concrete

Concrete is a brittle, anisotropic material that has different behaviour in compression and tension. A nonlinear material model should be chosen to appropriately model the concrete slab. The nonlinear material model has to capture both the anisotropic as well as damage behaviour of concrete. A review of the uniaxial behaviour of concrete in tension and compression was completed in the Literature Review (Section 2.6.2) and will be used as a basis and comparison for inputs used in the concrete model. This section is aimed at describing the material model chosen and the material inputs based on the literature, research previously completed at the University of Waterloo (Levy, 2010) and the ABAQUS Manual (2008).

ABAQUS contains three inelastic concrete models: concrete smeared cracking, cracking model for concrete, and concrete damaged plasticity model. All three models are intended primarily for the use with reinforced concrete, but can also be used with plain concrete structures. The concrete smeared cracking model is designed for monotonic straining at low confining pressures in ABAQUS/Standard, and defines cracking as the most important aspect of the behaviour. The cracking model for concrete is designed to model brittle discontinuities in a model, and is for use in ABAQUS/Explicit. The concrete damaged plasticity model assumes that the main two failure mechanisms in concrete are compressive crushing and tensile cracking (ABAQUS, 2008). The ABAQUS (2008) manual also notes that the concrete damaged plasticity model is capable of modeling concrete under cyclic loading. The concrete damaged plasticity model was chosen by Prabhu et al. (2007) and Levy (2010) to represent the concrete slab material behaviour.

ABAQUS represents the stress-strain relationship in the concrete damaged plasticity model using the original element stiffness matrix and the effective stress is defined in Equation (4-1).

$$\bar{\sigma} \overset{\text{def}}{=} D_0^{el} : (\varepsilon - \varepsilon^{pl}) \qquad (4\text{-}1)$$

$\bar{\sigma}$ is the effective stress

D_0^{el} is the original element stiffness;

ε and ε^{pl} are the elastic and plastic strains respectively

A single scalar degradation value is used to represent the damage in the concrete damaged plasticity model and the Cauchy stress is presented in Equation (4-2). The damage variable is used to represent the ratio of effective load carrying area (ABAQUS, 2008).

$$\sigma = (1 - d)\bar{\sigma} \qquad (4\text{-}2)$$

Where:

σ is the Cauchy Stress; and

$(1 - d)$ represents the ratio of effective load carrying area of the material or the overall area minus the damaged areas

The damage variable, d, is based on the effective stress in the material as well as a set of hardening variables that are inputs to the material model. ABAQUS assumes the strain rate to be additive as shown in Equation (4-3).

$$\dot{\varepsilon} = \dot{\varepsilon}^{el} + \dot{\varepsilon}^{pl} \qquad (4\text{-}3)$$

Where:

$\dot{\varepsilon}^{el}$ and $\dot{\varepsilon}^{pl}$ are the elastic and plastic strain rates respectively

The hardening variables represent the damaged behaviour of the material in tension and compression (ABAQUS, 2008). The general equations for the hardening variables are presented in Equation (4-4).

$$\tilde{\varepsilon}^{pl} = \begin{bmatrix} \tilde{\varepsilon}_t^{pl} \\ \tilde{\varepsilon}_c^{pl} \end{bmatrix};\ \dot{\tilde{\varepsilon}}^{pl} = h(\bar{\sigma}, \tilde{\varepsilon}^{pl}) \cdot \dot{\varepsilon}^{pl} \qquad (4\text{-}4)$$

Where:

$\tilde{\varepsilon}_t^{pl}$ and $\tilde{\varepsilon}_c^{pl}$ are the plastic equivalent strains in tension and compression respectively;

Inputs for the behaviour of concrete in compression and tension are explained in detail first for the damage variables as well as inelastic stress-strain relationship before proceeding into a detailed description of the three dimensional aspect. The hardening variables are related to the equivalent plastic strain in tension and compression which is used to relate the damage values input for compression and tension as explained below.

The inputs used in the concrete damaged plasticity model for density, Young's Elastic Modulus, Poisson's Ratio and thermal expansion are presented in Table 4-1. The density is used to apply the self-weight loading on the concrete. Young's Elastic Modulus and Poisson's ratio are used to model the elastic range of the concrete and to formulate the original element stiffness matrix (D_0^{el}). The thermal coefficient of expansion is used to apply straining functions due to thermal and shrinkage strains to the concrete.

Table 4-1 – Concrete General Material Properties

Description of Value	Value	
Density	2.40E-09	tonne/mm^3
Young's Elastic Modulus (E_0)	22576	N/mm^2
Poisson's Ratio	0.18	Unitless
Coefficient of Thermal Expansion	1.10E-05	/ ^{o}C

Figure 4-1 presents the behaviour of concrete in uniaxial compression used by the ABAQUS concrete damaged plasticity model.

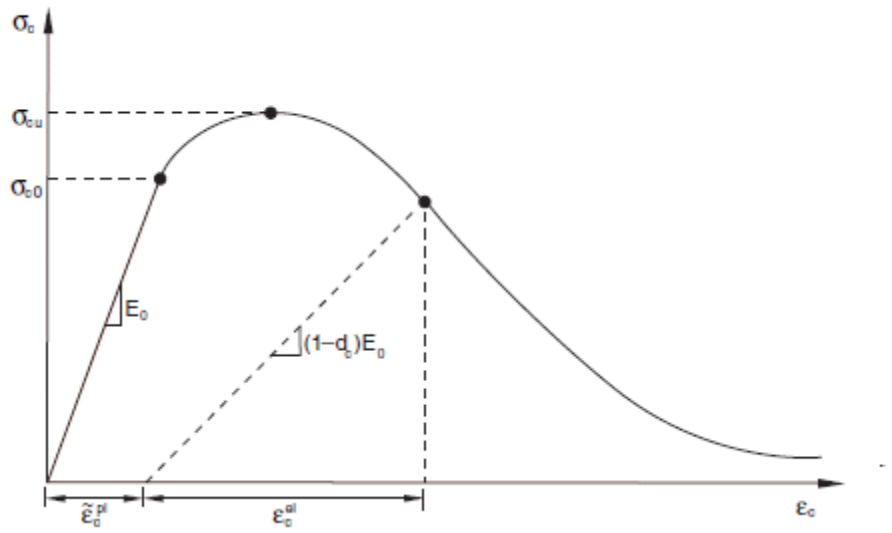

Figure 4-1 – Compressive stress-strain behaviour of Concrete used in ABAQUS (2008)

The material initially behaves linear elastically with a modulus of elasticity of E_0 until it reaches an elastic limit (σ_{c0}). Strain hardening occurs between σ_{c0} and σ_{cu} in Figure 4-1 where the material requires further stress to increase the strain beyond the elastic limit (σ_{c0}). After the material reaches the ultimate stress of σ_{cu} the material resistance reduces as plastic strains develop which is known as strain softening. As plastic straining occurs in concrete in compression crushing of the material occurs which reduces the stiffness of the damaged material. The reduced stiffness is shown in the unloading portion of Figure 4-1 and is represented using the damage value d_c, which is a scalar value used to reduce the stiffness of the material based on the inelastic strain reached (described later in this Chapter). The strain remaining in the material after unloading is the plastic strain in the material and the strain recovered upon unloading is the elastic strain (which are shown as ε_c^{pl} and ε_c^{el} in Figure 4-1).

The elastic modulus was input as 22,500 N/mm^2, based on the input used by Levy (2010), to model the elastic range of the concrete. To define the remainder of the compressive behaviour of the concrete, stress and corresponding inelastic strain values, presented in Table 4-2, were input. Both the elastic modulus and the and the inelastic strains are estimated based the Equations from the CEB-FIB-Model code presented previously in Equations (2-8) and (2-9). These values were established by fitting a curve for a typical 30 MPa concrete.

Table 4-2 – Concrete stress and inelastic strain

Stress (MPa)	Inelastic Strain
21	0
22.2	1.66E-05
25.8	0.000107
28.25	0.0002486
29.6	0.000439
30	0.0006712
24.68	0.001157
18.92	0.0016619
13.95	0.0021321
10.13	0.0025513
7.36	0.0029241
5.39	0.0032613
3	0.003867
1.09	0.004516
0.04	0.009998
0.002	0.02

When the yield stress is reached there is no plastic strain in the concrete. Beyond the yield stress plastic strains begin to occur in uniaxial compression as can be noticed from the increase in the stress from 21 to 30 MPa as the plastic strain increases to 0.00067. Beyond this point the stress is reduced as the plastic straining continues to occur which is represented in Table 4-2 by the reduction in stress from 30 to 0.002 MPa while the strain increases from 0.00067 to 0.02.

The final inputs needed to model the uniaxial compressive behaviour of the concrete are the damage characteristics. In order to define an amount of damage in compression, manual inputs were used that related the damage value (which reduces the elastic modulus by the damage value as a ratio of damaged area) to the amount of inelastic strain.

The damage values assumed were based on the values presented in the ABAQUS verification manual (ABAQUS, 2008). Generally, as the compressive inelastic strain increases more damage occurs which results in less load carrying area due to crushed concrete in compression and results in reduced stiffness in the material as it is unloaded.

Table 4-3 – Concrete compressive damage associated with inelastic strain (ABAQUS, 2008)

Damage value, dc	Inelastic Strain
0	0
0.13	0.0004
0.24	0.0008
0.34	0.0012
0.43	0.0016
0.5	0.002
0.57	0.0024
0.71	0.0036
0.82	0.005
0.97	0.01

The uniaxial tensile behaviour of the concrete used in the ABAQUS concrete damaged plasticity model is presented in Figure 4-2. The behaviour is linear elastic with the same modulus of elasticity used for compression (E_0) until the yield stress is reached (σ_{t0}). Microcracking occurs beyond this point and is represented by strain softening (where the plastic strains increase with a reduction in stress). Damage associated with the plastic straining is used to reduce the stiffness of the material during unloading as represented by variable d_t. The elastic strain is represented by ε_t^{el} and the plastic strain is represented by ε_t^{pl} in Figure 4-2.

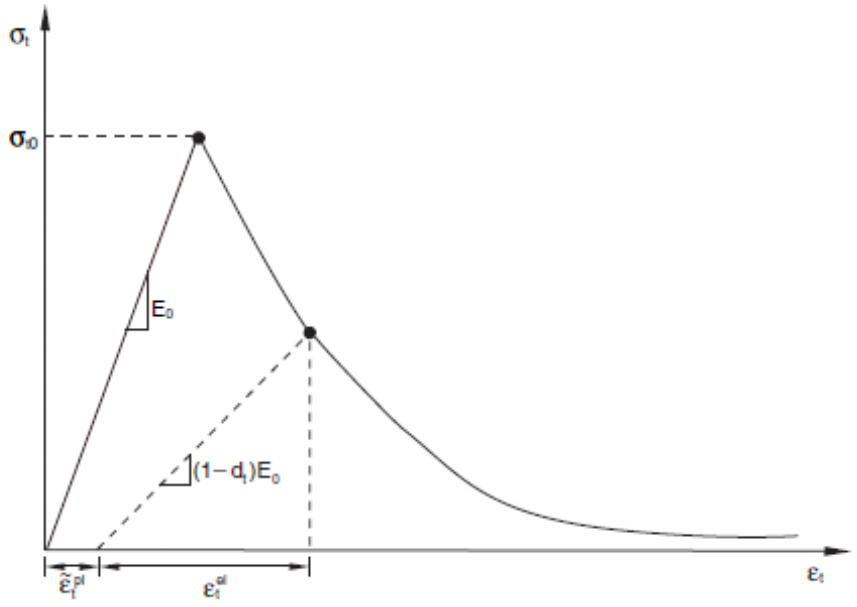

Figure 4-2 – Tensile stress-strain behaviour of Concrete used in ABAQUS (ABAQUS, 2008)

Tension stiffening must be defined properly to ensure that the model does not become unstable when local failures occur. The tension stiffening is based around the reduction in stress as plastic straining occurs in the material. If this reduction is too rapid, a sudden loss of stress will occur in the material locally, which will cause the model to be unstable. Tension stiffening can be either defined by a stress-strain relationship or a fracture energy criterion. In order to avoid potential complications in the plain concrete models and based on the ABAQUS Manual (ABAQUS, 2008), suggestions fracture energy was selected to define tension stiffening.

The fracture energy criterion used in the model is developed based on the Hillerborg fracture energy proposal in which a concrete material will crack under tension. The value G_F is the fracture energy necessary to create a unit crack surface. The fracture energy can be either defined as a constant or using tabular data to represent the stress-displacement relationship. The fracture energy is presented in Figure 4-3.

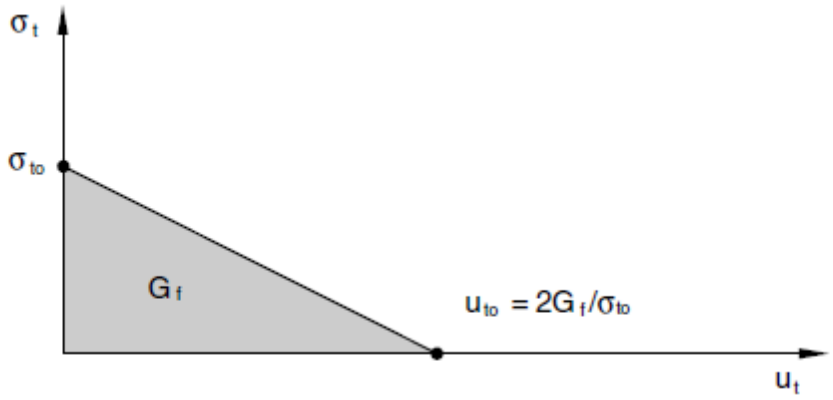

Figure 4-3 – Tensile fracture energy in concrete based on Hillerborg proposal (ABAQUS, 2008)

In Figure 4-3, the horizontal axis is represented by u_t which is the tensile crack displacement when the concrete reaches a stress of σ_{t0} and cracking begins. Energy is released depending on the crack opening length until the material has no strength left at a crack opening length of u_{to}. This representation shown of the fracture energy constant is the area under the stress displacement relationship presented in Figure 4-3. A constant value for fracture energy was used for the modeling of concrete in tension. A value of 0.1338 N/mm was used based on the value calculated previous in research completed at the University of Waterloo by Levy (2010), which is based on the CEB-FIP Model code approximation presented previously in Equation (2-14).

The tensile strength of concrete, σ_{t0}, was taken as 3 MPa based on the value used by Levy (2010).

The finite element model associates a crack length based on characteristic length of a line across a first-order element. Since the model assumes this length based on element geometries, elements with high aspect ratios may have different results depending on the direction of cracking. Mesh refinement to ensure the aspect ratio does not impact on the non-linear concrete material is completed in the wheel load model section (Chapter 5.0) to investigate these effects and to determine approximate mesh geometries to be used in the quarter-slab models.

Tensile damage is not included in the concrete model used. This means that upon reloading in tension, the concrete will not have a scalar decrease in the material stiffness model. Under cyclic loading the behaviour of the concrete will behave differently depending on the previous damage that has occurred. Stiffness recovery values are input for the compressive and tensile behaviour of concrete under reversed loading. The ABAQUS Manual (2008) suggests that when load is reversed from compression to tension, the micro cracking occurring during crushing of the concrete does not recover stiffness upon reversed loading. The opposite is true when the load is reversed from tension to compression. This is represented using a value of 1 for the stiffness recovery variable, w_t, and 0 for the stiffness recovery value, w_c. The uniaxial behaviour is depicted in Figure 4-4.

The behaviour of the concrete in compression and tension has been explained above. In order to model the three dimensional behaviour of the material, a yield function that defines the failure plane in effective stress space is required. The concrete damage model in ABAQUS defines the amount of damage in the concrete as a function of the plastic strain rate and the effective stress. The effective stress is based on original element stiffness and the total strain minus the plastic strain. The damage variable in the model is used to represent a reduction in the amount of effective load carrying area due to the damaged areas. The damage variable can be applied to the effective stress to determine the Cauchy stress. The yield function in the concrete damaged plasticity model is defined based on the work of Lubliner et al. (1989) with the Lee and Fenves (1998) alterations to account for the differences in tension and compression, and is presented in Equation (4-5) (ABAQUS, 2008).

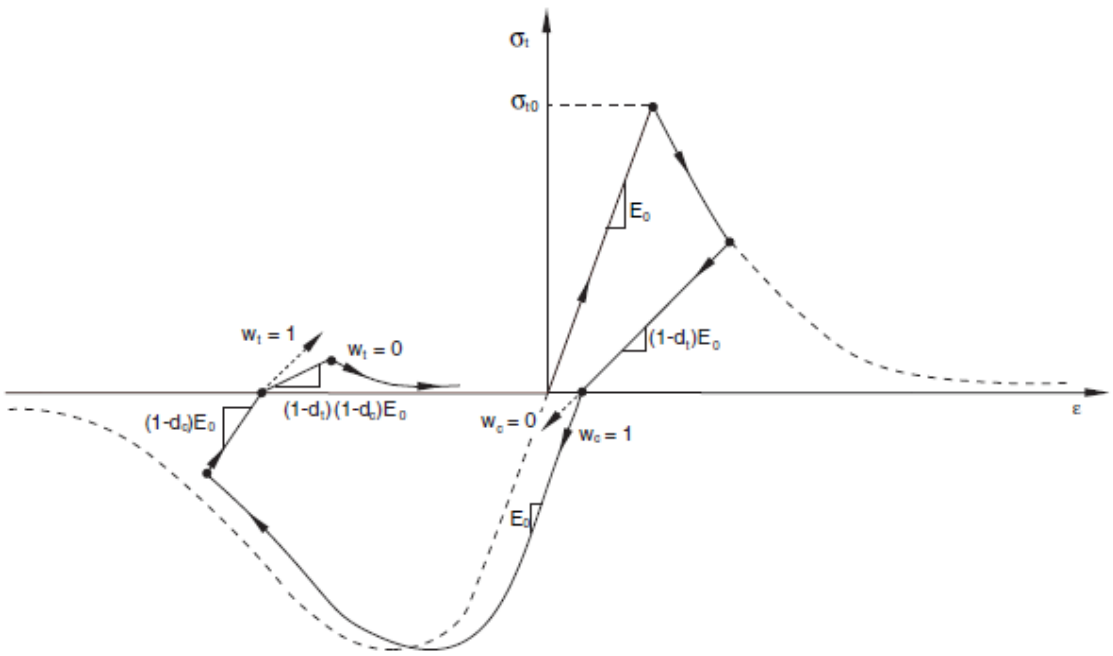

Figure 4-4 – Tension and Stiffness recovery under compressive and tensile loading in ABAQUS (2008)

$$F(\bar{\sigma}, \bar{\varepsilon}^{pl}) = \frac{1}{1-\alpha}\left(\bar{p} - 3\alpha\bar{q} + \beta(\bar{\varepsilon}^{pl})\langle\hat{\bar{\sigma}}_{max}\rangle - \gamma\langle-\hat{\bar{\sigma}}_{max}\rangle\right) - \bar{\sigma}_c(\bar{\varepsilon}_c^{pl}) \leq 0 \tag{4-5}$$

Where:

$$\bar{p} = -\frac{1}{3}\bar{\sigma}{:}\,I$$

$$\bar{q} = \sqrt{\frac{3}{2}\bar{S}{:}\,\bar{S}}$$

$$\bar{S} = \bar{p}I + \bar{\sigma}$$

$$\alpha = \frac{\sigma_{bO} - \sigma_{cO}}{2\sigma_{bO} - \sigma_{cO}}$$

$$\beta(\bar{\varepsilon}^{pl}) = \frac{\bar{\sigma}_c(\bar{\varepsilon}_c^{pl})}{\bar{\sigma}_t(\bar{\varepsilon}_t^{pl})}(1-\alpha) - (1+\alpha)$$

In the above Equation (4-5): $\bar{p}$ is known as the hydrostatic stress, $\bar{q}$ is the Mises equivalent effective stress, $\bar{S}$ is the deviatoric part of the effective stress tensor $\bar{\sigma}$, $\hat{\bar{\sigma}}_{max}$ is the maximum

eigenvalue of $\bar{\sigma}$, $\sigma_{bO}$is the equibiaxial compressive yield stress, σ_{cO} is the uniaxial yield stress, α and γ are material constants. In the function for β, the values $\bar{\sigma}_c$ and $\bar{\sigma}_t$ are the effective compressive and tensile cohesion stresses.

In order for the plastic model to be applied in ABAQUS, the ratio σ_{bo}/σ_{co} , which is the ratio of biaxial compressive strength to the uniaxial compressive strength of concrete, must be input. The average values of σ_{bo}/σ_{co} for concrete as stated in the ABAQUS Theory manual range from 1.10 to 1.16. This range will correspond to values of α from 0.08 to 0.12 (ABAQUS, 2008). The biaxial behaviour of Equation (4-5) for a typical concrete is presented in Figure 4-5.

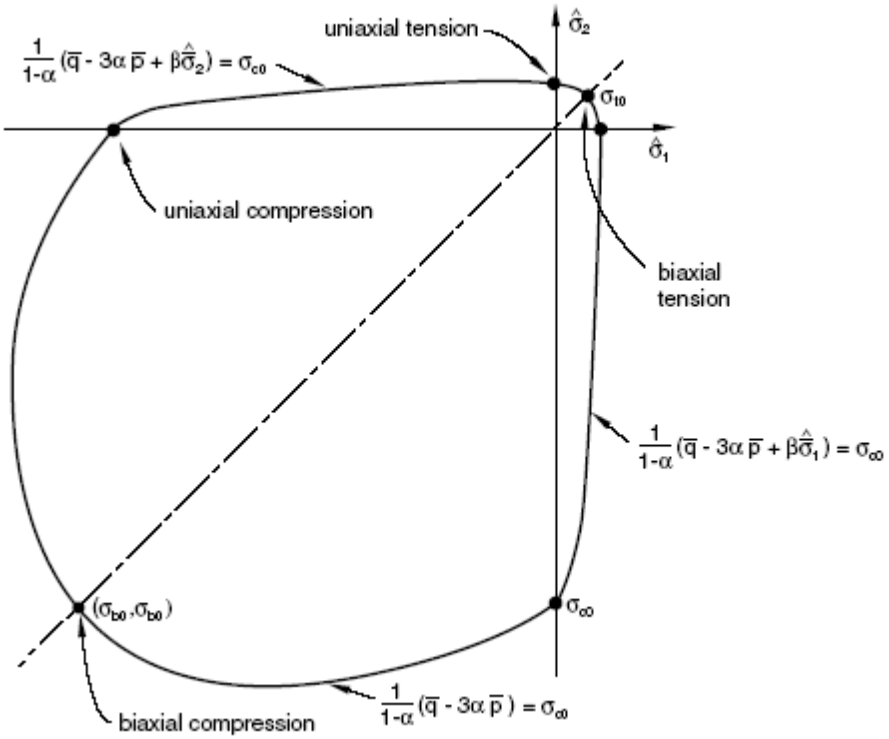

Figure 4-5 – Biaxial stress yield surface for concrete (ABAQUS, 2008)

The yield surface in the model will be similar to the behaviour presented in Figure 4-5, with the concrete having additional strength in biaxial compression compared to axial compression.

The variable, γ, is a dimensionless material constant that is used in the model (Equation (4-5)) when the there is a state of triaxial compression (ABAQUS, 2008). The value for γ is determined

by comparing the tensile and compressive meridians. The tensile meridian is defined as the stress states where $\hat{\bar{\sigma}}_{max} = \hat{\bar{\sigma}}_1 > \hat{\bar{\sigma}}_2 = \hat{\bar{\sigma}}_3$ and the compressive meridian is stress states $\hat{\bar{\sigma}}_{max} = \hat{\bar{\sigma}}_1 = \hat{\bar{\sigma}}_2 > \hat{\bar{\sigma}}_3$ ($\hat{\bar{\sigma}}_{i=1-3}$ are the eigenvalues of the effective stress tensor). The value for $\hat{\bar{\sigma}}_{max}$ is evaluated for the tensile and compressive meridians as $(\hat{\bar{\sigma}}_{max})_{TM} = 2/3\,\bar{q} - \bar{p}$ and $(\hat{\bar{\sigma}}_{max})_{CM} = 1/3\,\bar{q} - \bar{p}$ as mentioned in the ABAQUS Manual (ABAQUS, 2008). The yield conditions for $\hat{\bar{\sigma}}_{max} < 0$ as stated in the ABAQUS manual are presented in Equation (4-6) and (4-7)for the compressive and tensile meridians.

$$\left(\frac{1}{3}\gamma + 1\right)\bar{q} - (\gamma + 3\alpha)\bar{p} = (1-\alpha)\bar{\sigma}_c \tag{4-6}$$

$$\left(\frac{2}{3}\gamma + 1\right)\bar{q} - (\gamma + 3\alpha)\bar{p} = (1-\alpha)\bar{\sigma}_c \tag{4-7}$$

ABAQUS (2008) introduces a constant value, $K_c = \bar{q}_{(TM)}/\bar{q}_{(CM)}$, that must be input by the user. The ABAQUS Manual suggests that a typical value for K_c for concrete is 2/3. Using Equations (4-6) and (4-7) the value for K_c is presented in Equation (4-8). The suggested value for K_c from the ABAQUS manual gives a value of $\gamma$of 3 using Equation (4-8).

$$K_c = \frac{\gamma + 3}{2\gamma + 3} \tag{4-8}$$

The yield surface in the deviatric plane for K_c values of 1 and 2/3, as presented in the ABAQUS Manual (2008), is presented in Figure 4-6.

Equations (4-9) and (4-10)present the yield conditions along the compressive and tensile meridians respectively for $\hat{\bar{\sigma}}_{\max} > 0$ from the ABAQUS Manual (2008).

$$\left(\frac{1}{3}\beta + 1\right)\bar{q} - (\beta + 3\alpha)\bar{p} = (1-\alpha)\bar{\sigma}_c \tag{4-9}$$

$$\left(\frac{2}{3}\beta + 1\right)\bar{q} - (\beta + 3\alpha)\bar{p} = (1-\alpha)\bar{\sigma}_c \tag{4-10}$$

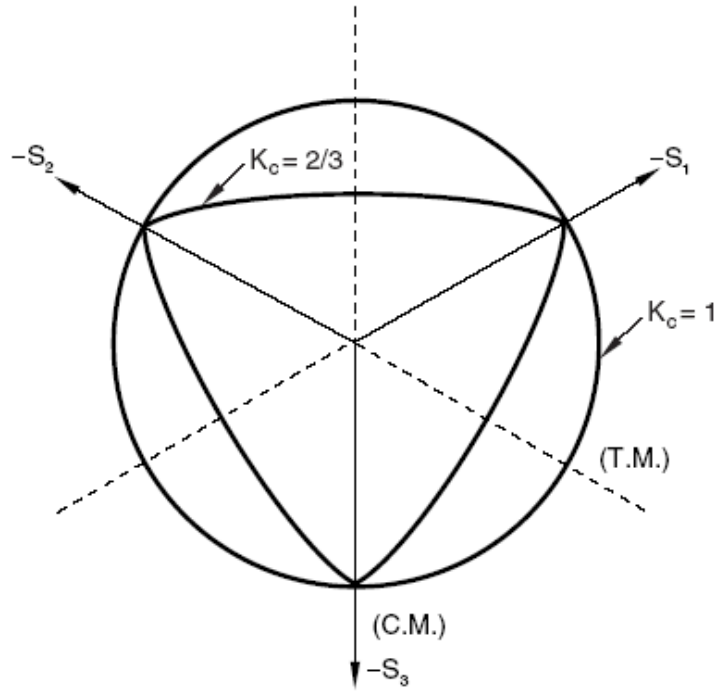

Figure 4-6 – Yield Surface in the deviatric plane (ABAQUS, 2008)

After establishing the yield surface, the flow potential is required to describe the plastic flow of the concrete. The concrete damaged plasticity model in ABAQUS (2008) assumes non-associated potential flow given by Equation (4-11).

$$\dot{\varepsilon}^{pl} = \dot{\lambda} \frac{\partial G(\bar{\sigma})}{\partial \bar{\sigma}} \tag{4-11}$$

The flow potential in the concrete damaged plasticity model in ABAQUS (2008) is based on the Drucker-Prager hyperbolic function given in Equation (4-12).

$$G = \sqrt{(\epsilon \sigma_{t0} tan\Psi)^2 + \bar{q}^2} - \bar{p} tan\Psi \tag{4-12}$$

Where:

ϵ is the eccentricity

Ψ is the dilation angle measured in the p-q plane at high confining pressure

$\bar{p}$ is the hydrostatic pressure stress

$\bar{q}$ is the Mises equivalent effective stress

σ_{tO} is the uniaxial tensile stress at failure

The dilation angle is input to describe the flow potential. The value assumed by Levy (2010) and Prabhu et al. (2007) for the dilation angle was 15^{o}. This value was also assumed for the concrete model in the current research.

The eccentricity refers to the rate at which the function approaches the asymptote; as the value approaches zero, the potential becomes a straight line. A value of 0.1 was assumed for the eccentricity as recommended by the ABAQUS Manual (ABAQUS, 2008).

The concrete damaged plasticity model also includes an option to include viscoplastic regularization in which stress states are able to go beyond the yield stress by introducing a viscoplastic strain rate tensor. This is used to help solutions converge faster with little effect on solutions. Viscoplastic regularization was not used in the concrete model implemented.

The strain rate of the material under multiaxial loading in the concrete damaged plasticity model used in ABAQUS (2008) is represented using the maximum and minimum eigenvalues of the plastic strain rate tensor. Equation (4-13) represents the equivalent compressive and tensile plastic strain rates used for multiaxial loading.

$$\dot{\tilde{\varepsilon}}_t^{pl} \overset{\text{def}}{=} r(\hat{\bar{\sigma}})\dot{\hat{\varepsilon}}_{max}^{pl} \qquad (4\text{-}13)$$

$$\dot{\tilde{\varepsilon}}_c^{pl} \overset{\text{def}}{=} -(1 - r(\hat{\bar{\sigma}}))\dot{\hat{\varepsilon}}_{min}^{pl}$$

Where:

$$r(\hat{\bar{\sigma}}) \overset{\text{def}}{=} \frac{\sum_{i=1}^{3}\langle\hat{\bar{\sigma}}_i\rangle}{\sum_{i=1}^{3}|\hat{\bar{\sigma}}_i|}; \; 0 \le r(\hat{\bar{\sigma}}) \le 1$$

$$\langle\hat{\bar{\sigma}}_i\rangle = 1/2(|\hat{\bar{\sigma}}_i| + \hat{\bar{\sigma}}_i)$$

The variable $r(\hat{\bar{\sigma}})$ is a stress weight factor that is equal to one if all the principal stresses are positive and equal to zero if they are negative. Equation (4-13) separates the compressive and tensile equivalent strain rates to use the inputs from compressive and tensile plastic strain rates described above. Finally, the damage in multiaxial loading also has to be established to relate the damage in a concrete material under multiaxial loading to the damage variables input for uniaxial

loading. Equation (4-14) presents the general damage variable used in the model for multiaxial loading.

$$(1-d) = (1-s_t d_c)(1-s_c d_t),\ 0 \le s_t, s_c \le 1 \qquad (4\text{-}14)$$

Where:

$$s_t = 1 - w_t r(\hat{\bar{\sigma}});\ 0 \le w_t \le 1$$

$$s_c = 1 - w_c(1 - r(\hat{\bar{\sigma}}));\ 0 \le w_t \le 1$$

The values for w_t and w_c represent the stiffness recovery under reversed loadings, as described above. Values of $w_c = 1$ and $w_t = 0$ were assumed which are the default values used in ABAQUS (2008) for concrete.

4.1.2 Steel Dowel Properties

The steel material used for the dowel bar is assumed to be a linear-elastic isotropic material. Table 4-4 presents the steel material inputs. These material properties were based on the material properties used in previous research completed at the University of Waterloo by Levy (2010). The steel is modeled as being elastic assuming that the dowel bar does not yield. It is assumed that the weaker strength of the concrete and stress concentrations near the dowel will cause failure in the concrete before the dowel. Maximum Von Mises stresses in the dowel bar will be compared to the yield strength of the dowel taken as 420 MPa based on ASTM 615 Billet Grade 60 steel. This was done for ease of modeling, since the study is focused more on the behaviour of the concrete around the device and overall pavement behaviour.

Table 4-4 – Steel Material Properties

Description	Value	
Density	7.80E-09	tonne/mm^3
Young's Elastic Modulus	200000	N/mm^2
Poisson's Ratio	0.3	Unitless
Coefficient of Thermal Expansion	1.20E-05	/ ^{o}C

4.1.3 GFRP Properties

Based on the review of the literature completed, ABAQUS simulations of pavements have used GFRP dowels, but have not considered GFRP pultruded shapes. The GFRP properties were assumed to be linear elastic and isotropic for ease of modelling and capturing the global response of the slab as well as focus on the concrete behaviour around the device. The elastic properties of the pultruded shapes were provided by the manufacturer. The values used in the model are given in Table 4-5.

Table 4-5 – GFRP Material Properties (Fibergate Custom Structures, 2003)

Description	Value	
Density	1.94E-09	tonne/mm^3
Young's Elastic Modulus	19310	N/mm^2
Poisson's Ratio	0.161	Unitless
Coefficient of Thermal Expansion	8.00E-06	/ ^{o}C

4.1.4 Continuous Joint Device Compressible Material Properties

For the development of continuous joint devices, material properties were assumed for the devices. The material was generally assumed to be a hard plastic material with linear isotropic properties. Material inputs used in the continuous joint device material model are presented in Table 4-6.

Table 4-6 – Continuous Joint Material Properties

Description	Value	
Density	1.06E-09	tonne/mm^3
Young's Elastic Modulus	2275	N/mm^2
Poisson's Ratio	0.15	Unitless
Coefficient of Thermal Expansion	5.00E-05	/ ^{o}C

The continuous joint device elastic modulus, coefficient of thermal expansion and density were assumed based on general material properties for ABS plastics found on an online material database (Anon., n.d.). The Poisson's ratio assumed for the continuous joint device material is

similar to the GFRP material, and a value of 0.15 is used in the finite element analysis model. Further research into the Poisson's ratio for plastics completed after the analysis was completed found a typical value tends to be closer to 0.3 to 0.4 for ABS plastics. The Poisson's ratio for the plastic material was not adjusted as a part of the current study. If further research on the continuous joint devices is completed, a specific material should be chosen and more accurate material data should be used or a material with similar behaviour to that input should be sourced.

4.2 Contact Modeling

The contact between dowels and concrete, as well as the slab and base layers, have been shown in previous studies to affect the behaviour of the slab (See Sections 2.6.5 and 2.6.6). Slab to device interaction and base slab interaction properties assumed in the models are explained in this section.

4.2.1 Slab Device Interaction

A review of the behaviour between concrete and conventional steel dowels was provided in the Literature Review (Section 2.6.5). Generally, the tangential behaviour of the dowel-concrete interface can be modeled using a frictional coefficient as described by Prabhu et al. (2007). The range for the dowel frictional coefficients was from 0.076 to 0.384 depending on surface preparation based on testing completed by Shoukry (2000). Although information about the interaction between the GFRP pultruded shapes and concrete could not be obtained, the same frictional coefficients were applied to the contact surfaces using GFRP. Similarly the compressible material assumed for the continuous joint devices used the same interaction conditions at the interface of the device and the concrete slab. It is assumed that by using the same inputs, the surface was consistently modeled for all of the devices. Varying the coefficient of friction provides a general comparison at different frictional values to understand the effect of different frictional contact between the device and the slab.

The slab and device interaction is modeled as a contact surface in ABAQUS using hard contact pressure definition between the two surfaces. The hard contact formulation is a rule used in ABAQUS to define the contact pressure, p, at a point as a function of the penetration of the two surfaces, h. Equation (4-15) presents the general relationship assumed in the hard contact formulation (ABAQUS, 2008).

$$p = 0 \; for \; h < 0$$
$$h = 0 \; for \; p > 0 \qquad (4\text{-}15)$$

The first line in Equation (4-15) is used when the two surfaces are not in contact and no pressure is applied at the point. The second line represents the situation when the surfaces come into contact and the pressure increases. Behaviour between the slab and device allows the two surfaces to separate after coming in contact as well.

The tangential behaviour of the device is modeled using Coulomb frictional contact between the surfaces. Using the Coulomb Friction model at the contact surface allows for shear stress and slip at the interface to be modeled. The Coulomb friction model assumes no relative slip occurs between the surfaces if the equivalent shear stress on at the surface presented in Equation (4-16)is less than the critical stress presented in Equation (4-17) (ABAQUS, 2008).

$$\tau_{eq} = \sqrt{{\tau_1}^2 + {\tau_2}^2} \qquad (4\text{-}16)$$

Where:

τ_1 and $\tau_2$are the shear stresses on the surface; and

$\tau_{eq}$is the equivalent shear stress on the surface

$$\tau_{crit} = \min(\mu p, \tau_{max}) \qquad (4\text{-}17)$$

Where:

μ is the frictional coefficient input to the model; and

τ_{max} is the shear stress limit put into the model

Depending on the behaviour of the contact surface, τ_{max}, can be included or not included in the model. This represents the maximum shear stress on the surface for which under any contact pressure slip will occur. For the interaction between the device and concrete, a value for τ_{max} of 2.1 MPa was used based on the work of Shoukry (2000). For the wheel path model, two frictional values of 0.3 and 0.1 were used to model the concrete device interface. Both frictional coefficient values are used in the wheel path model to investigate the effect of the frictional coefficient on the behaviour of the devices for steel-concrete and GFRP-concrete interaction. In the quarter slab analysis, a single value of 0.3 is used for the frictional coefficient.

As the shear stress exceeds the critical shear stress input using Equation (4-17), slip occurs. The friction between the device and the concrete is assumed to be isotropic in the finite element models where the slip and frictional stresses are in the same direction. The isotropic behaviour is expressed using the relationship in Equation (4-18) (ABAQUS, 2008).

$$\frac{\tau_i}{\tau_{eq}} = \frac{\dot{\gamma}_i}{\dot{\gamma}_{eq}} \tag{4-18}$$

Where:

$\dot{\gamma}_i$ is the slip rate in direction i; and

$\dot{\gamma}_{eq}$ is the magnitude of slip velocity

The magnitude of slip velocity used in Equation (4-18) is defined in ABAQUS (2008) using Equation (4-19).

$$\dot{\gamma}_{eq} = \sqrt{\dot{\gamma}_1{}^2 + \dot{\gamma}_2{}^2} \tag{4-19}$$

To model no relative slip between the surfaces based on the above relationships, ABAQUS uses a stiff elastic behaviour from zero shear stress to the elastic slip value input. The elastic slip value, γ_{crit}, for the interaction between the devices and concrete was assumed to be 0.5% of the average contact element size based on the default value used in ABAQUS (2008). The slip behaviour is represented using the relationship, shown in Figure 4-7.

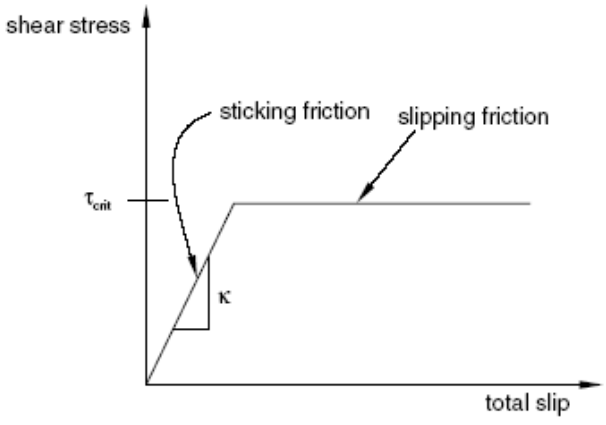

Figure 4-7 – Frictional Shear Stress vs. Slip Relationship for Sticking and Slipping Friction (ABAQUS, 2008)

In Figure 4-7, there are two different types of friction: slipping friction and sticking friction. The sticking friction corresponds to a stiffness, k, calculated according to Equation (4-20) (ABAQUS, 2008).

$$k = \frac{\tau_{crit}}{\gamma_{crit}} \tag{4-20}$$

This function will change with different values of contact pressure when the value of τ_{crit} is less than the shear stress limit input (2.1 MPa). When the shear stress at the surface exceeds the critical shear stress, slip occurs at the surface between the nodes. Equation (4-21) is used by ABAQUS (2008) in the contact model used to represent the change in slip on the contact surface during the time increment.

$$\Delta\gamma_i = \gamma_i^{el} - \bar{\gamma}_i^{el} + \Delta\gamma_i^{sl} \tag{4-21}$$

Where:

$\Delta\gamma_i$ is the change in slip in direction i

γ_i^{el} is the elastic slip at the end of the increment

$\bar{\gamma}_i^{el}$ is the elastic slip at the start of the increment

$\Delta\gamma_i^{sl}$ is the plastic slip occurring during the increment

The shear stress on the contact surface is then defined using Equation (4-22) using the stiffness value, *k*, and the elastic slip at the end of the increment, γ_i^{el}.

$$\tau_i = k\gamma_i^{el} = \frac{\tau_{crit}}{\gamma_{crit}}\gamma_i^{el} \tag{4-22}$$

ABAQUS (2008) introduces an elastic predictor strain term presented in Equation (4-23).

$$\gamma_i^{pr} \overset{\text{def}}{=} \bar{\gamma}_i^{el} + \Delta\gamma_i \tag{4-23}$$

Using Equation (4-24), the equivalent predictor strain is then represented using the two values for the elastic predictor strain term.

$$\gamma_{eq}^{pr} \stackrel{\text{def}}{=} \sqrt{\gamma_1^{pr\,2} + \gamma_2^{pr\,2}} \tag{4-24}$$

The slip increment is defined using Equation (4-25) in ABAQUS (2008) for the contact surface used for the dowel concrete interaction relating the slip to the shear stress on the surface.

$$\Delta\gamma_i^{sl} = \frac{\tau_i}{\tau_{crit}} \Delta\gamma_{eq}^{sl} \tag{4-25}$$

Where the term $\Delta\gamma_{eq}^{sl}$ represents the change in equivalent slip which is equal to Equation (4-26) (ABAQUS, 2008).

$$\Delta\gamma_{eq}^{sl} = \gamma_{eq}^{sl} - \gamma_{crit} \tag{4-26}$$

The shear stress is then represented using Equation (4-27) (ABAQUS, 2008).

$$\tau_i = \frac{\gamma_i^{pr}}{\gamma_{crit} + \Delta\gamma_{eq}^{sl}} \tau_{crit} \tag{4-27}$$

The normalized slip direction is introduced into the equation using variable, n_i, and Equation (4-27) becomes Equation (4-28) (ABAQUS, 2008).

$$\tau_i = n_i \tau_{crit} \tag{4-28}$$

Where:

$n_i = \frac{\gamma_i^{pr}}{\Delta\gamma_{eq}^{sl}}$ is the normalized slip direction

Finally the slip formulation is linearized and the final form is presented in Equation (4-29) which is altered from the ABAQUS Manual (2008) for a constant frictional coefficient (one that does not change depending on slip rate as used in the interaction between the device and the slab).

$$d\tau_i = (\delta_{ij} - n_i n_j)\frac{\tau_{crit}}{\gamma_{eq}^{pr}} d\gamma_j \qquad \text{if} \quad \tau_{crit} = \tau_{max} \tag{4-29}$$

$$d\tau_i = \left(\delta_{ij} - n_i n_j\right)\frac{\tau_{crit}}{\gamma_{eq}^{pr}} d\gamma_j + n_i \left(\mu + p\frac{\partial \mu}{\partial p}\right) dp \ \text{ if } \quad \tau_{crit} = \mu p$$

4.2.2 Slab Base Interaction

The interaction between the slab and base layer is also modeled using hard normal contact that allows the surfaces to separate after coming in contact. Isotropic Coulomb friction is also used to model the tangential behaviour similarly to the contact described for the device slab interaction. A coefficient of friction of 0.965 and an elastic slip of 0.465 mm are used for the slab base interaction based on the work of Levy (2010). No shear stress limit is included in the interaction between the slab and base layer. The first line of Equation (4-29) is not used to describe the behaviour of the slab base interaction as $\tau_{crit} = \mu p$ is always valid.

4.3 Slab Support Descriptions

4.3.1 Slab Support Used in the Wheel Path Model

The wheel path model assumes a single 300 mm base layer with linear isotropic material properties based on a previous study completed by Shoukry et al. (2003), among others including Levy (2010). The bottom face of the 300 mm layer is assumed to be vertically restrained in the model by applying vertical restraint to the bottom surface nodes. Base properties assumed for the wheel path model were also intended to reflect conditions in an experimental testing arrangement where a thin consistent base layer is more practical. A single base layer of with a linear elastic isotropic material with a modulus of elasticity of 100 MPa is assumed for the preliminary analysis. This single layer with a modulus of elasticity of 100 MPa serves as a consistent comparison of the devices. The Poisson's ratio is assumed to be 0.3. The density of the base layer used in the wheel path model is 2.10×10^{-9} tonne/mm^3.

4.3.2 Base and Subbase Properties Used in the Full, Half and Quarter Slab Models

A base and subbase layer are used in the full, half and quarter slab models to support the slab. The base layer is 125 mm thick and the subbase layer is 1200 mm thick. The bottom face nodes of the subbase are restrained against vertical movement. The subbase and base layers are tied to one another at the top of the subbase and the bottom of the base layer. The base and subbase

properties are modelled as linear isotropic materials. The base layer is modelled with an elastic modulus of 207 MPa and the subbase is 103 MPa. Both the base and subbase materials use a Poisson's ratio of 0.3 and a density of 2.10×10^{-9} tonne/mm^3 in the full, half and quarter slab models.

4.4 Model Loading

A general description of the load application used for the wheel, shrinkage and thermal strains is explained in this section.

4.4.1 Gravity Loading

The gravity loading is applied in the model by inputting the densities of each of the respective materials and applying a constant acceleration equal to the gravity constant. This is applied in the first loading step of the finite element analyses completed.

4.4.2 Wheel Loading

Static vertical wheel loading at the joint is investigated in the finite element analysis. The effects of tire friction and velocity of the wheel moving across the surface were not considered. Wheel loading is applied using a pressure on the top surface of the concrete slab over a foot print of 250 mm x 600mm. The area of the wheel load was chosen based on the CL-625 truck dual tire footprint in the Canadian Highway Bridge Design Code. The design footprint for the dual truck tire also corresponds to the highest wheel loads on the CL-625 truck of 87.5 kN. Wheel loads are only applied on one side of the joint and directly at the edge of the slab in the wheel path(s). Further investigation into the effect of boundary conditions applied and the effects to the wheel load are explained later in the analysis sections.

4.4.3 Shrinkage Strain

The shrinkage loading is applied to the slab using an effective thermal loading (temperature gradient) necessary to obtain the desired unrestrained strain profile. The temperature function proposed by Levy (2010) and presented in Equation (4-30) is used. Equation (4-30) is based on a shrinkage strain that includes the limiting effect of creep, and varies over the depth of the slab to simulate a typical pavement slab shrinkage profile. The shrinkage strain profile is converted to an equivalent thermal strain profile based on the coefficient of thermal expansion of the concrete.

$$T_{sh}(y) = -2.232 - 0.04059 \cdot e^{0.0269y} \quad (4\text{-}30)$$

Where:

y is the depth of the slab

The shrinkage strain profile applied to the model based on Equation (4-30) is presented in Figure 4-8.

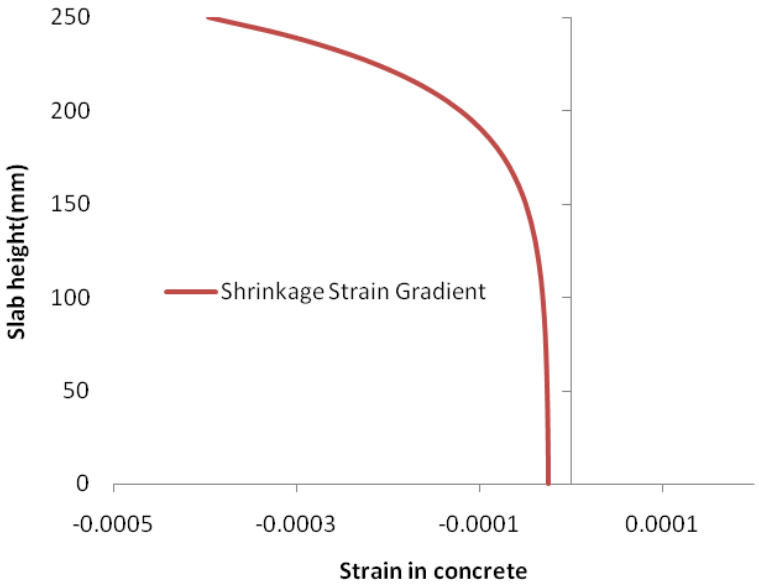

Figure 4-8 – Shrinkage Strain Profile Applied to Slab

4.4.4 Temperature Thermal Strain Gradients

The temperature variations applied in the thermal analysis completed in the service load analysis are the same temperature distributions in the slab used by Levy (2010) and were adopted from another previous study (Shoukry, 2000). The thermal gradients were presented previously in the Literature review in Equations (2-20) and (2-21)for day and night respectively. The general slab gradient for day and nighttime thermal strains using Equations (2-20) and (2-21) and as applied in the service load analysis is presented in Figure 4-9. The thermal gradients used to represent the effects of daily temperature cycles were added to the thermal gradient used to simulate shrinkage strain (Section 4.4.3).

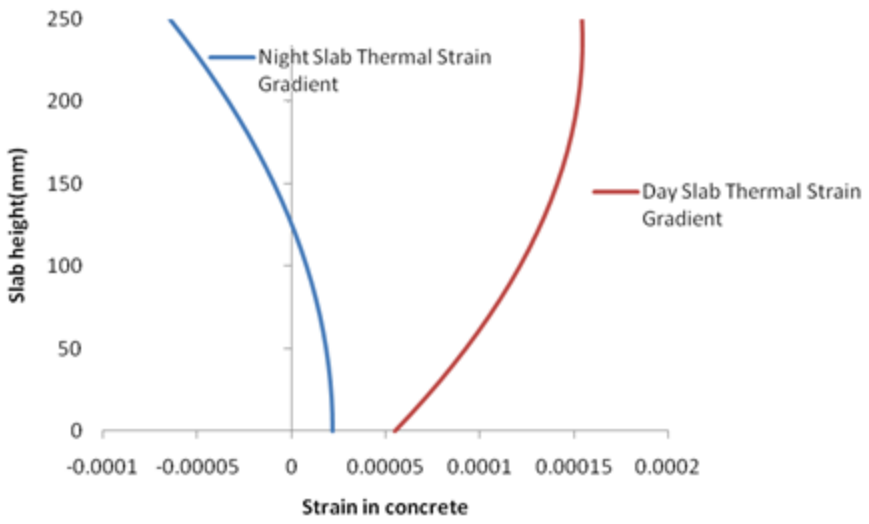

Figure 4-9 – Day and night thermal gradients applied to slab

4.5 Finite Element Model Development - Summary

The material properties, contact modeling, support conditions, and loading to be applied in a three dimensional finite element analysis were developed in this Section. The following aspects of the model were developed:

- A nonlinear concrete material model was chosen from the predefined models in ABAQUS and inputs were discussed in detail.
- Linear elastic material properties for the different devices were established and determined to be sufficient for overall joint behaviour but not to capture local effects and failures in the devices themselves.
- Contact at the device concrete interface was determined to be modeled using Coulomb friction with a maximum shear stress limit.
- Contact between the slab and base layer was also determined to be modeled using Coulomb friction and the inputs were described.
- Linear Elastic material properties for the base and subbase layers were established.
- Wheel loading, thermal and shrinkage strain gradients were established and presented to be applied in the service loading analysis.

5.0 Finite Element Load Transfer Study for Discrete Devices

This section presents the finite element analysis results for the discrete devices under static wheel load application using the wheel path finite element analysis model.

The finite element analysis results were used to evaluate the performance of the discrete devices using the ABAQUS wheel load model (geometry described later in this section) in terms of the following behaviour:

- The differential deflection across the joint;
- Localized failure in the concrete by comparing the plastic equivalent compressive strain (PEEQ) and plastic equivalent tensile strains (PEEQT) in the concrete;
- The maximum stress in the base layer to identify the load transfer ability and stress distribution to the slab; and,
- General discussion of the stresses developed in the concrete and how the device is functioning to transfer load.

The development of the wheel load model included comparisons to larger scale models to investigate the effects of boundary conditions and length of slab. A comparison was also made between the effects of wheel load transfer at the joint in a full slab model and a wheel load model with and without dowels to understand the transfer and requirements for a device at the joint and to verify the adequacy of the wheel load model.

The finite element analysis using the wheel load model for wheel load transfer investigation compared the devices at three load levels when a single static load was applied to the slab (as described in Section 4.4.2). A load level of half the maximum wheel load (43.75kN), which is close to the load level used for falling weight deflectometer (FWD) tests (and also the load level that joint efficiency ratios are based on), was considered as well as at the maximum wheel load and twice the maximum CL-625 truck wheel load (87.5kN and 175kN).

The wheel load analysis consisted of first investigating each device in detail when subjected to a single wheel load. A mesh refinement study for each device was completed using the wheel load model with a single static load applied. After completing the mesh refinement study, a parametric study that consisted of changing the frictional coefficient from 0.1 to 0.3 was also

completed on each device to determine the effects of the device concrete interaction on device behaviour (for static wheel loading). Each device is also compared with a quasi-static reversed loading using increments of the static wheel load applied to either side of the joint was investigated with 100 MPa base and 0.1 frictional coefficient.

5.1 Methods Used to Compare Load Transfer Performance of Devices

Due to the complex nature of the behaviour of the joint, an investigation into the joint behaviour and comparison of the devices for load transfer ability will compare the analysis results in a number of different areas. The following presents the methods used to compare the devices.

The load transfer ability is an important device characteristic since slabs that have not used dowels have shown signs of distress and require rehabilitation earlier in the life of the pavement than slabs with dowels. Also, for rider comfort and functionality of the pavement, the differential joint deflection needs to be minimized. Three measures of the joint deflection are presented for each device in the wheel path model. The first two measures are joint efficiency, calculated using Equation (5-1), and the Load Transfer Efficiency (LTE) presented in Equation (5-2). These measures have been used in previous studies to gauge the efficiency of the joint.

$$Joint\ Efficiency(\%) = \frac{2\Delta_u}{\Delta_u + \Delta_l} x100\% \quad (5\text{-}1)$$

$$LTE(\%) = \frac{\Delta_u}{\Delta_l} x100\% \quad (5\text{-}2)$$

Where:

Δ_u and Δ_l are the deflection of the unloaded and loaded side of the slab respectively

The LTE and joint efficiency are usually based on the values from testing of the joints using the FWD. Sargand and Figueroa (Sargand & Figueroa, 2010) found ranges of LTE on pavements after they were constructed with various dowels to be 78 to 95%. The minimum joint efficiency calculated using Equation (5-1) for a slab with dowels should be 85% at approximately 40 kN based on data from a FWD test. A general comparison of the LTE and joint efficient in the wheel load transfer study to these was made, although the effects of slab length and boundary

conditions affect the LTE and joint efficiency results when compared to a full slab model (as shown later in this section).

The third measure of performance based on joint deflection is the overall differential deflection based on the differential deflection at the edge of the model slab at either side of the joint. The point used for joint deflection will be the edge of the wheel path slab joints as presented in Figure 5-1.

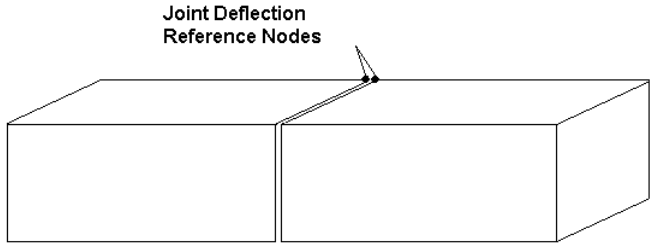

Figure 5-1 – Joint deflection reference nodes

The concrete surrounding the devices is subject to significant localized stress as the load is concentrated around the dowel as it is transferred to the other side of the joint. High stress levels can lead to damage in the concrete slab in these areas which can lead to failure of the joint. Localized damage will occur in the concrete as noted by Levy (2010). The localized damage failure criteria used by Levy (2010) was adopted in the current study to define failure in compression using plastic equivalent compressive stresses (PEEQ). The main failure mechanism of concrete modeled in compression is compressive crushing of the concrete. The concrete crushing criteria used by Levy (2010) is based on the total uniaxial strain in compression reaching 0.005 at which point the PEEQ strain would be 0.00474. The tensile damage criterion for tensile cracking in concrete using equivalent plastic strain in tension (PEEQT) value of 0.003 adopted from Prabhu et al. (2007) was used. The maximum plastic strains around the joint were compared for the different alternatives. The stress locations and the inelastic areas were also investigated to further quantify the damage occurring.

The maximum stresses in each direction was also investigated to determine the device behaviour and to identify problematic areas and gain knowledge into alternative options for device design. This evaluation was mostly based on visual investigation of the stress profiles generated using

the analysis and using the peak stresses in the slab in each direction. The profiles of stresses distributions in the devices as well as the slab are presented and compared.

5.2 Wheel Path Model Development

As described previously, the wheel path model was developed to provide a computationally efficient evaluation of the discrete devices. The wheel path model also matches the geometry of the experimental specimens. During development of the wheel path model the analysis results were compared to results from a full slab and half slab model to validate the model and to determine the effects of slab length and boundary conditions. This section describes the development and validation of the wheel path model.

5.2.1 Model Geometries

The typical model geometry assumed by Levy (2010) was used for the models. The slab is 250 mm thick, with a lane width of 3600 mm and a joint spacing of 4500 mm for all three models. The joint was modeled as a 10 mm gap between the adjacent concrete faces and no interaction between the slab faces is modeled. The slab was based on twelve dowel bars being placed along the lane width at a spacing of 300 mm with the corner dowels 150mm from the edge. The models without dowels included pockets in the concrete slab where the dowels would be placed. Model geometries and boundary conditions for each of the full, quarter and wheel path models are presented in Figure 5-2, Figure 5-3 and Figure 5-4, respectively.

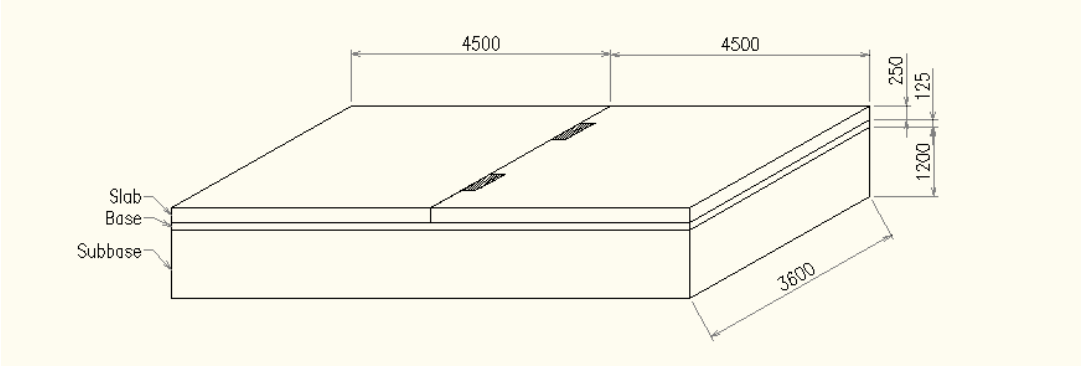

Figure 5-2 – Full Slab Model Geometry (12 dowels, 300 mm spacing)

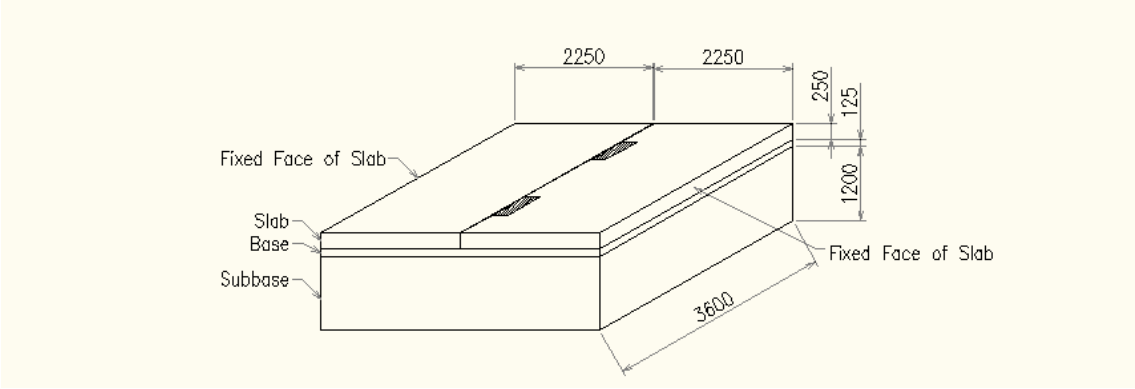

Figure 5-3 – Half Slab Model Geometry (12 dowels, 300 mm spacing)

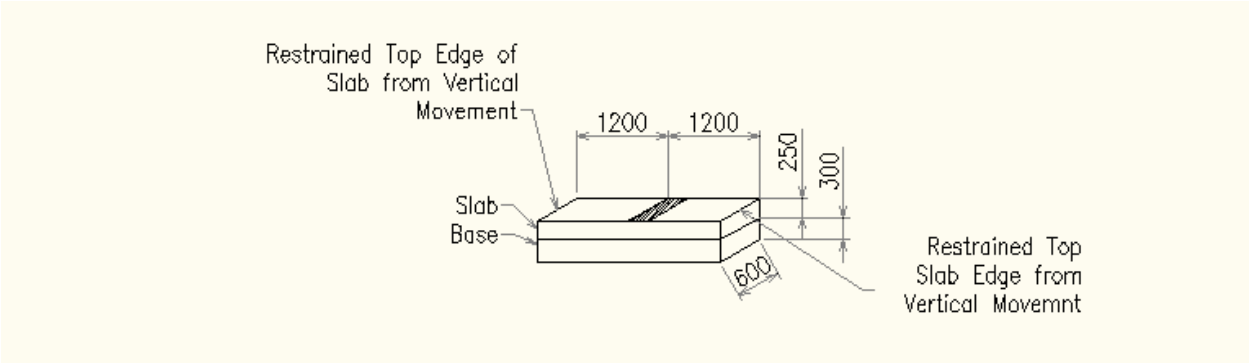

Figure 5-4 – Wheel Path Model Geometry (2 dowels, 300 mm spacing)

In Figure 5-2, Figure 5-3 and Figure 5-4 the shaded area on top of the slab presents the wheel loading applied to the slabs for the different models. In the full slab model, no restraint was placed on the unloaded edge of the slab that represents the adjacent transverse joint. In the half slab model, the face along the middle of the slab section was restrained from longitudinal movement perpendicular to the face. Loading at the edge of the slab with a boundary condition similar to that applied to the half slab model will model a wheel load at either end of the slab at the joint location as shown in Figure 5-5.

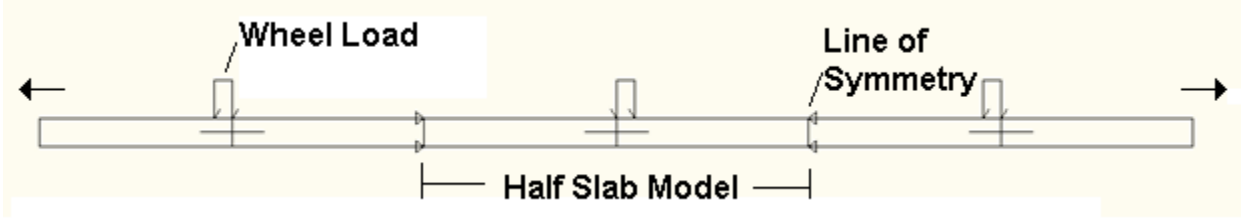

Figure 5-5 – Loading and Boundary Condition Implications for Half Slab

The dimensions of the wheel path model were based on the width of one wheel path and on a previous lab testing setup adopted by Eddie et al. (2001). A slab length of 1.2 m in each direction from the joint was used for the wheel path model based on Eddie et al. (2001). The base layer was 300 mm. The model size was chosen to fit in a testing apparatus where multiple devices will be tested as discussed in Chapter 6.0 in more detail.

5.2.2 Model Loading for Wheel Path Model Development

The loading sequence applied to the full, half and wheel path models for wheel path model development was a gravity load followed by a single static wheel load to 200kN (the method of load application was described previously in Section 4.4.

5.2.3 Slab Deflection Profile Comparisons between Full, Half and Wheel Path Models with Dowels

In order to ensure that the smaller slab section of the wheel path model was behaving similarly to the full slab model, slab vertical deflection profiles of each model are compared in Figure 5-6 to Figure 5-9. These figures present the full, half and wheel path top of slab deflection profiles at 20, 45 85 and 175 kN, respectively.

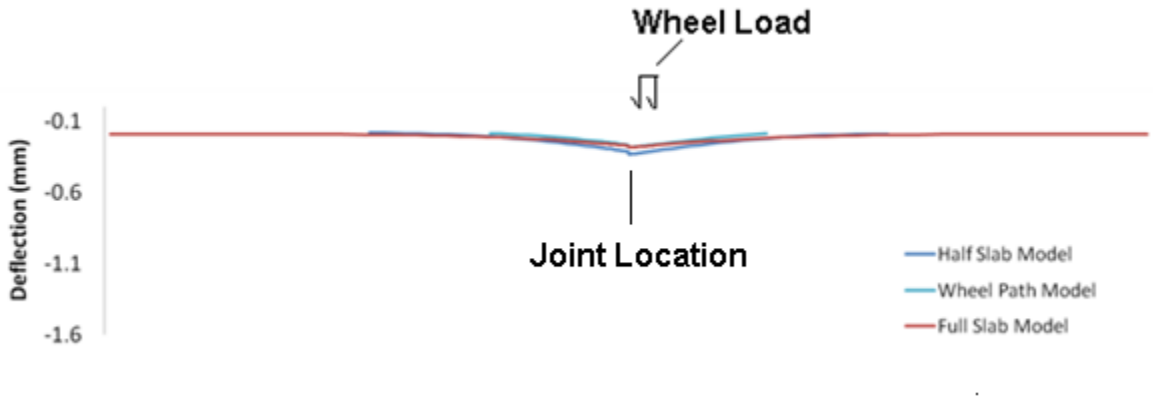

Figure 5-6 – Deflection Comparison of Full/Half Slab Model to Wheel Path Model at 20kN Wheel Load

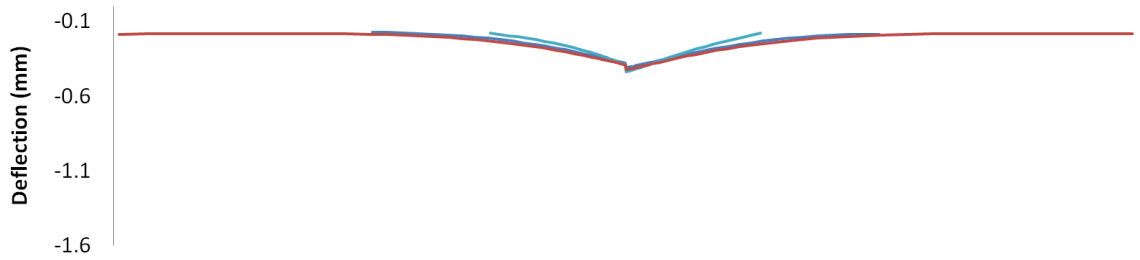

Figure 5-7 - Deflection Comparison of Full/Half Slab Model to Wheel Path Model at 45kN Wheel Load

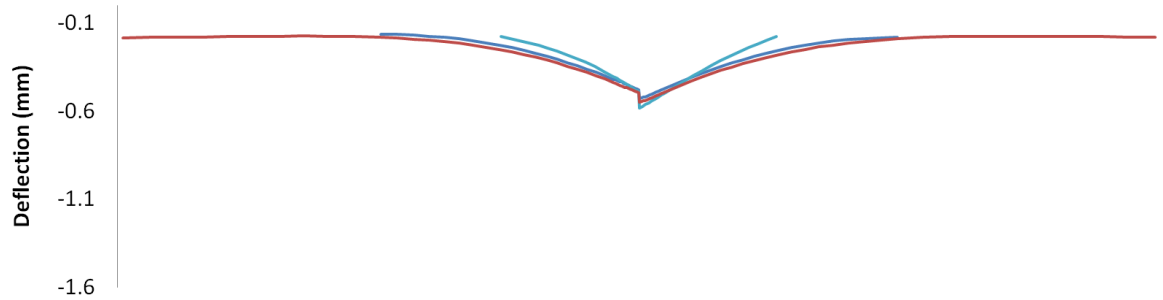

Figure 5-8 - Deflection Comparison of Full/Half Slab Model to Wheel Path Model 85kN Wheel Laod

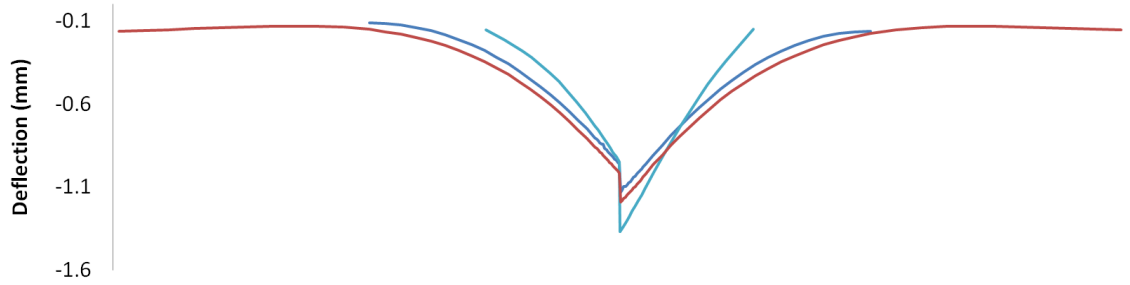

Figure 5-9 - Deflection Comparison of Full/Half Slab Model to Wheel Path Model 175kN Wheel Load

After the application of the 20 kN point load, the deflection profiles of the half slab and the wheel path model are similar. The full length slab had less curvature than both of the half slab and wheel path model slabs, as the load was distributed further along the slab length. The differential deflection at the joint in all three models after 20 kN was very similar. The half slab model and the wheel path model both had increased curvature compared to the full length slab but had a similar differential deflection at this load level.

After 45 kN (approximately half of the design wheel load), the deflection of the wheel path model on the loaded side of the joint was the greatest but was similar to the other two models. On the loaded side of the joint in the full slab model, the deflection was greater than the half slab model. The additional deflection in the full slab model was assumed to occur because the half slab model was restrained along the length of the slab from movement which will help to restrain the slab from deflecting downward as it was required to elongate to enable the deflection to occur. The full slab model was only resisted by friction and allows more movement of the slab. The full slab model was less restrained than in an actual setting as an adjacent joint would add some restraint to the slab movement. The deflection on the unloaded side of the slabs at the 45 kN load level were all similar. The slabs all deflected further as the wheel load level increased to 85 kN similar results were observed at the 85kN load to that described for the 45 kN load level.

As the load was increased to approximately 175 kN the deflection of the loaded side of the wheel path model increased considerably more than the half and full slab models. However, on the unloaded side of the wheel path model deflection was less than that for the full and half slab models. The comparison of the joint deflection using the wheel path model to the full and half slab models clearly showed higher differential deflection was estimated using the wheel path model, and larger curvatures occurring in the concrete slab at all of the load levels. Additional deflection of the base below the slab will also cause higher stress concentrations to be expected in the base layer when using the wheel path model. The deflection and joint stepping profiles are similar enough near the joint using each model to consider the loading and boundary conditions applied to the half and wheel path model to adequately compare the devices for transferring load. The half and full slab models have very similar deflection profiles and the effects of the line of symmetry (and creating a symmetric loading) compared to an unrestrained full length slab appear to be minimal on the overall curvature of the slab and stepping at the joint.

The analysis shows the wheel path model is capable of predicting behaviour at the joint similar to a full slab model. A more detailed comparison of the deflection profiles as well as the stress in the slab is completed next section as part of an investigation into the load transfer with and without dowels for each of the different slab geometries.

5.2.4 Load Transfer Comparisons for the Wheel Path, Quarter and Full Slab Models with and without Dowels

Conventional design of transverse joints used in concrete pavements consists of a sawcut being placed in the slab at the location of round steel dowels placed at the planned sawcut locations. Some low volume concrete parking lots and roads may be constructed without the use of dowels. Although highway pavements rarely use transverse joints without dowels, the model without dowels is presented to understand further the transfer of load at the joint with and without a dowel.

In a slab without any dowels, it would be assumed that no load is transferred across the joint. In reality, cracking occurring at the joint still provides some load transfer through aggregate interlock; although, aggregate interlock was not considered in the current study. No dowels (or mechanical load transfer devices) provide the least amount of load transfer and have been shown to be unacceptable for differential deflection across the joint. Table 5-1 presents the joint performance comparison of the half slab models with dowels and without dowels to the wheel path models with and without dowels. The full slab model with dowels is also shown as the baseline condition. In the half slab model without dowels, the differential deflection across the joint at a load of 43.75 kN was 0.16 mm. The wheel path model, which had less load transfer along the length of the joint through the concrete slab (because the slab was loaded to the edges) as well as along the length of the slab (because the slab was not as long), had a larger differential deflection for the same load with a differential deflection at the joint of 0.37 mm. Similarly, in models with dowels the differential deflection increased from the half slab model to the wheel path model from 0.03 mm to 0.06 mm. In both cases (dowels and no dowels) the differential deflection across the slab in the wheel path model was higher than that predicted using the half and full slab models; the differential deflection predicted for the wheel path model was approximately double that for the half slab model. The differential deflection across the joint between the half slab model and full slab model was almost the same. At each load increment the differential deflection in the full slab model was less than that estimated using the half slab model. Based on the comparisons between the wheel path model and the half slab model, the wheel path model geometry used will have affects on the differential deflection at the joint and will generally predict higher differential deflection than what would be expected using a full slab model with more realistic boundary conditions for wheel load transfer.

Table 5-1 – Analytical Joint Performance Comparison for Dowelled and Undowelled Joints Using Full, Half and Wheel Path Models

Model	Load (kN)	Vertical Deflection of Loaded Side (mm)	Vertical Deflection of Unloaded Side	LTE (%)	Joint Efficiency (%)	Differential Deflection (mm)
Full Slab Model with Dowels	43.75	-0.424	-0.394	93.0%	96.4%	-0.03
	87.50	-0.629	-0.571	90.7%	95.1%	-0.06
	175.00	-1.058	-0.927	87.7%	93.4%	-0.13
Half Slab Model with Dowels	43.75	-0.414	-0.383	92.5%	96.1%	-0.03
	87.50	-0.611	-0.549	89.9%	94.7%	-0.06
	175.00	-1.019	-0.881	86.4%	92.7%	-0.14
Half Slab Model without Dowels	43.75	-0.441	-0.284	64.4%	78.4%	-0.16
	87.50	-0.737	-0.347	47.0%	64.0%	-0.39
	175.00	-1.282	-0.462	36.0%	53.0%	-0.82
Wheel Path Model with Dowels	43.75	-0.274	-0.216	78.7%	88.1%	-0.06
	87.50	-0.514	-0.385	75.0%	85.7%	-0.13
	175.00	-1.031	-0.720	69.8%	82.2%	-0.31
Wheel Path Model with Dowels	43.75	-0.381	-0.010	2.7%	5.2%	-0.37
	87.50	-0.809	-0.018	-2.2%	-4.5%	-0.83
	175.00	-1.594	-0.071	-4.5%	-9.4%	-1.67

The joint efficiencies and LTE values computed for the slab with dowels meets the requirements previously presented. The value for the load transfer efficiency for the half slab model, 95%, is also on the high end of the range, which would make sense considering the slab has not been exposed to temperature and shrinkage straining and is modeled assuming perfect alignment. Curling due to temperature and shrinkage will also affect the measured values, and these factors are not considered in this portion of the analysis of the devices. The wheel path model has a value for LTE at the low end of the range (78%) suggested at a load of 43.75 kN while the joint efficiency is above the suggested minimum of 85% at 87.5kN. Although the values will be presented for joint efficiency and LTE for the remaining discrete device comparisons, the ranges established as being acceptable for an actual pavement will not be used since the wheel path model over estimates the differential deflection at the joint compared to a full slab.

An investigation into the behaviour of the half slab model using dowels and no dowels will provide information into where stresses are developed in the concrete with the addition of the

dowels, as well as how this affects the concrete around the joint. Firstly, in order to understand the wheel load transfer behaviour along the joint in the half slab model with dowels, the normal stresses in the vertical direction on both sides of the joint in the concrete are shown in **Figure** 5-10 and Figure 5-11. The stresses are given in MPa. A load of 200 kN was chosen to be able to capture more local failure occurring at the joint and provide consistent profiles for the stress and plastic straining figures presented as not as enough plastic straining was generally occurring at the 175 kN load level to provide plastic strain profiles.

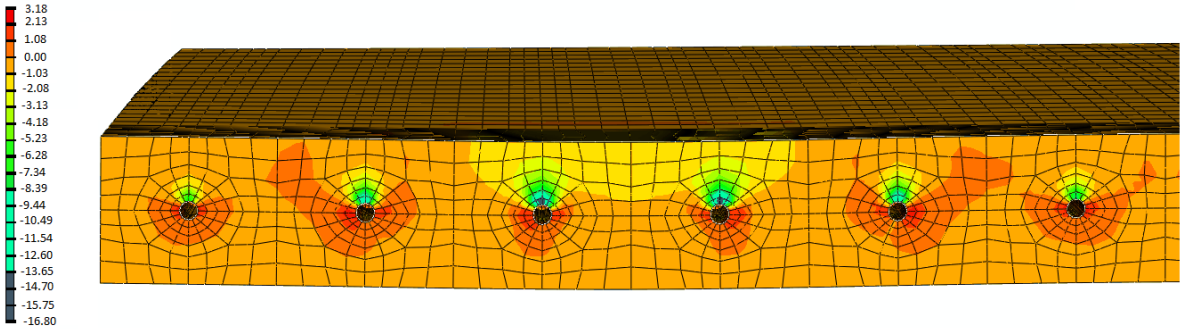

Figure 5-10 - Half Slab Model with Dowels Concrete Vertical Normal Stress Loaded Side at 200 kN Wheel Load (MPa)

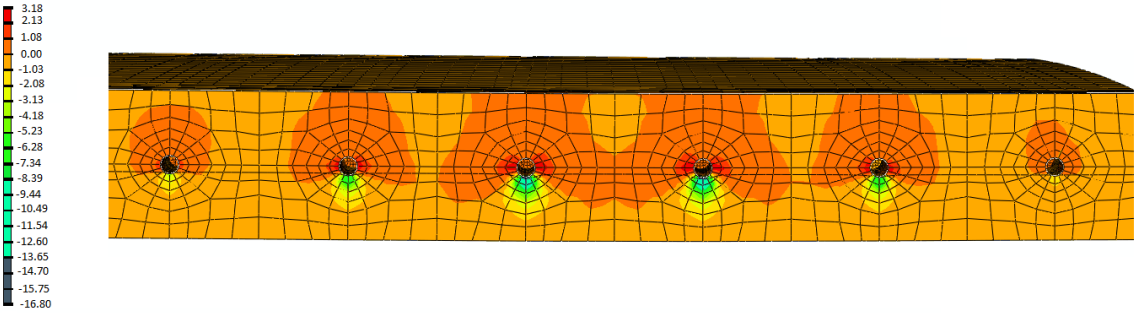

Figure 5-11 - Half Slab Model with Dowels Concrete Vertical Normal Stress Unloaded Side at 200 kN Wheel Load (MPa)

As would be expected, the highest vertical stresses are concentrated directly under the loaded portion of the slab. A concentration of compressive stresses exists above the dowel on the loaded side and a similar concentration of compression stress is present below the dowel on the unloaded side. The location of the compression stress concentrations on opposite sides of the dowel will change depending on which side of the joint is loaded. This observation is important when comparing the behaviour of the devices at different load levels for joint performance.

Although applying the load to one side of the joint will be able to predict an approximate failure load and the response of the pavement to that load, it will not take into account the damage occurring around the dowel on either side under the reversed cyclic loading caused when the wheel crosses to the other side of the joint. The maximum vertical compression stress in the concrete on the loaded side of the slab above the dowel is 14.9 MPa, and on the unloaded side the maximum vertical compressive stress below the dowel at the joint is 13.4 MPa.

The normal stress conditions in the vertical direction for a longitudinal section through the joint are shown in Figure 5-12 and Figure 5-13 for the half slab model with and without dowels, respectively. The applied wheel load is 200 kN. The stresses are presented in MPa where negative values represent compression and positive stresses represent tension.

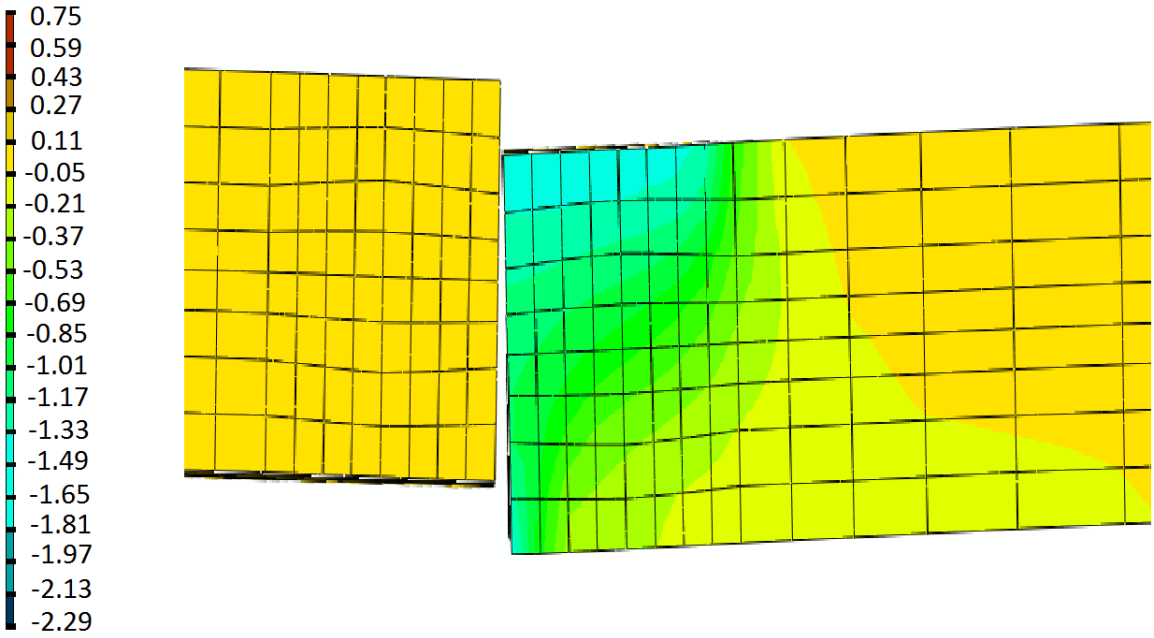

Figure 5-12 – No Dowel Half Slab Model Concrete Vertical Normal Stress at 200 kN Wheel Load (MPa)

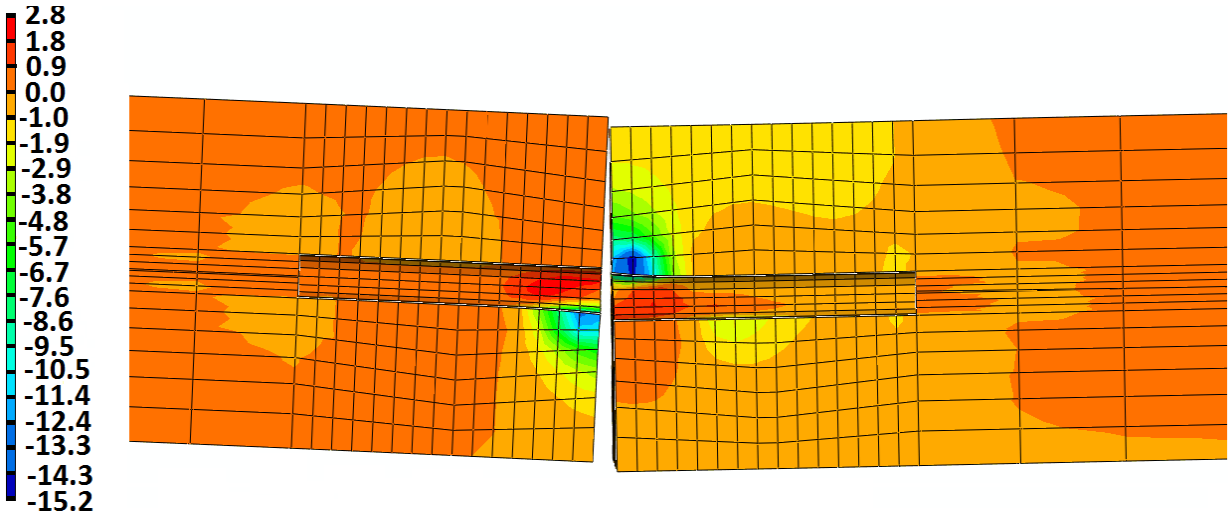

Figure 5-13 –Half Slab Model with Dowels Concrete Vertical Normal Stress at 200 kN Wheel Load (MPa)

As the wheel load is applied to the slab without dowels, the load is distributed through the slab to the base layer below. Generally the stresses in the concrete in the slab without dowels are not approaching failure stresses at the 200 kN load level as presented in Figure 5-12. However, the differential deflection is very large as visible in the figure.

The dowels cause concentrations of vertical stress in the concrete along the length of the dowel as presented in Figure 5-13. These stresses are approaching failure stresses near the dowel where very high normal stress is concentrated on either side of the joint at the dowel location. Stress concentrations along the length of the dowel are similar to that predicted using conventional dowel bar theory where a concentration of vertical stress in the concrete exists at the joint location as well as second and third vertical stress concentrations along the dowel length on each side of the joint (Figure 5-13). The tension stresses around the dowel are close to the uniaxial tensile strength of concrete and the vertical concrete stresses in compression are approaching the uniaxial failure strength of concrete at the 200kN load level. Observation of the stress concentrations around the dowels promted the concepts for the continuous devices in an attempt to eliminate localized load transfer stresses in the while still providing adequate load transfer across the joint.

No plastic straining occurs in the concrete when dowels are not included in either the half slab or the full slab models under a static 175kN wheel load. Introducing the dowel creates concentrations of stress around the dowel causing the concrete to plastically deform around the joint as presented in Figure 5-14 which shows a longitudinal section of the PEEQ strains through a dowel directly beneath the wheel load in the half slab model (the dowel bar has been omitted for clarity).

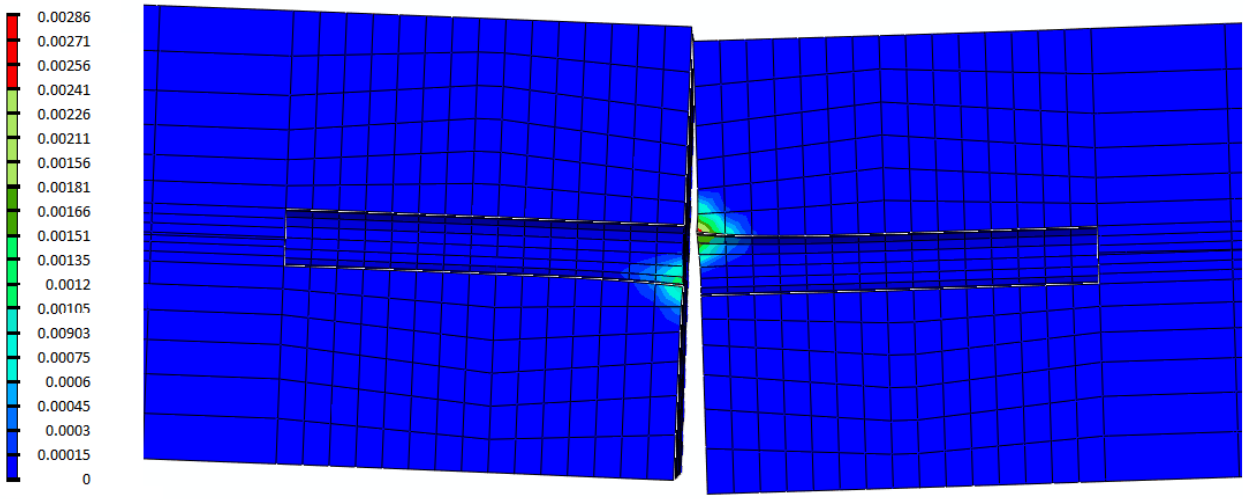

Figure 5-14 –Half Slab Dowel Model PEEQ Strain at 200kN Wheel Load

The plastic strains due to concrete compressive damage occurs above the dowel on the loaded side of the joint and below the dowel on the unloaded side of the joint at the 200 kN load level. The plastic straining is isolated to the joint location and dowels near the wheel path at this load level. The concrete tensile plastic strains can be represented by the PEEQT strain and a section through the dowels directly beneath the load application at the 200kN load is shown in Figure 5-15.

The PEEQT strains are similar on both the loaded and loaded sides of the joint as the tensile zone and distribution of tensile stresses around the joint are similar on both sides of the joint. Based on the locations of the PEEQ and PEEQT zones when wheel loading is applied to one side of the joint, it will be important to apply the load to both sides of the joint to adequately assess the behaviour of the joint at a given load level as in service wheel loads will pass across the joint reversing the plastic straining zones presented. In developing a test to compare devices this reversed loading should be modeled to understand how the plastic zones occurring on either

sides of the joint will affect the overall behaviour of the joint as plastic straining causes damage and softening of the concrete which may affect load transfer and differential deflection at the joint. This will be investigated as a part of the finite element analysis for load transfer comparison of discrete devices in Section 5.6.3.

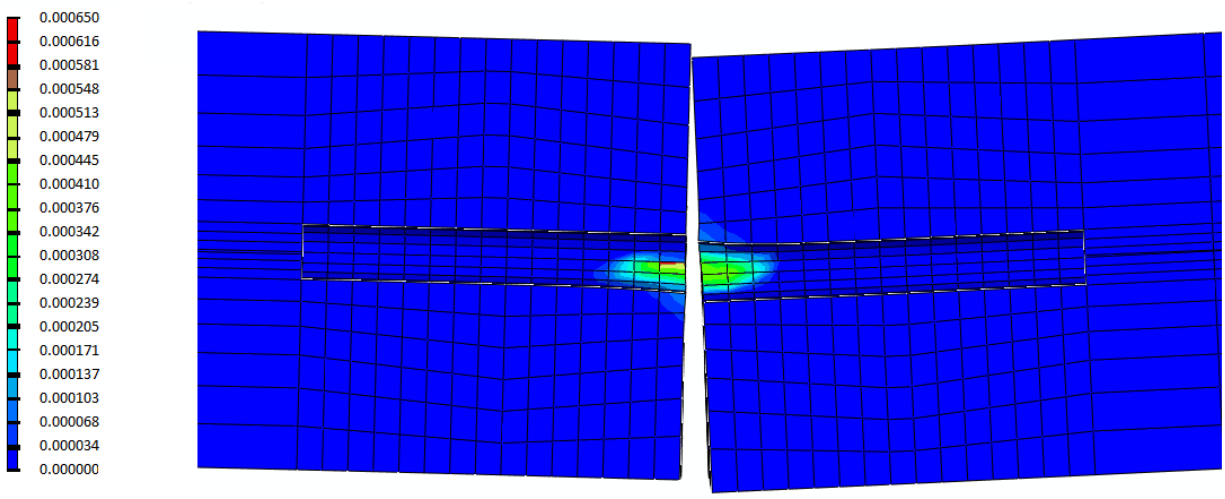

Figure 5-15 –Half Slab Dowel Model PEEQT Strain at 200 kN Wheel Load

The plastic strains in the half slab model are compared to the values obtained using the wheel slab model to determine how much more plastic straining is occurring around the dowel in the wheel slab model. The maximum plastic strain values were used for comparison and also to determine if failure was occurring in the slab. Table 5-2 presents the maximum concrete PEEQ and PEEQT for the wheel path, half, and full slab models with dowels and without dowels.

In the models that contain steel dowels, the plastic straining that occurred at the joint in the wheel load model was generally greater than the plastic straining that occurred in the half slab model. The differences varied at some of the load levels. The half and full slab models had some differences between the plastic strains in tension and compression. In the half slab model and full slab models with dowels, the plastic strain in compression was quite similar at all three load levels. The PEEQ strains in the half slab model ranged from being 1.0 to approximately 1.08 times the value obtained using the full slab model. Values obtained for maximum PEEQT were on the same order of magnitude in both the half slab and full slab models, but the values were not as consistent between the models. At the 43.75kN and 175kN load levels, the half slab model estimated the plastic strain in tension as being 1.26 and 1.72 times the values obtained using the

full slab model and by 0.48 times the value at the 87.5kN load level. It was assumed that the low magnitude of the plastic straining values obtained, the analysis being nonlinear, and using maximum values causes the inconsistency in the maximum plastic strains at the wheel load level.

Table 5-2 – Analytical Concrete Plastic Strain Comparison for Dowelled and Undowelled Joints Using Full, Half and Wheel Path Models

Model	Load (kN)	PEEQ	PEEQT
Full Slab Model with Dowels	43.75	0.00018	0.00001
	87.50	0.00059	0.00026
	175.00	0.00205	0.00031
Half Slab Model with Dowels	43.75	0.00018	0.00001
	87.50	0.00064	0.00012
	175.00	0.00215	0.00052
Wheel Path Model with Dowels	43.75	0.00018	0.00005
	87.50	0.00089	0.00032
	175.00	0.00396	0.00074

Comparing the values for PEEQ between the half slab model and the wheel path model, the wheel path model predicted larger values for the maximum PEEQ at each load level. The PEEQ values in the wheel path model are 1.02, 1.39 and 1.84 times the values obtained using the half slab model at each of the three load levels presented in Table 5-2 in increasing order. The values for PEEQT in the wheel path model are 4.51, 2.56, and 1.4 times the values obtained using the half slab model at the three load levels. All of the values obtained for PEEQ and PEEQT are below the values assumed for concrete failure (0.003 for PEEQT and 0.00474 for PEEQ) in the half slab, full slab, and wheel path models with dowels. Values for the models without dowels were not included in Table 5-2 since no plastic straining occurred.

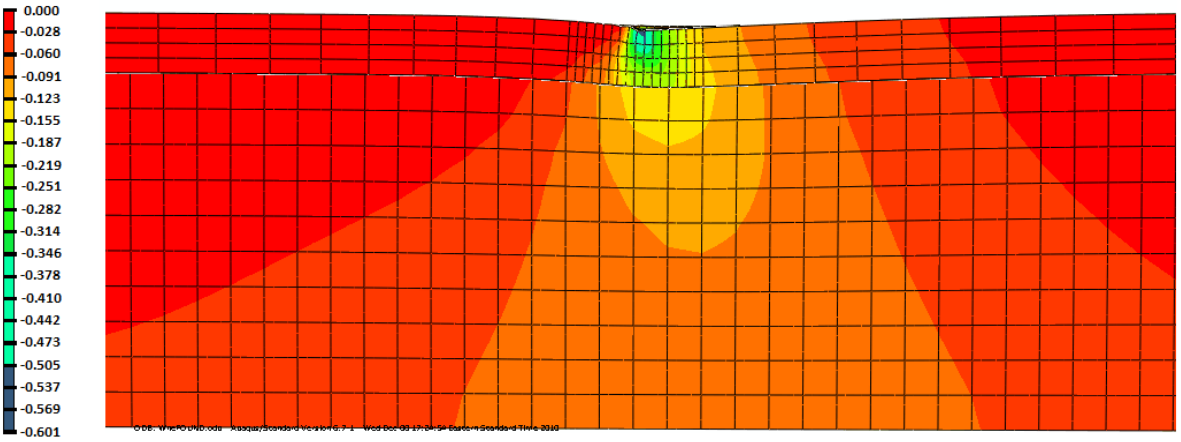

Figure 5-16 –Vertical Normal Stress in Base/Subbase for the Half Slab Model without Dowels at 200 kN Wheel Load (MPa)

Figure 5-16 presents the vertical normal stresses in the base and subbase layers in the half slab model with no dowels. The normal stress was concentrated to one side of the base where the load was transferred in the model without dowels, as was expected, since there was no load transfer across the joint in the concrete slab. Generally, the stress was distributed through the base layers from the concentrated load point with the highest stress concentrated along the edge of the loaded side of the slab (as was expected since the highest deflection of the slab was occurring at this point). The maximum bearing stress in the half slab model without dowels was 600 kPa at a load of 200 kN.

When the dowels were introduced across the joint in the concrete slab, the stress concentration in the base layers was reduced at the joint as the load was transferred across the slab to the other slab and through to the base layers over a larger area. Figure 5-17 shows the vertical stress distribution in the base layers in the half slab model with dowel bars.

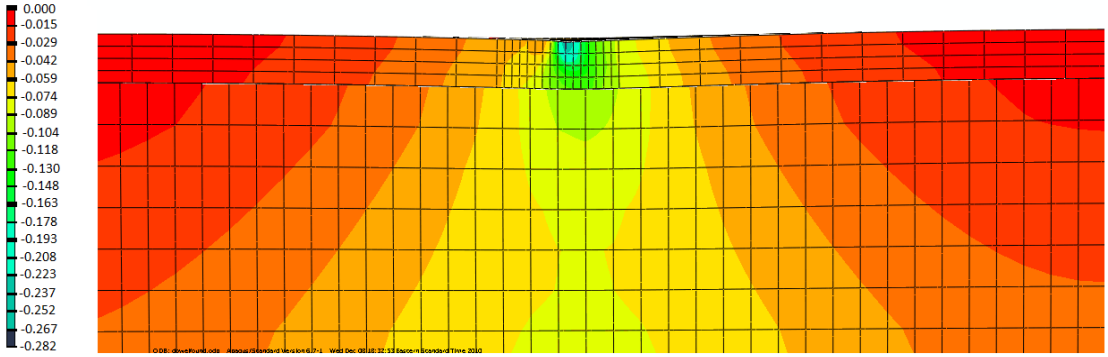

Figure 5-17 –Vertical Normal Stress in Base/Subbase for the Half Slab Model with Dowels at 200 kN Wheel Load (MPa)

The model with dowels had a concentration of normal stress where the loaded side of the joint was pushing into the base material (as differential joint deflection was still occurring). Maximum vertical stress in the base layer in the half slab model at the edge of the loaded slab was reduced in to 310 kPa from 600 kPa. Reducing the stresses in the base layer will help maintain the support of the slab at the joint location, and under poor soil conditions would be required to limit the deflection of the concrete slab. The peak stress in the base layer for the wheel path, half and full slab models with dowels and without dowels are presented in Table 5-3 at different load levels.

The wheel path model with dowels predicted higher vertical stresses in the base layer than the half slab model. The wheel path model estimated vertical stresses that were 1.78, 1.85, and 1.92 times the values obtained using the half slab model at the wheel load levels of 43.75, 87.50 and 175 kN, respectively. The reduced length of slab to distributed the force, as well as the reduced depth of base layer to deflect and allow for the vertical distribution of the stresses to the vertically restrained base were assumed to cause the increased stresses in the base layer of the wheel path model. The equivalent stiffness of the wheel path model base is also relatively higher than the base layers used in the half slab model. This increased stiffness was not done intentionally as the base layer in the wheel path model was based on a general base that could be used in the lab when an unknown assumed crushed granular layer similar to the crushed limestone layer used in the work of Eddie et al. (2001).

Table 5-3 – Subgrade Maximum Vertical Normal Stresses for the Full, Half, and Wheel Path Models with Dowels and Without Dowels

Model	Load (kN)	Subgrade Vertical Normal Stress (kPa)
Full Slab Model with Dowels	43.75	-73
	87.50	-134
	175.00	-270
Half Slab Model with Dowels	43.75	-72
	87.50	-134
	175.00	-269
Half Slab Model without Dowels	43.75	-118
	87.50	-248
	175.00	-489
Wheel Path Model with Dowels	43.75	-128
	87.50	-248
	175.00	-516
Wheel Path Model without Dowels	43.75	-243
	87.50	-518
	175.00	-1021

An investigation was also completed into the behaviour of the dowels for the half, full and wheel path models (containing dowels). The dowels had a vertical normal stress along the length of the dowel on either side of the joint, and also had bending stresses in produced by bending deformations of the dowel. At the joint, the dowel had a large concentration of shear stress as the load is transferred from one side of the joint to the other. A section of the vertical stress distribution in the dowel is presented in Figure 5-18. The longitudinal normal stress distribution along a longitudinal section through the dowel bar in the half slab model is presented in Figure 5-19 at after a 200 kN wheel load is applied. The shear stress distribution through the dowel bar section at the joint location is presented in Figure 5-20.

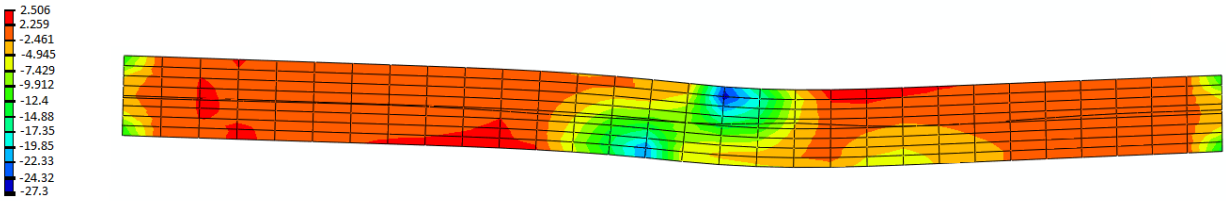

Figure 5-18 – Half Slab Dowel Model Vertical Normal Stress in the Dowel at 200 kN Wheel Load (MPa)

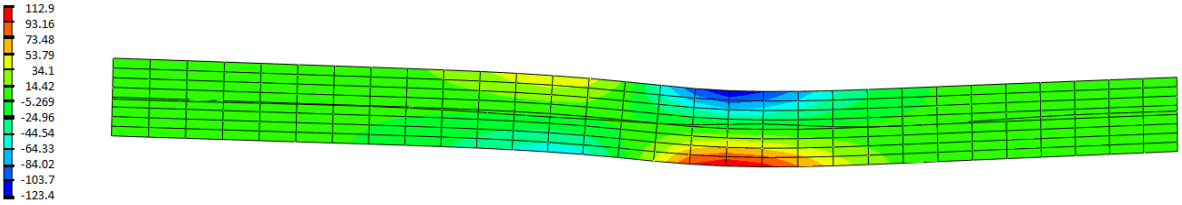

Figure 5-19 – Half Slab Dowel Model Longitudinal Normal Stress in the Dowel at 200 kN Wheel Load (MPa)

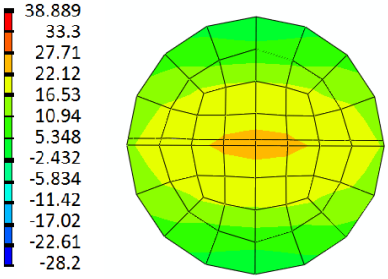

Figure 5-20 – Half Slab Dowel Model Shear Stress in Dowel at Joint at 200 kN Wheel Load (MPa)

Bearing of the concrete on the dowel at the joint caused high vertical normal stresses in the dowel on either side of the joint. On the loaded side of the joint, the stresses were concentrated on the top side of the dowel, while stress concentrations developed at the bottom of the dowel on the unloaded side. This is consistent with the stress concentrations observed in the concrete slab. The longitudinal normal stress distribution suggests the maximum moment in the bar was located on the loaded side of the slab under the load, with compression stresses at the top and tension at the bottom. A second large concentration of moment with compression at the bottom of the dowel was located near the joint on unloaded side of the slab as visible in Figure 5-19. The profile of the shear force at the dowel showed the shear transfer at the joint which appeared to be

similar to an assumed pure shear transfer at this location, meaning that the stress in a section in shear would have higher shear stresses concentrated at the neutral axis. In order to estimate the force transferred across the joint, the shear stresses in the dowel were averaged over the area and multiplied by a representative area to determine a shear force.

Figure 5-21 presents the dowel shear force for the different dowels along the length of the joint of the half slab model to present the load sharing along the length of the joint not captured in the wheel path model. The dowels located directly under the wheel path and load applications take majority of the wheel load transferred. Dowels located further from the load application have less shear transfer occurring at the joint location. To determine the amount of force being transferred across the joint using the half slab model, the sum of the force transferred by all of the dowels is compared to the total load applied to the slab. In Figure 5-21, the highest shear force was transferred by the dowels directly below the wheel load application by four dowels with an approximate maximum force transferred of 12 kN each at the 200 kN wheel load. The four dowels directly adjacent the wheel load application area had the second highest shear force transfer and are represented in Figure 5-21 by the line with a maximum force of approximately 7 kN at the 200 kN wheel load application. The maximum shear force decreases on the dowels moving further from the location of the wheel load application.

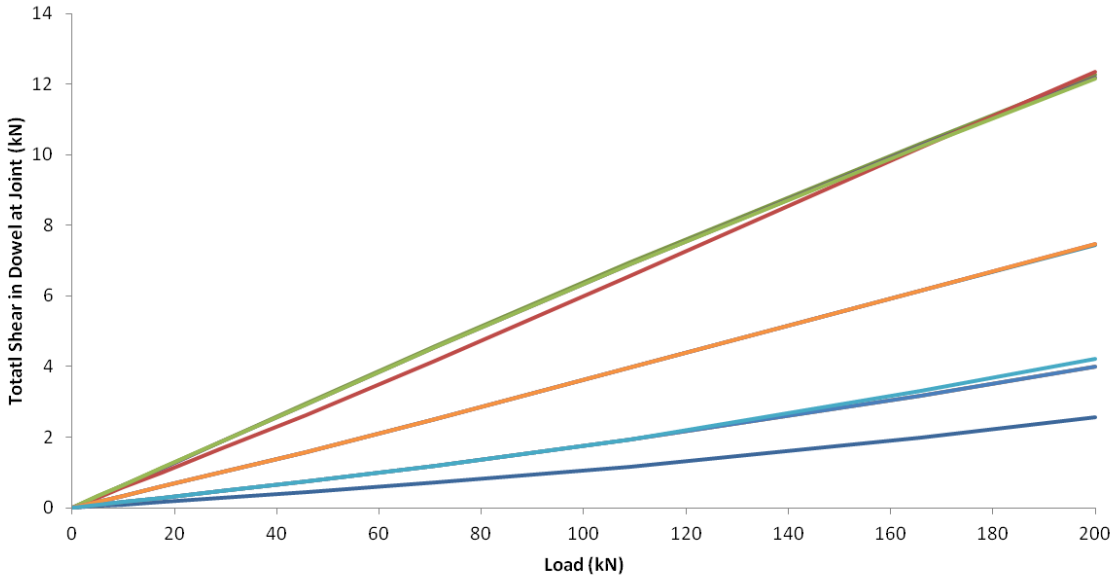

Figure 5-21 – Half Slab model dowel Shear Force Transfer

The dowels transferred from 22 to 23% of the total wheel load through the dowels to the unloaded side of the slab for each load increment investigated in the half slab model. The wheel path model with only two dowels and no transverse load distribution also had a similar percentage of total load transfer across the joint ranging from 20% to 22%. In the wheel path model, both dowels transferred approximately the same amount of load (which is expected due to the symmetric arrangement of the dowels).

A comparison of the maximum shear force in the dowel at the joint, the maximum Von Mises stress in the dowel and percentage of load transferred at each load level (using the shear stress in the dowel) for the wheel path, and half slab models with dowels is presented in Table 5-4.

Table 5-4 – Half Slab and Wheel Path Transfer Model Dowel Bar Behaviour

Model	Wheel Load (kN)	Von Mises Stress (MPa)	Max Shear Transfer (kN)	Percentage of Load Transferred
Half Slab Model Dowels	43.75	28.8	3.0	22.41%
	87.50	55.2	5.6	22.68%
	175.00	110.2	10.8	22.86%
Wheel Path Model with Dowels	43.75	46.1	5.1	22.47%
	87.50	92.3	9.6	22.06%
	175.00	200.6	18.3	20.96%

In the wheel path model, the maximum shear transfer at the joint through the dowels was approximately 1.69 to 1.7 the peak vertical shear transferred in the half slab model. The maximum Von Mises stress in the dowel in the wheel path model was 1.60 to 1.82 the values obtained using the half slab model (as presented in Table 5-4).

5.2.5 Wheel Path Model Development – Summary of Findings

The adequacy of the wheel path model to represent load transfer behaviour was demonstrated by comparing predicted behaviour to that estimated by half slab and full slab models. The wheel path model has been shown to predict the behaviour of the slab similarly to the half slab model through comparisons of the overall deflection at the joint and differential deflection occurring at the joint. Higher differential deflection is predicted using the wheel path model as less load transfer occurs along the length of the slab and for the same reason the slab curvature to due to applied wheel loading is greater. The wheel path model generally concentrates more of the load

over a smaller area (and through fewer devices when they are used). The smaller zone for stress distribution in the wheel path model causes increases in the maximum stresses in both the concrete and dowels.

5.3 Dowel Wheel Path Model Mesh Refinement and Preliminary Analysis

The wheel path model was regenerated using different meshes to investigate the mesh sensitivity in the results. Three different meshes were compared for the wheel path model with dowels. Table 5-5 presents the total number of elements for each model in the mesh sensitivity investigation. Table 5-6 presents the comparison of the joint performance for the dowel bar models with the three different meshes.

Table 5-5 – Dowel Wheel Path Model Mesh Comparisons

Mesh description	Number of Elements
Coarse	34664
Medium	42864
Fine	74812

Table 5-6 –Dowel Wheel Path Model Joint Deflection Mesh Refinement Comparison

	Wheel Load (kN)	Vertical Deflection Loaded side (mm)	Vertical Deflection Unloaded side (mm)	LTE (%)	Joint Effectiveness (%)	Differential Deflection (mm)
Coarse	43.75	-0.273	-0.217	79.52%	88.59%	-0.056
	87.50	-0.514	-0.384	74.74%	85.55%	-0.130
	175.00	-1.045	-0.706	67.52%	80.61%	-0.340
Medium	43.75	-0.274	-0.216	78.73%	88.10%	-0.058
	87.50	-0.514	-0.385	74.96%	85.69%	-0.129
	175.00	-1.031	-0.720	69.82%	82.23%	-0.311
Fine	43.75	-0.273	-0.217	79.5%	88.6%	-0.056
	87.50	-0.514	-0.385	74.9%	85.6%	-0.129
	175.00	-1.054	-0.696	66.0%	79.5%	-0.358

The results in Table 5-6 show that there was some mesh sensitivity in the overall joint performance, but all three of the meshes predict the behaviour on the same order of magnitude. The difference between the joint performance for the different mesh geometries investigated may suggest that a mesh sensitivity existed due to the plastic straining occurring in the concrete. Both sides of the joint in all three models at the 43.75kN load level had a deflection on either side of

the joint being estimated within a thousandth of a millimeter. Similarly at the 87.50 kN load level the deflection either side of the joint were estimated within a thousandth of a millimeter. At 175kN the deflection of the slab on the loaded side of the slab differed by 0.023 mm and the unloaded side differed by 0.024 mm for the coarse, medium and fine meshes used. This comparison suggested that the mesh geometry does not significantly affect the overall joint performance, although some sensitivity could be seen in the dowel models at high wheel load increments.

The dowel bar equations presented in Section 2.1.3 that were used for device development were compared during the preliminary analysis of the different devices to determine validity of the equations when compared to the analysis results. Comparing the model results with the expected deflection of a dowel bar using the equations, the modulus of dowel support can be back calculated to approximately 2400 N/mm^3, 1850 N/mm^3 , 1250 N/mm^3 for each of the 43.75, 87.5 and 175 kN load increments. The modulus of dowel support was variable at different load levels for conventional models based on the analysis results.

The maximum Von Mises stress in the dowel, the vertical shear transferred at the joint by the dowels and the maximum vertical stress in the subgrade are compared in Table 5-7 for the different model mesh geometries.

Table 5-7 –Dowel Wheel Path Model Base and Dowel Stress/Force Comparison

	Wheel Load (kN)	Subgrade Max Vertical Stress (kPa)	Dowel Von Mises Max (MPa)	Shear Transferred (kN)
Coarse	43.75	-139	48.9	10.3
	87.50	-275	95.8	19.3
	175.00	-591	209.4	36.9
Medium	43.75	-128	46.1	10.3
	87.50	-248	92.3	19.3
	175.00	-516	200.6	36.7
Fine	43.75	-146	47.1	11.8
	87.50	-283	92.7	22.2
	175.00	-594	200.6	41.6

The shear transferred by the dowels is very similar between the coarse and medium meshes used; however, there was less shear transfer predicted using these models than in the finely meshed

model. The maximum Von Mises Stress was more similar between the medium and the finely meshed models, but there was a larger difference between those models and the coarsely meshed model. The subgrade maximum stress in each model was similar and no specific similarities appear between the model behaviour. Once again, the local response listed in Table 5-7 show some mesh sensitivity, although the results are generally comparable and were still on the same order of magnitude.

The values for maximum plastic straining in the concrete were compared for the three mesh densities as presented in Table 5-8. The maximum plastic straining appears to have the most variability in results depending on the meshing chosen. It is suggested in the ABAQUS manual (ABAQUS, 2008) that there may be mesh sensitivity in the concrete damaged plasticity model when there are large areas of unreinforced concrete. Generally the values obtained using each mesh density for the dowel bar models are on the same order of magnitude for the different mesh geometries. The values obtained for PEEQ and PEEQT using the medium mesh density are the lowest. The values obtained for PEEQT vary more than the values obtained for PEEQ using the three different meshes. The values are still on the same order of magnitude at each load level.

Table 5-8 –Dowel Wheel Path Model PEEQ and PEEQT Mesh Sensitivity

	Wheel Load (kN)	PEEQ	PEEQT
Coarse	43.75	0.00020	0.00034
	87.50	0.00081	0.00053
	175.00	0.00401	0.00140
Medium	43.75	0.00018	0.00005
	87.50	0.00089	0.00032
	175.00	0.00396	0.00074
Fine	43.75	0.00025	0.00019
	87.50	0.00094	0.00064
	175.00	0.00459	0.00160

In summary of the mesh refinement study completed for the wheel path dowel bar models, the predicted deflection, stresses in the concrete and device, as well as plastic straining are on the same order of magnitude although some mesh sensitivity exists. The medium mesh was used for the remaining wheel path analysis completed and similar mesh densities were used for the half slab model based on this mesh refinement study.

5.4 GFRP I-beam Wheel Path Model Mesh Refinement and Preliminary Analysis

The GFRP I-beam load transfer device was designed using conventional dowel bar theory, as described previously in Section 3.2.1. The performance of this device will be compared to dowel bar behaviour and theory. In modeling the GFRP I-beam in the wheel path model a single I-beam was modeled compared to the two dowels.

Three different models for the GFRP I-beam device were generated with three different mesh geometries, and the results of each were compared. The number of elements in each of GFRP I-beam model is presented in Table 5-9.

Table 5-9 –GFRP I-beam Wheel Path Model Meshes

Mesh description	Number of Elements
Coarse	62024
Medium	73022
Fine	149656

The differential deflection across the joint at three distinct load increments (43.75, 87.5 and 175 kN) are presented in Table 5-10 along with the LTE, and joint effectiveness.

Table 5-10 – GFRP I-beam Wheel Path Model Joint Performance Comparison

	Wheel Load (kN)	Vertical Deflection Loaded side (mm)	Vertical Deflection Unloaded side (mm)	LTE (%)	Joint Effectiveness (%)	Differential Deflection (mm)
Coarse	43.75	-0.332	-0.154	46.2	63.2	-0.178
	87.50	-0.627	-0.261	41.7	58.8	-0.365
	175.00	-1.288	-0.433	33.6	50.3	-0.855
Medium	43.75	-0.332	-0.153	46.3	63.3	-0.178
	87.50	-0.625	-0.262	42.0	59.1	-0.363
	175.00	-1.289	-0.430	33.3	50.0	-0.859
Fine	43.75	-0.297	-0.153	51.4	67.9	-0.144
	87.50	-0.557	-0.263	47.2	64.1	-0.294
	175.00	-1.143	-0.439	38.4	55.5	-0.704

The joint effectiveness of the GFRP I-beam at the half wheel load level ranged from 63.2 to 67.9%. The joint effectiveness and LTEs were below the suggested values; however, it was hard

to compare the ranges due to the difference in the behaviour of the half slab and wheel path models as previously presented. At the 43.75 kN load level, the deflection on the loaded side was 0.035 mm different from the medium and coarse mesh to the fine mesh; however, on the unloaded side the difference was 0.001 mm. The modulus of dowel support is much less than the value calculated for the conventional dowel. Note that the GFRP I-beam had higher differential deflection than the dowel bar (See Table 5-6); however, the GFRP I-beam was capable of maintaining the differential deflection between the slabs to below 1 mm which was much better than a slab without dowels.

Based on the differential deflection of the medium and coarsely meshed models the modulus of dowel support using conventional dowel bar theory at each of the three load increments was back calculated to be 375, 360 and 245 N/mm^3 for each of the three load increments in increasing order of load magnitude. Modulus of dowel support at the given load levels varies based on the analysis completed and does not show any direct correlation to the values obtained when compared to dowel bars except that the values are decreasing with increasing load.

To understand how the load is being transferred through the concrete at the joint a section of the vertical stresses in the concrete through the GFRP I-beam are shown in Figure 5-22. Similar to the dowels, the vertical stress distribution on the loaded and unloaded sides of the slab is different. In the GFRP I-beam model, two vertical compressive stress concentrations occur above both flanges on the loaded side. Since only the top flange on the unloaded side bears on concrete, the bottom flange does not apply a vertical compressive force to the slab since it bears directly on the base material. On the unloaded side, larger tensile vertical stress concentrations occur around the sides of the top flange of the device, as is shown in the section through the loaded side in Figure 5-22.

To identify areas of damage in the concrete around the GFRP I-beam, a section of the PEEQ strains are presented in Figure 5-23. Similar to the vertical compressive strain concentrations observed for the dowels, the plastic straining in the concrete in GFRP I-beam model was limited to the joint location. Most of the damage occurred on either side of the top flange. On the loaded side, similar to a conventional dowel, above the top flange an area of compressive damage was occurring extending from the joint interface. Alternatively, on the unloaded side of the joint, compressive damage was occurring at the joint interface below the top flange. The only areas

that have PEEQT strains were a localized area extending out from the top flange on both sides of the joint (also similar to dowel bar behaviour). Although the damaged areas appeared to be local to the joint, the maximum values for plastic compressive strains were near the failure limit. The PEEQT profile in the concrete is not presented; however, local areas of damage were limited to the area immediately adjacent to the top flange of the device.

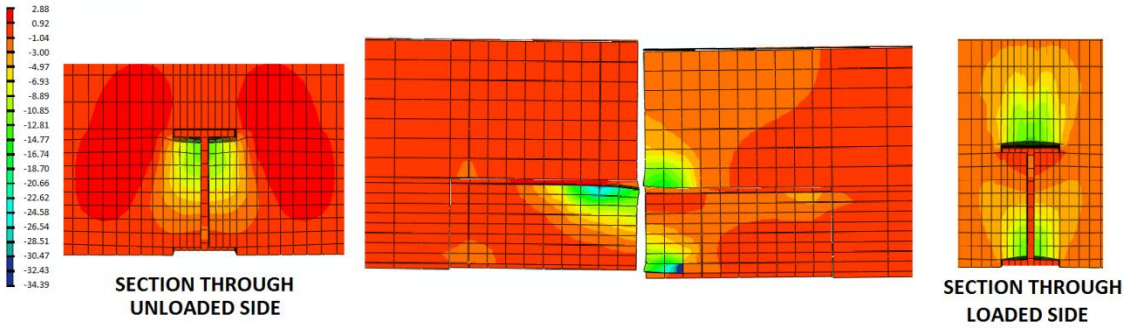

Figure 5-22 – GFRP I-beam Wheel Path Model - Vertical Stress Distribution in Concrete at 200 kN Wheel Load (MPa)

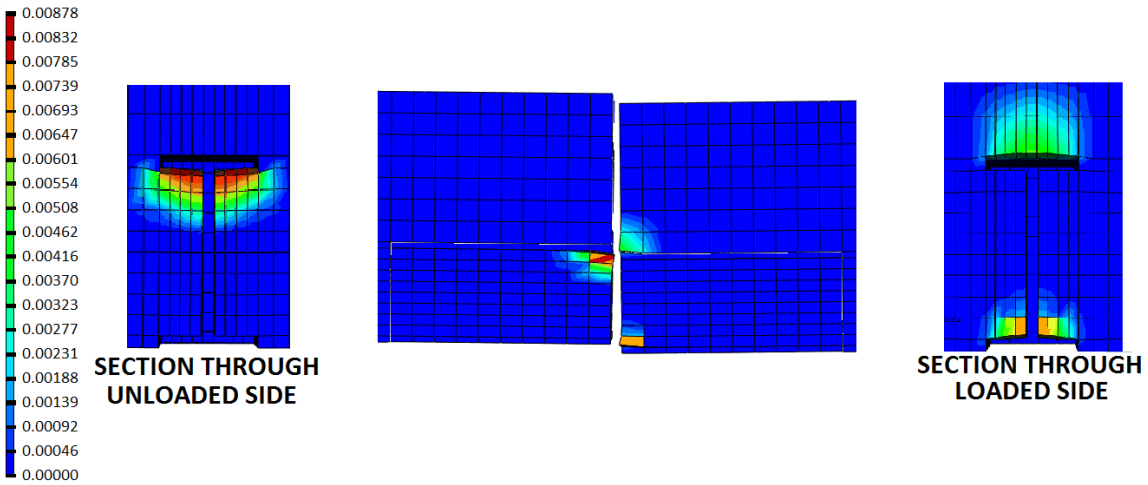

Figure 5-23 – GFRP I-beam Wheel Path Model PEEQ at 200 kN Wheel Load (MPa)

The PEEQ and PEEQT strains are similar in all three model mesh geometries, with the values for maximum PEEQ and PEEQT in the concrete presented in Table 5-11. All three of the models predict the failure of the concrete in both compression and tension to be occurring at the 175kN load level. The plastic strains in tension at the wheel load level (87.5 kN) are approaching the failure in tension for the coarse and medium meshed models. The values obtained for plastic

strains in tension and compression for the GFRP I-beam were larger than those predicted for the dowel bar model.

Table 5-11 – GFRP I-beam Wheel Path Model PEEQ and PEEQT Maximum Values

	Wheel Load (kN)	PEEQ	PEEQT
Coarse	43.75	0.00011	0.00084
	87.50	0.00177	0.00315
	175.00	0.00704	0.01207
Medium	43.75	0.00011	0.00090
	87.50	0.00167	0.00315
	175.00	0.00743	0.01320
Fine	43.75	0.00018	0.00093
	87.50	0.00190	0.00297
	175.00	0.00818	0.01191

To understand the load transfer to the base layer when the GFRP I-beam is set directly on the base, and to understand how well it transfers load at the joint to the base layer, a longitudinal section through the middle of the base layer is shown in Figure 5-24. The load was not transferred through to the base layer using a GFRP I-beam as well as observed for the dowels. There was evidence of the load being transferred from one side of the slab to the other; however, there was a higher concentration of stress located at the joint in the GFRP I-beam model. There was also a clear location where the stresses in the base layer were increased beneath the GFRP I-beam in comparison to the behaviour for the dowel bar model.

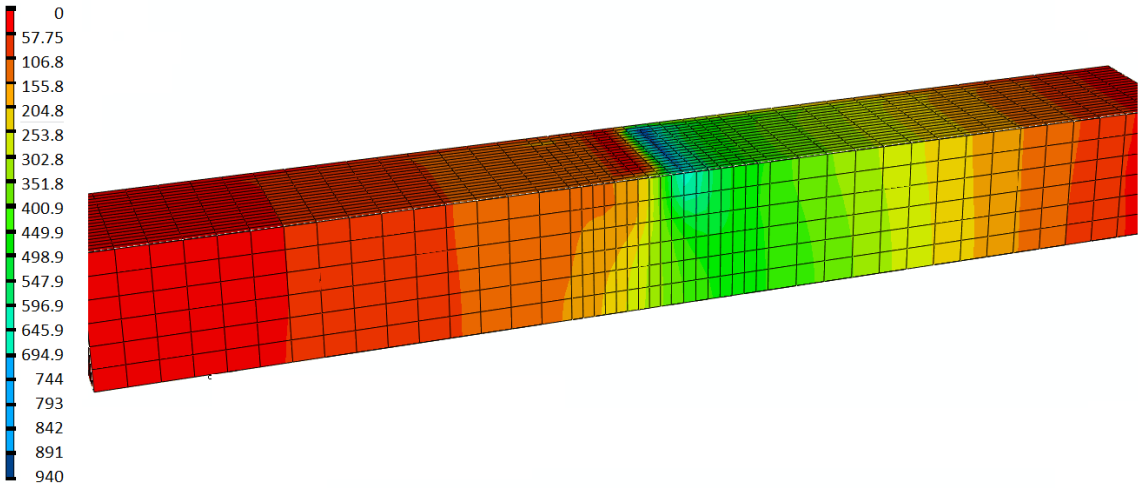

Figure 5-24 - GFRP I-beam Wheel Path Model Vertical Stress Distribution in base layer at 200 kN Wheel Load (MPa)

The vertical and longitudinal normal stresses in the GFRP I-beam are shown in Figure 5-25 and Figure 5-26, respectively. The GFRP I-beam had vertical concentrations on either side of the joint and provided shear transfer across the joint as well as a bearing directly on the ground across its entire length.

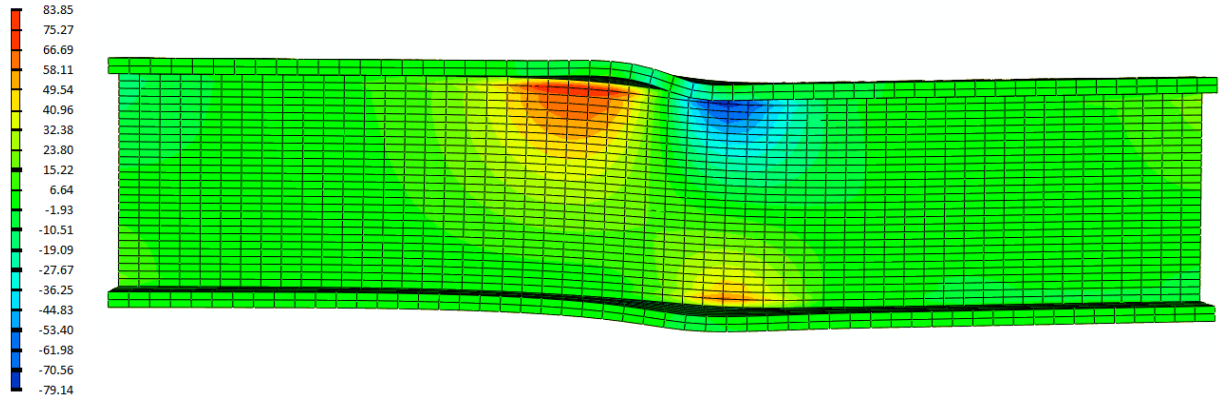

Figure 5-25 – GFRP I-beam Wheel Path Model Vertical Normal Stress in GFRP I-beam at 200 kN Wheel Load (MPa)

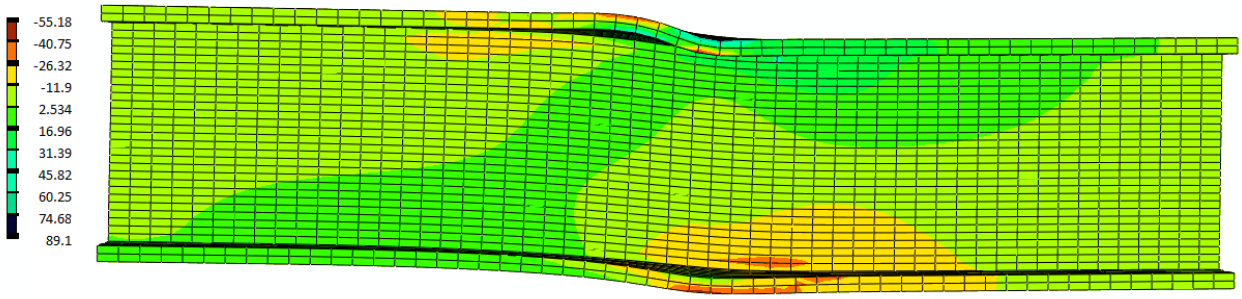

Figure 5-26 – GFRP I-beam Wheel Path Model Longitudinal Normal Stresses in GFRP I-beam at 200 kN Wheel Load (MPa)

The vertical normal stresses in the GFRP I-beam were concentrated in the same locations as they were concentrated in the slab (as would be expected). These stresses were concentrated on either side of the joint at the edges of the slab. The vertical stresses in compression and tension ranged from about -79 to 84 MPa. The vertical stress distribution was not shown across the width of the flange. However, the vertical stresses were concentrated in the middle of the flange and were transferred through to the web.

Longitudinal normal stresses in the top flange near the joint in Figure 5-26 were in tension and compression with opposite sense on either side of the joint, indicating that the top flange was bending at the joint location in the top flange on either side of the joint. The behaviour and the deflected shape of the top flange are very similar to that of a conventional dowel bar at the joint location. The bottom flange shows bending behaviour on the loaded side of the slab; however, it does not show the same distinct bending as in the flange where bending with opposite sense occurs on either side of the joint. The relatively weak support provided by the base layer on the unloaded side of the slab compared to the support provided by the concrete to the top flange is assumed to cause this difference in behaviour.

The vertical shear in the GFRP I-beam was estimated using the vertical shear stresses at the joint. Figure 5-27 shows the vertical shear distribution in the GFRP I-beam at a wheel load of 200 kN. The shear is mostly being transferred in the web which would be expected in the GFRP I-beam.

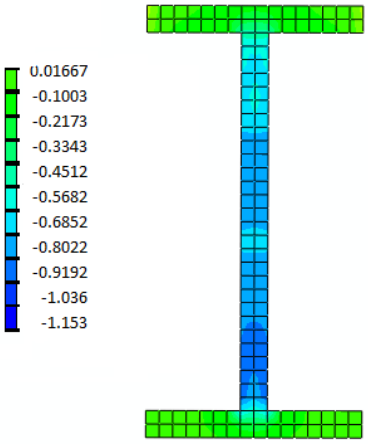

Figure 5-27 – GFRP I-beam Wheel Path Model Vertical Shear Stress at Joint Location at 200 kN Wheel Load (MPa)

A comparison of the maximum vertical base stress, I-beam Von Mises stress and estimated shear transferred by the GFRP I-beam is presented in Table 5-12 for the three different mesh geometries used.

Table 5-12 – GFRP I-beam Wheel Path Model Dowel and Base Stress/Force Comparison

	Wheel Load (kN)	Subgrade Max Vertical Stress (kPa)	GFRP I-beam Von Mises (MPa)	Shear Transferred (kN)
Coarse	43.75	-191	45	8.6
	87.50	-367	84	16.1
	175.00	-770	167	28.5
Medium	43.75	-190	45	8.6
	87.50	-363	84	16.2
	175.00	-764	162	28.4
Fine	43.75	-216	41	10.0
	87.50	-415	79	18.5
	175.00	-873	155	30.7

The maximum vertical stress predicted in the base with the GFRP I-beam was much greater than in the wheel path model with dowels; however, the GFRP I-beam had a lower maximum vertical stress in the base when compared to the slab without dowels. The maximum base vertical stress was different between the fine, medium and coarse models. The Von Mises Stresses in the GFRP I-beam were lower than in the steel dowel at all load levels. As the mesh was refined, the maximum Von Mises stress are generally reduced. The shear transferred by the I-beam was also similar in each mesh. The amount of shear transferred across the joint was lower than with the dowel bar models; however, it was transferring more than half the amount transferred by two dowels.

Based on the preliminary analysis of the GFRP I-beam, it was determined that a further investigation into the behaviour of the GFRP I-beam be should completed. The size and spacing of the I-beam would have to be altered to behave similarly to the dowel; however due to availability of GFRP shapes and proposed testing arrangement, the same size and shape GFRP I-beam and was selected for further testing based on the preliminary analysis. All three mesh geometries used predicted similar overall joint behaviour and the medium mesh was more refined near the top and bottom flanges than the coarse mesh but was more efficient than the fine mesh. Mesh geometry similar to the fine mesh was used for further finite element modeling completed.

5.5 GFRP Tapered plate Wheel Path Model Refinement and Preliminary Analysis

The GFRP tapered plate dowel was designed based on conventional dowel bar theory. The wheel path model investigation will compare the behaviour to a conventional dowel, the behaviour of the device, concrete and subgrade, as well the overall joint performance.

In order to assess the behaviour of the devices, three different meshes were generated for the tapered plate dowel. The number of elements in each of the three different mesh geometries used is presented in Table 5-13. Table 5-14 presents the joint performance comparison for the different meshes used for the GFRP Tapered plate wheel path models.

Table 5-13 – GFRP Tapered Plate Wheel Path Model Meshes

Mesh description	Number of Elements
Coarse	15936
Medium	23632
Fine	44070

Table 5-14 – GFRP Tapered Plate Wheel Path Model Joint Performance

	Wheel Load (kN)	Vertical Deflection Loaded side (mm)	Vertical Deflection Unloaded side (mm)	LTE (%)	Joint Effectiveness (%)	Differential Deflection (mm)
Coarse	43.75	-0.284	-0.213	75.2%	85.8%	-0.070
	87.50	-0.511	-0.371	72.6%	84.2%	-0.140
	175.00	-1.148	-0.545	47.5%	64.4%	-0.603
Medium	43.75	-0.309	-0.208	67.4%	80.5%	-0.101
	87.50	-0.566	-0.330	58.4%	73.7%	-0.236
	175.00	-1.220	-0.553	45.4%	62.4%	-0.667
Fine	43.75	-0.295	-0.184	62.4%	76.9%	-0.111
	87.50	-0.604	-0.332	54.9%	70.9%	-0.272
	175.00	-1.241	-0.536	43.2%	60.3%	-0.706

The differential deflection at all load levels investigated was well below 1 mm. The maximum differential deflection measured at the joint using the fine model was estimated to be 0.706 mm. Joint effectiveness for the GFRP Tapered plate dowel ranged from about 85% to 60%. At low load levels, the joint effectiveness was very similar to the dowel bar. The joint effectiveness in a dowel at the half wheel load level was approximately 88%; however, at higher load levels, the

joint effectiveness was reduced in comparison to the steel dowel bar models where the joint effectiveness of the dowels at twice the wheel load was approximately 79.5%. The LTE of the GFRP Tapered plate dowel ranged from 43% to 75% for the three load ranges. At the lower load increments, the LTE differed more between the different model geometries than at the higher load increments. The LTE differed by 13% at the 43.75 kN load level and only by 4% at the 175 kN load increment.

Based on the dowel bar equations the modulus of dowel support at each of the three load increments is back calculated to be approximately 1000, 750 and 315 N/mm^3 in increasing order of load application. The modulus of dowel support was reduced as the wheel load increased similar to both conventional dowels and the GFRP I-beam. Estimated values for the modulus of dowel support for the GFRP tapered plate were higher than the GFRP I-beam but lower than values estimated for conventional round steel dowels.

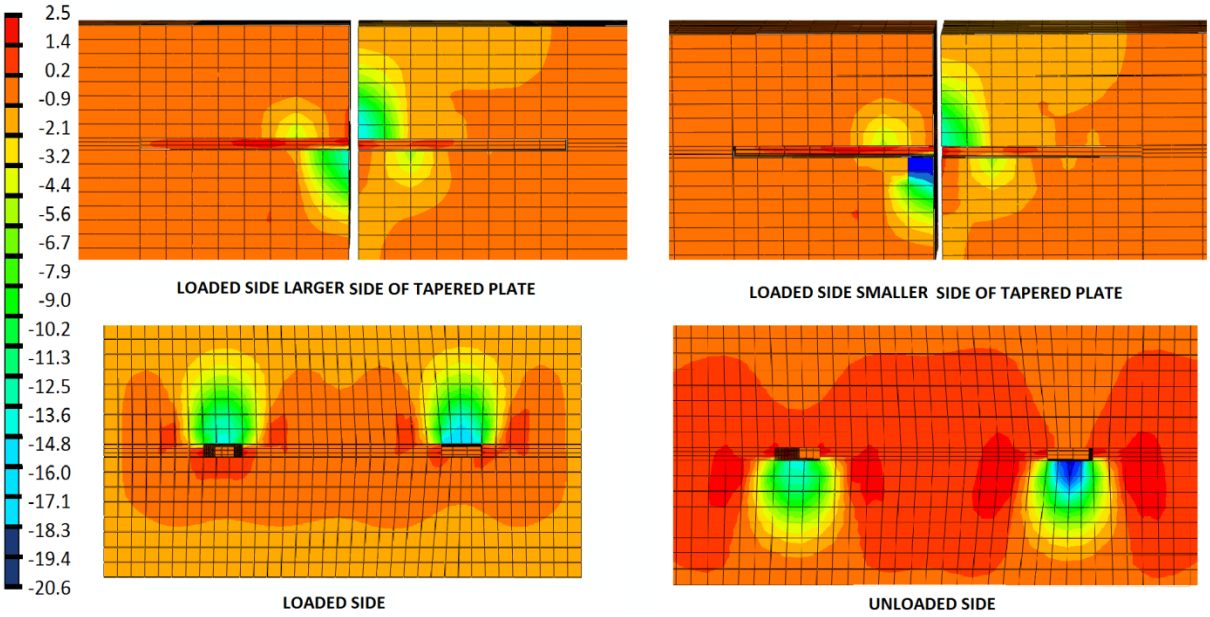

Figure 5-28 – GFRP Tapered plate Wheel Path Model Vertical Stress Distribution in the concrete at 200 kN Wheel Load (MPa)

The vertical normal stress distribution on both of the GFRP Tapered plates was similar to dowel bars in that distinct zones of vertical tensile and compressive stresses occurred on either side of the joint above and below the dowel. A zone of compressive stress was present on the loaded side of the joint above both of the tapered plates. This zone of compressive stress in the concrete

at the joint interface, on the loaded side of the joint, was larger with a higher maximum stress above the wider side of the tapered plate. On the other side of the joint, a similar local zone of compressive vertical normal stress occurred beneath the tapered plate. Beneath the wider end of the GFRP tapered plate, on the unloaded side, the compressive stress was greater than the narrower end of the tapered plate. The vertical normal tensile stresses that occurred around the dowel locations were larger near the wider ends of the GFRP tapered plate dowels.

To assess the damage occurring around the GFRP tapered plate in the concrete, several sections through the slab showing the plastic strain around the plate dowels are presented in Figure 5-29 and Figure 5-30.

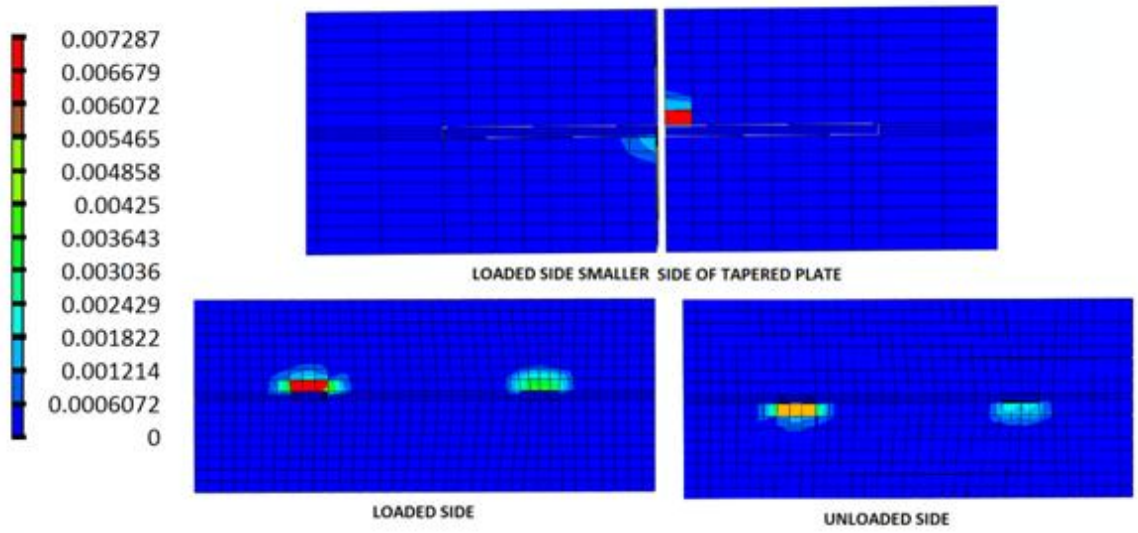

Figure 5-29 – GFRP Tapered plate Wheel Path Model Slab PEEQ at 200 kN Wheel Load

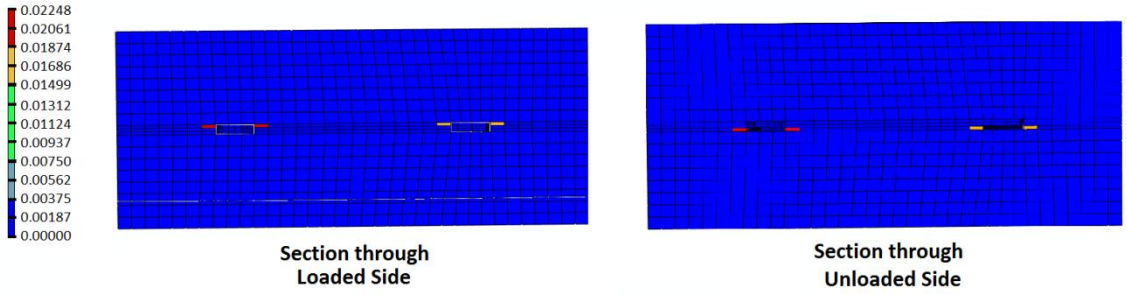

Figure 5-30 – GFRP Tapered plate Wheel Path Model PEEQT at 200 kN Wheel Load

Plastic strain profiles in the concrete for the GFRP tapered plate were similar to conventional steel dowels where compressive plastic straining was occurring above the dowel on the loaded side and below the dowel on the unloaded side of the dowel. The compressive damage on the loaded side of the slab above the smaller tapered plate end was greater than the larger end of the plate dowel. Similarly, on the unloaded side of the slab the PEEQ strains were also greater on the smaller tapered plate width. Tensile plastic straining in the concrete occurred at the top face of the tapered plate on the loaded side of the slab and at the bottom face of the tapered plate on the unloaded side. The tensile straining was localized at the joint.

The PEEQ and PEEQT values obtained using the different meshes for the tapered plate model are presented in Table 5-15.

Table 5-15 – GFRP Tapered Plate Wheel Path Model PEEQ and PEEQT

	Wheel Load (kN)	PEEQ	PEEQT
Coarse	43.75	0.00000	0.00004
	87.50	0.00002	0.00144
	175.00	0.00406	0.00849
Medium	43.75	0.00000	0.00036
	87.50	0.00025	0.00224
	175.00	0.00318	0.00778
Fine	43.75	0.00000	0.00159
	87.50	0.00031	0.00539
	175.00	0.00361	0.01715

The tensile plastic strains in all the models were similar. At the 43.75 kN level, none of the meshes predicted plastic straining to occur in compression. The plastic strains at all the load levels were on the same magnitude between the different model mesh geometries in both compression and tension. The plastic straining in compression in all the models at all the load levels were below the assumed crushing failure plastic strain value of 0.00474. The tensile plastic strain was below the cracking failure strain assumed (0.003) for all of the models at the 43.75 kN load level. The fine mesh predicted the plastic strain in tension at the edge of the tapered plate to exceed the failure strain assumed at the wheel load level (87.5 kN); however, the coarse and medium meshes did not predict that the plastic tensile strains exceed the assumed

cracking failure value. Although this was an assumed failure, it is noted that this was obtained with a fine mesh and that the zone was very localized.

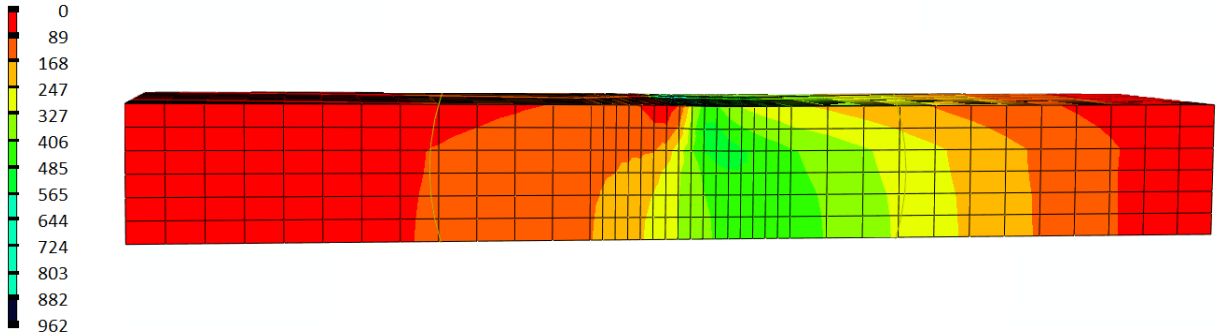

Figure 5-31 – GFRP Tapered plate Wheel Path Model Vertical Stress in the Base – 200 kN (MPa)

The vertical normal stresses predicted in the base layer of the tapered plate wheel path model is presented in Figure 5-31 with a 200 kN wheel load applied. The vertical stress in the base layer was concentrated on the side of the wheel load application suggesting that the load was not being evenly transferred across the joint, as the stresses in the base layer were more concentrated than in the steel dowel bar model. However, the stress was reduced compared to an undowelled joint and there was some evidence of load transfer and reduced stress in the subgrade.

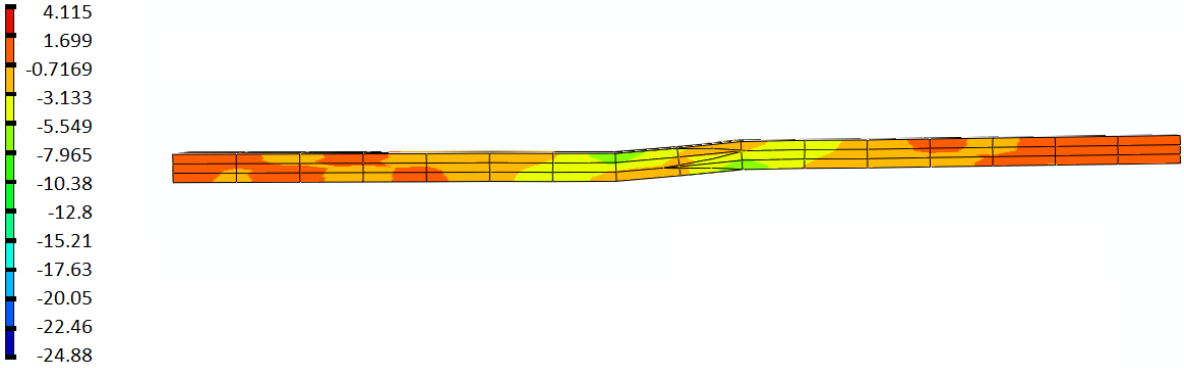

Figure 5-32 – GFRP Tapered Plate Wheel Path Model Vertical Normal stress Distribution in the GFRP Tapered Plate at 200 kN Wheel Load (MPa)

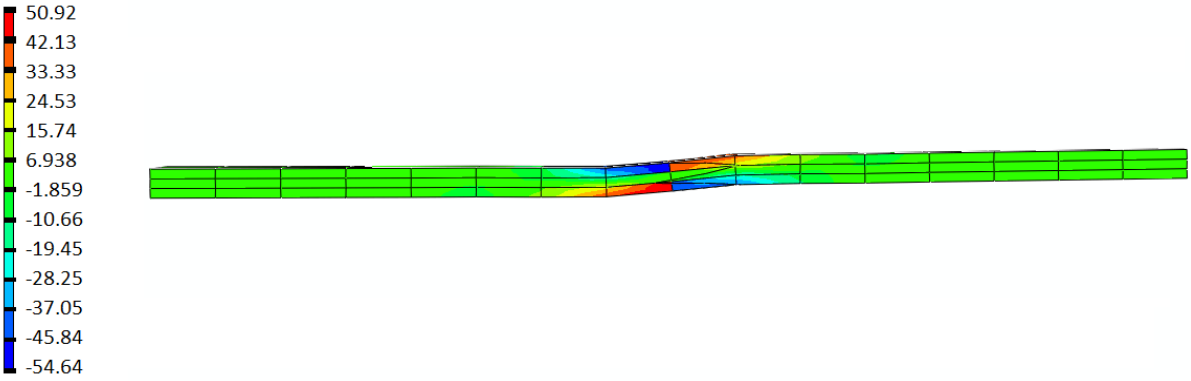

Figure 5-33 – GFRP Tapered Plate Longitudinal Normal Stress Distribution in the GFRP Tapered Plate at 200 kN Wheel Load (MPa)

Figure 5-32 and Figure 5-33 present the vertical and longitudinal normal stress in the GFRP tapered plate for the wheel path model with a 200 kN wheel load applied to the slab. The GFRP tapered plate behaved similarly to a conventional dowel at the joint location and across the joint. Bending stresses were concentrated in the device on either side of the joint as presented in Figure 5-33. The sense of the bending stresses indicated a reversal in the sense of bending. The vertical normal stress concentrations in compression and tension were also similar to the steel dowel with distinct zones at the joint location, and also spread along the length of the dowel in the vertical stress distribution.

Table 5-16 – GFRP Tapered Plate Subgrade and Dowel Comparison

	Wheel Load (kN)	Subgrade Max Vertical Stress (kPa)	Dowel Von Mises (MPa)	Shear Transferred (kN)
Coarse	43.75	-142	4	1
	87.50	-262	8	1
	175.00	-658	19	3
Medium	43.75	-162	5	1
	87.50	-323	10	2
	175.00	-709	23	6
Fine	43.75	-159	5	6
	87.50	-340	11	13
	175.00	-729	25	29

A summary of the peak vertical stress in the base layer, dowel shear force transferred and the maximum Von Mises stress in the dowel are presented in Table 5-16. The maximum base vertical stress varied from 142 kPa to 162 kPa at the 43.75 kN wheel load for the three models,

with the maximum stress occurring with the medium mesh. At the 87.5 kN load level, the maximum subgrade reaction stress varied from 262 kPa to 340 kPa with the maximum subgrade stress occurring in the fine mesh model. At the 175 kN load level, the maximum subgrade reaction was 729 kPa and the minimum was 658 kPa with the coarse mesh having the lowest subgrade reaction. The medium and coarse meshes were very similar at the 43.75 kN load level although the medium mesh had a higher maximum subgrade stress. It appears that the predicted device behaviour was affected by the model meshing. The smaller thickness of the section and the fineness of the meshing used appeared to affect the results. The shear force calculated with the coarse and medium meshes were assumed to not be realistic and more mesh refinement would be required to properly assess the shear force transfer at the joint. The values for the maximum predicted base reaction were greater than conventional steel dowels; however, they were less than the GFRP I-beam.

The maximum Von Mises stress in the dowel ranged from 4 to 5 MPa at the 43.75 kN load level, 8 to 11 MPa at the 87.5 kN load level and 19 to 25 MPa at the 175 kN load level. These values were much lower than the values for the dowel and GFRP I-beam models. It was assumed that the reduced maximum Von Mises stress in the GFRP tapered plates was due to the mesh refinement in the plate not capturing the bending stresses in the plate properly. The values for the GFRP I-beam and dowel bars for device Von Mises stresses were approximately 160 MPa for the GFRP I-beam and 200 MPa for the dowel section. Similarly, the shear load transferred values were also calculated to be much lower using tapered plate dowels compared to the GFRP I-beam or conventional dowels. Using the finer mesh should help to ensure realistic behaviour is estimated. However, the low load transfer may also be a result of the lower relative stiffness of the tapered plate and increasing the thickness of the GFRP I-beam to increase the relative stiffness of the tapered plate could be completed to increase the force transfer in the device. Further modeling and analysis in the current study did not consider increasing the thickness of the tapered plate due to available materials for experimental testing. The fine mesh geometry is used for the remaining modeling of the tapered plate to capture this behaviour more effectively and in comparisons with the other device behaviour.

5.6 Load Transfer Comparison of Discrete Devices – Parametric Study

The frictional coefficient used for the contact surface between the devices and concrete were chosen based on range of values for steel dowel and concrete interaction based on the work of Shoukry et al. (2003).The results for each of the discrete devices investigated with the following different model combinations are compared in this section:

- Low Friction Static Load - dowel to concrete slab friction coefficient of 0.1, single static load (results used as basis for wheel load comparison presented above)
- High Friction Static Load - dowel to concrete slab friction coefficient of 0.3, single static load
- Quasi-Static Reversed Loading - dowel to concrete slab friction coefficient of 0.1, quasi-static reversed loading with 43.75 kN load increments (Figure 5-44).

The maximum base reaction, maximum dowel bar Von Mises stress, joint deflection and concrete plastic strains for each discrete device in an aligned condition will be compared for each of the different model combinations. A vertically misaligned dowel bar and apered plate will also be compared in under quasi-static reversed loading.

5.6.1 Low Friction Comparison

The mesh refinement study was completed using a 100 MPa base layer with a 0.1 dowel slab frictional coefficient for each of the model mesh refinement studies completed above. The graphs presented in this section are comparisons of the results from the model mesh geometry chosen. Figure 5-34 presets a comparison of the differential deflection at the joint for the tapered plate, GFRP I and dowel bar wheel path model with a friction coefficient of 0.1 and subjected to static loading. The GFRP I-beam allowed the most differential deflection at the joint, while the conventional dowel bar reduced the differential deflection at the joint more than the tapered plate or GFRP I-beam. At the load levels above 87.5 kN, the tapered plate and GFRP I-beam showed reduction in stiffness at the joint in comparison to the dowel bar, indicated by the increase in slope in the GFRP I and Tapered plate deflections shown in Figure 5-34.

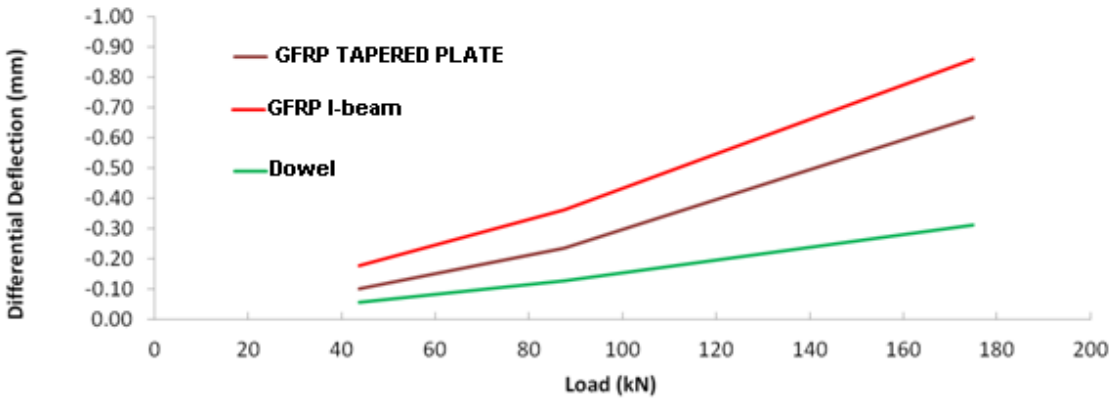

Figure 5-34 - Low Friction Static Load Model - Differential Deflection Comparison

Figure 5-35 presents the maximum Von Mises Stress in the devices for the Tapered plate, GFRP I and dowel model with a friction coefficient of 0.1 and a static wheel load application. The maximum Von Mises stress in the Tapered plate are much lower than the maximum stresses in the dowel and GFRP I-beam which is assumed to be due to the mesh geometry as mentioned previously (Section 5.5). The GFRP I-beam and conventional dowels have a similar maximum Von Mises stress occurring in the device.

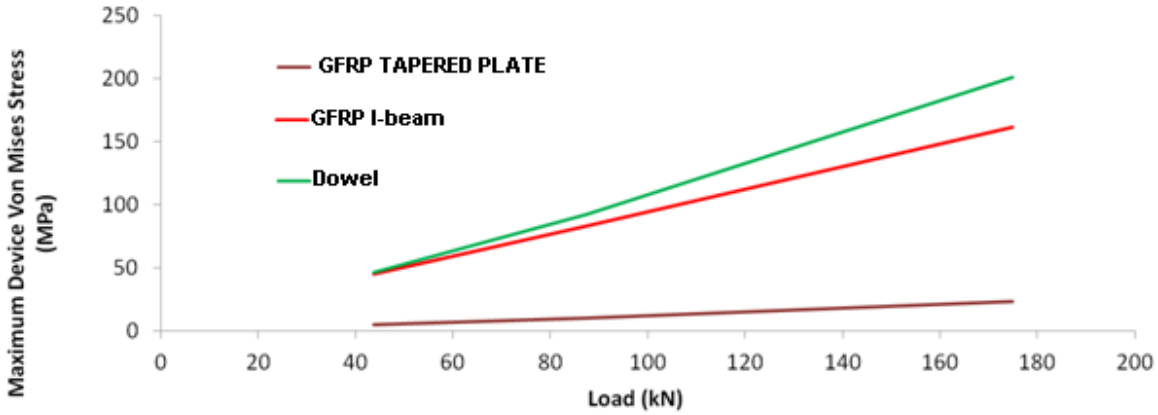

Figure 5-35 – Low Friction Static Load Model –Device Von Mises Stress Comparison

The maximum stress in the base layer for each device is compared in Figure 5-36 for the low friction static load case. The comparison between the maximum base stress is very similar to the behaviour for the differential deflection. Although the GFRP I-beam was resting directly on the base layer and it may be expected that some additional stress may occur here compared to the

conventional dowels, the results do not indicate a strong difference between the three devices. The behaviour of the tapered plate and GFRP I-beam were almost the same between with the conventional dowel bar model having a slower increase in maximum stress at load levels above 87.5kN.

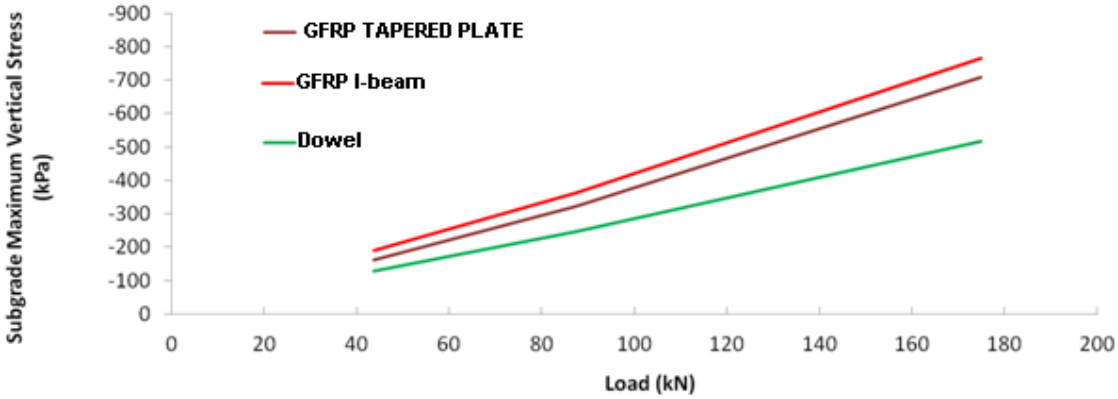

Figure 5-36 – Low Friction Static Load Wheel Path Model - Maximum Subgrade Vertical Stress Discrete Device Comparison

A comparison between the maximum PEEQ in the concrete slab for the tapered plate, GFRP I and dowel bar model is presented in Figure 5-37 for the low friction static load model. The maximum PEEQ in the concrete in the dowel bar model was higher than in the tapered plate. The GFRP I-beam produced the highest PEEQ in the concrete, and the PEEQ in the concrete increases rapidly at load levels above 87.5 kN for the GFRP I-beam in comparison to the tapered plate and conventional dowel bar models. The PEEQ in the concrete between the 87.5 and 175 kN load levels for the dowel bar and Tapered plate dowels are very similar. This suggests that the Tapered plate dowel is causing approximately the same damage in the concrete at the joint as the dowel.

Figure 5-38 presents the maximum PEEQT for the low friction static load model for each of the discrete devices in an aligned condition. Similar to the PEEQ, the GFRP I-beam caused the highest PEEQT in the concrete. Lower values of PEEQT in the concrete occurred with the tapered plate than the GFRP I-beam; however, the dowel bar produced the lowest PEEQT in the concrete. It is assumed that the concentrations of stress that occur at the sharp edges of the GFRP I-beam and Tapered plate dowel are causing the increase in the PEEQT in the concrete. Possibly using thicker sections with slightly rounded edges to reduce the concentration of stress and

cracks that occur from the corners of the devices could be done to reduce the PEEQT in the concrete with the GFRP I and Tapered plate sections.

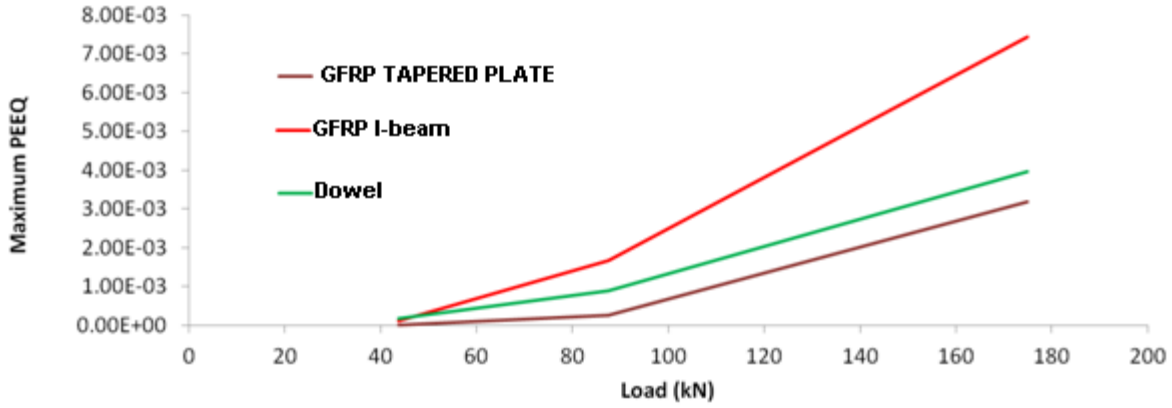

Figure 5-37 - Low Friction Static Load Wheel Path Model – Maximum Concrete PEEQ Discrete Device Comparison

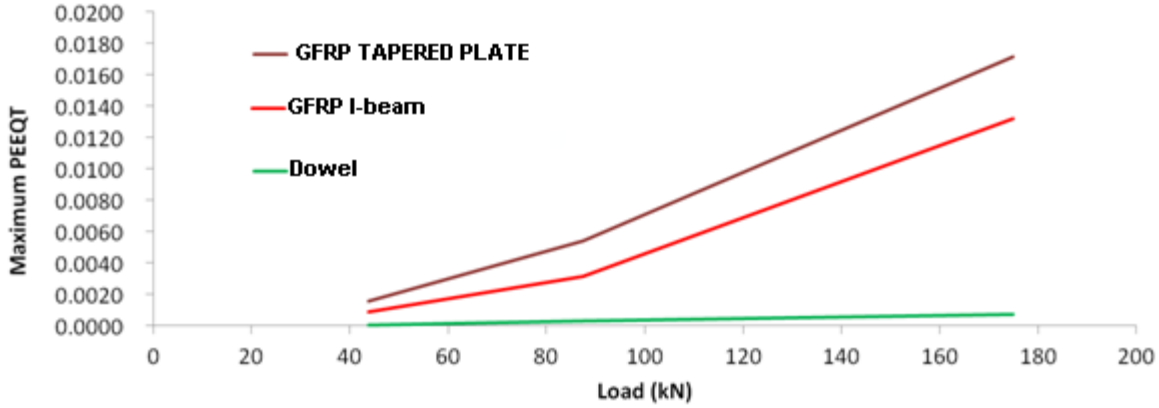

Figure 5-38 - Low Friction Static Load Wheel Path Model – Maximum Concrete PEEQT Discrete Device Comparison

5.6.2 High Friction Static Load - Wheel Path Model Discrete Device Comparison

The performance of each discrete device was also compared using an increased frictional coefficient of 0.3 at the contact surface between the device and the concrete slab. Figure 5-39 presents the differential deflection occurring at the joint with a frictional coefficient at the concrete device interface of 0.3.

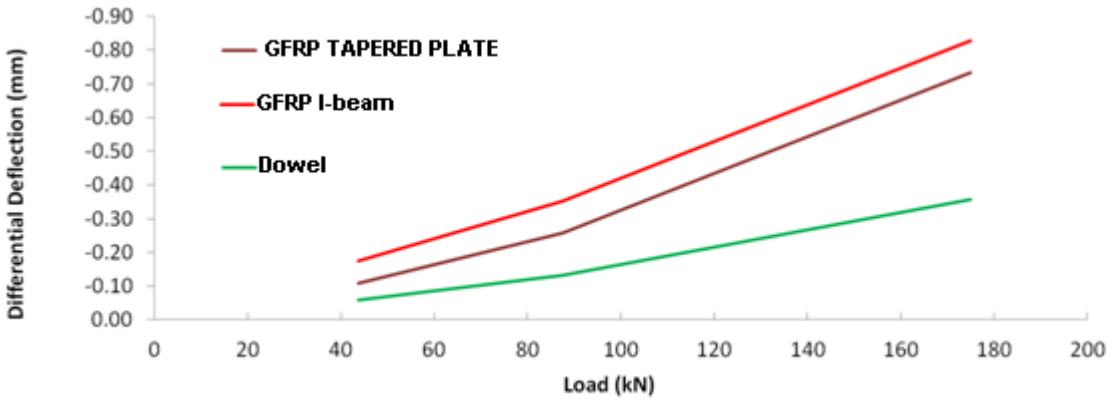

Figure 5-39 - High Friction Static Load Wheel Path Model - Differential Deflection Comparison

The differential deflection occurring at the joint for the discrete devices under static loading did not appear to be affected by the frictional coefficient assumed at the device concrete interface. The relative comparisons between the differential deflection that occurred at the joint and the maximum deflection were similar to those presented previously in Figure 5-34 for each device. The frictional coefficient at the slab device interface did not appear to affect the behaviour perpendicular to the device which will govern the displacement of either side of the slab as well as the base support.

Figure 5-40 presents the maximum Von Mises stress in the devices for wheel path model with a frictional coefficient of 0.3 between the device and the concrete. Little change in the maximum Von Mises stress in the device occurred in all three discrete devices examined. No relative increase was observed for the GFRP I-beam, where as the dowel and tapered plate dowels both predict slightly higher maximum Von Mises stress with a frictional coefficient of 0.3 compared to 0.1. The increase in Von Mises stress in the GFRP tapered plate section is the greatest. At the 43.75 kN load, the maximum Von Mises stress is approximately 8 MPa where with a 0.1 frictional coefficient the maximum stress is approximately 5 MPa. At the 87.5 kN and 175 kN loads the maximum Von Mises stress in the GFRP tapered plate using a 0.3 frictional coefficient are approximately 18 MPa and 40 MPa respectively whereas with a frictional coefficient of 0.1 between the device and the concrete values of approximately 10 and 23 MPa respectively. The large affect on the maximum Von Mises stress for the tapered plate is assumed to be due to the bending stress not being adequately captured due to the mesh geometry in the GFRP tapered

plate. The change in the friction coefficient at the device-concrete interface has a larger affect when the bending stresses are not adequately being captured in the device.

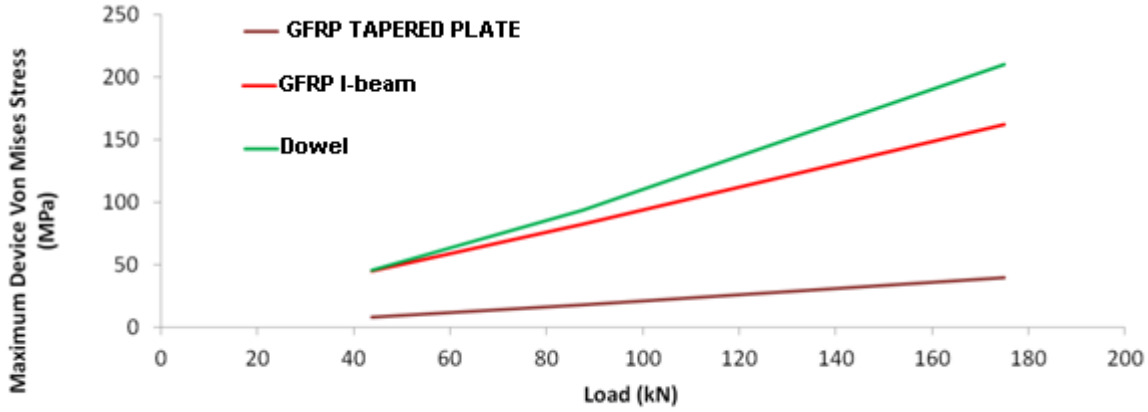

Figure 5-40 - High Friction Static Load Wheel Path Model - Device Von Mises Stress Comparison

Figure 5-41 presents the comparison of the maximum vertical stress in the base layer for the wheel path model comparison of the discrete devices using a frictional coefficient between the device and the concrete of 0.3 and a single static wheel load application applied to the slab. Increasing the frictional coefficient of between the device and the concrete appeared to have little effect on the maximum base reaction using the tapered plate and dowel bar models. However, an increase in the maximum base stress occurred for the GFRP I-beam. Using a 0.1 friction coefficient between the slab and device, the maximum base stress is 875 kPa and with a frictional coefficient of 0.3 the value increases to 1190 kPa. Increasing the friction coefficient between the device and the slab may have altered the relative slippage between the device and the slab causing the device to penetrate into the base layer. The general behaviour and comparison between the devices using either frictional coefficient (0.1 or 0.3) between the device and slab for maximum vertical stress in the base layer is the same.

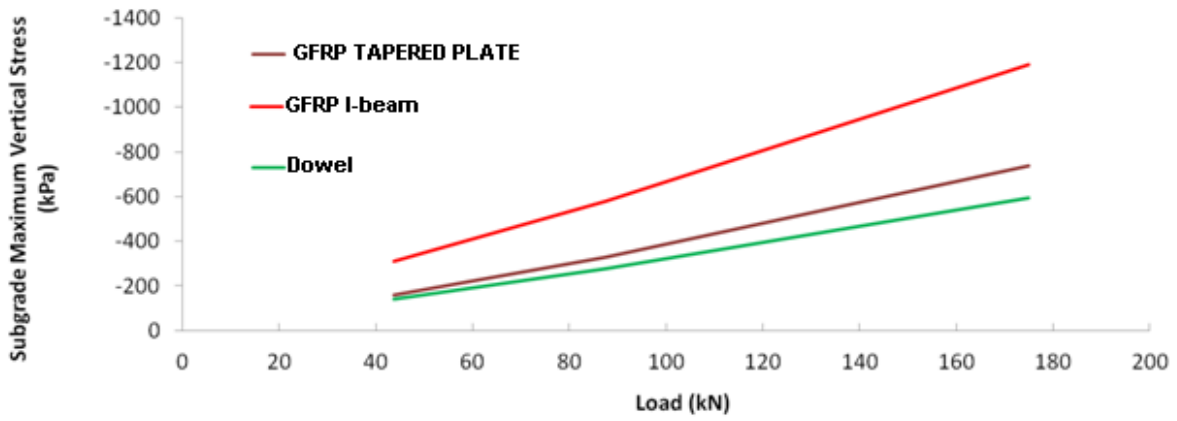

Figure 5-41 - High Friction Static Load Wheel Path Model - Maximum Vertical Stress in the Base Comparison

Figure 5-42 presents the maximum PEEQ in the concrete for the discrete devices with a frictional coefficient of 0.3 between the slab and the device. The general comparison between the different devices with a frictional coefficient of 0.3 compared to 0.1 was the same. Highest PEEQ in the concrete were predicted with the GFRP I-beam while the conventional steel and GFRP tapered plate dowel predict very similar maximum PEEQ in the concrete. Generally, the PEEQ in the concrete at the joint interface were reduced with a higher frictional value. This behaviour is similar to that presented by Levy (2010) for conventional dowels. The effect of the contact between the slab and the device was more pronounced at the end of the dowel where the frictional contact was trying to restrain the device from moving. The plastic straining in the concrete at the back of the dowel has not been considered as the maximum plastic strains in the wheel path model were occurring at the near the joint.

Figure 5-43 presents a comparison of the PEEQT in the concrete for the discrete devices using the wheel path model with a frictional coefficient of 0.3 and single static wheel load application. The results indicate that increasing the friction coefficient to 0.3 from 0.1 does not significantly affect PEEQT in concrete. The tapered plate experienced the highest PEEQT in concrete, while conventional steel dowels cause the lowest maximum PEEQT to occur in the concrete.

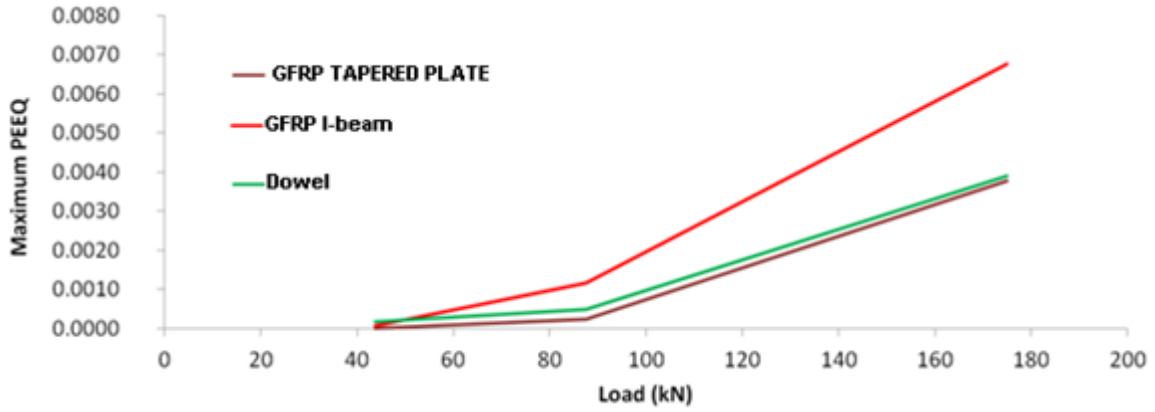

Figure 5-42- High Friction Static Load Wheel Path Model – Maximum Concrete PEEQ Strain Comparison

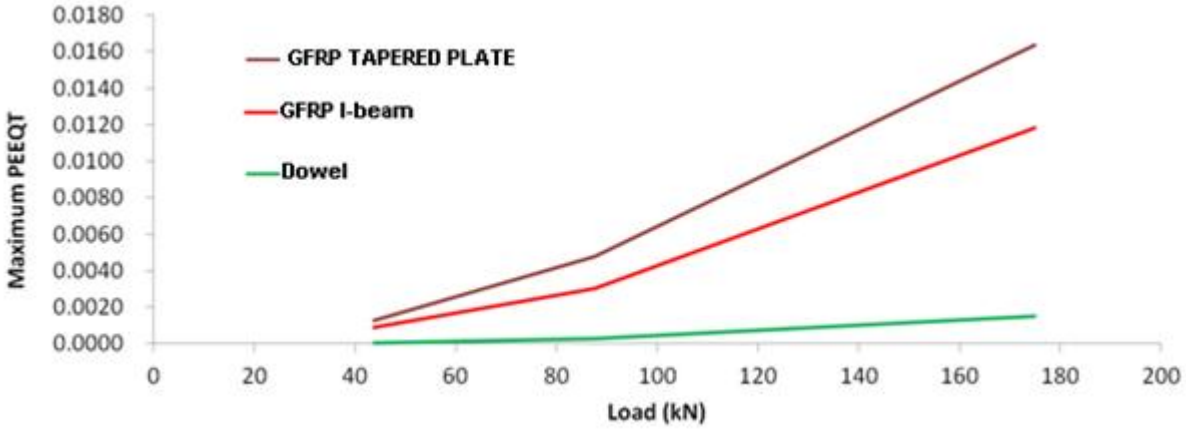

Figure 5-43- High Friction Static Load Wheel Path Model – Maximum Concrete PEEQT Comparison

Based on the review and comparison of the devices to an applied wheel load with two different frictional coefficients, the overall behaviour and comparison between the devices is not affected significantly by depending on the frictional coefficients for wheel load transfer. Results from the service load analysis may be affected more by altering the coefficient of friction; however, varying the effects will not be investigated as part of the current study due to the limited effect on wheel load transfer results and time constraints.

5.6.3 Quasi-Static Reversed Load Wheel Path Model Discrete Device Comparison

Finally the discrete devices were each modeled with a frictional coefficient of 0.1 between the device and the concrete and subjected to the quasi-static reversed loading history presented Figure 5-44. In Figure 5-44, the horizontal axis represents time; however, no scale was applied as

the material properties used and loading applied did not include time as a variable. The quasi-static reversed loading is aimed at capturing the effects of the plastic straining occurring in the concrete on either side of the joint and the effects of a load moving across the joint. This is also the loading that will be applied in the experimental work to investigate the effects of a moving load without actually applying a dynamic load due to the complexity of the testing apparatus required or computational effort in a model. A vertically misaligned tapered plate dowel and conventional steel dowel were also included to determine the effects of vertical misalignment on these devices. The vertical misalignment was taken as an angular displacement of 60 degrees in the vertical plane, and is denoted as V60 in the following figures. Since the GFRP I-beam was set directly on the base it is assumed that it will not become vertically misaligned, and thus vertical misalignment was not considered for the GFRP I-beam.

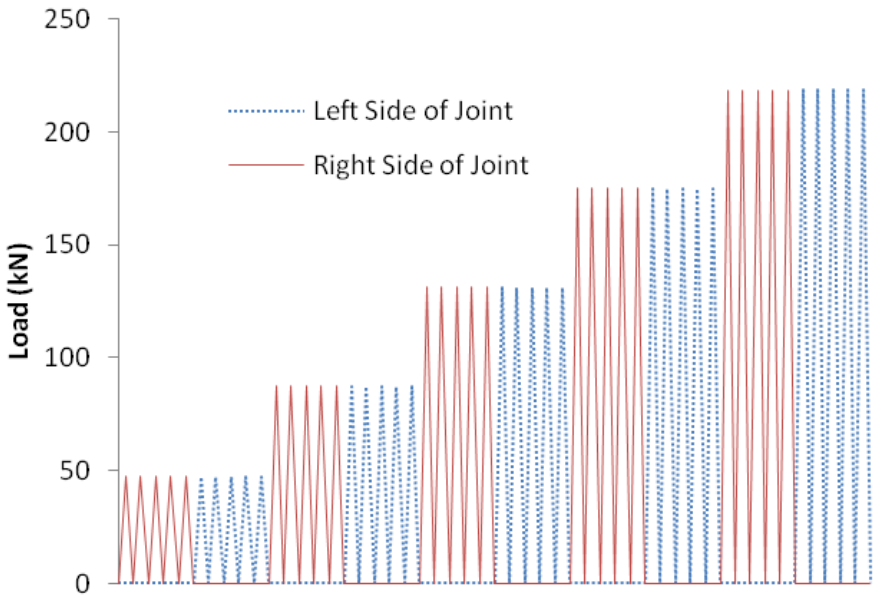

Figure 5-44 – Quasi-Static Reversed Loading

Figure 5-45 presents the differential joint deflection comparison for the discrete devices under quasi-static reversed loading. The conventional steel dowel maintained the lowest differential deflection throughout the course of the quasi-static loading applied. The tapered plate and the misaligned tapered plate dowels behaved similarly to the dowels and Figure 5-45 shows the differential deflection at the joint with a misaligned tapered plate dowel initially improved the joint load transfer on one side of the device and worse on the other. As the load was increased

and subsequent load applications were applied, the misaligned tapered plate does not appear to be more effective on one side than the other. The GFRP I-beam failed to converge after the 4th load application at 1.5 wheel load (131.25 kN); however, before that had more differential deflection than the Tapered plate or conventional dowel at the load increments below this level. The results for the misaligned dowel bar failed to converge after the 2nd load application at twice the wheel load (175kN). The vertically misaligned conventional steel dowel predicts more differential deflection than a conventional dowel at each load level.

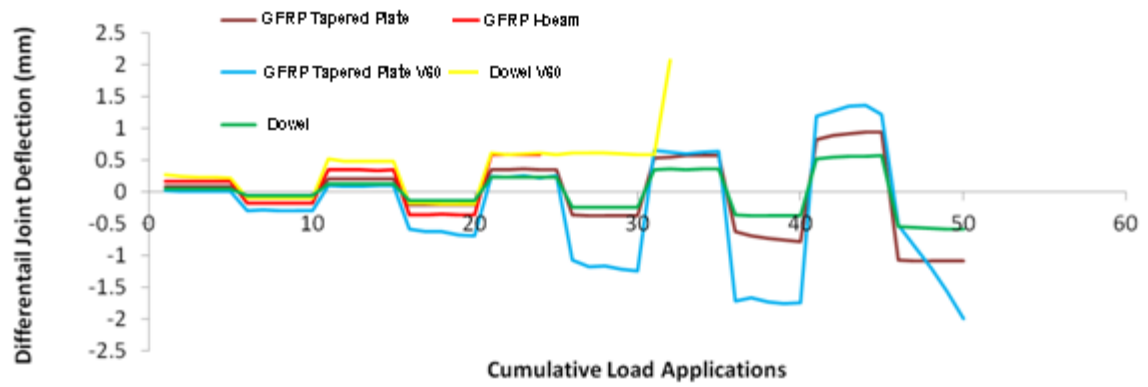

Figure 5-45 - Quasi-static Reversed Load Wheel Path Model – Differential Deflection at the Joint Comparison

Figure 5-46 and Figure 5-47 present the maximum Von Mises stress in the devices on either side of the joint for the quasi-static loading history.

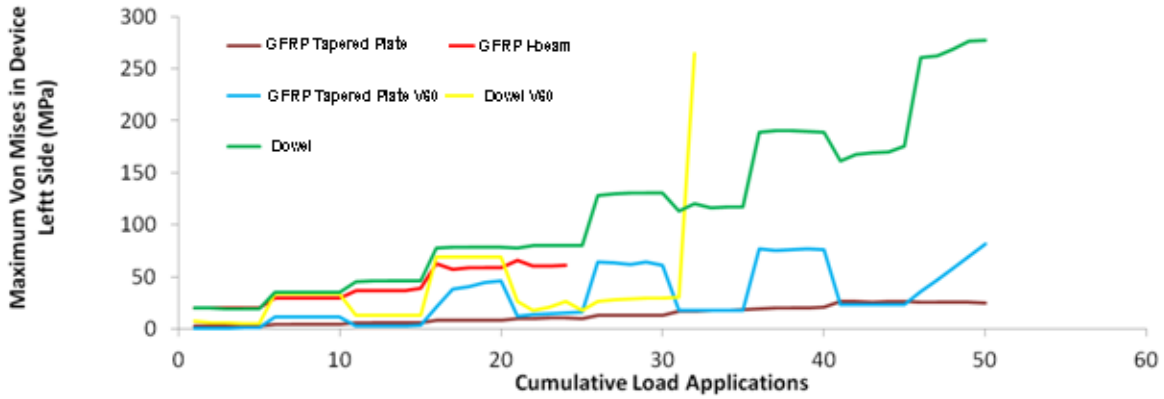

Figure 5-46 - Quasi-static Reversed Load Wheel Path Model - Maximum Von Mises Stress in Left Side of Device Comparison

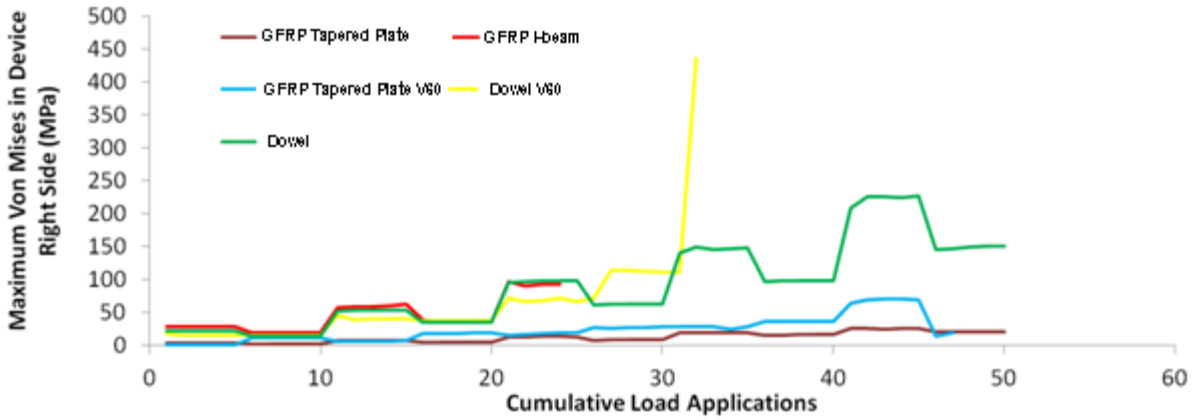

Figure 5-47 - Quasi-static Reversed Load Wheel Path Model - Maximum Von Mises Stress in Right Side of Device Comparison

The conventional dowel bar had the highest maximum Von Mises stress occur in the device, although all the stresses in the aligned dowel were below a failure level for all the load increments. The dowel bar was approaching its yield strength near the end of the load applications. Increased load levels caused larger increase in the maximum stress in the dowels through subsequent load applications at the same load for the GFRP I-beam and dowel bars. This may suggest that further damage and plastic straining is occurring in the concrete surrounding the device increasing the stress in the devices as the load is cycled. The misaligned dowel bar suddenly has an increase in maximum device Von Mises stress on both sides of the joint before the model fails to converge. It is assumed that this sudden increase may be due to increasing plastic strains and a local failure causing the model to be concrete to become unstable near the device increasing the load transferred to the base and dowel. The GFRP I maximum Von Mises stress are similar to the conventional dowel until the model fails to converge. The GFRP I-beam maximum Von Mises stress fails to converge after the 4th application of the 1.5 wheel load level (131.25 kN).

Figure 5-48 and Figure 5-49 present the comparison of the maximum vertical stress in the base layer on either side of the joint for the quasi-static reversed loading.

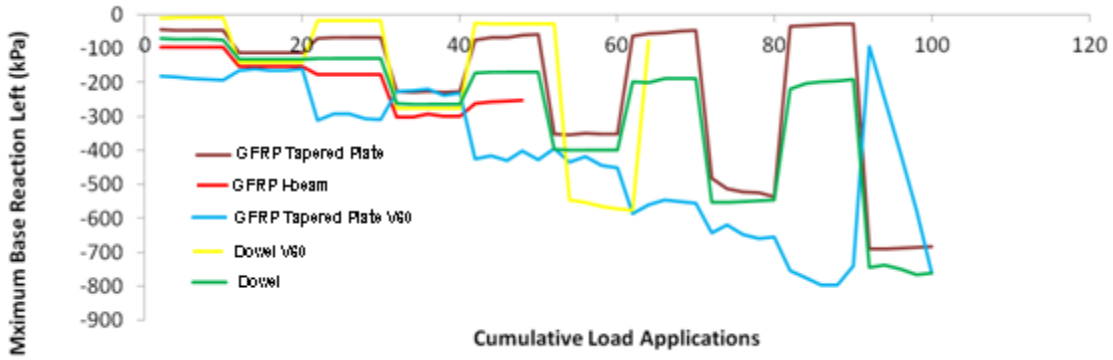

Figure 5-48 – Quasi-static Reversed Load Wheel Path Model - Maximum Base Vertical Stress on Left Side of Joint Comparison

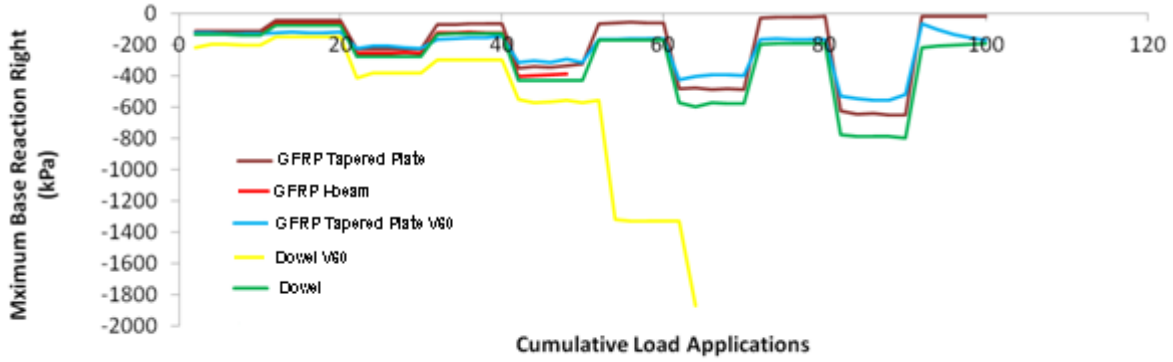

Figure 5-49 - Quasi-static Reversed Load Wheel Path Model - Maximum Base Vertical Stress on Right Side of Joint Comparison

The maximum vertical stress in the base layer for misaligned dowel bars increased rapidly on the right side of the joint prior to the model failing to converge. Vertical stress on the right side of the joint is very similar for all the remaining devices. The vertically misaligned dowel bar predicts the least maximum vertical stress in the base layer on the right side of the joint. The misalignment of the steel dowel may have caused the dowel to act as a lever pulling one side of the slab up as load is applied and hence reduce the maximum stress in the base layer. Conventional dowel bars predict the highest maximum vertical stress on the right side of the joint but are on the same order of magnitude and it is assumed that the increased load transfer occurring is causing the increased maximum vertical stress which should not be detrimental to slab performance. On the left side of the joint in Figure 5-48, the vertically misaligned GFRP Tapered plate dowel cause the highest vertical stress in the base layer. An aligned GFRP Tapered

plate dowel causes less maximum vertical stress than the conventional dowel but behaves similarly to a conventional dowel.

Figure 5-50 presents the comparison of maximum PEEQ occurring in the concrete for the discrete devices evaluated using the wheel path model for quasi-static reversed loading. The maximum PEEQ occurring in the concrete with the GFRP I-beam sharply increased prior to the model failing to converge which may show that failure was occurring in the concrete. The area was still localized and this may or may not represent a failure occurring, however, the model was not able to converge due to mesh refinement near the thin flanges of the GFRP I-beam. However, prior to the rapid increase the device passed the assumed failure in compression for PEEQ in the concrete at a value of 0.00474. All of the devices were below the failure in compression assumed at the wheel load level except the misaligned Tapered plate dowel. As the load levels were increased beyond the wheel load level the maximum PEEQ occurring in the concrete were above the failure value. PEEQ straining occurring in the tapered plate dowel was similar to the conventional steel dowel predicting slightly higher maximum PEEQ to occur in the concrete. Prior to the misaligned conventional dowel bar model failing to converge, the maximum PEEQ in the concrete increases to a similar level occurring in the misaligned tapered plate dowel. The vertically misaligned GFRP Tapered plate dowel does not appear to reduce the plastic straining occurring in the concrete under wheel loading. The failure level assumed for maximum PEEQ in the concrete occurs for the conventional dowel and GFRP Tapered plate dowel at twice the wheel load (175 kN).

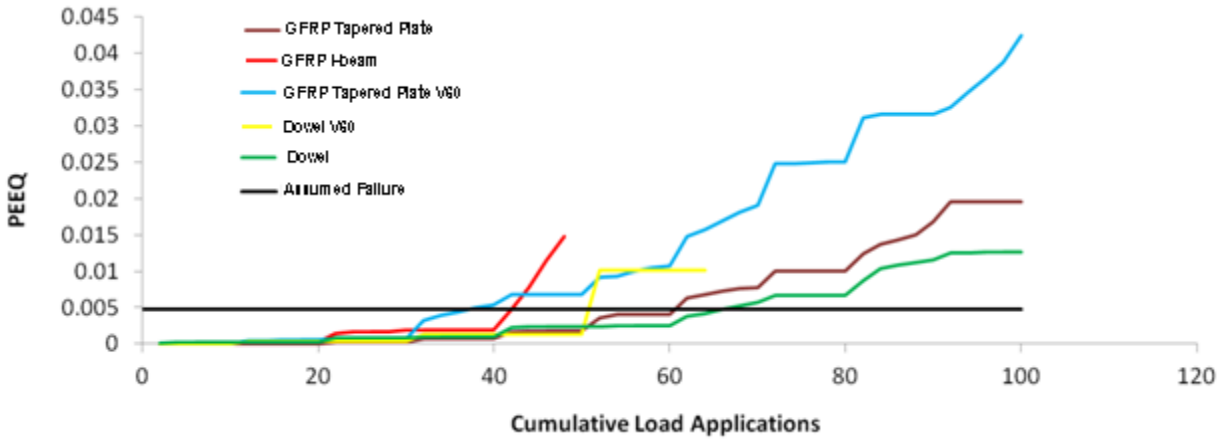

Figure 5-50 - Quasi-static Reversed Load Wheel Path Model - Maximum Concrete PEEQ Stress Comparison

Figure 5-51 presents a comparison of the maximum PEEQT occurring in the concrete for the discrete devices in the wheel load model under quasi-static reversed loading. The GFRP I-beam and both the misaligned tapered plate and aligned tapered plate dowel caused higher maximum PEEQT in the concrete to occur. This may have been due to the concentration of stress that occurred at the sharp edge of the device. The PEEQT occurring in the conventional steel dowel was much lower than the other devices. Misalignment of the dowel did not appear to affect the maximum PEEQT that occurred in the concrete for the conventional steel dowel; however it increases the maximum PEEQT in concrete when GFRP tapered plate dowels are used. Maximum PEEQT in the concrete at the device concrete interface for the tapered plate and GFRP I-beam exceed the failure level assumed at the wheel load level. The maximum PEEQT in the concrete was not increased at the wheel load level as the load was cycled which suggests that the devices were still functioning at the wheel load level although they had exceeded the failure for PEEQT assumed in the concrete.

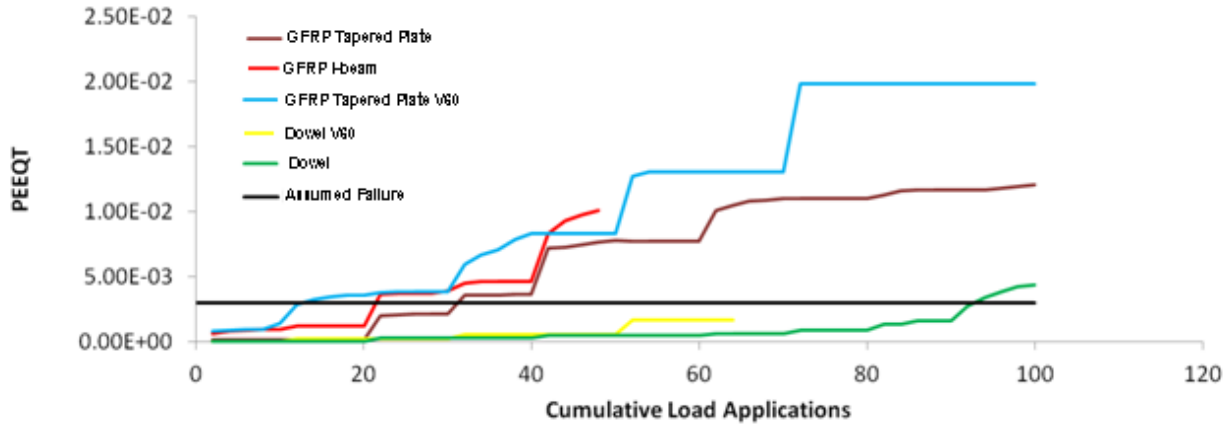

Figure 5-51 - Quasi-static Reversed Load Wheel Path Model – Maximum Concrete PEEQT Comparison

5.7 Summary of Load Transfer Study for Discrete Devices

The load transfer study for discrete devices and development of a wheel path model capable of comparing devices for load transfer provided insight into the behaviour of proposed load transfer devices, dowel bars, and overall slab behaviour under wheel loading.

The following conclusions were made based on the aforementioned finite element load transfer study for the selected discrete devices:

- A wheel path model with a thinner base layer was capable of predicting behaviour similar to a full slab with the back edge of the slab restrained. The stress concentrations, differential deflection and plastic straining occurring in the wheel path model were greater than in a full slab model, and predictions using the wheel path models will hence be greater.
- The assumption of symmetric boundary conditions on a quarter slab model when subjected to unsymmetrical wheel loading applied appeared to not significantly affect results.
- Based on the results from the finite element load transfer study completed using the wheel path model, all of alternative devices appeared to be effective at transferring wheel load at the joint. All of the devices reduced the maximum vertical stress in the base layer and differential deflection at the joint, when compared to no load transfer devices. The mechanical transfer provided at the joint reduced differential deflection across the joint.
- Differential deflection predicted using conventional steel dowels was lower than both the FRP I-beam and FRP tapered plate devices.
- The GFRP I-beam was the least effective at transferring load at the joint with highest plastic straining occurring in the concrete as well as the most differential deflection across the joint. The top flange of the GFRP I-beam provided most of the load transfer with the bottom flange being less effective which was assumed to occur because of the bottom flange rested directly on the base. Altering the size the FRP I-beam thickness or possibly creating an alternative shape with an increased upper flange thickness only could improve the efficiency of the device.
- Increasing the thickness of the GFRP tapered plate could reduce the differential deflection at the joint by increasing the relative stiffness of the device closer to that of the conventional dowel used.
- The presence of load transfer devices increased the maximum stress and plastic strain occurring in the concrete because the devices created high stress concentrations.
- Conventional steel dowels had the lowest plastic straining occurring in the concrete for both tension and compression. It is assumed that the sharp corners at the bearing surfaces for GFRP tapered plates and I-beams created the higher concentrations of stress when compared to round dowel bars.

- Altering the frictional coefficient at the device-concrete interface did not alter the comparative behaviour of the devices under wheel loading.
- Under quasi-static reverse loading the relative behaviour between the devices was similar to the behaviour observed from loading on only one side of the joint; however, as the load was repeated at maximum compressive concrete straining generally increased along with the differential deflection at the joint.
- The mesh refinement study completed showed that the mesh densities investigated had little effect on the overall result, and similar mesh densities will be used for the remaining analysis.
- Further mesh refinement in the tapered plate dowel could be completed to capture the shear and moment distribution more effectively, although global effects are captured in the current model.

6.0 Laboratory Testing of the Discrete Devices

6.1 Laboratory Testing Objectives

An experimental testing program was developed to supplement and verify general comparison of the discrete devices made using the wheel load model. The objectives of the experimental testing program were:

- To compare the ability of the devices to transfer load versus conventional dowels
- To gain knowledge on the placement and construction of the devices on a small scale
- To examine the effect misalignment has on load transfer

This section outlines the development of the experimental testing program as well as the experimental testing results for the discrete devices.

6.2 Lab Testing Slab Geometry

As described in the preliminary analysis section, the CL-625 design truck uses a wheel load application over a 600mm x 250mm area. The slab testing geometry selected was the same as the wheel path model geometry used for the computational load transfer analysis for discrete devices presented previously in Figure 5-4.

The wheel experimental specimen consisted of a 2.4m long concrete pavement slab strip, 600 mm wide and 250 mm thick. The pavement joint was located at mid-length of the slab strip. The slab specimen was placed on a simulated base layer (GeoFoam) as discussed below. The slab and base layer were placed in a 500 kN servo-hydraulic test frame for load testing, as shown in Figure 6-1. A structural steel frame was placed around the base layer to confine the base material (the base material is hidden by the steel frame in Figure 6-1). A steel double-channel section, anchored to the structural floor slab, was used to provide vertical restraint to the back edges of the pavement slab strip consistent with the boundary conditions assumed in the wheel path computational model (see Figure 5-4).

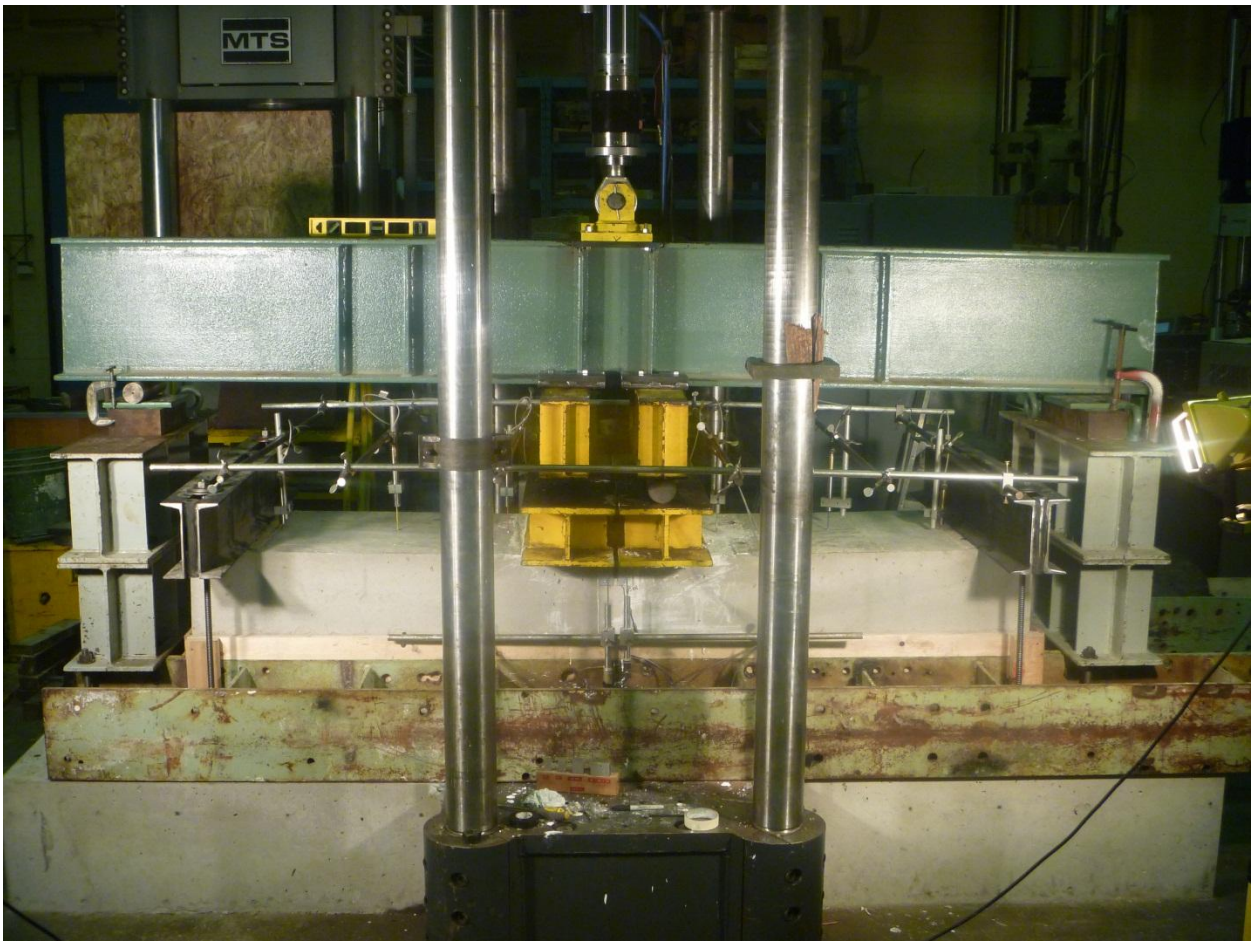

Figure 6-1 – Lab Testing Setup

For the base layer, as an alternative to using an actual base requiring a consistent compaction routine to provide consistent results from test to test and to save time in experimental testing, Geo-Foam was chosen for the base support. Geo-Foam is an expanded polystyrene product that comes in various densities to be used as a light-weight fill material. Geo-Foam comes in blocks of various sizes. The size of the Geo-Foam base used in experimental testing is a 305mm x 609mm x 2438mm. GeoSpec Type 22 Geo foam from Plastifab was chosen as the material to be used in the lab and the material properties of the GeoSpec Type 22 Foam are given in Table 6-1.

Table 6-1 – GeoSpec Type 22 Material Properties

Description of value/test	Value
Compressive Resistance @ 1% Deformation using ASTM D 1621	50 kPa
Compressive Resistance @ 5% Deformation using ASTM D 1621	115 kPa
Flexural Strength using ASTM C 203	240 kPa

The compressive and flexural strengths of the GeoSpec Type 22 GeoFoam are much lower than the values that were assumed in the wheel path model for the base layer. The GeoSpec Type 22 GeoFoam was chosen in the study because it was the most readily available GeoFoam. The weaker base support could be representative of a joint after it had been in use for years and some of the base support below the joint has eroded away as mentioned by Eddie et al., (2001).

6.3 Lab Testing Loading

The load transfer and the stress concentrations at the joint according to the finite element analysis of the discrete devices were used as a basis for the test. The wheel path model showed that the load should be alternated from one side of the joint to the other in order to reverse the compressive and tensile stress concentrations in the slab on both sides of the joint. A quasi-static reversed loading history similar to that presented in Figure 5-44 was used for the experimental testing program. Specific loading increments were determined based on finite element modeling of the dowel bar model with the base layer chosen for the experimental testing. Figure 6-2 presents the quasi static revesered loading applied using the experimental testing program.

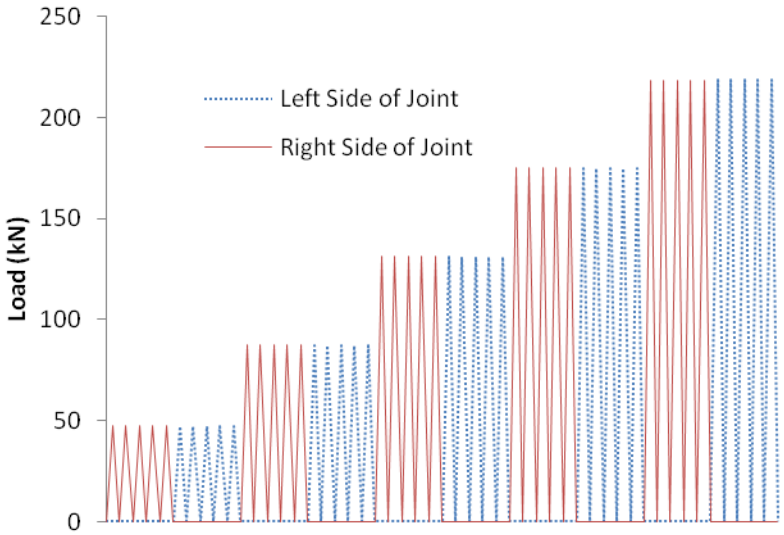

Figure 6-2 - Quasi Static Reversed Loading Application for Experimental Testing

6.3.1 Experimental Testing Loading Beam

In order to apply alternating loads to both sides of the joint and working with a single-actuator test-frame a loading beam was implemented in the experimental testing arrangement as shown in

Figure 6-1. The actuator was aligned with the slab joint and attached to a loading beam that ran parallel to the concrete slab length extending beyond the length of the slab, as shown schematicalyl in Figure 6-3. To load the slab on either side of the joint a removable pivot was placed beneath the load beam on the slab on the right (or left) side of the joint and a second pivot was placed on the left (or right) pedestal to as supports to the loading beam. In the described arrangement the actuator load was between the supports and the loading beam acted as a simple beam with the support providing the wheel load desired. In order to obtain the actuator load and apply the proper wheel loading, static equilibrium of a simply supported beam with dimensions shown in Figure 6-3 was used to calculate the load levels at the point of application knowing the load required at the joint location.

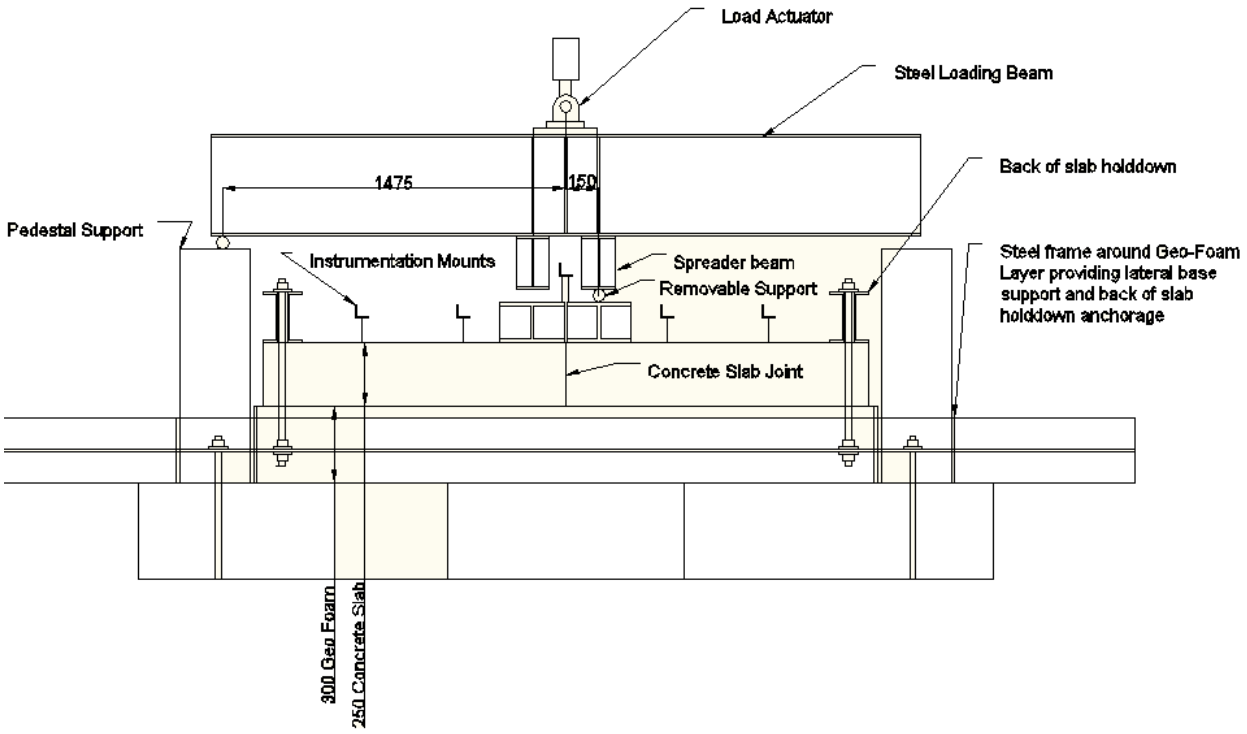

Figure 6-3 – Simple Beam Representation of the Lab Testing Setup

6.3.2 Analysis to Determine Wheel Loading Increments

To establish an estimated maximum load and initial load increments for the lab testing program, a computational model incorporating the Geo Foam layer in ABAQUS was used with the dowel bar model. The crushable foam material model available in ABAQUS was used to model the

GeoFoam layer. The model assumes that the cell wall buckling that occurs in crushable foam will behave as a plastic model. The model must be input with a linear isotropic material model. The yield surface assumed in the crushable foam material in ABAQUS is a Mises circle in the deviatoric stress plane and an ellipse in the p-q stress plane. The model was input using volumetric hardening where the point on the yield ellipse in the p-q plane that represents hydrostatic tension loading is fixed and the evolution of the yield surface is driven by the volumetric compacting plastic strain. The other available input for hardening is isotropic hardening, in which the yield surface is centered at the origin in the p-q stress plane and evolves in a geometrically self-similar manner. The ABAQUS manual suggests that for mainly compressive loading the two will give similar results. The yield surface of the foam for volumetric hardening model is defined using Equation (6-1) (ABAQUS, 2008).

(6-1)

$$F = \sqrt{q^2 + \propto^2 (p - p_o)^2} - B = 0$$

Where:

$p = \frac{1}{3} trace\sigma$	is the pressure stress
$q = \sqrt{\frac{3}{2} S : S}$	is the Mises stress
$S = \sigma + pI$	is the deviatoric stress
A	is the size of the (horizontal) p-axis of the yield ellipse
$B = \propto A = \propto \frac{p_c + p_t}{2}$	is the size of the (vertical) q-axis of the yield ellipse
$\propto = {}^{B}/_{A}$	is the shape factor of the yield ellipse that defines the relative magnitude of the axes
$p_o = \frac{p_c + p_t}{2}$	is the center of the yield ellipse on the p-axis
p_c	is the strength of the material in hydrostatic compression (always positive)
p_t	is the yield stress in hydrostatic tension

The yield surface and flow potential in the p-q stress plane as input using the above is represented in Figure 6-4 from the ABAQUS Manual (2008).

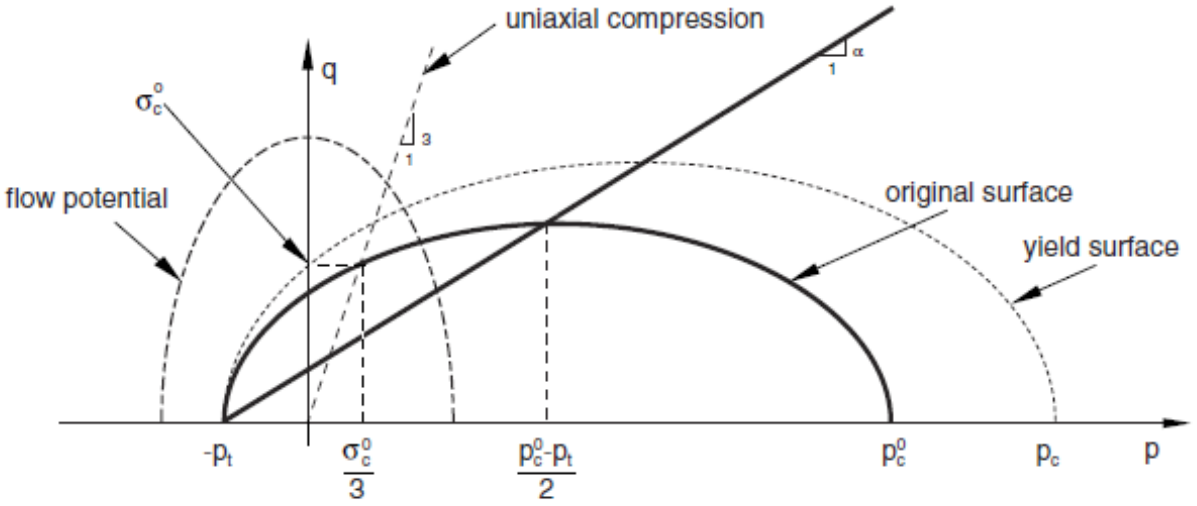

Figure 6-4 – Yield surface and flow potential in the p-q stress plane (ABAQUS, 2008)

The shape factor can be computed using the initial yield stress in uniaxial compression, yield stress in hydrostatic compression and the yield strength in hydrostatic tension using Equation (6-2):

(6-2)

$$\propto = \frac{3k}{\sqrt{(3k_t + k)(3 - k)}}$$

Where:

$$k = \frac{\sigma_c^o}{p_c^o} \text{ and } k_t = \frac{p_t}{\sigma_c^o}$$

In order to define the yield surface in ABAQUS the values of k and k_t must be input. These values both depend on both the yield stress in hydrostatic tension and compression based on the definitions given as part of Equation (6-2). A value for k of 1.1 was assumed based on the ABAQUS (2008) verification manual value and a second value of 0.8 was used to check the effects of changing the value for k on model results and to provide a range of solutions since the

value is unknown and time did not permit to determine a more realistic value for this parameter. The value for k_t of 0.05, as suggested in the ABAQUS User's Manual, was assumed in the GeoFoam material used to establish experimental testing instrumentation and loading increments for the pilot test slab.

The crushable foam material property in ABAQUS must be used in conjunction with linear elastic isotropic material properties. A Poisson's ratio for rigid behaviour similar to concrete would be equal to a Poisson's ratio of close to 0.1 where a fluid material would be close to 0.5. Two Poisson's ratios were assumed (in the assumed range of Poisson's ratio in the foam) of 0.1 and 0.3 for the GeoFoam base layer material model used in ABAQUS. Two values were assumed because little information on the value for the Poisson's ratio could be found for the foam and time to test did not permit as part of the current study. The initial yield of the crushable foam was assumed to be the 1 % deformation value given by the manufacturer. Using this as the first yield and an elastic response to this load level an elastic modulus of 5 MPa was assumed for the GeoFoam layer.

The ABAQUS crushable foam material model also required definition of the plastic behaviour to uniaxial loading. Based on the 1% and the 5% deformation values, the plastic behaviour in uniaxial compression was input into the crushable foam material model assuming linear plastic deformation from the 1% to the 5% compressive test data given by Plastifab (Table 6-1). All of the additional straining occurring after the 1% deformation was assumed to be plastic deformation. An additional input for the uniaxial compressive behaviour of GeoFoam was input as an assumed 150 kPa stress and 10% deformation of which 9% was assumed to be plastic. Figure 6-5 depicts the compressive behaviour used for the GeoFoam base layer assumed to establish the loading increments and data acquisition system.

Four different variations of the foam were modeled using the two different assumed Poisson's ratios and parameter k as outlined above. A single static wheel load was applied until the model failed to converge. Table 6-2 presents a summary of the results for the slab behaviour with the varying inputs for k and the Poisson's ratio for the GeoFoam layer.

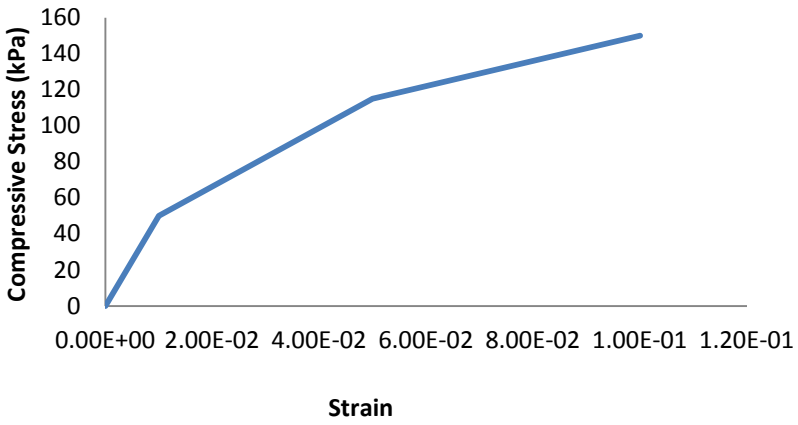

Figure 6-5 – GeoFoam Compressive Stress-Strain Curve for input in ABAQUS

Table 6-2 – Estimated Lab Behaviour of Dowels with Different Foam Material Properties

Poisson's Ratio	k	Max Load (kN)	Geo Foam Comp (kPa)	PEEQ	PEEQT	Deflection 1	Deflection 2	Joint Efficiency
0.1	0.8	83	122	0.0156	0.0012	-20.63	-19.85	98.07%
0.3	0.8	98	142	0.0165	0.0014	-18.17	-17.36	97.71%
0.1	1.1	85	134	0.0167	0.0012	-21.39	-20.57	98.04%
0.3	1.1	95	142	0.0173	0.0014	-19.55	-18.70	97.78%

The maximum load on the slabs from the four different arrangements ranged from about 82 kN to 99 kN until the models failed to converge. The maximum deflection at the joint is estimated to be 21.39 mm when the model fails to converge which was assumed to be the ultimate failure. The maximum deflection at the joint of 21.39 mm was used to establish the length of displacement transducers to be used on the pilot slab. Based on the differential deflection, the joint is still able to function through the duration of the test even though there is less support provided by the base layer.

To understand the behaviour of the foam layer, a section of the plastic strains along the length of the slab are shown in Figure 6-6 and the vertical plastic strains are shown in Figure 6-7.

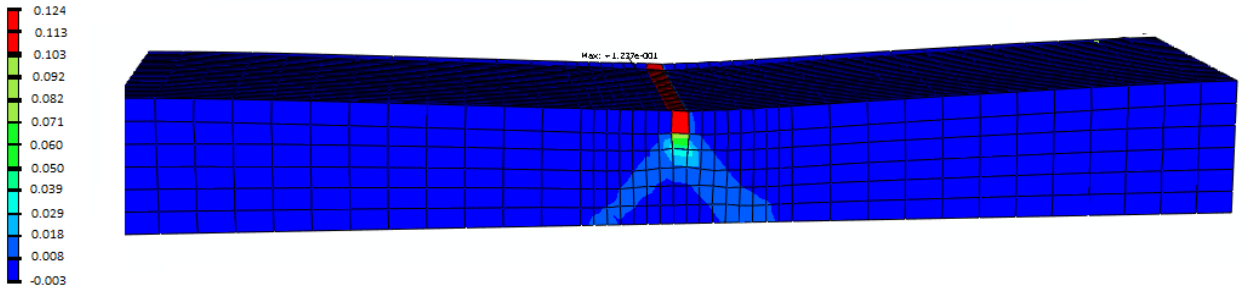

Figure 6-6 – Longitudinal Plastic Strain in Geo Foam

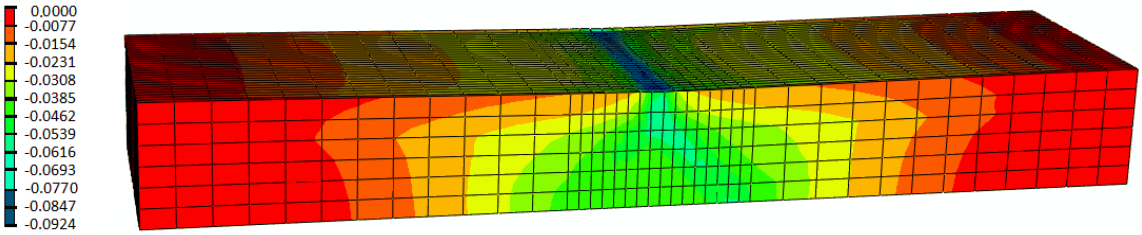

Figure 6-7 – Vertical Plastic Strain in Geo Foam

The plastic straining profile for the Geo Foam presents permanent displacement occurring along the entire length of the Geo Foam base layer with the maximum plastic strains occurring at the middle of the foam where the joint is located. The plastic strains along the length of the foam indicate a crack occurring in the foam at the location of the joint. The slab is spreading the load to the foam along the entire length and is causing the foam to permanently deflect vertically.

To ensure the Geo Foam will behave similarly to a stronger base and will not affect the response of the slab or the failure mechanisms in the slab, the strains in the concrete were investigated and compared to the preliminary analysis model using a 100 MPa elastic modulus for the base layer. The plastic strains in compression and tension in the concrete were localized to the same area around the dowel at the joint interface using the Geo Foam base assumed as the 100 MPa base layer. The values for the maximum PEEQT in the concrete were still below the failure criterion of 0.003; however, they were more than ten times the initial cracking strain. The PEEQ predicted by each model in the concrete were above the failure criterion assumed of 0.00474. Thus, it was concluded that the Geo Foam could be used to represent the base material in the experiments.

Based on the results using the crushable foam as a base layer it was determined that for the initial lab test a load increment of 1/8 of the wheel load would be used since the estimated failure load

was approximately equal to a single wheel load. The increment of 1/8 of the wheel load would allow the behaviour of the device at various stages of damage and progression to be studied for device comparisons. The load was applied at a rate of 1.6 kN/s, selected to avoid dynamic effects in the slab and testing arrangement, as well as to maintain an efficient experimental testing time.

6.4 Lab Testing Data Acquisition

In order to investigate the behaviour of the devices and compare the behaviour of the devices slab deflection data was obtained during the test. It was determined that a comparison of the deflection profiles of the slabs would be the most effective way to compare the behaviour of the different devices. A deflection profile of the slab shows how the slab is functioning at transferring the load along its length to the base material and through the joint. Two displacement transducers were used on either side of the joint to determine the differential deflection across the joint. Six additional transducers were placed on the top side of the slab along its length. The layout of the displacement transducers on the slab is presented in Figure 6-8.

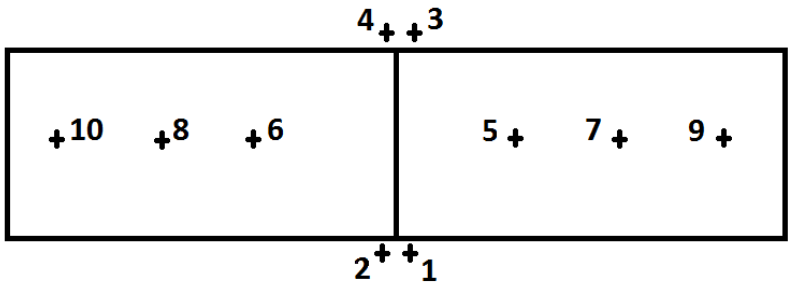

Figure 6-8 – Displacement Transducer Layout (Plan View)

Displacement transducers 1 through 4 are mounted below an angle that is attached to the side of the slab at either side of the joint as shown in Figure 6-8. The load is applied first to the right side of the joint as shown which is associated with the odd numbered transducers. The other transducers are mounted above the top of the slab and measure the displacement directly off the top of the concrete slab. The transducers are visible in Figure 6-1.

6.5 Experimental Testing Program

Similarly to the finite element wheel load analysis, the GFRP Tapered plate, the GFRP I-beam and steel dowel were all be tested in the lab under perfect conditions (i.e. no misalignment). The vertical skew misalignment of the devices was previously found to be the most detrimental in load transfer (Levy, 2010). Therefore, the devices that could be vertically misaligned, tapered plates and conventional dowels, were also tested in with a vertical misalignment of 60 mm.

To establish the testing procedure and ensure the testing setup will work for a general device comparison, a slab specimen with two conventional steel dowels was cast and tested 28 days after the concrete was cast. This was used to verify the loading and ensure the displacement transducers would capture the behaviour of the slab. After the pilot test was completed, the testing program including casting five slabs, one for each test alignment described in one concrete placement was completed.

6.6 Pilot Specimen Description and Test Results

In order to establish load increments and to verify the test setup, a single slab with dowels was cast and tested. The single slab was cast with a formed joint that was 6.4 mm at 1/4 the slab depth and it was 12.5 mm at the top of the slab. The formed joint was removed after the slab was in place. The slab was tested after 28 days of curing. The compressive strength of the concrete on the day of the test was 40.4 MPa and the tensile strength was 9.5 MPa using compressive and split cylinder tests.

During the first four increments, no damage occurred and the formed joint did not form into a full depth crack. At approximately 60 kN, the slab cracked at the joint location on the first load application on the first side of the sixth load increment. For the remainder of the test no further cracking was visible.

The crack extended from the bottom of the joint at an angle under the applied load on the side of the slab shown in Figure 6-9. On the other side of the slab the crack has less of an angle in the opposite direction towards the unloaded side. At the end of the test the crack opened to approximately 12 mm where visible. The test was stopped after a load 121 kN when the deflection transducers were out of range.

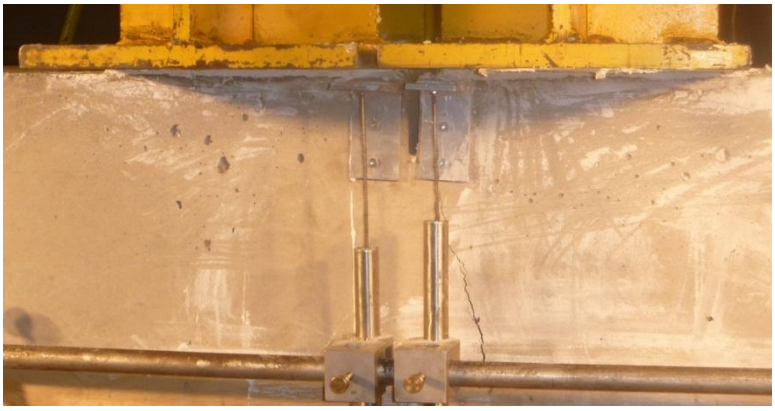

Figure 6-9 – Pilot Test Slab Crack Formation at 60 kN

The slab deflection profiles at load levels of 43.75 kN, 65.625 kN and 87.5 kN were plotted as shown in Figure 6-10. The deflection for the first and last load on each side is plotted at each load level to show the additional deflection that occurs through the cyclic loading.

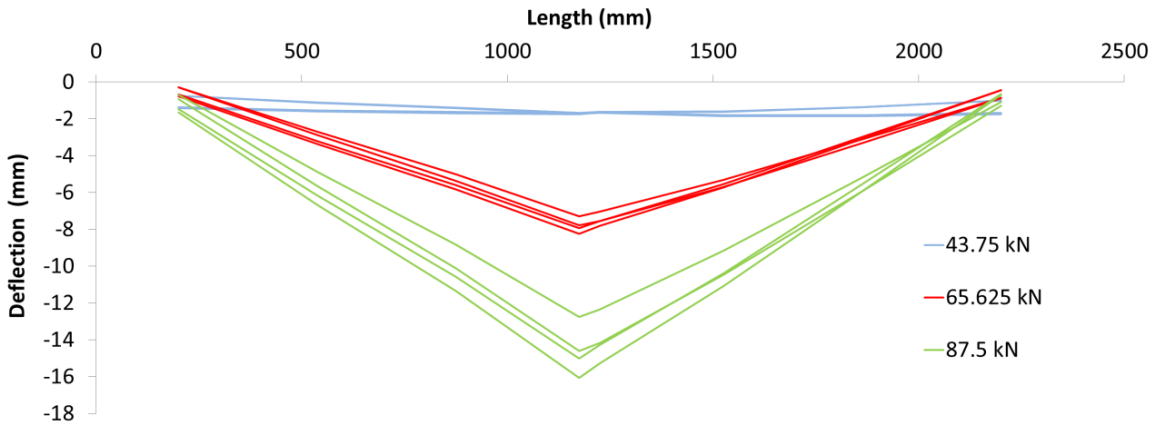

Figure 6-10 – Pilot Test Slab Deflection Profiles

At the 43.75 kN load level, the slab response was very linear as the crack had not formed yet at the joint location to create a discontinuity in the slab. After the crack occurred, stepping at the joint began to occur. As the load was increased to 65.625 kN and cycled, the joint deflected more, however, by the 5th cycle on the second side of the joint there was little further change occurring between load cycles. The deflection at the back ends of the slab were not plotted in the figure as the back displacement transducer was 200 mm from the ends. Based on Figure 6-10, the back end of the slab was rising slightly off the foam support behind the steel channel hold downs at the back end of the slab, which was noticed during the testing at both the 65.625 kN and 87.5

kN load levels. As the load was cycled at the 87.5 kN load level the slab deflected more as the load was cycled and as the load was switched from one side of the joint to the other. It was difficult to see distinct stepping across the joint from one side to the other as the load is reversed throughout the test.

In order to investigate the joint behaviour during the test, the deflection across the joint was compared. Deflection transducers were placed on either side of the joint at each side of the slab as shown in Figure 6-8. To estimate deflection of either side of the joint the average deflection of the two displacement readings on either side of the joint were used. The deflection of either side of the joint, the Load Transfer Efficiency (LTE), differential deflection and joint effectiveness at different load levels are presented in Table 6-3.

The differential deflection across the joint was below 1 mm for all of the load levels and cycles presented. At low load levels the differential deflection across the joint did not change as the load was switched from one side of the slab to other. The joint efficiency and LTE values were hence calculated as being greater than 100% because the deflection on the unloaded side of the slab was greater than the loaded side. It was difficult to explain why the loaded side of the slab had a lower deflection than the unloaded side. This could occur due to the nature of the crack that formed and the aggregate interlock. It could also have something to do with the plastic deformation that occurred in the Geo Foam layer. At the 5/4 wheel load level, the loaded side of the joint was greater than the unloaded side of the joint for all load applications. At this higher load and deflection level, the crack that had formed was significantly widened and the effects of aggregate interlock at the joint would have been reduced. The prescribed limits for adequate joint performance for LTE and joint effectiveness for a slab were maintained throughout the test from the load transfer that occurs due to the dowel bar and the aggregate interlock.

Table 6-3 – Pilot Test Slab Joint Performance

Load Level	Side of Joint Loaded	Cycle Number	Average Deflection of Right Side (mm)	Average Deflection of Left Side (mm)	Differential Deflection (mm)	Joint Effectiveness (%)	LTE (%)
		1	-0.69	-0.70	0.01	100.9%	101.9%
		2	-0.70	-0.72	0.02	101.4%	102.8%
		3	-0.69	-0.71	0.02	101.3%	102.7%
		4	-0.68	-0.71	0.03	101.8%	103.7%
	Right	5	-0.70	-0.72	0.02	101.3%	102.7%
		1	-0.68	-0.71	0.03	97.5%	95.2%
		2	-0.67	-0.71	0.03	97.5%	95.2%
		3	-0.68	-0.71	0.03	97.8%	95.7%
		4	-0.69	-0.72	0.03	98.0%	96.0%
1/4	Left	5	-0.69	-0.72	0.03	97.9%	95.9%
		1	-1.66	-1.70	0.03	100.9%	101.9%
		2	-1.69	-1.71	0.03	100.8%	101.6%
		3	-1.69	-1.73	0.04	101.1%	102.2%
		4	-1.70	-1.74	0.04	101.1%	102.2%
	Right	5	-1.71	-1.74	0.03	101.0%	101.9%
		1	-1.65	-1.74	0.09	97.4%	95.0%
		2	-1.67	-1.75	0.08	97.5%	95.2%
		3	-1.68	-1.76	0.08	97.5%	95.2%
		4	-1.69	-1.78	0.09	97.4%	94.9%
1/2	Left	5	-1.69	-1.78	0.09	97.3%	94.7%
		1	-7.08	-7.30	0.23	101.6%	103.2%
		2	-7.29	-7.52	0.23	101.6%	103.2%
		3	-7.42	-7.65	0.23	101.5%	103.1%
		4	-7.51	-7.74	0.23	101.5%	103.1%
	Right	5	-7.59	-7.82	0.24	101.5%	103.1%
		1	-7.57	-7.96	0.40	97.5%	95.0%
		2	-7.67	-8.09	0.42	97.4%	94.8%
		3	-7.74	-8.17	0.43	97.3%	94.8%
		4	-7.81	-8.24	0.43	97.3%	94.7%
3/4	Left	5	-7.86	-8.30	0.44	97.3%	94.7%
		1	-12.33	-12.76	0.43	101.7%	103.5%
		2	-13.00	-13.43	0.43	101.6%	103.3%
		3	-13.45	-13.90	0.45	101.6%	103.3%
		4	-13.84	-14.30	0.45	101.6%	103.3%
	Right	5	-14.15	-14.61	0.45	101.6%	103.2%
		1	-14.27	-15.00	0.73	97.5%	95.2%
		2	-14.60	-15.36	0.76	97.5%	95.1%
		3	-14.85	-15.62	0.76	97.5%	95.1%
		4	-15.09	-15.87	0.78	97.5%	95.1%
1	Left	5	-15.27	-16.07	0.79	97.5%	95.1%
		1	-36.41	-36.35	-0.06	99.9%	99.8%
		2	-39.91	-39.69	-0.22	99.7%	99.5%
		3	-40.40	-40.15	-0.25	99.7%	99.4%
		4	-40.54	-40.28	-0.25	99.7%	99.4%
	Right	5	-40.60	-40.34	-0.26	99.7%	99.4%
		1	-43.67	-43.86	0.20	99.8%	99.6%
		2	-46.16	-46.39	0.23	99.8%	99.5%
		3	-48.22	-48.52	0.30	99.7%	99.4%
		4	-49.88	-50.19	0.32	99.7%	99.4%
5/4	Left	5	-50.20	-50.53	0.33	99.7%	99.3%

In order to investigate the damage occurring in the system a plot of the load and deflection at the joint are plotted in Figure 6-11. As the load is cycled at low load levels before cracking, the response is very linear. At approximately 60kN the crack occurs and an increase in the deflection occurs and continues to increase as the load was cycled. At the 87.5 kN load level, as the load was cycled little additional deflection occured. As the load was cycled at load levels above 87.5 kN average deflection at the joint continued to increase with each load application, which indicated that plastic damage was occurring at the load level. When the load was increased to approximately 109 kN and 120 kN the first cycle showed plastic straining occurring as the load deflection curve flattened as the load was increased beyond the previous load increments. It is difficult to determine how much of the plastic deflection observed in the deflection profiles is from the concrete damage and from the Geo Foam damage as both will contribute to this type of behaviour.

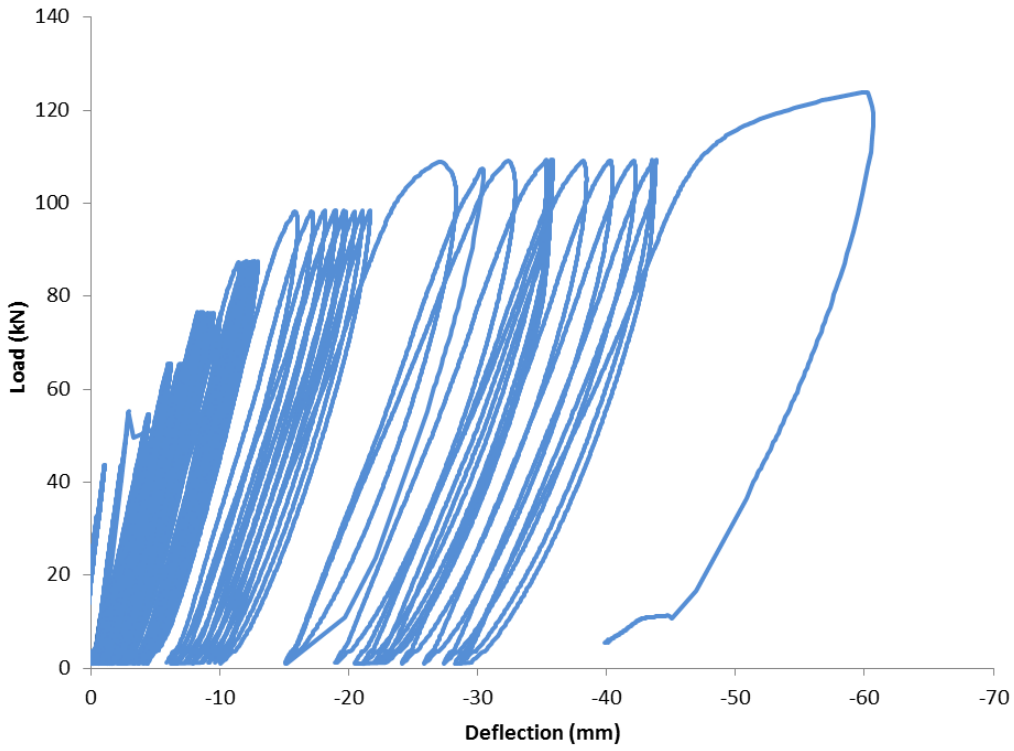

Figure 6-11 – Pilot Test Slab Load vs. Average Joint Deflection

After the test was completed an investigation into the damage in the slab and Geo Foam layer was completed. First the slab was removed from the testing frame using steel strongback beams

with shims in place so that the shape of the slab was not altered. Figure 6-12 presents the crack at the bottom of the slab after the test was completed.

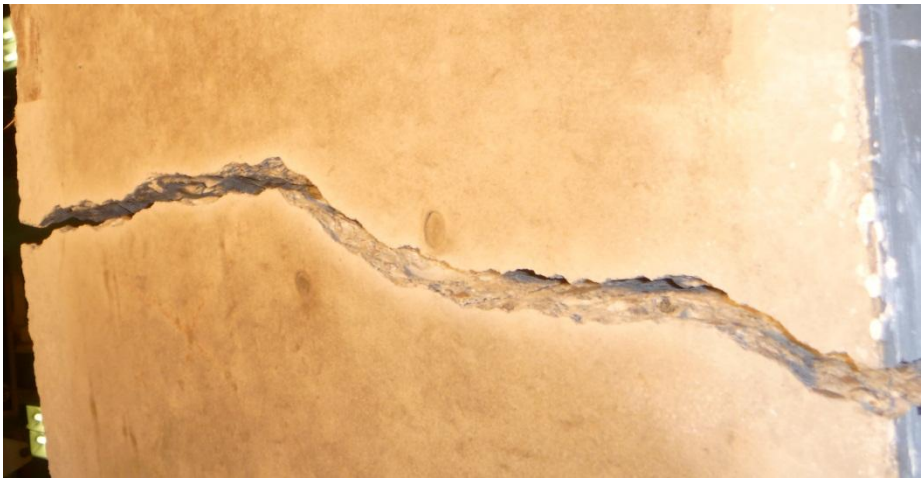

Figure 6-12 – Lab Pilot Bottom of Slab Crack after test

The observed crack tended to one side of the joint on one side of the slab and transitioned to the other at the other side of the slab. Most of the change occurred in the middle portion of the slab which is between the two dowels. In order to investigate the damage around the dowels, the slabs were pried apart. After prying the two slabs apart, one of the dowels remained in either side of the slab. The dowels were originally welded to the chairs and this weld was not broken during the test. The side of the dowel that was welded into the slab also corresponded to the side of the slab that the crack tended to be towards as shown in Figure 6-12. The Geo Foam layer also had a similar crack pattern to the bottom of the slab which extended through the layer from the top to the bottom of the Geo Foam layer. The final thickness of the Geo Foam in the middle at the crack was reduced from 305 mm to 265 mm, meaning approximately 40 mm of permanent deflection had occurred in the foam layer during the test at the joint location.

After pulling the two slabs apart, cracking could be noticed extending out from the middle of the dowel where PEEQT strains were noticed in the previous finite element analysis. More cracking in the concrete on the side of the dowel that was not welded was noticed on both of the two dowels. As the slabs were being pried apart, sections of the concrete above the dowel came off. It was assumed that the prying action alone would not cause this type of failure to occur and that the cracks had initially formed during the test and extended during prying. For the remaining tests a more controlled method of separating the slabs was used with a hand hydraulic jack

(explained later). Figure 6-13, depicts the crack extending from the dowel. The crack shown in Figure 6-13 on the left extends from the dowel and was noticed before the section of concrete came off as shown in the right of Figure 6-13. Similar cracking extending from the dowel was also noticed at the other dowels as well as some minor cracking occurring above the dowel.

Figure 6-13 – Pilot slab Cracking at dowel

In order to assess the damage in the dowel, the concrete was chipped away at the using a jack hammer to remove the dowels and look at the final shape of the dowels. The concrete had to be chipped to remove the dowels because the dowels would not come off the chair where they were tack welded in place. Figure 6-14 shows the dowel bars after the test was completed.

Figure 6-14 – Lab Pilot Dowels after test

It can be noticed in Figure 6-14 that some permanent deformation occurred in the middle of the bar at approximately the joint location. This suggests that the dowels yielded during the test at some point. However, yielding of the dowel did not cause the devices to stop transferring load and maintain the deflection across the joint throughout the test.

Based on the results of the pilot slab test, the same size of slab, concrete strength, and Geo Foam layers were chosen for the remaining slabsas the test setup appeared to adequately asses the performance of the dowel and concrete. The dowels tested were capable of transferring the load throughout the test and still worked as the Geo Foam support layer was plastically damaged. In order to obtain results throughout the entire test the amount of stroke was increased on transducers 1 through 6.

6.7 Alternative Joint Load Transfer Device Testing Program

After completing the pilot specimen testing and investigation, five additional slab specimens were cast to assess the behaviour of the alternative joint load transfer devices. The experiences from the pilot study were used to refine the specimen details and testing procedures for the additional slab specimens as follows:

- Instead of the formed joint used in the pilot test, it was decided to use a saw-cut to create the joint in the additional specimens, consistent with procedures used in actual pavements. The joint was cut using an electric concrete saw with a depth control jig and a wooden guide to ensure a straight cut. The depth of the saw cut was set at ¼ of the slab thickness, or 62.5 mm. The width of the saw cut was approximately 3mm.
- The slab specimens were not reinforced, consistent with JPCP design. Since the laboratory study is subjecting a slab strip to loads up to failure while supported on an intentionally substandard base material, it was decided to add external reinforcement to the slabs to ensure that cracking would be limited to the joint region. Strengthening of the slabs is described in Section 6.7.1.
- It was decided to pre-crack the slab joint prior to conducting the specified joint loading history described in Section 6.3. This is more consistent with actual conditions where it is assumed that the joint would be cracked due to concrete shrinkage and thermal strains

at an early age, and thus the joint load transfer behaviour of the cracked joint is of interest. The procedure for pre-cracking the joint is described in Section 6.7.2.

6.7.1 Slab Strengthening

After casting and removal from the formwork, the slab strip specimens were strengthened by adding external reinforcement to limit slab cracking to the joint region. The slabs were strengthened using Sika Carbodur S512 carbon-fibre reinforced polymer (CFRP) strips. The strips were installed longitudinally on the sides of the slab specimens, placed along the bottom edge of the slab side. Two strips, each 1000 mm long, were applied on each side of the slab. A gap between the two strips was left directly below the sawcut to ensure a weak plane existed below the sawcut joint location where the joint was expected to form by cracking. The strips were extended close to the joint location to ensure that they were adequately developed at the critical section where the dowel bar ended.

The Carbodur strips were installed following manufacturer's instructions. The sides of the concrete slabs were roughened by grinding until the coarse aggregate was visible prior to installation of the strips. Figure 6-15 shows a slab with the strips installed.

The slab specimens were moved using steel strongback beams attached to the slab using bolted inserts installed in the slabs during casting. In spite of this effort, several of the slabs experienced cracking away from the joint region prior to installation of the Carbodur strips. These cracks were repaired using epoxy injection prior to installation of the strips.

Figure 6-15 – Sika S512 Carbodur Strips attached

6.7.2 Slab Pre-cracking

Cracking in JPCP occurs in the due to shrinkage and thermal straining that causes upward curling (tension at the top fibre) and results in a crack initiating at the top surface. As described previously, the remaining slab specimens were pre-cracked prior to subjecting them to the cyclic wheel loading history to allow the joint behaviour to be realistically assessed in a cracked condition. In order to form the joint crack, the strengthened slab specimens were placed in the test frame on the GeoFoam and vertical loading was applied centered on the sawcut location. Although this load application produced tension at the bottom fibre rather than the top fibre, it was able to form the crack at the joint at relatively low load levels. It should be noted that a controlled procedure to produce tension at the top fibre could not be achieved in a practical manner with the test frame used in this research.

The arrangement in the test frame used to pre-crack the slab is shown in Figure 6-16. A single 100 mm wide plate was placed on neoprene pads centered on the sawcut location. The test frame was then used to apply direct downwards vertical loading at the joint until the joint crack was formed. Note that although the large spreader beam is visible in Figure 6-16, the ends of the

spreader beam were not supported at the pedestal locations so that a direct load (as opposed to offset load) was applied to the joint location.

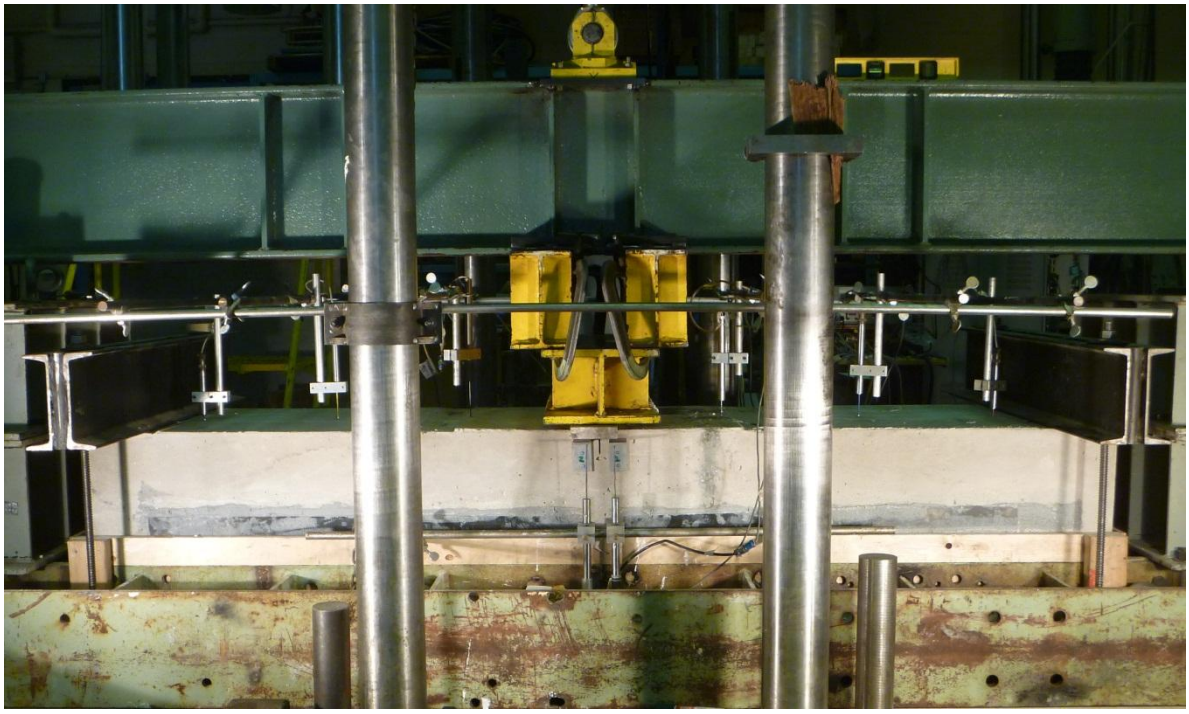

Figure 6-16 – Crack Initiation Setup

6.8 Dowel Bar Slab Specimen Description and Results

The control specimen for the laboratory study was a specimen with two dowel bars. The conventional round steel dowels used in the experimental testing investigation were epoxy-coated 32 mm steel dowels complete with a dowel chair. Two ends of the dowels were tack welded to the chair at opposite ends. The chairs and dowels represent a typical setup used in the field. The dowels were set at mid height of the slab. A picture of the dowel arrangement placed in the slab centered on the sawcut is shown in Figure 6-17.The dowels were spaced laterally at 300 mm and were placed 150 mm from each side of the slab.

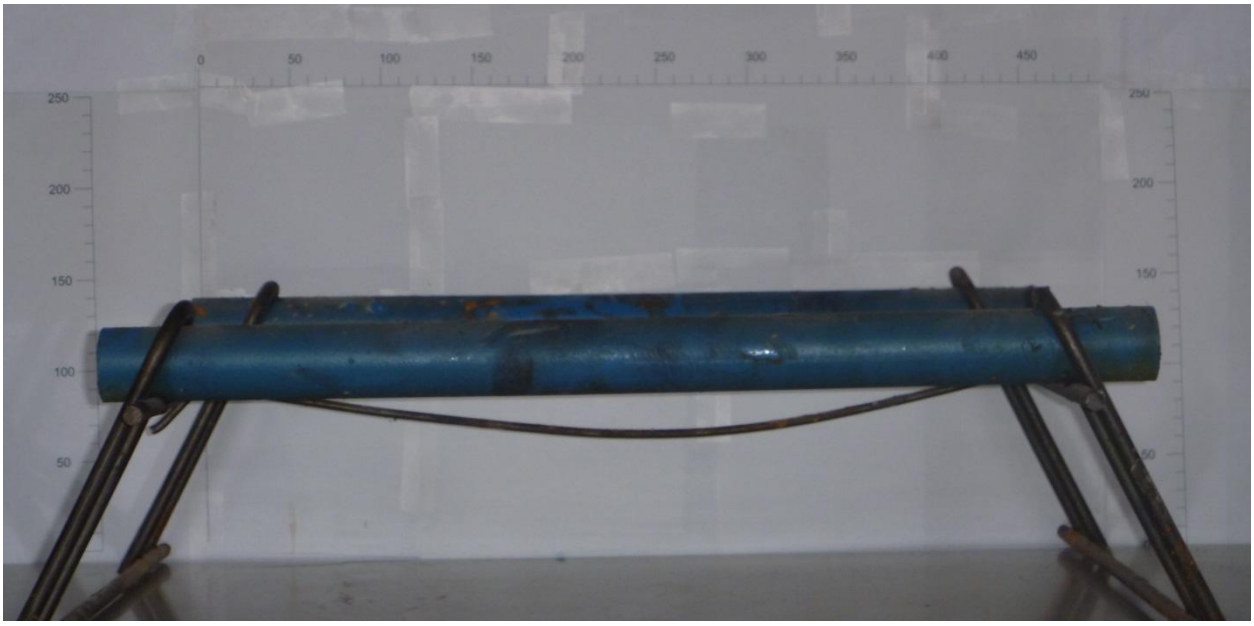

Figure 6-17 – Aligned Dowel Bar

The dowel bar specimen was subjected to the quasi-static reversed cyclic loading history as described in Section 6.3. The response of the specimen in terms of variation of average joint deflection is with load is presented in Figure 6-18. Similar to the pilot test slab with dowels the deflection does not increase as the load is cycled below the wheel load level (87.5 kN). The 87.5 kN wheel load increment was entered manually and was increased from the 3/4 wheel load increment to the 5/4 increment. This is noticed in Figure 6-18 as the load does not cycle at the 87.5 kN load level. A large increase in deflection occurs at the joint from the 66 kN to 110 kN wheel load increment. As the load was cycled at loads above the wheel load level the average deflection at the joint increased with each load cycled. When the load was increased to the 131 kN wheel load level the slab was determined to have failed on the first cycle as the average deflection at the joint increased and the slope of the load deflection plot flatted as plastic deformation was occurring. At the end extensive cracking was occurring at the joint but no visible concrete crushing or additional cracking could be noticed at the slab exteriors. The Geo Foam layer at this level is also failing and the test was stopped as the differential deflection of the slab was well beyond reasonable limits for serviceability.

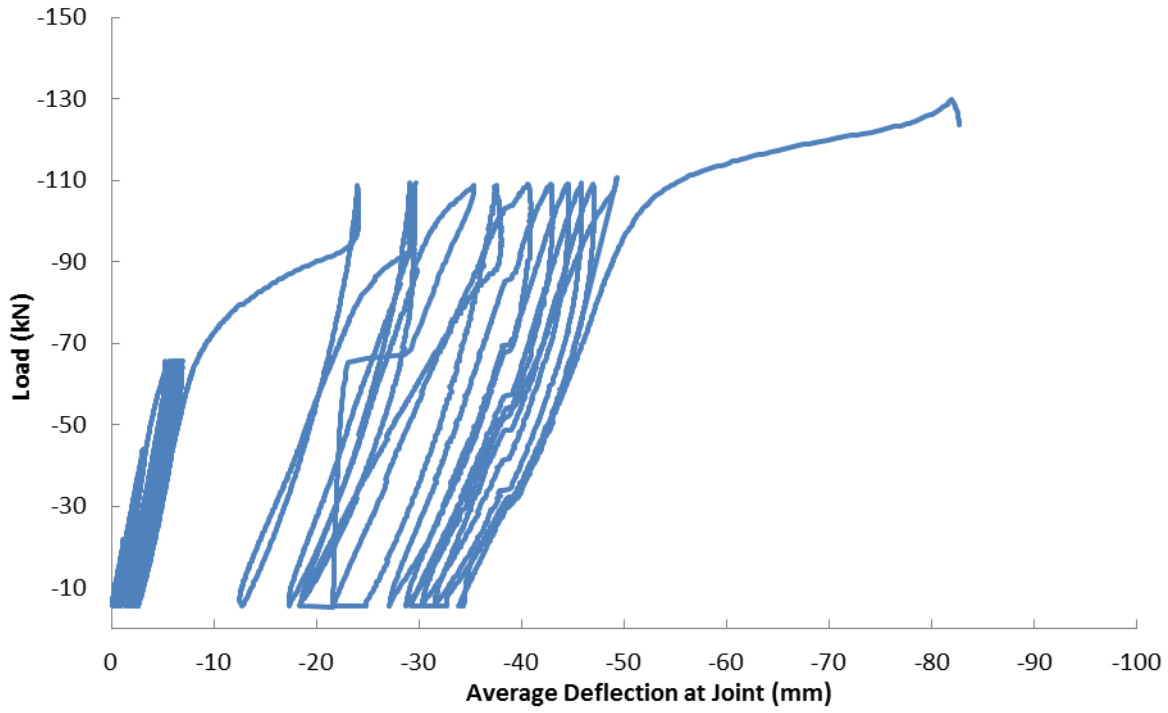

Figure 6-18 – Dowel Bar Specimen: Average Joint Deflection vs. Load

Figure 6-19 presents the differential deflection at the joint for the conventional round steel dowel test plotted against the load. The behaviour of the slab at load levels below the wheel load level (87.5 kN) showed that the differential deflection across the joint did not increase as the load was switched from the left to the right side of the slab. This portion of the test was represented by the dark section of Figure 6-19. The differential deflection on the first side of the slab loaded was consistently lower than the second side of the slab at the load levels below 87.5kN which is represented in Figure 6-19 as negative differential deflection. As the load was increased to 110kN, the differential deflection across the joint was consistent with the loading applied where the loaded side of the slab was lower than the unloaded side (which would be expected in a pavement setting). The maximum differential deflection that occurs is approximately 3 mm on the second side loaded at the 110kN load increment.

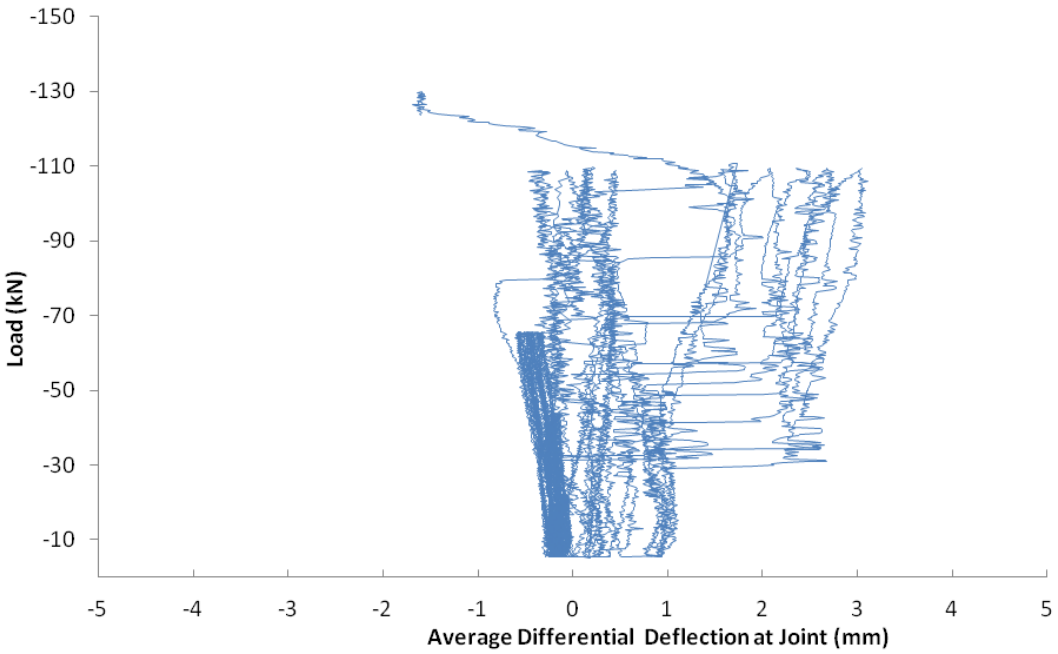

Figure 6-19 – Dowel Bar Specimen: Differential Joint Deflection vs. Load

The initial joint crack produced by pre-cracking is shown in the left-hand photograph of Figure 6-20. The crack widened over the course of the cyclic loading history, until it was noticeably wider as visible in the right-hand photograph in Figure 6-20. At the start of the test the crack was very narrow. Black points were added to the photo of the crack at the start of the test to highlight the crack location. After the test was completed the crack width increased to approximately 5 mm at the slab base interface. Since the bending of the slab due to the simulated wheel load produces tension at the bottom of the slab, the crack did not widen significantly near the top of the joint, as visible in the right-hand photograph in Figure 6-20.

Figure 6-20 – Dowel Experimental Slab Joint Crack Comparison

After the experiment was completed, the slab specimen was removed from the testing frame and the slabs were jacked apart as shown in Figure 6-21 to allow the damaged condition of the joint to be assessed further. A small hydraulic cylinder bearing against steel plates anchored to the two slab halves was used to separate the specimen into two pieces.

Figure 6-21 – Slab Jacking Arrangement to Separate Slab Halves

Figure 6-22 depicts the damaged condition of the concrete slab after the testing was completed.

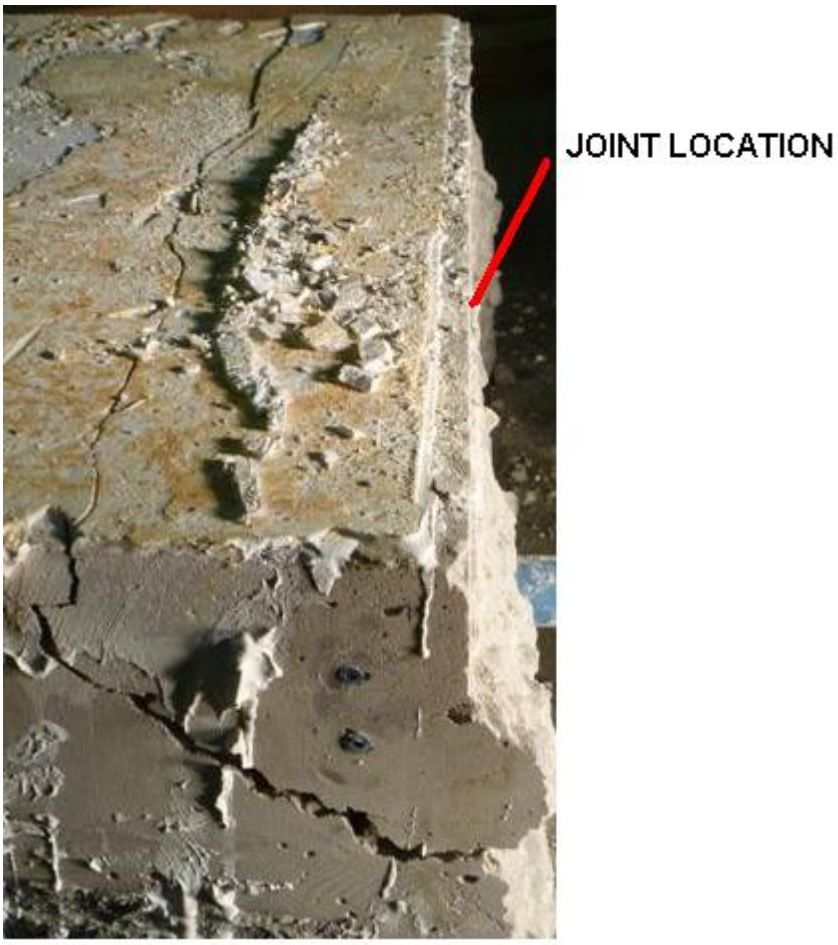

Figure 6-22 – Top Side of Slab Crack Extending from Joint

A crack extends across the width of the slab approximately 100 mm from the joint location as shown in Figure 6-22. This crack then extends an angle to above half the slab depth at the joint interface as can be noticed in Figure 6-22. Figure 6-23 presents the crack presented in Figure 6-22 extending between the dowels which suggest that the cracks start at the side of the dowel, consistent with the predicted PEEQT observed in the finite element investigation. On the side of the slab that was unloaded at the moment of failure, small cracks can be noticed extending from the dowel location in the bottom picture shown in Figure 6-23. Similar to the pilot test slab, the tack weld between the dowels and the chairs did not break during the testing.

Figure 6-23 – Dowel Bar Specimen: Slab Joint Face Showing Damage Extending from Dowels

The failure in the slab appeared to occur in the concrete before the dowels failed which means that the dowels will provide additional load transfer after failure occurs in the concrete. This would also provide more warning before complete failure of load transfer at the device as concrete distress and large displacement would occur before the failure. The dowel also was able to limit the differential deflection even after concrete failure.

6.9 GFRP I-Beam Slab Specimen Description and Results

A single standard 100 x 50 x 6.4 mm Dynaform pultruded GFRP I-beam provided by Fibergrate Composite Structures used to investigate the GFRP I-beam configuration. The section was placed directly on the bottom of the form centered on both the length and width of the slab. The top flange of the section was below the mid-height of the slab, and was centered at 96.8 mm from the bottom of the slab. Figure 6-24 presents the GFRP I-beam that was used in the test.

Figure 6-24 – 100 mm x 50mm x 6.4 mm Dynaform GFRP I-beam

The GFRP I-beam specimen was subjected to the cyclic loading history discussed in Section 6.3. The specimen response in terms of average deflection at the joint and load applied to the slab is presented in Figure 6-25. As the applied load was cycled below the wheel load level (87.5kN) very little additional differential deflection was measured. As the load was increased to the wheel load level, the average deflection at the joint increased as the load was cycled on the first side of the slab. After the load was switched to the opposite side at the wheel load level, the average deflection at the joint did not increase further as the load was cycled. At the 5/4 wheel load level,

a large increase in average deflection of approximately 20 mm at the joint occurred showing plastic damage as the slope of the load deflection curve flattened. As the load was cycled at the 5/4 wheel load, the average deflection at the joint increased each cycle until failure occurred on the first load cycle application on the second side of the joint.

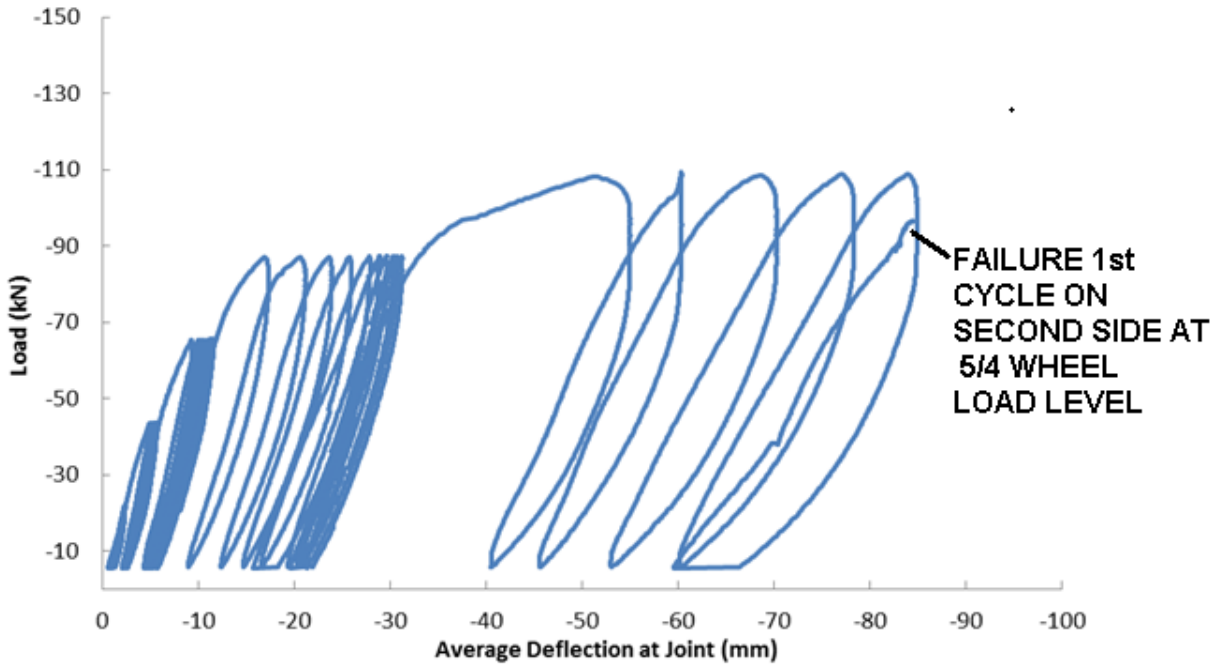

Figure 6-25 - GFRP I-beam Specimen: Average Joint Deflection vs. Load

Figure 6-26 presents the specimen response in terms of differential deflection at the joint versus the load applied. At applied load levels below the 3/4 wheel load level, there was little noticeable change in differential deflection as the load was switched from the first side of the joint to the second. At the 3/4 load level, the differential deflection of the joint was still within 1 mm on either side of the joint. When the load was increased to the wheel load level (87.5kN) on the first side of the joint, the differential deflection was below 1mm. As the load is switched to the second side of the slab the differential deflection increased to a maximum of approximately 2.25 mm. The differential deflection for the GFRP I-beam specimen was higher than that measured for the dowel bar specimen at similar load levels. The GFRP I-beam still maintained the differential deflection occurring at the joint at the wheel load level. After the load was increased to the 5/4 wheel load level, the GFRP I-beam specimen appeared to become ineffective at maintaining the differential deflection, evidenced by a steady increase in the differential

deflection as the load was cycled until failure occurred. The differential deflection at failure was larger than 5mm.

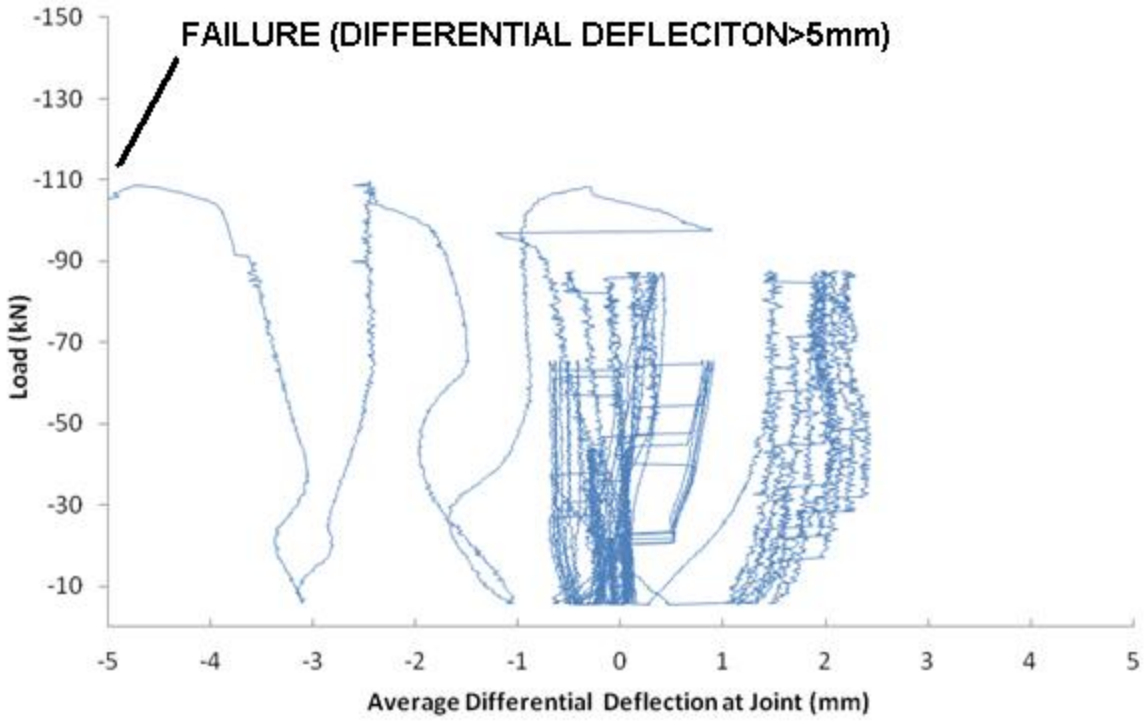

Figure 6-26 – GFRP I-Beam Specimen: Differential Joint Deflection vs. Load

Figure 6-27 presents the joint crack progression through the test. The initial crack (formed by pre-cracking) was quite fine. There was no visible increase in crack width until the full wheel load level (87.5kN) was reached. At this point, the crack at the joint increasesd to approximately 4 mm however little or no stepping was noticed at the joint. At failure the joint opened to more than 10 mm and major stepping occurred, as visible in the right-hand photograph in Figure 6-27.

Figure 6-27 – GFRP I-Beam Specimen: Joint Crack Comparison

The bottom view of the slab after the test is presented in Figure 6-28 and Figure 6-29 presents the Geo Foam base after removing the slab from the test frame.

Figure 6-28 –GFRP I-Beam Specimen: GFRP I-Beam Penetration through Slab at Failure

Figure 6-29 –GFRP I-Beam Specimen: GFRP I-Beam Penetration into Geo Foam Layer

The GFRP I-beam failed during the test and penetrated through the slab causing additional permanent deformation in the Geo Foam layer as visible in Figure 6-29. The finite element model (Chapter 5.0) also showed additional stress in the base layer beneath the device. Increased stresses in the base layer are not ideal as this may cause more deflection of the device and slab.

Further investigation of the GFRP I-beam and concrete damage at failure is presented in Figure 6-30.

As expected based on the GFRP I-beam penetrating through the concrete slab, failure of the GFRP I-beam occurred. At the joint location, the top flange sheared off the remaining portion of the device which allowed the device to penetrate into the slab on the unloaded side as the device was loaded. The top flange also failed in shear at the joint location. The failure in the device is not ideal as a shear failure provides little warning and little strength after failure occurs (unlike the steel dowel bar). Increasing the thickness of the top flange would help reduce the chance of shear failure of the top flange. Based on the observed failure the section dimensions need to be increased, the spacing needs to be reduced, or both. A reduced spacing of 450 mm will be used in the service load finite element analysis (Chapter 7.0) in an attempt to improve the performance of the device.

Figure 6-30 –GFRP I-Beam Specimen: Joint and Device Condition at Failure

6.10 GFRP Tapered Plate Specimen Description and Results

The GFRP tapered plate dowels were 12.5 mm thick Dynaform plate cut to 75 mm at one end and 25 mm at the other. The plates were provided by and prepared by Fibergrate Composite Structures. The plates were installed similar to a dowel bar aligned in the middle of the slab at a height of 125 mm. The GFRP tapered plate was placed into a chair arrangement to set the height of the dowel. No attachment was provided between the two chairs so that only the plates cross the pavement joint. The GFRP tapered plates were spaced horizontally at 300 mm and were centered within the length and width of the slab specimen.

Figure 6-31 presents the layout of the GFRP Tapered plate dowel with the thick ends alternating as described above.

Figure 6-31 – Aligned GFRP Tapered Plate Dowels and Chair Arrangment

Unlike the standard dowel bar, the GFRP tapered plate was not fixed to the chairs. During placement of the concrete, the chairs were able to come apart and the devices had to be held in the chairs manually. Further consideration of the attachment of the GFRP tapered plates to the chairs is needed for practical concrete placement, particularly considering that in an actual paving setting a slip form paver is typically used with low or no slump concrete.

The GFRP tapered plate dowel specimen was subjected to the cyclic loading history described in Section 6.3. The specimen response in terms of average joint deflection and load is presented in Figure 6-32. Average deflection at the joint for the GFRP tapered plate dowel was similar to the GFRP I-beam specimen where the average deflection at the joint did not appear to increase at the load levels below the wheel load level (87.5kN). At the wheel load level, the average deflection increased as the load was cycled; however the average deflection at the joint did not increase in the final cycles applied. When the load was increased to the 5/4 wheel load, a large increase in average deflection at the joint occurred (approximately 20mm), and as the load was cycled the average deflection continued to increase suggesting failure was occurring.

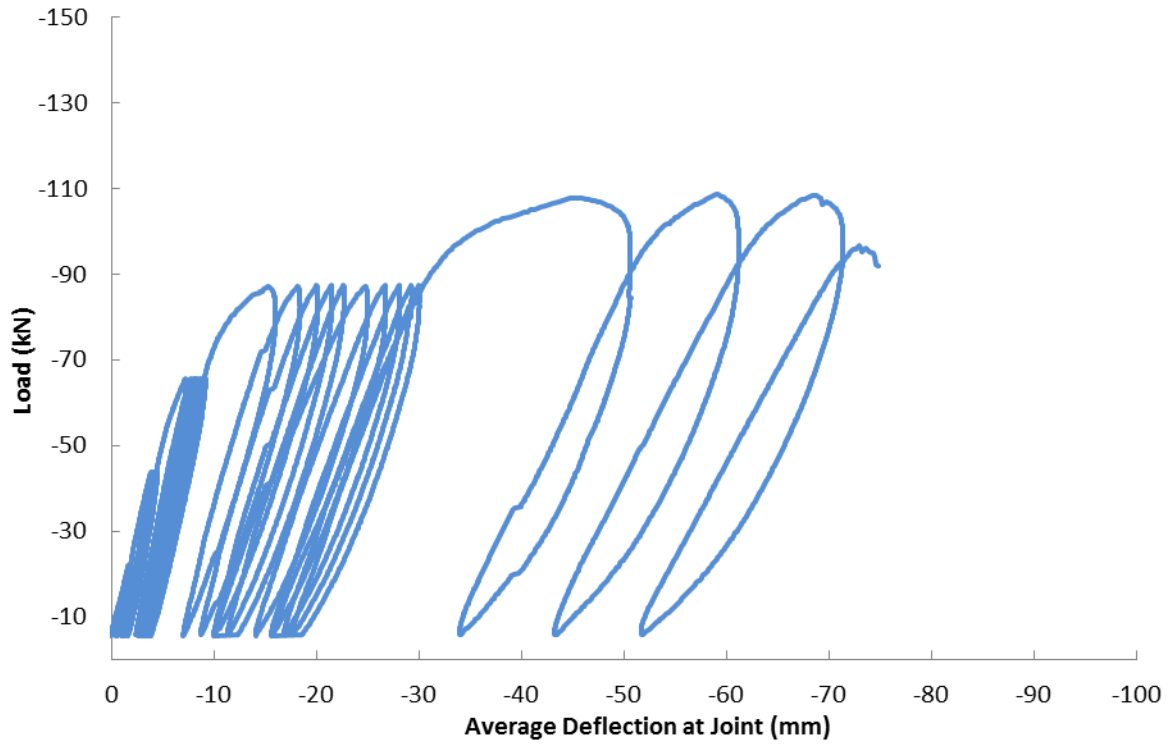

Figure 6-32 –GFRP Tapered Plate Dowel Specimen: Average Joint Deflection vs. Load

Figure 6-33 presents the differential deflection occurring at the joint for the aligned GFRP tapered plate dowel specimen. Again, the general behaviour of the GFRP tapered plate dowel was similar to that for the GFRP I-beam specimen. At the wheel load level, the GFRP tapered plate dowel maintained the differential deflection on the first side of the joint below 1 mm and on the second side of the slab below 2 mm. The GFRP tapered plate dowel reduced the differential deflection occurring at the wheel load level when compared to the experimental results for the GFRP I-beam. Similar to the GFRP I-beam specimen, as the load was increased beyond the wheel load level to the 5/4 wheel load level the differential deflection at the joint increased rapidly as the load was cycled until the differential deflection was greater than 5 mm.

Figure 6-34 presents the crack progression at the joint throughout the coarse of the experimental testing of the GFRP Tapered plate device specimen. The crack condition is shown at the start of the test, after the 87.5 kN load has been applied, and at the end of the test after failure.

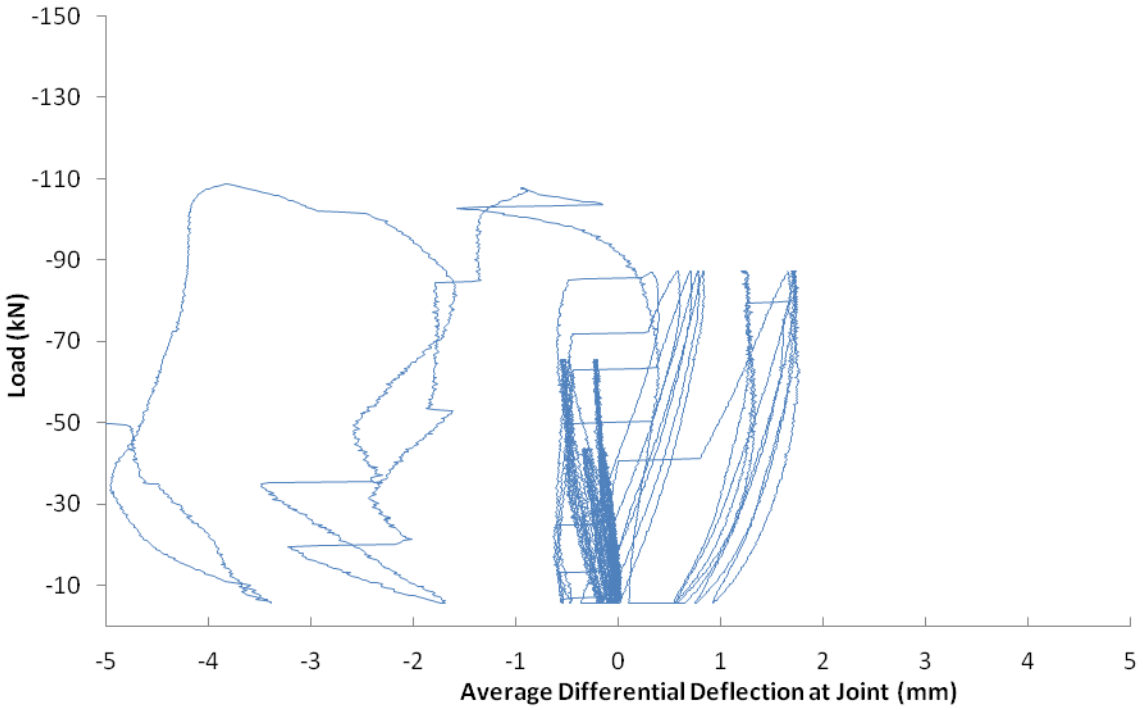

Figure 6-33 - GFRP Tapered Plate Dowel Specimen: Differential Joint Deflection vs Load

Figure 6-34 - GFRP Tapered Plate Dowel Specimen: Joint Crack Comparison

The initial crack formed during pre-cracking extended fairly directly from the saw cut to the slab bottom. The crack did not increase significantly until the wheel load level (87.5kN) was reached, where the width was approximately 4 mm. After failure, there appeared to be some crushing of the concrete occurring at the joint due to the angular crack that formed during the test. Major

stepping was observed at the joint when failure occurred. The stepping was sudden, suggesting a shear failure of the device at failure of the joint.

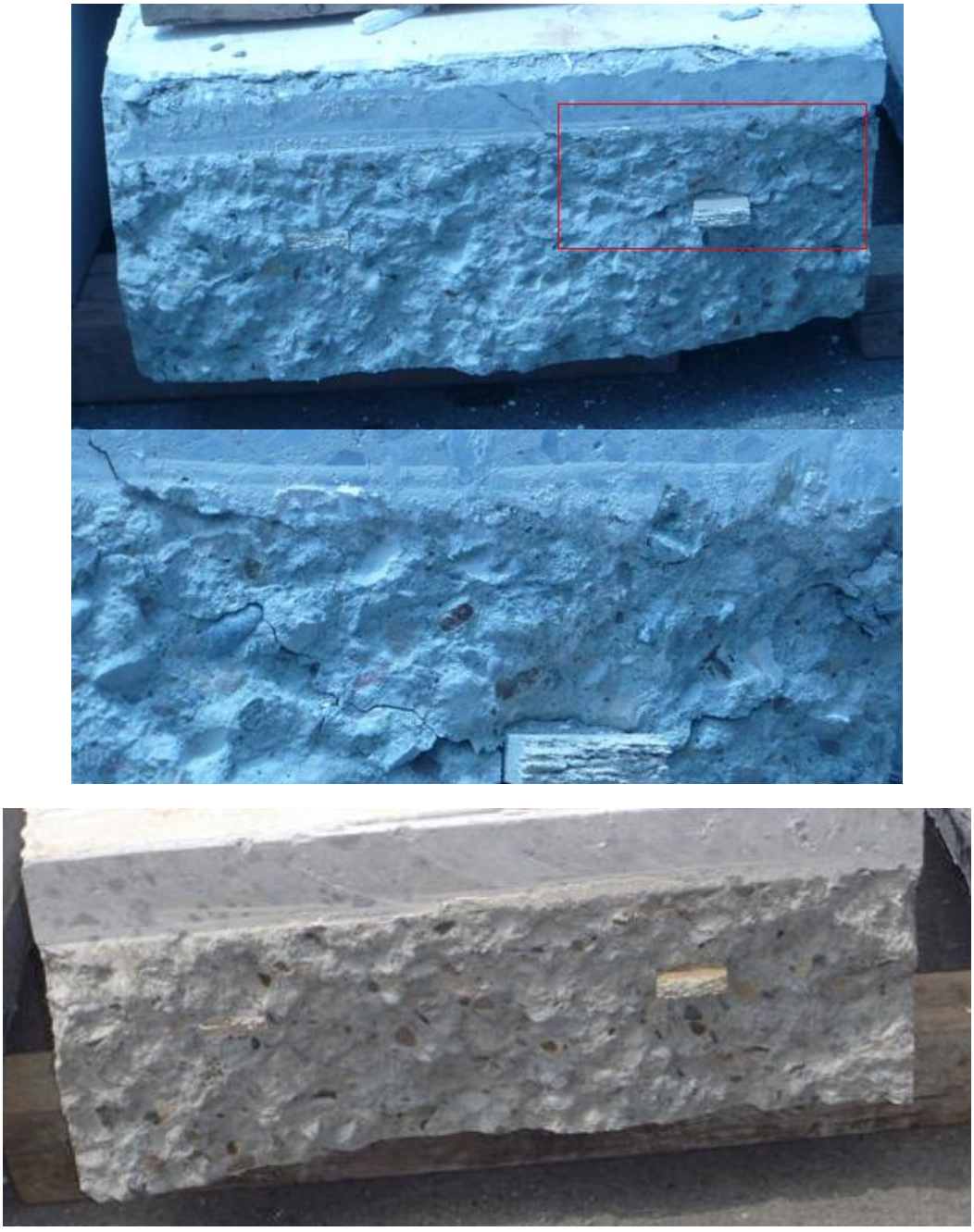

Figure 6-35 - Experimental GFRP Tapered plate Dowel Concrete Joint Faces

The failed specimen condition after testing is shown in Figure 6-35. Cracking extending from the top of the GFRP tapered plate dowel is consistent with the PEEQT in the concrete predicted using the finite element model. The GFRP Tapered plate dowel has also failed at the joint

location with a shear failure. This is not an ideal failure mode, as the stepping at the joint occurs quickly after the shear failure of the device occurs.

6.11 Misaligned GFRP Tapered Plate Dowel Specimen Description and Results

The misaligned GFRP Tapered plate is similar to the aligned case except the chair on one side of the joint was raised by 30 mm and on the other end the chair was lowered by 30 mm. Increasing the height of the chairs on one side and lowering on the other side places the middle of the dowel at the joint location at the mid-depth of the slab and investigates the behaviour of a vertical skew misalignment. Similar to the aligned GFRP Tapered plate dowel, an attachment between the chair and the GFRP Tapered plate was not provided. During placement of the concrete the chairs were manually stabilized and further investigation into the placement and this stability would be required in order to construct the devices in an actual pavement setting. A dowel bar inserter would also be possible alternative. Figure 6-36 presents the vertically skew misaligned Tapered plate dowels used in the experimental testing program.

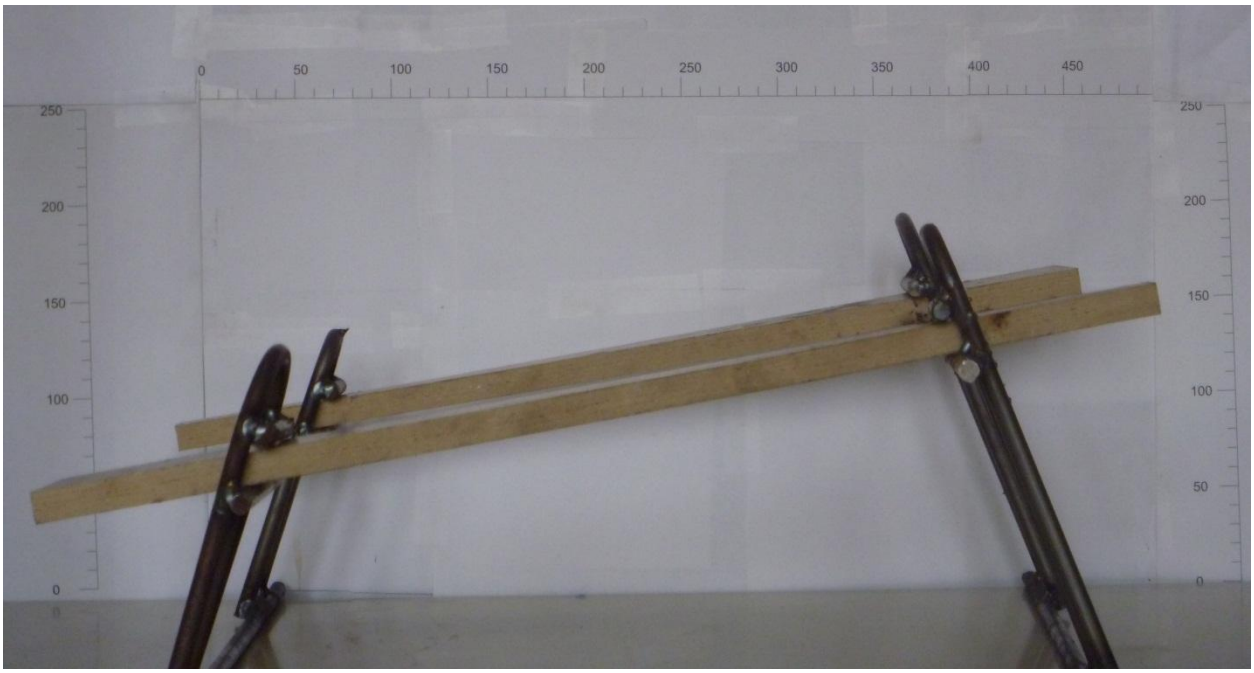

Figure 6-36 – Misaligned GFRP Tapered plate Dowels

The specimen was subjected to the cyclic loading history (Section 6.3), and the specimen response is presented in terms of the average deflection at the joint and the load applied to the slab in Figure 6-37. The vertically misaligned Tapered plate dowel had less average deflection

occurring at the joint location compared to the aligned Tapered plate dowel. At the wheel load level (87.5kN) the average deflection at the joint location did not increase significantly as the load was cycled, and at the 5/4 wheel load level the average deflection at the joint increased as the load was cycled although the was less than that observed for the aligned tapered plate dowel. The misaligned tapered plate dowel specimen failed at a load greater than the aligned tapered plate dowel. The increased failure load may be due to the nature of the GFRP material, where misalignment of the GFRP plate skews the principal directions of the plate material and the tensile strength of the device is used to reinforce the shear transfer at the joint.

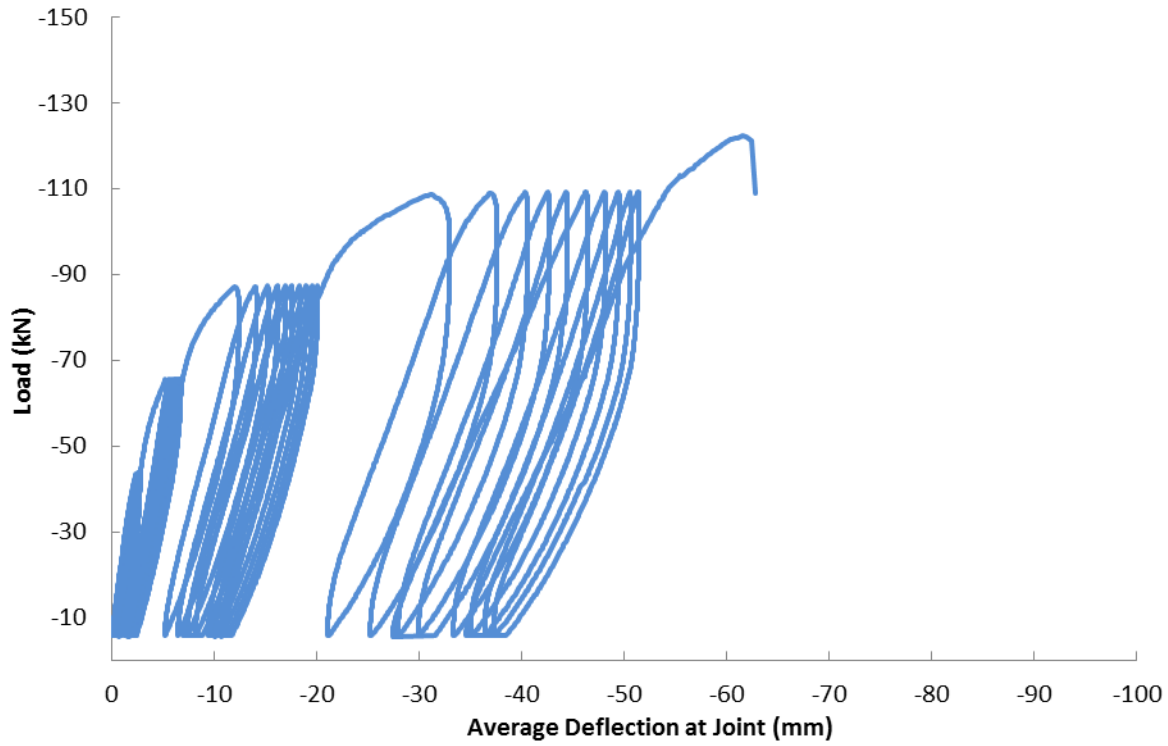

Figure 6-37 – Experimental Misaligned GFRP Tapered plate Average Joint Deflection vs. Load

Figure 6-38 presents the average differential deflection at the joint versus applied load for the vertically skew misaligned GFRP Tapered plate dowel specimen.

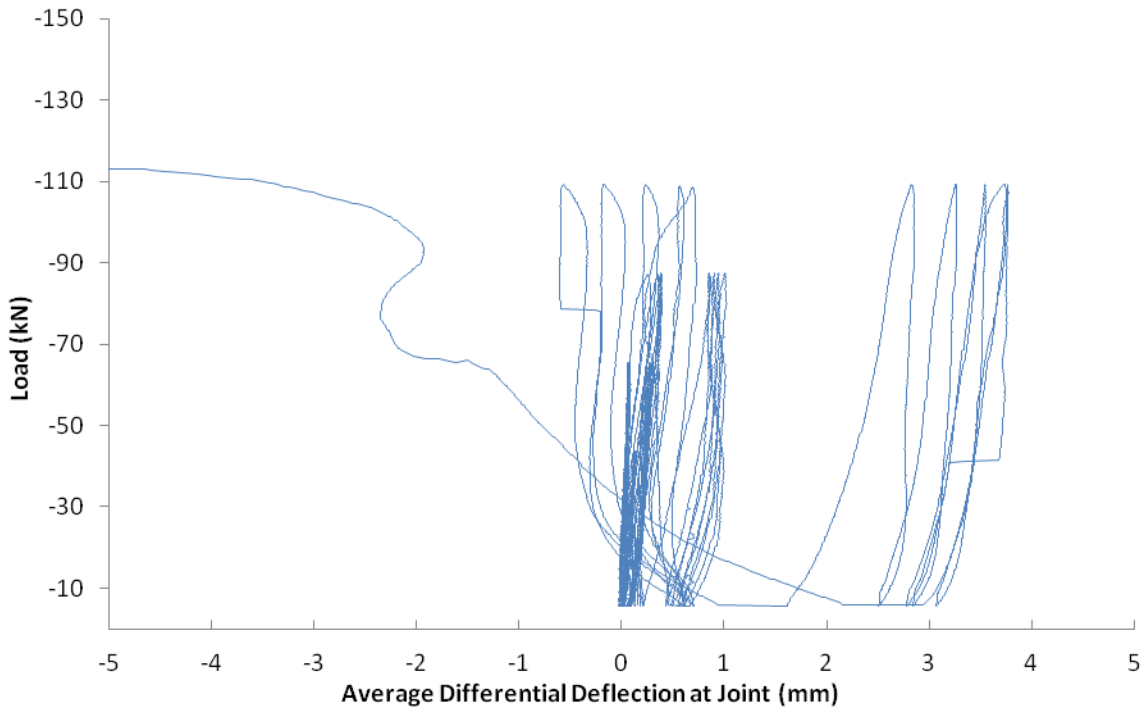

Figure 6-38 – Misaligned Tapered Plate Dowel Specimen: Differential Joint Deflection vs Load

The differential deflection at the joint was less than 1 mm for load cycles up to and including the wheel load level (87.5kN). At the 5/4 wheel load level, the differential deflection on the first side was between 1 mm and -1 mm. When the second side of the joint was loaded at the 5/4 wheel load level, the differential deflection at the joint increased to between 2.5 mm to 4 mm. The differential deflection at the joint increased with each load cycle. As the load was increased beyond the 5/4 wheel load level, the differential deflection at the joint quickly increased as failure occurred.

Figure 6-39 presents the crack progression at the joint for misaligned GFRP tapered plate dowel specimens. The picture on the left in Figure 6-39 presents the crack at the start of the test, where a small hairline crack exists from the sawcut generally straight down to the bottom of the slab. After the quasi-static loading was applied up to the wheel load level, the crack opened to approximately 5 mm at the bottom of the slab (where visible), and was beginning to come in contact at the top of the joint (as shown in the middle picture in Figure 6-39). Failure with the vertically misaligned GFRP Tapered plate dowel was less sudden than with the aligned GFRP

Tapered plate dowel; however, it was noticed in the picture on the right in Figure 6-39 that when the device failed (in shear), major stepping occurred at the joint.

Figure 6-39 – Misaligned GFRP Tapered Plate Specimen: Joint Crack Comparison

Figure 6-40 presents the joint and device after the completion of the experimental testing. The bottom two pictures in Figure 6-40 show either side of the joint. The photograph in the bottom left of Figure 6-40 is the low end of the misaligned GFRP tapered plate dowels, and the photo in the bottom right is the raised end of the GFRP Tapered plate dowel. The devices appear to have failed in a shear at the joint. A shear failure is not an ideal failure as it provides little warning as all strength is lost after the failure occurs. In the top left of Figure 6-40, cracking can be noticed on the smaller lower end of the GFRP tapered plate. This cracking was extending from the sides of the GFRP tapered plate dowel similar to the plastic straining predicted by the finite element model causing failure, as well as with the aligned GFRP tapered plate dowel. The top right hand photo in Figure 6-40 presents the smaller end of the raised side of the GFRP tapered plate dowel, when damage is observed above the plate. The device has clearly failed, and the laminations in the GFRP material can be noticed to have lost contact with one another.

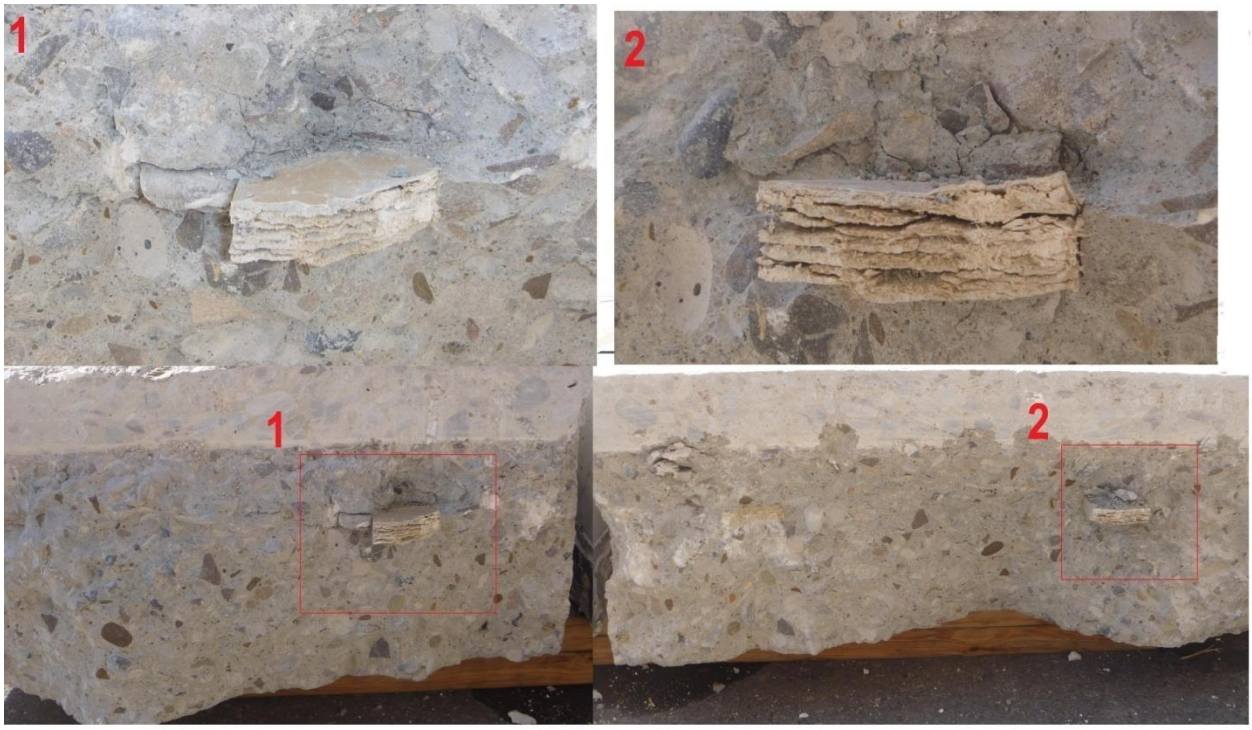

Figure 6-40 – Misaligned GFRP Tapered Plate Dowel Specimen: Joint and Device Condition at Failure

After investigating the effects of a vertically misaligned GFRP tapered plate dowel to quasi-static reversed loading in an experimental testing setup, the misalignment does not show any signs of degrading the load transfer behaviour compared to an aligned GFRP tapered plate dowel. The misalignment of the GFRP tapered plate increased the maximum load in the experimental testing program in comparison to the aligned GFRP tapered plate.

6.12 Summary of Experimental Testing

An experimental testing procedure and setup was developed to evaluate the wheel loading applied to a slab specimen configuration based on the wheel path model with static increments of the wheel load applied to either side of the slab. The testing arrangement was capable of testing the devices to failure and investigating the deflection at the joint to allow comparison of the behaviour between devices.

Based on the experimental testing program, the following conclusions were made:

- The conventional steel dowel bar failed at the highest load level and also maintained joint deflection better than the GFRP I-beam and GFRP tapered plate dowel as predicted by the wheel path finite element modeling completed.
- The GFRP I-beam supported a higher maximum load than the aligned GFRP tapered plate. Finite element modeling predicted failure with the GFRP I-beam at a lower load than the tapered plate dowel. The finite element modeling did not capture shear failures of the devices and the behaviour of the GFRP. The material behaviour of the GFRP was also assumed to be isotropic which was not capable of modeling the shear behaviour of the devices at high stress levels.
- The GFRP tapered plate failed at the lowest load because it has the lowest shear strength.
- Misalignment of the GFRP tapered plate increased the maximum load transferred at the slab compared to the aligned GFRP tapered plate and had a higher maximum load capacity than the GFRP I-beam. The misalignment of the device also misaligns the orientation of the main fibres in the plate which are strong in tension but weak in shear. The alignment of the fibres increases the strength of the main shear plane.
- The differential deflection at the joint is lower with the GFRP tapered plate at the wheel load level in the experimental testing compared to the misaligned GFRP tapered plate and GFRP I-beam. The finite element modeling also predicted similar behaviour suggesting that at higher load levels the finite element model does not capture the behaviour of the devices adequately.
- The GFRP I-beam allowed the highest differential deflection to occur. Finite element modeling also predicted the differential deflection at the joint to be the largest for the GFRP I-beam.
- The failure at the joint with conventional dowels allows warning and major stepping did not occur at the joint when the device failed.
- The aligned GFRP tapered plate dowel failed in shear suddenly and major stepping occurred.
- Misalignment of the GFRP tapered plate dowel did not change the failure of the device and still experienced a sudden shear failure with large stepping occurring.

- Failure in the GFRP I-beam gives some warning of failure and has post failure strength as the bottom portion of the GFRP I-beam is bearing on the Geo Foam layer below as a shear failure occurs between the top flange and web of the section.
- Cracking failure occurred extending from the sides of the dowel bar similarly to the predicted locations of PEEQT that occurred in the finite element analysis.
- Zones of cracking in the concrete extending from the top flange of the GFRP tapered plate section occurred similarly to the PEEQT that was predicted using the finite element model.
- The GFRP I-beam had some very local cracking occurring near the top flange of the device; however, it appeared that the most of the failure was in the base layer and the device itself.
- Based on the testing results and failure mechanisms observed, it would be important in device design to ensure that the shear failure of the devices does not occur. The sudden failure of the device in shear caused sudden stepping to occur at the slab. Slab support was poor at the joint which had an effect on the stepping that occurred; however, pumping at the joint could also cause poor support at the slab.
- The damage locations observed in the experimental testing were similar to the locations predicted using the finite element analysis.
- General predictions about behaviour of the joint in the experimental study is similar to the results predicted using finite element analysis.
- Experimental testing captured the failure of the devices which was not captured in the finite element analysis. The material model used for the devices would need to be refined further to include nonlinear behaviour as well as anisotropic material properties to capture these effects but was not included in this study.

7.0 Service Load Finite Element Analysis

7.1 Service Load Finite Element Analysis

The alternative joint load transfer devices proposed in this research were categorized as discrete or continuous as described in Chapter 3.0. The wheel load transfer behaviour of the discrete devices (steel dowel bars, GFRP I-beam, and GFRP plate dowels) up to failure of the device or concrete was investigated computationally and experimentally in Chapters 5.0 and 6.0, respectively. The finite element analysis presented in this chapter examines the performance of the discrete devices and selected continuous devices (horizontal V device and horizontal pipe) under service load conditions consisting of the combined effects of concrete shrinkage, thermal loading and service wheel loading. Details of the shrinkage, thermal and wheel loading were presented previously in Section 4.4. The service loading history used in the finite element analysis is listed in Table 7-1.

The loading history in Table 7-1 was determined based on the work completed by Levy (2010). Wheel load transfer of the slab at the two extremes for temperature gradient conditions was investigated under this sequence of loads. The wheel load was also applied to both sides of the slab since some of the devices are non-symmetric, and because the results from the wheel path analysis show that the reversed cyclic loading condition causes stress reversals and may affect the overall behaviour of the slab.

This chapter begins by presenting the detailed model geometry including boundary conditions. Similar to the wheel path analysis, a detailed description of the results for each model will be presented separately, and then comparisons between the device behaviours will follow. The detailed descriptions of the results will focus on presenting the stress distributions through the thickness. Comparisons of the devices will be presented using graphs with the behaviour of each device presented through the loading history.

In order to capture the effects of shrinkage and thermal gradients a quarter slab was chosen. To capture the behaviour of the devices three-dimensional thermal and shrinkage, straining needs to be investigated accounting for the full slab geometry. Applying restraint normal to the joint faces

on the quarter slab model captures the effects of the straining occurring in three dimensionally based on the full slab geometry using the smallest model.

Table 7-1 - Service Loading History

Load Type	**Description**	
Gravity	Gravity is applied to the entire model	Section 4.4.1
Shrinkage Strain	Shrinkage applied to the concrete slabs	Section 4.4.3 (Figure 4-8)
Three Day and Night Thermal Cycles	Temperature day distribution applied to the slabs and devices	Section 4.4.4 (Figure 4-9)
	Temperature night distribution applied to the slabs and devices	
	Temperature day distribution applied to the slabs and devices	
	Temperature night distribution applied to the slabs and devices	
	Temperature day distribution applied to the slabs and devices	
	Temperature night distribution applied to the slabs and devices	
Thermal Day Profile (sustained)	Temperature day distribution applied to the slabs and devices	Section 4.4.4 (Figure 4-9)
Wheel Load 1	87.5 kN wheel load and unload on one side of the joint in the wheel path	Section 4.4.2
Wheel Load 2	87.5 kN wheel load and unload on the other side of the joint in the wheel path	
Thermal Night Profile (sustained)	Temperature night distribution	Section 4.4.4 (Figure 4-9)
Wheel Load 3	87.5 kN wheel load and unload on one side of the joint in the wheel path	Section 4.4.2
Wheel Load 4	87.5 kN wheel load and unload on the other side of the joint in the wheel path	

7.2 Quarter Slab model

The quarter slab model consists of two quarter pavement slabs with a joint containing load transfer devices between them. The interior edges of the concrete slab are fixed from horizontal

displacement normal to the slab face to create a symmetric boundary condition. Figure 7-1 presents the location of the quarter slab model relative to the overall slab in plan view.

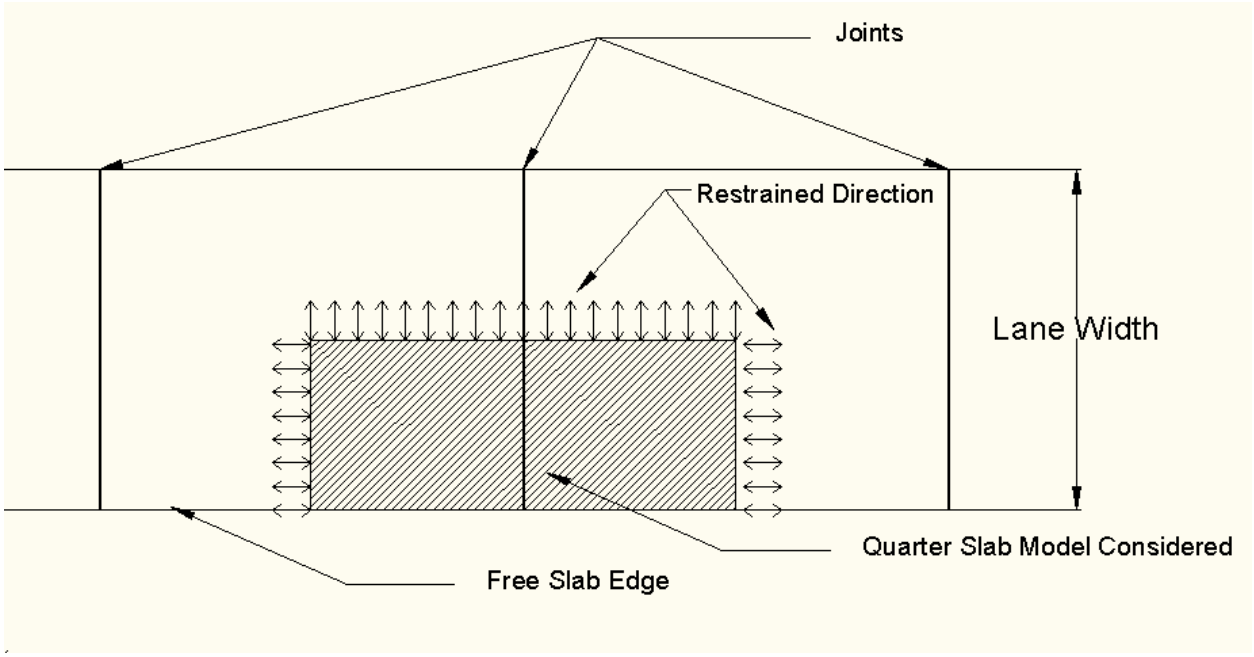

Figure 7-1 – Quarter Slab Model Section of Pavement (Plan View)

7.2.1 Quarter Slab Model Objectives

The objectives of the quarter slab model are:

- To create a model that is efficient computationally to apply shrinkage and temperature cycles to the slab for the different devices
- To create a model to understand the stress distributions in the concrete due to thermal and shrinkage strains.
- To understand how the device alternatives function under environmental loading and slab shrinkage strains

7.2.2 Quarter Slab Model Geometry

The quarter slab model geometry was aimed at being as small as possible while capturing the effects of the entire slab geometry. For the thermal and shrinkage strain gradients occurring in both longitudinal directions a quarter slab was chosen with movement restrained perpendicular to the faces on the two interior concrete edges simulating a symmetric boundary for the thermal and

shrinkage strains. Figure 7-2 presents the geometry of the quarter slab model used for the finite element service load analysis. The wheel path is centered 900 mm from the middle of the slab. Although the wheel load footprint is only presented on one side of the joint the wheel load was applied to the both side of the joint mirrored across the joint. Similarly the boundary conditions presented in Figure 7-2 are also mirrored across the joint on the other side of the slab as well.

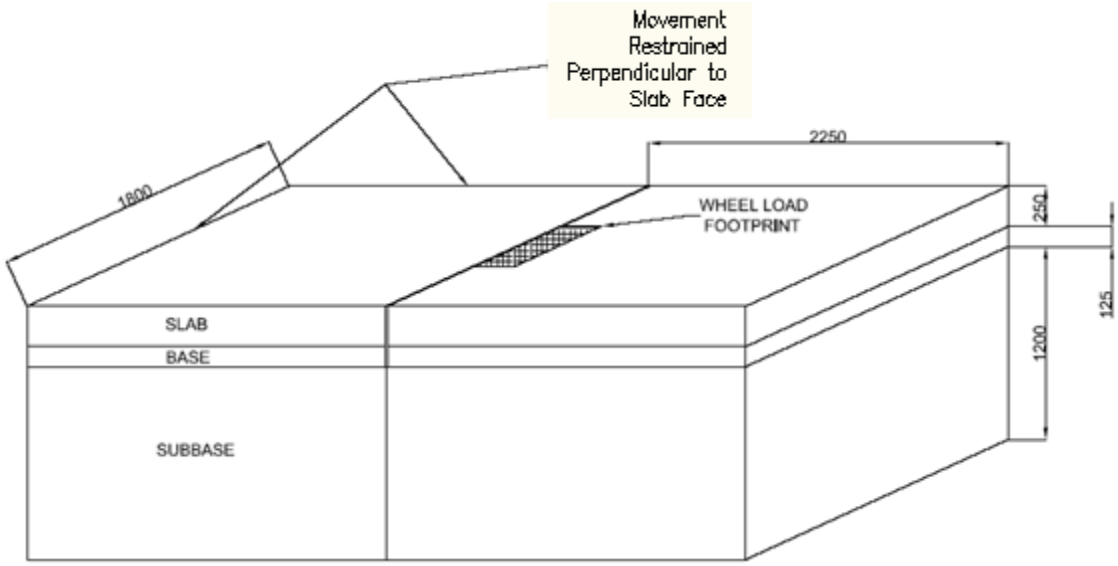

Figure 7-2 – Finite Element Analysis Quarter Slab Model Geometry (mm)

7.3 Dowel Bar Model Service Load Finite Element Results

A model with dowel bars spaced at 300 mm was created and served as the control model for the service load analysis. A detailed investigation of the behaviour of the dowel bar model subjected to the service loading history shown in Table 7-1 is presented herein.

Figure 7-3 presents the deflection of the concrete at the top of the slab on either side of the joint for the dowel bar model with service loading applied. As the gravity loading was applied, the top of the slab on either side of the joint deflected evenly and together. The shrinkage straining caused the edges of the slab at the free end to deflect upward 2 mm as the slab curled. The daytime thermal gradient application reduces the upward curling compared to shrinkage; however, still an overall upward curling of the slab at the joint edges of 0.8 mm occurs. Nighttime thermal gradients increase the upward curling occurring at the edges of the joint to 2.9 mm.

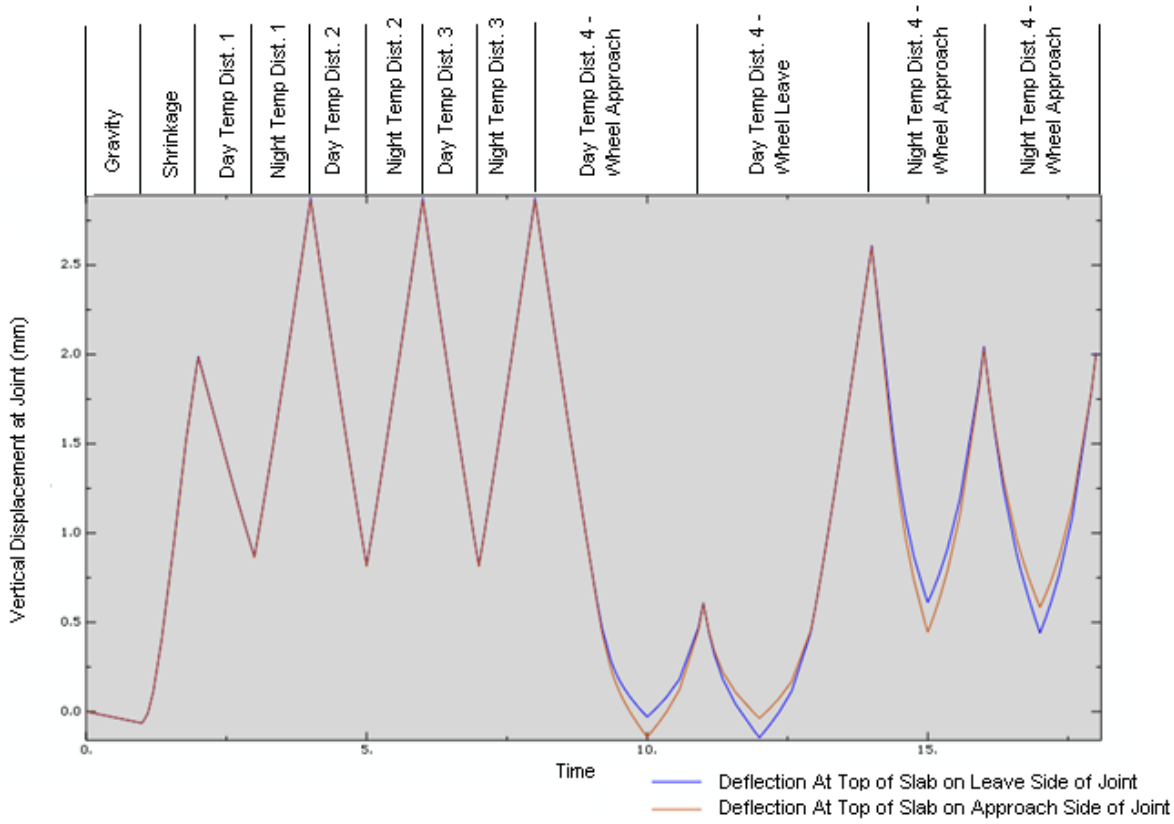

Figure 7-3 – Dowel Bar Model Top of Slab Deflection History

During each strain application the two edges at the joint maintained consistent deflection with negligible differential deflection. As the load was applied to both sides of the joint with the daytime thermal gradient applied, the deflection at the slab edge was below the initial starting point at approximately an average deflection of -0.06 mm. The differential deflection at the joint was 0.125 mm. There did not appear to be any progression of further deflection occurring in the dowel bar model with service loading applied based on the thermal cycles and wheel load application applied as presented in Figure 7-3.

Figure 7-4 presents the Von Mises stress distribution in the dowel after the shrinkage loading was applied to the slab. The distribution of the Von Mises stress shows the dowel bar bending upwards as the dowel is resisting the free edge of the slab from curling due to the shrinkage gradient. This upward curling of the slab is expected during shrinkage straining. The maximum stress in the top of the dowel bar is approximately 17.5 MPa.

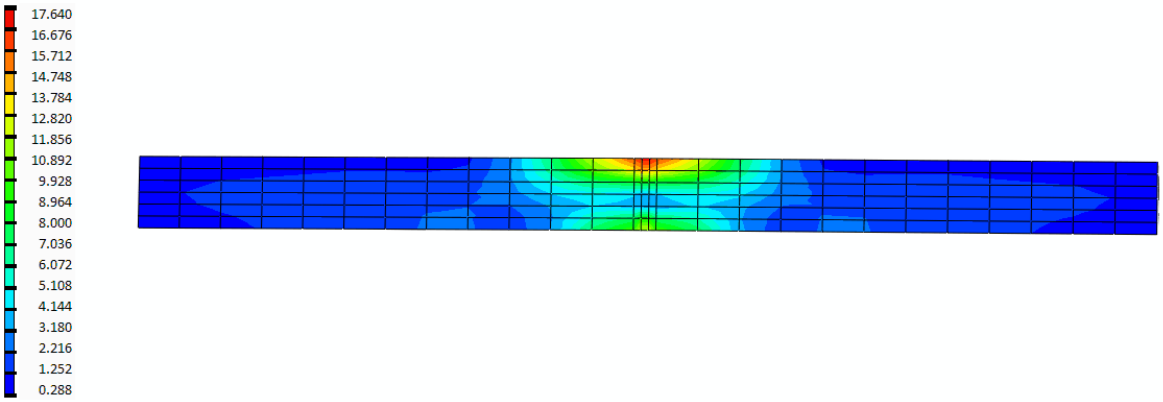

Figure 7-4 – Dowel Bar Von Mises Stress Distribution after Shrinkage (MPa)

The vertical stress distribution in the concrete at the joint around a dowel (with the dowel bar removed from the figure) is presented in Figure 7-5. The vertical stress in the concrete created tensile stress zones at the middle of the dowel on either side of the joint. This tensile stress concentration at the edge of the dowel occurred because the dowel does not curl. The straightness of the dowel bar relative to the curled slab caused a bearing force at the dowel concrete interface as the curling was restrained. The bearing of the dowel on the concrete pries the top and bottom of the slab apart at the sides of the dowels that caused tensile stress concentrations in this location. Maximum tensile stress at the dowel after shrinkage application was 2.48 MPa which is between the minimum and mean tensile strength for 30MPa concrete according to the CEB-FIP Manual (see Table 2-3). Compressive zones exist below the dowel in the concrete where the device was bearing on the concrete. The maximum compressive vertical stress at the dowel joint interface is 2.18 MPa. Stress in the base and subbase layers were very small during shrinkage step when no wheel load had been applied. After the shrinkage step was applied, the thermal daytime gradient was applied. The Von Mises stress distribution in the dowel switched to a concentration in the bottom of the dowel that is increased to 20.4 MPa. The distribution of Von Mises stress in the dowel after the daytime thermal gradient was not shown as it was very similar to Figure 7-4 but with the stress concentration flipped.

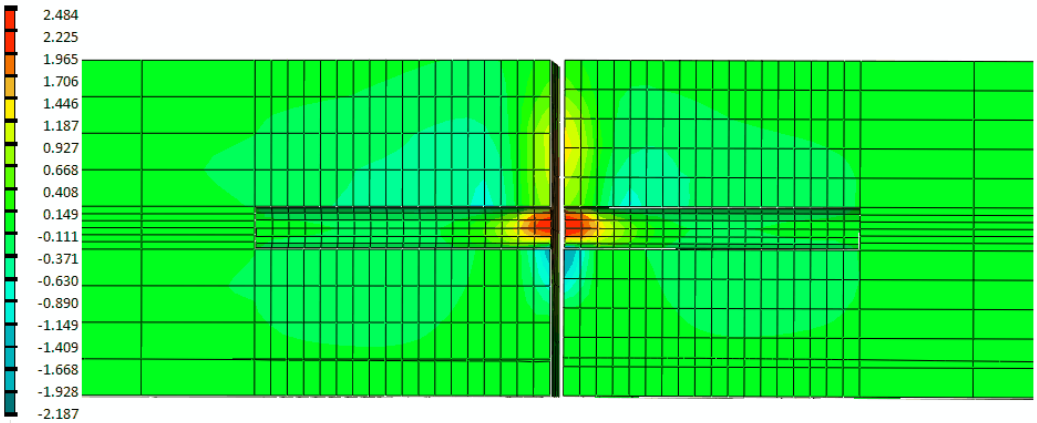

Figure 7-5 – Concrete Vertical Stress Distribution after Shrinkage (MPa)

The vertical stress distribution after the daytime thermal gradient was applied in the concrete is presented in Figure 7-6. A tensile vertical stress distribution exists in the concrete at the middle of the dowel at the joint location where the dowel is resisting the curling of the slab. Although a portion of these stresses will be due to differential expansion of the steel and concrete, the main portion was assumed to be due to the restraint of curling caused by the dowel. The maximum vertical tensile stress in the concrete was 2.85 MPa after the daytime thermal gradient was applied, which is nearing the mean tensile strength of 30 MPa concrete according to the CEB FIP Manual of 2.91 MPa. A small concentration of vertical compressive stress in the concrete can be noticed beneath the dowel similar to after the shrinkage step. The compressive stress along the length of the dowel increased as the thermal daytime gradient was applied as well.

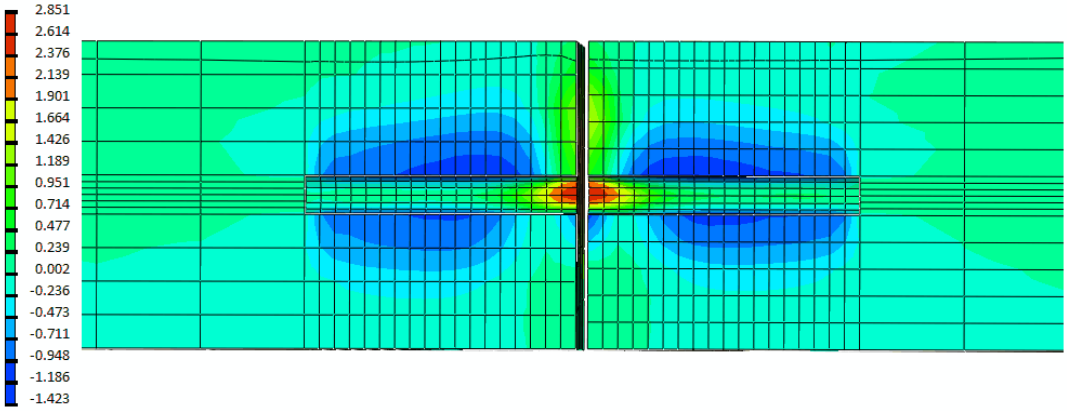

Figure 7-6 - Concrete Vertical Stress Distribution after Daytime Thermal Gradient (MPa)

After applying a daytime thermal gradient, the thermal gradient was switched to a nighttime thermal gradient. The Von Mises stress in the dowel reversed and the Von Mises Stress was greatest at the top of the dowel bar (similar to after the shrinkage step) at the joint location. The maximum Von Mises stress in the dowel after the application of the nighttime thermal gradient was 23.1 MPa.

Figure 7-7 presents the vertical stress distribution in the concrete after the nighttime thermal gradient was applied to the slab. Tensile stress concentration in the concrete at the middle of the dowel at the joint location still exists and the maximum vertical tensile stress was 2.91 MPa after the application of the nighttime thermal gradient. The tensile stress in the concrete has reached the mean tensile strength of concrete according to the CEB-FIP Model code. The maximum vertical compressive stress concentration below the dowel is 3 MPa which is well below allowable compressive stress limits for concrete. The thermal gradients were then re-applied to the model, and the results were similar to the first application of the thermal gradients. The daytime thermal gradient was then applied to the slab for a fourth time and the wheel load was applied to the slab.

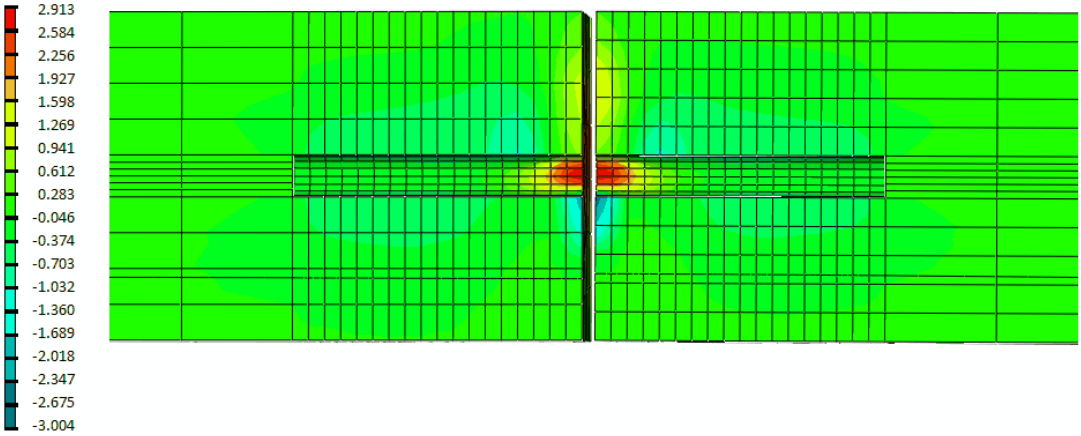

Figure 7-7 - Concrete Vertical Stress Distribution after Nighttime Thermal Gradient (MPa)

Figure 7-8 presents the Von Mises stress distribution through a section of the dowel after the first wheel load is applied to the slab along with with a daytime thermal gradient. The maximum Von Mises stress in the dowel after the wheel load application during a daytime thermal gradient is 22.9 MPa which is much less than the 92.3 MPa predicted using the wheel path model without shrinkage and thermal gradients applied. The upward curling occurring due to thermal and

shrinkage strains is in the opposite direction to wheel loading and hence the reduced Von Mises stress in the dowel when wheel loading with thermal and shrinkage straining applied to the slab would be expected to be lowered. Von Mises stress concentrations in the dowel are located at the top side of the of the loaded side of the dowel and across through the joint to the bottom of the dowel on the unloaded side of the slab. The distribution of stresses appears to be similar to when wheel loading is applied alone.

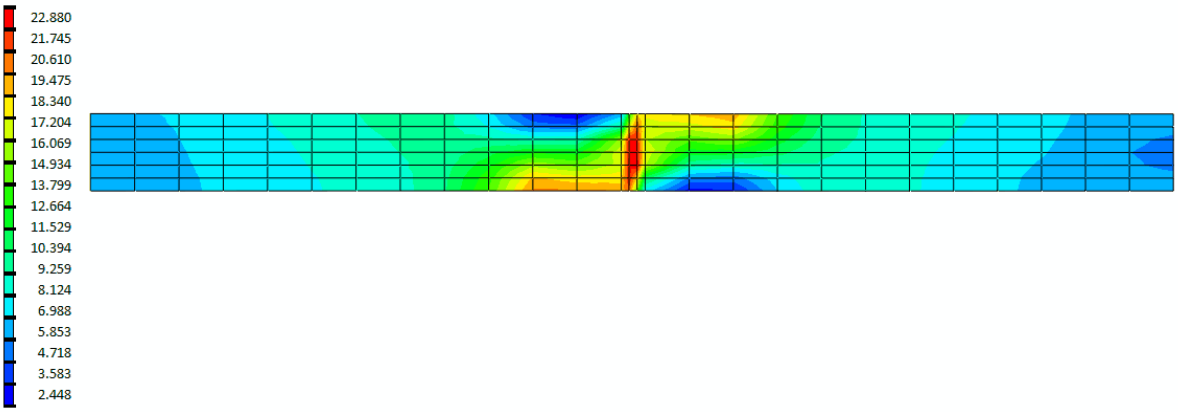

Figure 7-8 – Dowel Bar Von Mises Stress Distribution after Wheel Load Application 1 (MPa)

Vertical stress in the concrete after the wheel load application on the first side of the joint with a daytime thermal gradient applied to the model is presented in Figure 7-9. The maximum tensile vertical concrete stress at the joint interface was 2.81 MPa which is less than after the nighttime thermal gradient and is approaching the mean tensile failure strength of 2.91MPa. The zone of high tensile stress at the joint has increased with the application of the wheel load. Both the thermal gradient and wheel load cause high concentrations of tensile vertical stress in the concrete which causes an overall increase in maximum tensile stress in the cocnrete at the sides of the dowels. Compressive concentrations of stress above the dowel on the loaded side of the slab and below the dowel on the unloaded side of the slab exist. The maximum vertical compressive stress is 9.66 MPa above the dowel. A tensile zone exists above the dowel on the unloaded side and below the dowel on the loaded side of the slab as well as beyond the dowel extending from the end of the dowel.

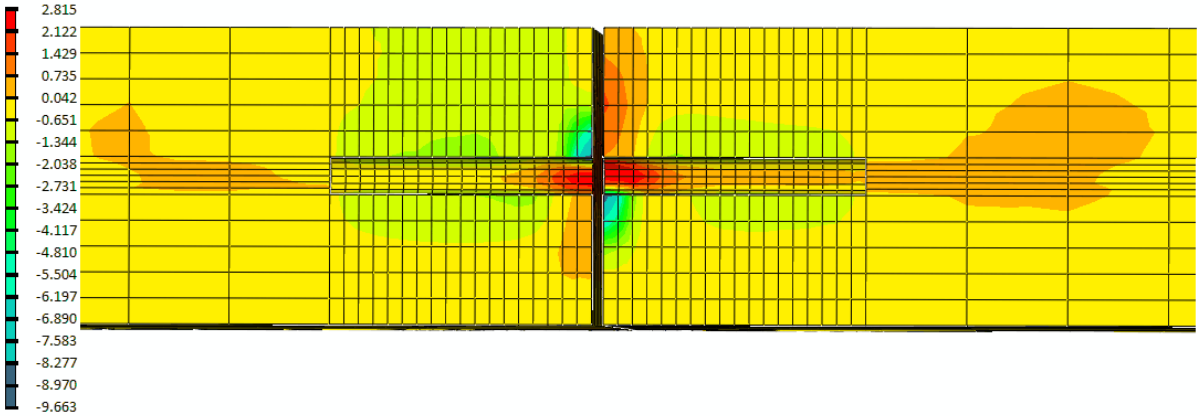

Figure 7-9 - Concrete Vertical Stress Distribution after Wheel Load Application 1 (MPa)

The vertical stress distribution in the base layers after the first wheel application is presented in Figure 7-10. The maximum stress at the joint interface was 127 kPa. The load was distributed through the slab to the other side beyond the device length where some additional stress concentration occurred. Maximum stresses under the unloaded side of the slab are lower than the loaded side in the base layers beneath the slab.

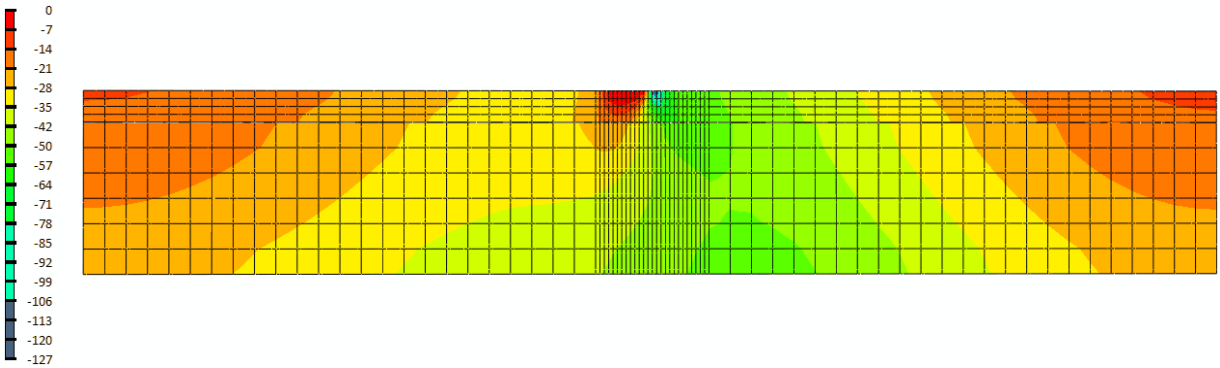

Figure 7-10 – Base Layer Vertical Stress Distribution after Wheel Load Application 1 (kPa)

After the second application of the wheel load to the slab (on the other side of the joint) the results presented for the first wheel application were reversed as would be expected. The results were generally the same and are not presented in detail herein. The third and fourth applications of the wheel load were applied on either side of the joint along with a nighttime thermal gradient applied to the slab. The third application of the wheel load had similar results to the fourth with concentrations from the wheel load transfer reversed, and only the fourth wheel load application

is presented. Figure 7-11 presents the Von Mises stress distribution in the dowel bar after the application of the fourth wheel load.

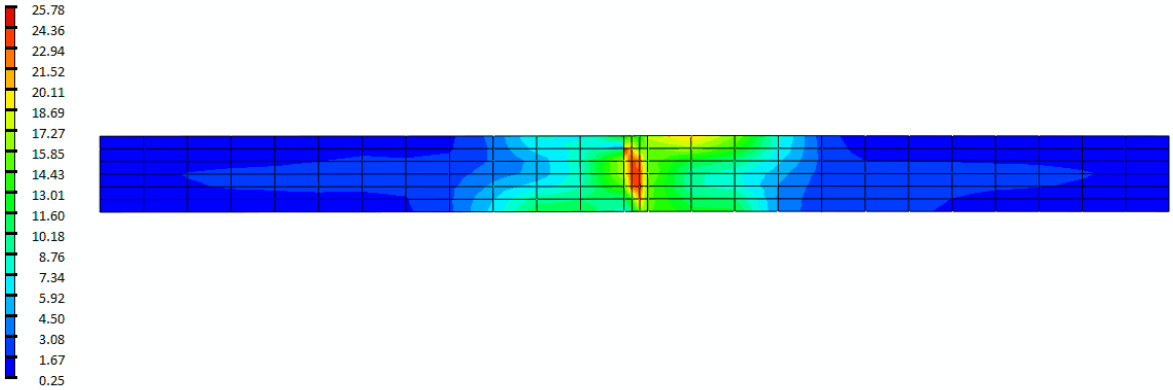

Figure 7-11 – Dowel Bar Von Mises Stress Distribution after Wheel Load Application 4 (MPa)

The maximum Von Mises stresses occur across the joint with other concentrations extending from the top of the loaded side of the slab to the bottom of the dowel on the unloaded side of the joint. The maximum Von Mises stress in the dowel was 25.78MPa which is again lower than with the wheel path model but upward curling due to thermal gradients exists and the wheel loading is generally in the opposite direction. The maximum Von Mises stress is increased when compared to the daytime gradient which may be partially due to the increased upward curling that causes the slab to be out of contact with base and load transferred through to the base layer is reduced increasing the load transferred through the dowel.

The vertical stress distribution in the concrete in a section through the dowel bar after the fourth application of the wheel load is presented in Figure 7-12. Vertical tensile stress concentrations exist at the joint location on both sides of the joint at mid dowel height. The maximum vertical tensile stress at this location is 2.8 MPa which is nearing the mean tensile strength of concrete and has exceeded the minimum tensile strength of concrete. Compressive vertical stresses at the top of the dowel on the loaded side and the bottom of the unloaded side exist in the concrete as well. The maximum compressive stress above the device on the loaded side is 13.1 MPa. Little tensile stress exists at the back of the dowels on the fourth wheel load application as the slab is curling upward and from thermal and shrinkage gradients while the wheel load is pushing the slab down.

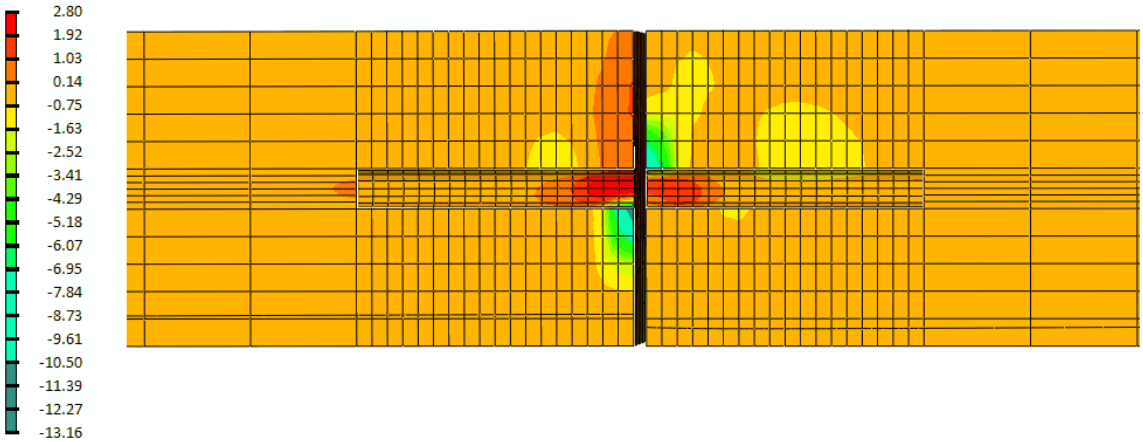

Figure 7-12 - Concrete Vertical Stress Distribution after Wheel Load Application 4 (MPa)

The vertical stress distribution in the base layers is presented in Figure 7-13. The maximum compressive stresses occur away from the wheel load as the slab was curled upward from the application of the nighttime thermal gradient. The maximum vertical stress in the base layer was reduced to 72 kPa during the nighttime.

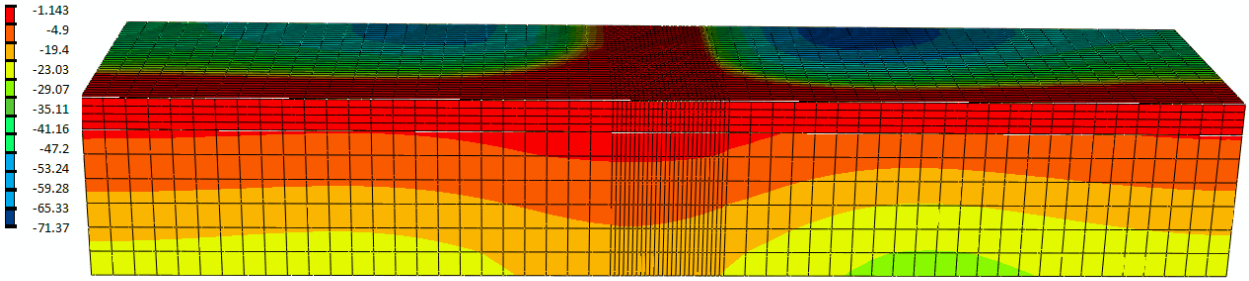

Figure 7-13 - Base Layer Vertical Stress Distribution after Wheel Load Application 4 (kPa)

After the fourth application of the wheel load, the plastic straining in the concrete slab was investigated to determine the current state of the concrete. Figure 7-14 presents the plastic tensile straining in a section through the dowel after the fourth wheel load application. Minor tensile plastic straining existed in the top of the slab in line with the dowels which is captured in Figure 7-14 at the top of corners of the slab section presented. Concentrations of the plastic tensile strains exist extending from the mid height of the dowel on either side of the slab. Compressive plastic straining has occurred on either side of the dowel below the device in the concrete as well (not shown as only local areas similar to wheel loading presented previously).

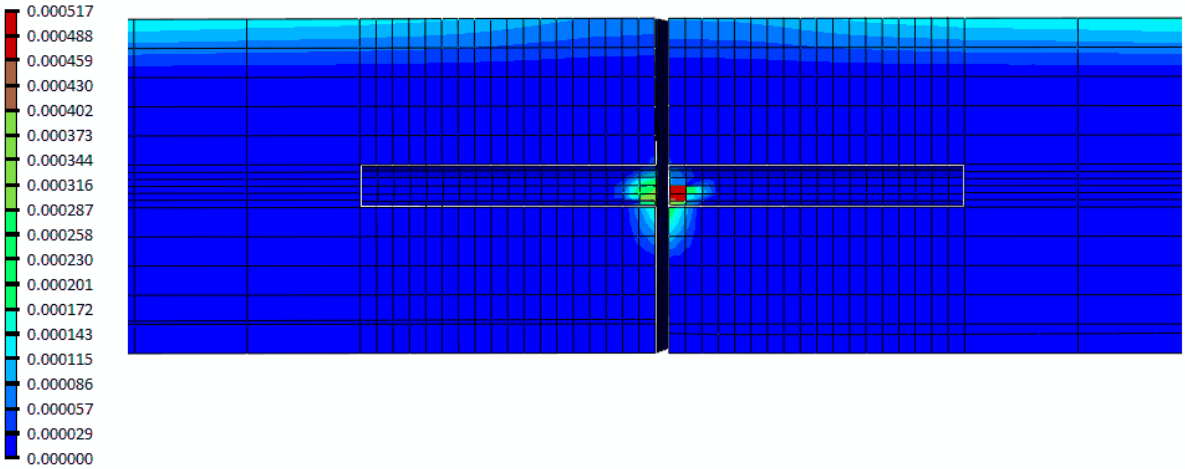

Figure 7-14 – Concrete Plastic Equivalent Strain (PEEQT) Distribution after Wheel Application 4

Generally dowel bars are intended to transfer the load and maintain the deflection of either side of the slab under service loading. Shrinkage and thermal gradients on the slab with the geometry used is nearing concrete tensile cracking strength at the sides of the dowel bars causing some local damage to occur at device locations where high stress concentrations exist. Wheel loading increases the stress concentrations at the dowel compared to only thermal gradients and shrinkage loads being applied to the slab. Under shrinkage and thermal strain applications the plastic regions of the concrete are localized to the joint and excessive damage did not appear to occur. The service analysis shows that the thermal and shrinkage strains change the distribution of stresses in all of the device, concrete and base support layers below compared to wheel loading only being applied but similar stress distributions still exist.

7.4 GFRP Tapered Plate Service Load Finite Element Results

An aligned GFRP tapered plate dowel with the dimensions described in Section 3.2.2 was input in the quarter slab model. Five GFRP plate dowels were spaced at 300 mm, and the wide end of the tapered plate was alternated from device to device in the model. A detailed investigation of the stress distribution in the GFRP Tapered plate model under service loading is presented in this section.

The deflection profile for the top of the slab at either side of the joint for GFRP tapered plate quarter slab model is presented in Figure 7-15 for the service loading history described in Table

7-1. Figure 7-15 shows that the GFRP tapered plate dowel behaves similarly to steel dowels with the deflection on either side being essentially equal. The top of the slab after shrinkage gradient, thermal daytime and thermal nighttime temperature gradients was curled upwards approximately 1.5 , 0.6 , and 2.6 mm respectively. After the application of the first and second wheel load, the differential deflection of the two slabs was approximately 0.125 mm. There does not appear to be any degradation of the load transfer behaviour at the joint throughout the service loading application in Figure 7-15. As the wheel load was applied on the approach side of the slab with the nighttime temperature gradient the model failed to converge.

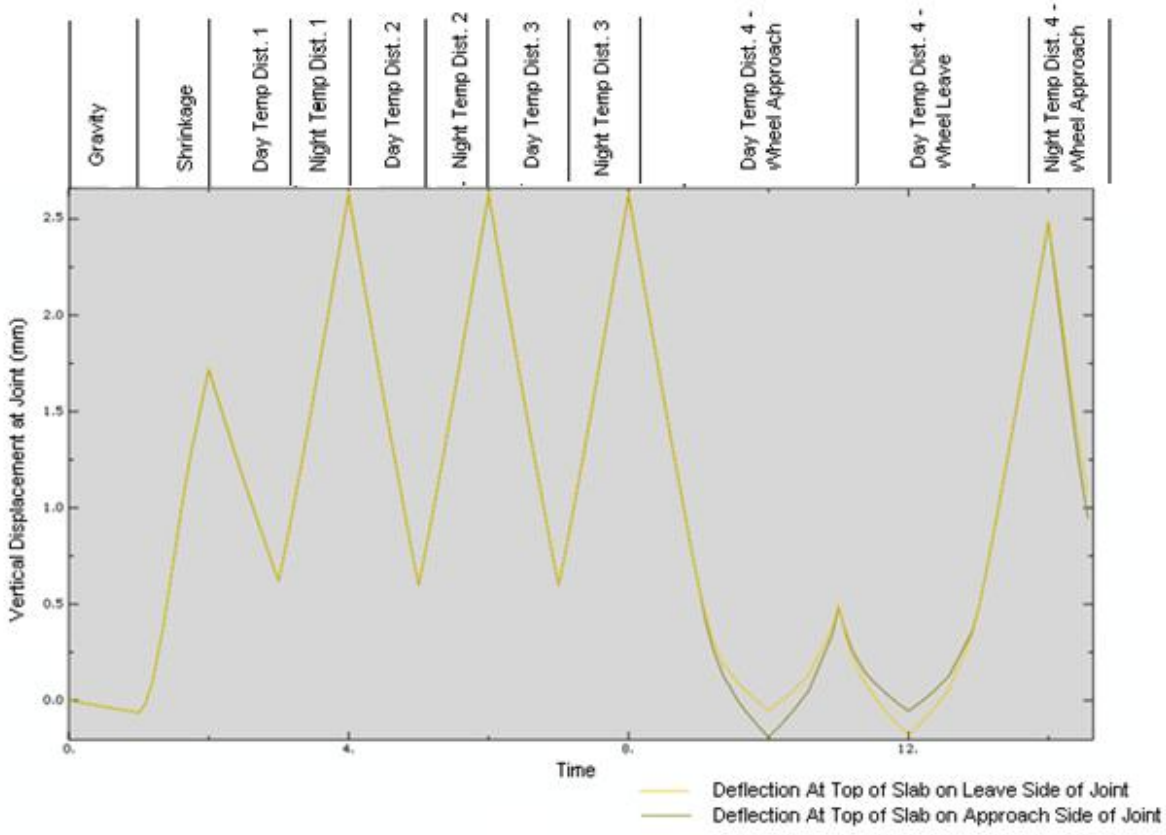

Figure 7-15 – GFRP Tapered Plate Dowel Model: Top of Slab Deflection History

Figure 7-16 presents the distribution of Von Mises stress in the GFRP tapered plate dowel after the shrinkage step was applied. The maximum Von Mises stress in the GFRP tapered plate of 9.9MPa occurs at the joint location. This stress is low compared to the GFRP failure strength in tension along the length of the device of 205 MPa; however, it is assumed that stress concentrations in the GFRP tapered plate dowel may be underestimated due to the mesh

refinement across the depth of the tapered plate. The distribution of stress in the GFRP tapered plate was very similar to the steel dowel (presented previously) after the shrinkage strain was applied to the slab.

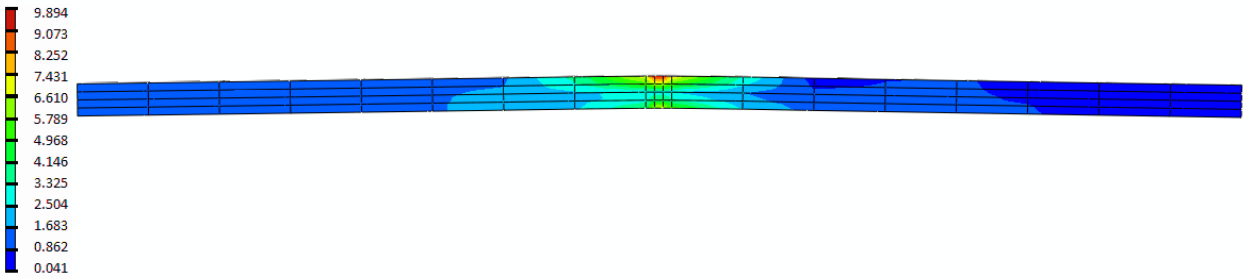

Figure 7-16 – GFRP Plate Dowel Von Mises Stress Distribution after Shrinkage (MPa)

Figure 7-17 presents the distribution of vertical stress in the concrete for the GFRP tapered plate dowel model after the shrinkage strain is applied to the slabs. Vertical tensile stress concentrations existed in the concrete at the middle of the device height on either side of the joint in the GFRP tapered plate model similar to the steel dowel model. The maximum vertical tensile stress in the concrete was 2.27 MPa which is greater than the minimum cracking strength of 30 MPa concrete but less than the mean cracking strength. Small concentrations of compressive vertical stress also exist beneath the GFRP tapered plate at the joint after the shrinkage strain is applied.

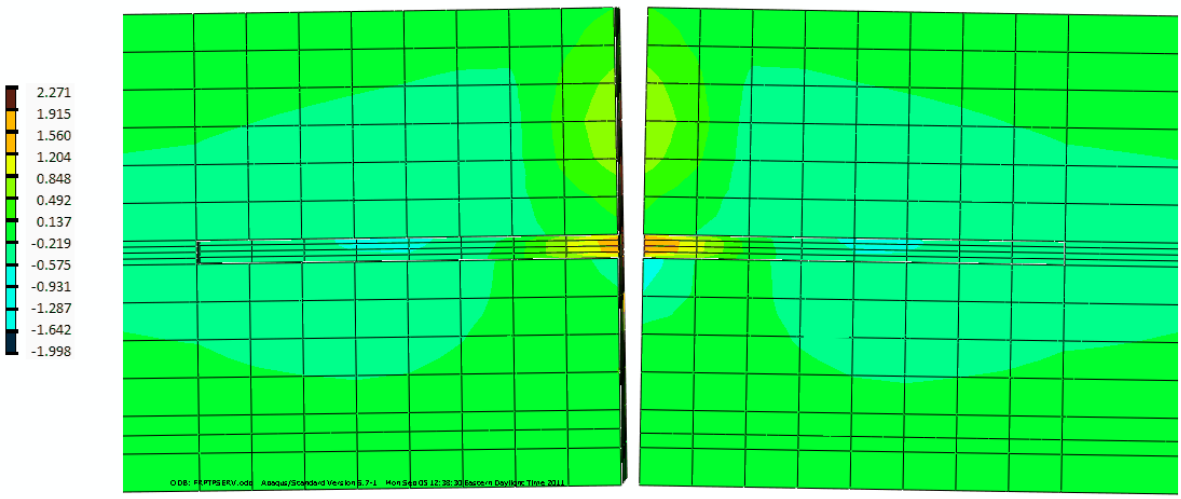

Figure 7-17 – Concrete Vertical Stress Distribution after Shrinkage (MPa)

Figure 7-18 presents the Von Mises stress distribution in the GFRP tapered plate dowel after a daytime thermal gradient was applied to the slab. The thermal daytime thermal gradient caused a concentration in maximum Von Mises stress at the bottom of the device at the middle of the joint, as can be seen in Figure 7-18. The maximum Von Mises stress in the GFRP tapered plate after the application of the first thermal daytime thermal gradient was 14.4 MPa, much below GFRP failure strengths. The distribution was similar to the steel dowel after the thermal daytime gradient was applied except that the distribution at the joint appears to be off center with the concentration occurring towards the smaller end of the tapered plate.

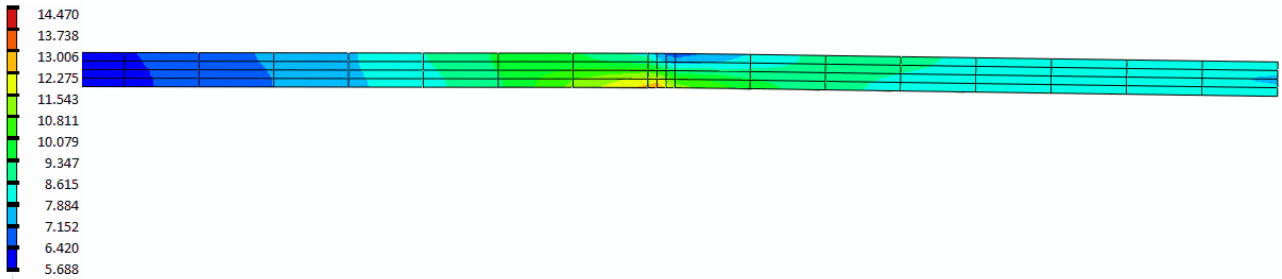

Figure 7-18 – GFRP Plate Dowel Von Mises Stress Distribution after Daytime Thermal Gradient (MPa)

Figure 7-19 presents the vertical stress distribution in the concrete around the device after the daytime thermal gradient is applied to the slab. The maximum compressive stresses in the concrete were low as the thermal straining occurs. A concentration of tensile stress existed in the concrete at the middle of the GFRP tapered plate location at the interface. A large concentration of vertical stress occurred beyond the end of the larger side of the GFRP tapered plate. The maximum vertical tensile stress in the concrete after the daytime thermal gradient was applied occurred at the joint location on the smaller end of the GFRP tapered plate side The maximum stress at this location was between the minimum and mean cracking strengths for 30 MPa concrete at 2.56 MPa.

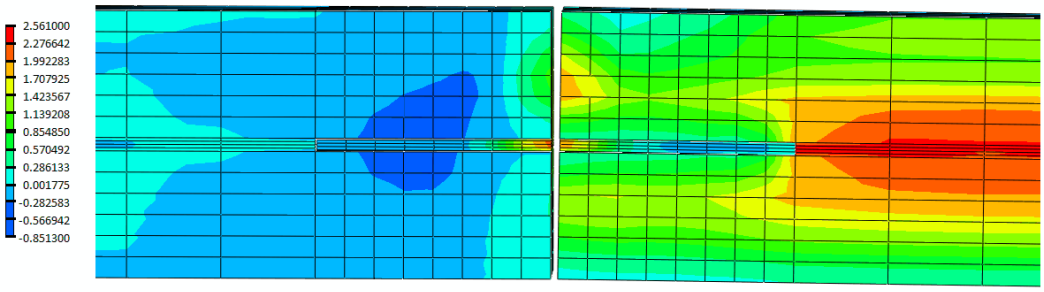

Figure 7-19 - Concrete Vertical Stress Distribution after Daytime Thermal Gradient (MPa)

Figure 7-20 presents the Von Mises stress distribution in the GFRP tapered plate device after the nighttime thermal gradient was applied to the model. The maximum Von Mises stress in the GFRP tapered plate was 14.1 MP, and occurred at the top of the GFRP tapered plate after the nighttime thermal gradient was applied to the slab. The distribution of the Von Mises stress in the GFRP tapered plate dowel was very similar to the distribution with the steel dowel as well.

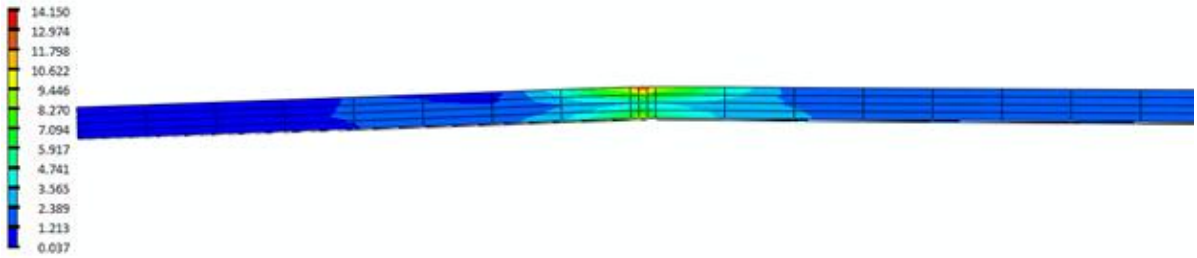

Figure 7-20 – GFRP Plate Dowel Von Mises Stress Distribution after Nighttime Thermal Gradient (MPa)

The vertical stress distribution in the concrete for the GFRP tapered plate model is presented in Figure 7-21 after the application of the nighttime thermal gradient. The maximum vertical stresses in the concrete occur at the middle of the GFRP tapered plate at the joint location. The maximum tensile vertical stress in the concrete at the joint location was 2.5 MPa, again between the mean and minimum concrete cracking strengths. A small concentration of compressive vertical stress occurs below the GFRP tapered plate at the device. Compressive vertical stress concentrations occurred above the device where the device was bearing on the concrete.

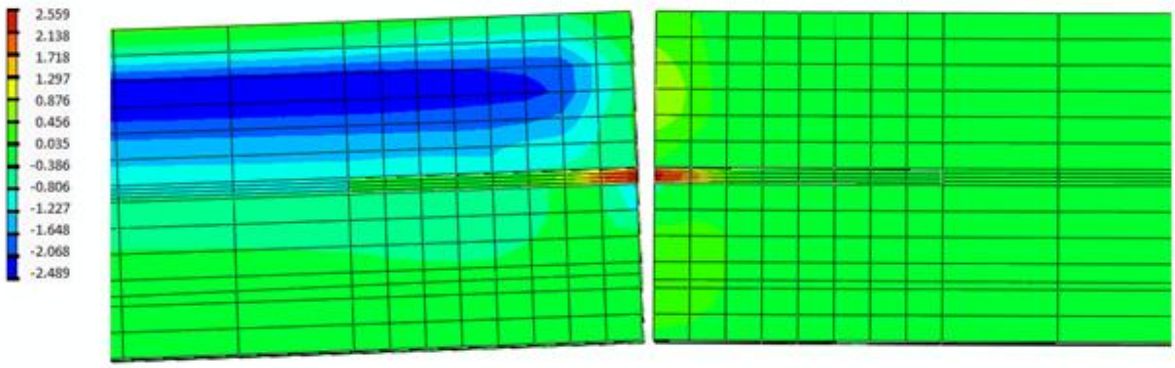

Figure 7-21 - Concrete Vertical Stress Distribution after Nighttime Thermal Gradient (MPa)

The Von Mises stress distribution in the GFRP Tapered plate is presented in Figure 7-22. The maximum Von Mises stress distribution in the GFRP tapered plate was similar to the steel dowel after the first wheel load application with the concentrations occurring on the top of the device on the loaded side and the bottom of the device on the unloaded side. The maximum Von Mises Stress in the devices is 34.6 MPa.

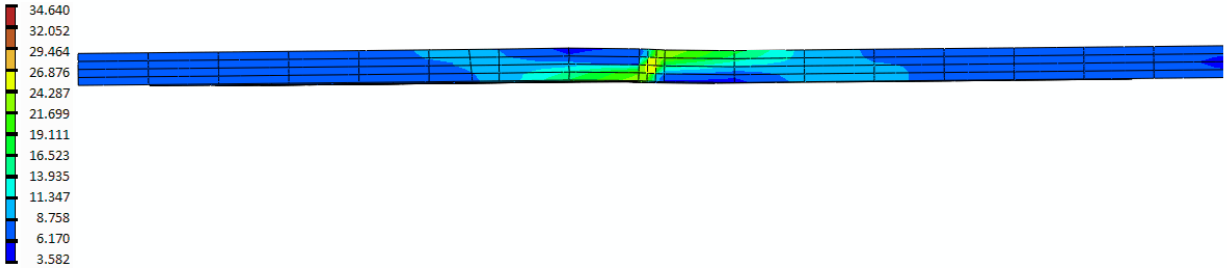

Figure 7-22 – GFRP Plate Dowel Von Mises Stress Distribution after Wheel Load Application 1 (MPa)

Vertical stress distribution in the concrete after the application of the first wheel load is presented in Figure 7-23. The maximum vertical stress in the concrete in tension occurred at the middle of the device height at the joint location. The vertical compressive stress in the concrete occurred beneath the applied load and in sections along the length of the GFRP tapered plate on the unloaded side of the dowel. The compressive stress concentration on the unloaded side of the slab below the GFRP plate dowel shows the load transfer. The behaviour of the GFRP tapered plate is similar to the dowel bar for load transfer.

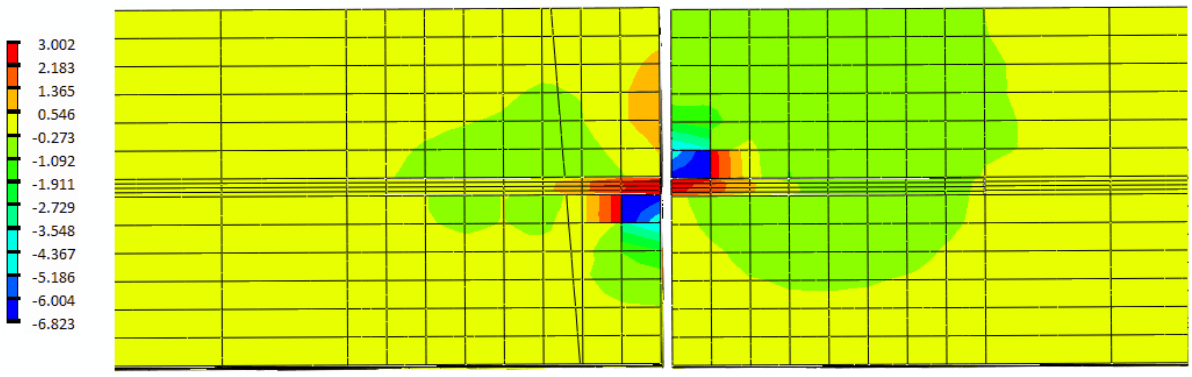

Figure 7-23 - Concrete Vertical Stress Distribution after Wheel Load Application 1 (MPa)

Figure 7-24 presents the vertical stress distribution in the base layer after the first wheel load application for the GFRP Tapered plate model. The maximum stress in the base layer is approximately 150 kPa along the edge of the loaded side of the slab where the load slab edge penetrates the most into the base layer.

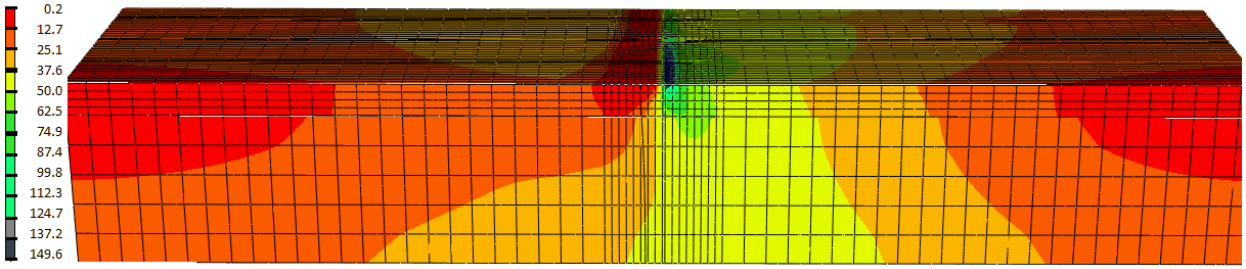

Figure 7-24 – Base Layer Vertical Stress Distribution after Wheel Load Application 1 (kPa)

Since the GFRP tapered plate dowel is not symmetric about the plane of the joint, the reversed wheel loading where the load was applied to the opposite side of the joint was also investigated.

Figure 7-25 presents the distribution of Von Mises stresses in the GFRP tapered plate dowel after the application of the second wheel load. The distribution of the stress was similar to the first side of the slab being loaded as the maximum Von Mises stress were concentrated near the joint at the top of the GFRP tapered plate on the loaded side of the joint and at the bottom on the unloaded side of the joint. The maximum Von Mises stress in the GFRP tapered plate with reversed loading applied was 32.71 MPa, which is still well below the tensile strength along the length of the device of 205 MPa. The maximum stress in the GFRP tapered plate when the load

was applied to the narrower end of the device was reduced slightly from when the load was applied to the wider side of the GFRP tapered plate. The increased bearing area on the loaded side of the slab with the wider portion of the tapered plate is assumed to attract more load transfer causing the increase in the device stresses.

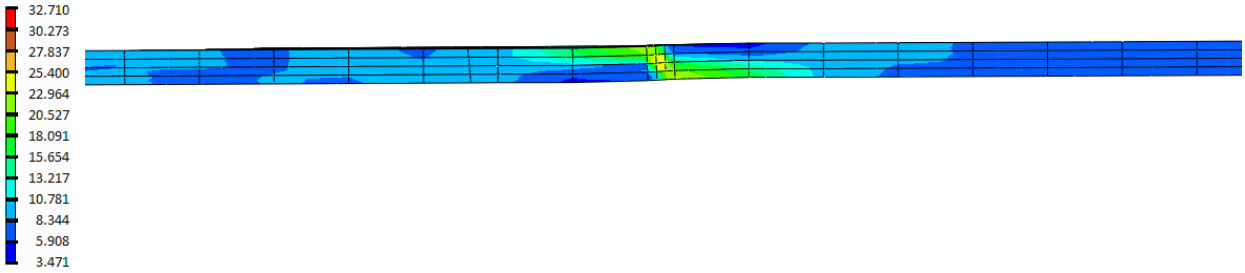

Figure 7-25 – GFRP Plate Dowel Von Mises Stress Distribution after Wheel Load Application 2 (MPa)

The vertical stress distribution in the concrete around the GFRP Tapered plate after the second wheel application is presented in Figure 7-26. As the load was applied to the other side of the slab along with a daytime thermal gradient, tensile vertical stress zones occur in the concrete at mid height of the GFRP tapered plate. The maximum tensile stress was greater than the mean cracking strength for 30 MPa concrete in this zone at 2.99 MPa. Compressive stress maximums of approximately 6 MPa occurred near the joint above the GFRP tapered plate on the loaded side and below the device on the unloaded side. A second concentration of vertical stress also occurred beneath wheel load being applied and along the length of the GFRP tapered plate where load transfer was occurring. When the load was applied to the second side of the joint, the area with high vertical tensile stress near the joint was reduced from the first side of the joint presented in Figure 7-23. The larger bearing area of the dowel on the loaded side during the first wheel load application was assumed to attract more load that caused the increased stress in the surrounding concrete.

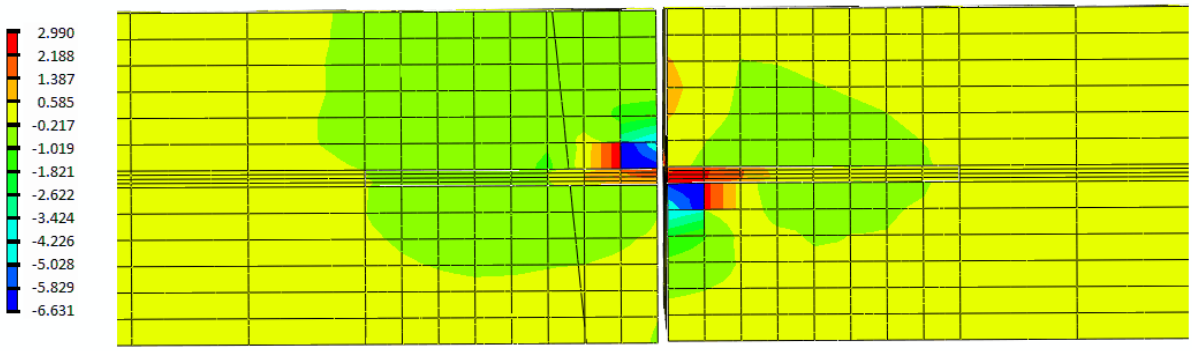

Figure 7-26 - Concrete Vertical Stress Distribution after Wheel Load Application 2 (MPa)

The third wheel load application was applied with a nighttime thermal gradient that in combination with shrinkage straining caused the slab to curl upward at the joint and the as the wheel load was applied the slab was pushed back down. The distribution of the Von Mises Stresses in the GFRP Tapered plate dowel is presented in Figure 7-27. The model failed to converge during the application of the load at a load of approximately 50 kN and results are presented for the device when the model failed to converge.

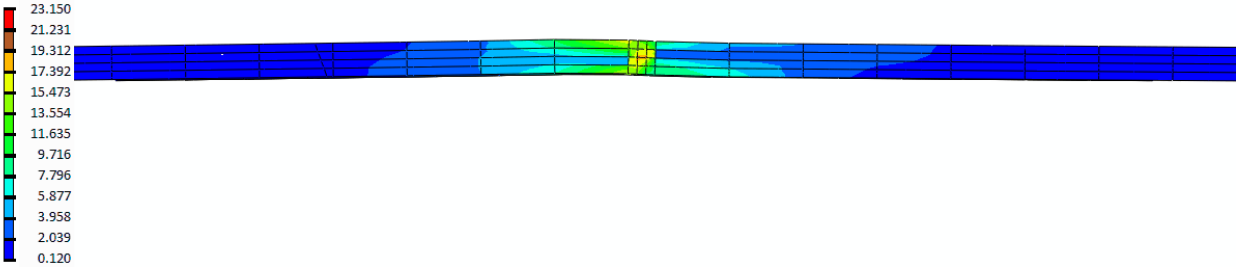

Figure 7-27 – GFRP Plate Dowel Von Mises Stress Distribution at 50 kN during Wheel Load Application 3 (MPa)

As the nighttime thermal gradient was applied to the slab, the bending of the slab was upward and opposite to that produced by the wheel loading. The maximum Von Mises stress in the GFRP tapered plate dowel was lower than the previous wheel load applications with a maximum of 23.1 MPa. The stress in the GFRP tapered plate dowel is still well below the maximum tensile strength of the device.

The vertical stress distribution in the concrete around the device as the third wheel load was applied to the slab is presented in Figure 7-28. The vertical compressive stress on the loaded side of the slab at the top of the dowel shows that a smaller concentration of stress existed after the

third wheel application compared to the second and first which is assumed to be due to the lower load level when the model failed to converge. The maximum compressive vertical stress in the concrete after the third application of load is 6.5 MPa. The distribution of tensile stress for the third application is similar to that observed for the second application; however, the concentrated tensile stress at the GFRP tapered plate joint interface was reduced due to the reduced load when the model failed to converge. The maximum tensile and compressive stresses in the concrete do not suggest that the slab should be failing at this load level as the stresses are reduced compared to previous load applications when the model failed to converge at 50 kN wheel loading.

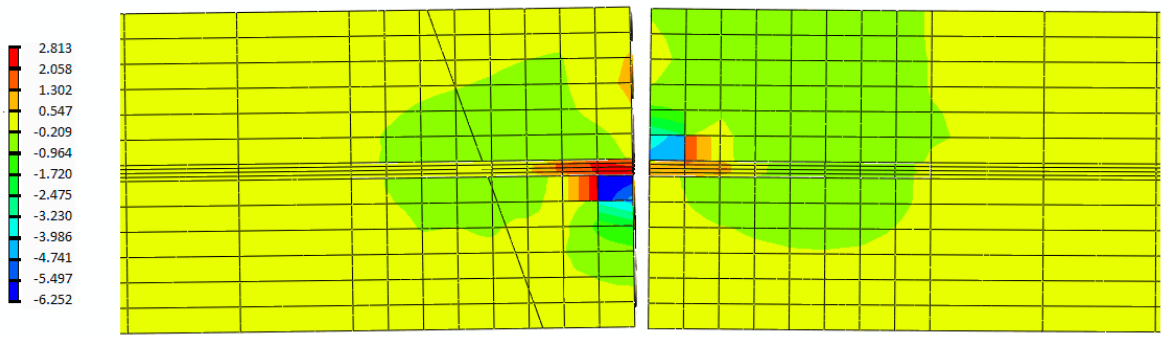

Figure 7-28 - Concrete Vertical Stress Distribution at 50 kN durin Wheel Load Application 3 (MPa)

The GFRP tapered plate section appears to transfer load and behave similarly to conventional steel dowels. As the service loads are applied to the slab, there does not appear to be a benefit to the tapered shape of the device as the device still causes stress concentrations to occur in the concrete near the device during thermal and shrinkage gradient applications. The curling in the slab still causes the device to bend and cause stress concentrations around the device. Although the device is able to come out of one side of the pocket, the opposite side is locked and additional bearing forces exist here where the device is restrained. The results indicate the device is capable of behaving similarly to steel dowels. Based on the results it appears a thicker plate section would produce behaviour more similar to the 32 mm steel dowels.

7.5 GFRP I-beam Service Load Finite Element Results

A quarter slab model with three and a half GFRP I-beams spaced at 450 mm was analyzed with the service loading sequence described in Table 7-1, except the model failed to converge at approximately 74 kN wheel load during the third load application. Similar to the tapered plate

dowel and the conventional steel dowel, a detailed investigation of the stresses in the device and concrete around the device at each strain/load increment is presented in this Section.

Figure 7-29 presents the top of slab deflection for either side of the joint for the GFRP I-beam quarter-slab model subjected to the service loading history shown in Table 7-1.

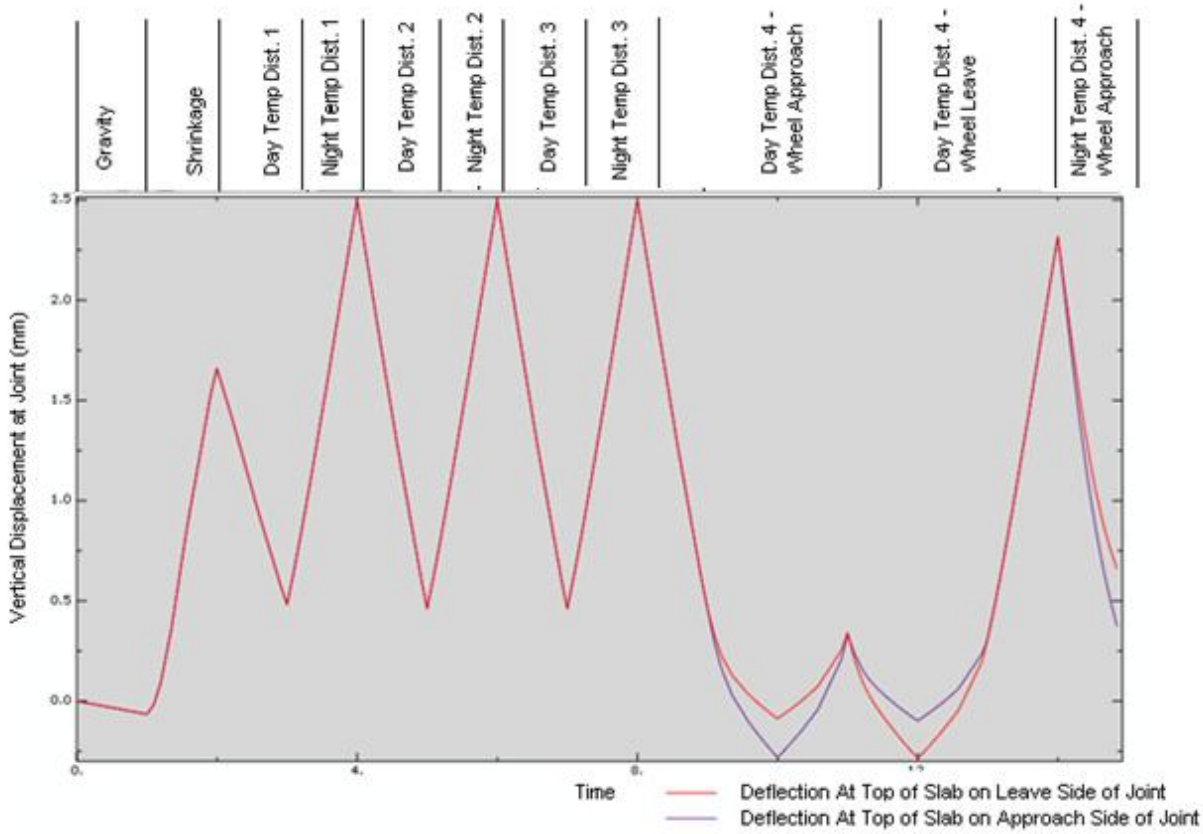

Figure 7-29 – GFRP I-beam Model: Top of Slab Service Joint Deflection History

The deflection of the GFRP I-beam model on either side of the joint is very similar to the conventional steel dowels and the GFRP plate dowels. The maximum curling deflection at the top of the slab was approximately 1.6 mm after the application of shrinkage. After the thermal daytime temperature gradient was applied the deflection at the top of the slab was reduced to 0.5 mm of upward curling. The upward curling then increased to 2.5 mm after the application of the thermal nighttime gradient. After the wheel loads were applied along with the daytime gradient, the differential deflection is approximately 0.12 mm. There was not any noticeable degradation in the joint behaviour over the service loading history.

The distribution of Von Mises stress in the GFRP I-beam after the application of the shrinkage straining is presented in Figure 7-30. The maximum Von Mises stress in the top and bottom flanges of the GFRP I-beam after the shrinkage strains were applied was approximately 15 MPa which is much below the failure strength in tension along the length of the device of 205 MPa. The highest Von Mises stress concentration was centered on the joint in the top and bottom half of the device. There was larger concenetration of stress in the top portion of the GFRP I-beam as noticed in Figure 7-30. It is assumed that the additional stressing in the top portion of the GFRP I-beam is due to the slab restraining both faces of the top flange of the beam as the slab curls due to shrinkage, where the bottom flange is only restrained at the top where the concrete lifts away from the device.

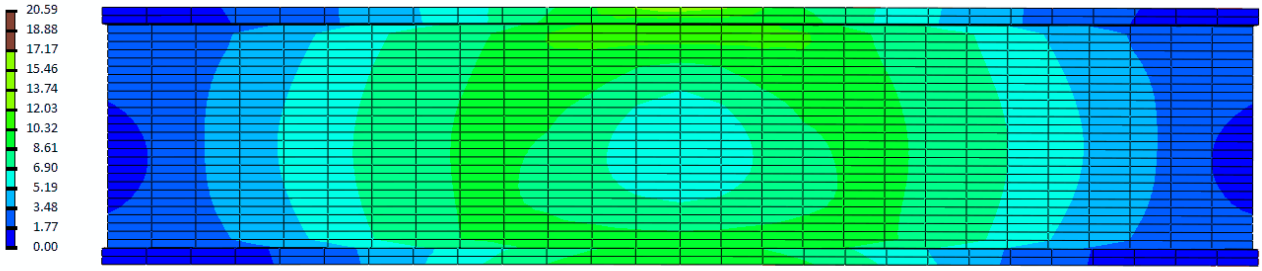

Figure 7-30 – Device Von Mises after Shrinkage Application (MPa)

Figure 7-31 presents the distribution of vertical stress in the concrete after the application of shrinkage strains. A long narrow band of tensile vertical strains existed in the concrete along the opening of the top flange of the GFRP I-beam. Restraint to shrinkage in the GFRP I-beam is only provided at the top flange as the concrete is able to curl away from the bottom flange. As the concrete tries to curl upward the GFRP I-beam top flange bears on the concrete to restrain the curling at the joint location causing high tensile stress concentrations at the sides of the top flange. As previously noticed in the load transfer study, the top flange of the GFRP I-beam behaved similarly to a conventional dowel bar and the concentration of tensile vertical stress in the concrete suggests that as shrinkage is applied the top flange acts similar to a conventional dowel. The maximum tensile stress is 3 MPa which is higher than for conventional steel dowels and GFRP plate dowels for the shrinkage step and is greater than the mean tensile strength of 30 MPa concrete. Compressive vertical stress concentrations exist on both sides of the joint below the top flange with a maximum compressive vertical stress after shrinkage of 8.8 MPa.

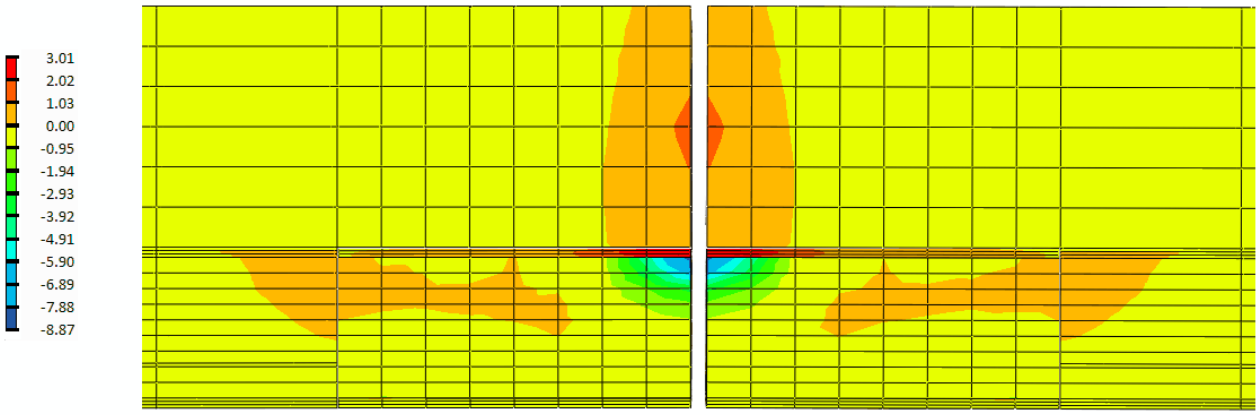

Figure 7-31 – Concrete Vertical Stress Distribution after Shrinkage Application (MPa)

Figure 7-32 presents the Von Mises stress distribution in the GFRP I-beam after the daytime thermal gradient is applied to the model. The maximum Von Mises stress occurs in the bottom flange at the joint location. The increased stress in the bottom of the GFRP I-beam occurred because the daytime thermal gradient causes downward curling. The location of the device relative to the middle of the slab is assumed to increase the daytime thermal gradient behaviour in the device. The Von Mises stress distributed away from the highest stress gradually. The distribution of the Von Mises stress in the GFRP I-beam after the nighttime thermal gradient was not presented here as the distribution was similar to that observed after shrinkage, with the maximum Von Mises stress increased to 29.1 MPa after the nighttime thermal gradient was applied.

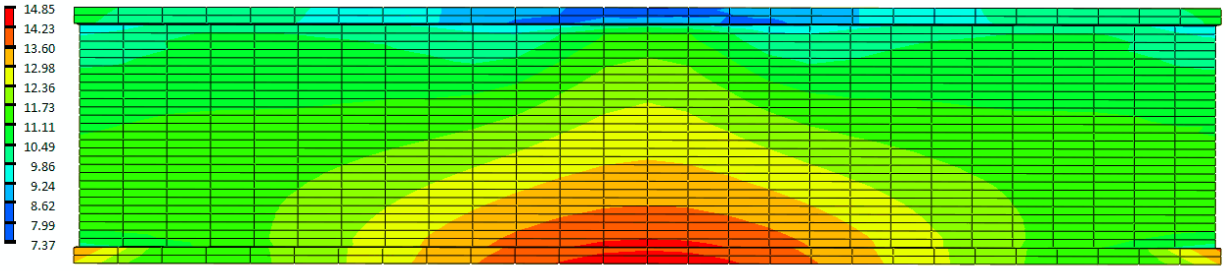

Figure 7-32 – GFRP I-beam Von Mises Stress Distribution after Daytime Thermal Gradient (MPa)

The vertical stress distribution in the concrete around the GFRP I-beam after the daytime thermal gradient is applied to the model is presented in Figure 7-33. As the daytime thermal gradient was

applied, the maximum vertical stress concentration at the middle of the top flange at the joint location was reduced in size and the maximum vertical stress in the concrete decreased to 2.6MPa compared to the shrinkage step. The thermal gradient causes curling in the opposite direction to shrinkage with a similar deflection, hence, the stress concentrations are in the same location but reduced. A small amount of vertical tensile stress occurs between the flanges of the GFRP I-beam near the ends of the section. Compressive stress concentrations occur below the top flange at the joint with a maximum of 3 MPa.

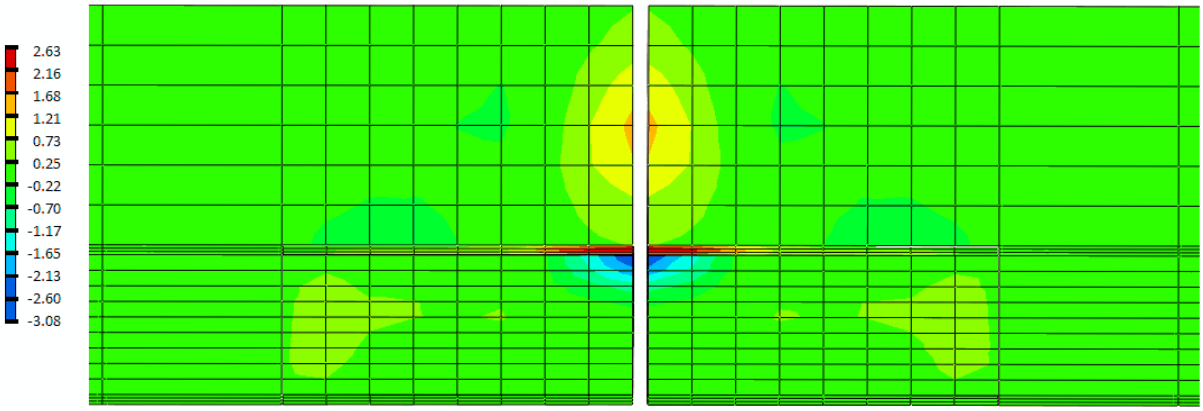

Figure 7-33 – Concrete Vertical Stress Distribution after Daytime Thermal Gradient (MPa)

The distribution of vertical stress in the concrete around the GFRP I-beam after the application of the nighttime thermal gradient is presented in Figure 7-34. Tensile vertical stresses were concentrated at the top flange near the joint location with maximum tensile stresses of 3 MPa which is greater than the mean cracking strength of 30 MPa concrete. Vertical compressive stress concentrations exist in the concrete below the top flange of the device.

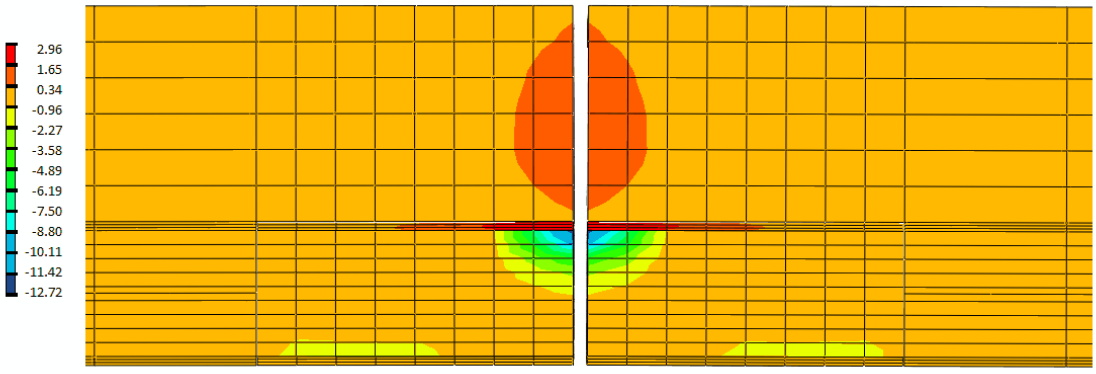

Figure 7-34 - Concrete Vertical Stress Distribution after Nighttime Thermal Gradient (MPa)

Figure 7-35 presents the Von Mises stress distribution in the GFRP I-beam after the first application of the wheel load in the service load history (Table 7-1). A concentration of Von Mises stress in the GFRP I-beam occurred at the joint location in the web of the GFRP I-beam. Also, higher Von Mises stress occurred on the top of the GFRP I-beam on the loaded side of the slab and bottom of the unloaded side of the slab. The maximum Von Mises stress in web at the joint location was 35.6MPa which is much lower than the tensile strength of the device along the length of the device but is beyond the shear failure strength of 31 MPa.

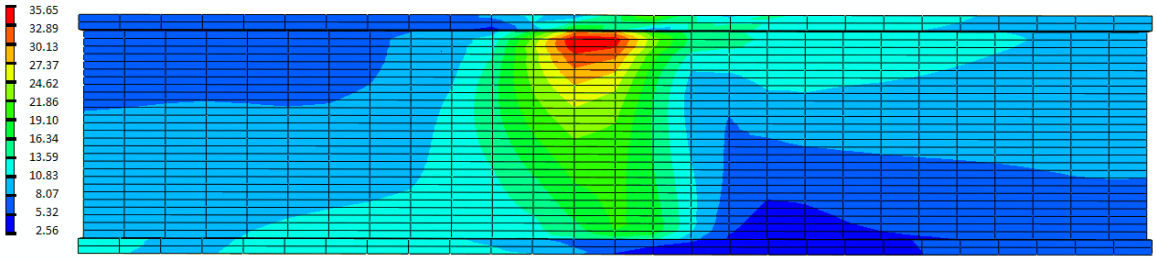

Figure 7-35 – GFRP I-beam Von Mises Stress Distribution after Wheel Load Application 1 (MPa)

The vertical stress distribution in the concrete after the first wheel application is presented in Figure 7-36. As expected from the wheel load transfer analysis, the top flange behaved similarly to the conventional steel dowel with concentrations of vertical compressive stress above the top flange on the loaded side of the device and below the top flange on the unloaded side of the joint. A third concentration of vertical compressive stress also was present on loaded side of the joint above the bottom flange. On the loaded side of the slab, wheel load directly bears on the bottom flange causing this stress concentration and a concentration of stress in the base layer is expected as well.

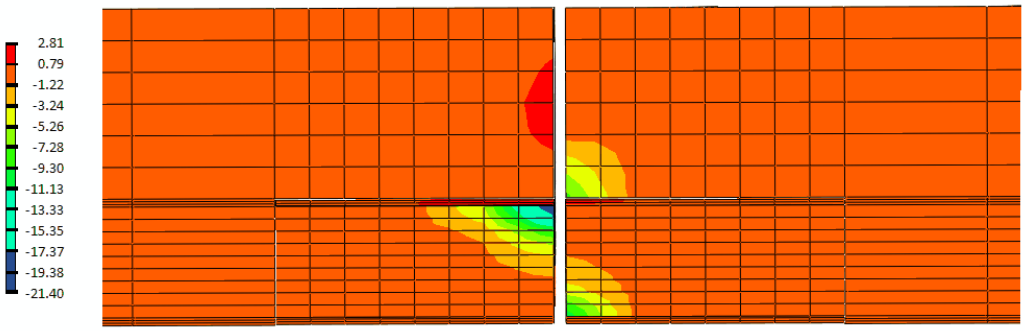

Figure 7-36 - Concrete Vertical Stress Distribution after Wheel Load Application 1 (MPa)

Figure 7-37 presents the distribution of vertical stress in the base layers after the first application of the wheel load in the GFRP I-beam model. The GFRP I-beam increased the stress locally where the bottom flange of the GFRP I-beam is in contact with base layer. There was also a concentration of stress along the slab edge consistent with that observed for both the GFRP tapered plate and conventional dowels. The maximum vertical stress in the base layer was 214 kPa, which was increased from the conventional dowel bar model. The bottom flange of the GFRP I-beam in direct contact with the base layer causes the increase in stress in the base layer because the base is providing support to the device directly instead of the concrete.

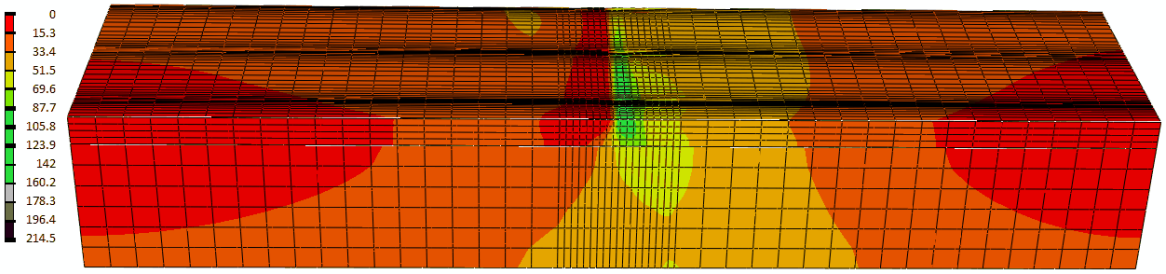

Figure 7-37 – Base Layers Vertical Stress Distribution after Wheel Load Application 1 (kPa)

The second wheel load application had similar stress distributions to those presented above with stress reversals due to the load being applied to the other side of the joint. The GFRP I model failed to converge during the third application of the wheel load. The plastic strain distribution in the concrete around the device before the model failed to converge is presented in Figure 7-38. Plastic compressive straining has occurred below the top flange of the GFRP I-beam as can be seen in Figure 7-38. Plastic tensile straining occurred at the edge of the GFRP I-beam flange. Plastic straining is limited with the GFRP I-beam to the areas immediately adjacent the joint. The local compressive plastic straining below the flange will cause a weakened support of the device and may cause minimal increased differential deflection due to the plastic straining that has occurred in the concrete bearing surface. Excessive compressive damage could cause a complete loss of support of the device below but it is expected that the tensile plastic strains at the edges of the top flanges will cause excessive cracking to occur which will result in the failure of the device.

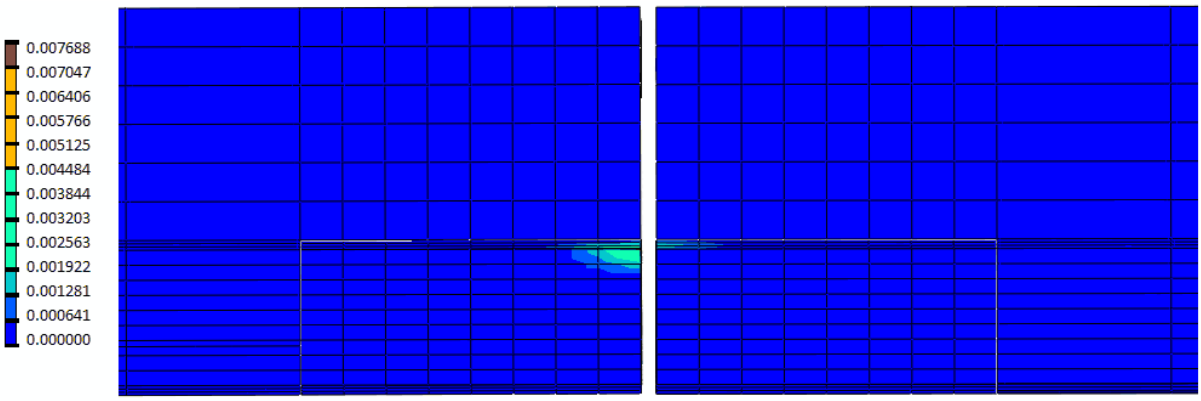

Figure 7-38 – Plastic Straining in Concrete after Wheel Load Application 3 (MPa)

Failure under service loading occurred for the GFRP I-beam due to excessive compressive and tensile plastic straining in the concrete. Although the GFRP I-beam was capable of transferring loads and maintaining the joint deflection, the size of the device used in the models does not appear to be adequate for wheel loading under service conditions. It could be possible to further reduce the spacing of the devices to 300 mm in order to reduce the maximum stress in the concrete at the top flanges and reduce concrete plastic straining. The flat thin top flange will still cause large stress concentrations at the edge of the devices adjacent the bearing surface even with a different spacing. Increasing the top flange or rounding the top flanges to reduce stress concentrations could be completed to reduce the plastic straining occurring in the concrete at this location.

7.6 Horizontal V Service Load Finite Element Results

The Horizontal V continuous load transfer device (see Section 3.3.1 for details) was analyzed in the quarter slab model with service loading history described in Table 7-1. A detailed investigation into the stress around the joint is presented in this section to determine the feasibility of implementing the Horizontal V device in pavement applications.

The top of slab deflection on either side of the joint for the Horizontal V device model subjected to the service loading history is presented in Figure 7-39. The top of slab deflection during the shrinkage and thermal gradients varies slightly on either side of the joint for each load application. The average top of slab curling for shrinkage, daytime and nighttime strain gradients are 1.6, 0.125, and 2.25 mm respectively. During the simultaneous daytime thermal gradient and

wheel load application, the differential deflection at the joint is less than 0.06 mm; however under nighttime thermal gradient and wheel loading the differential deflection is greater than 0.5 mm. The sliding of the slabs along the faces of the device allows shrinkage and thermal gradients to curl freely from the joint face and a gap forms at the joint. When the downward daytime thermal gradient is applied there is little or no gap at the device concrete interface allowing for a adequate load transfer to occur. During nighttime thermal gradient the upward curling and slipping at the joint concrete interface allows the slab and device to not be in contact and no load transfer occurs until the slab and device come in contact. There is also noticeable additional deflection on the nighttime wheel loading increments after the unloaded slab remains lower after the wheel application. The geometry of the device and slip surfaces at the joint are assumed to cause the differential deflection that is still present after the wheel loading is removed.

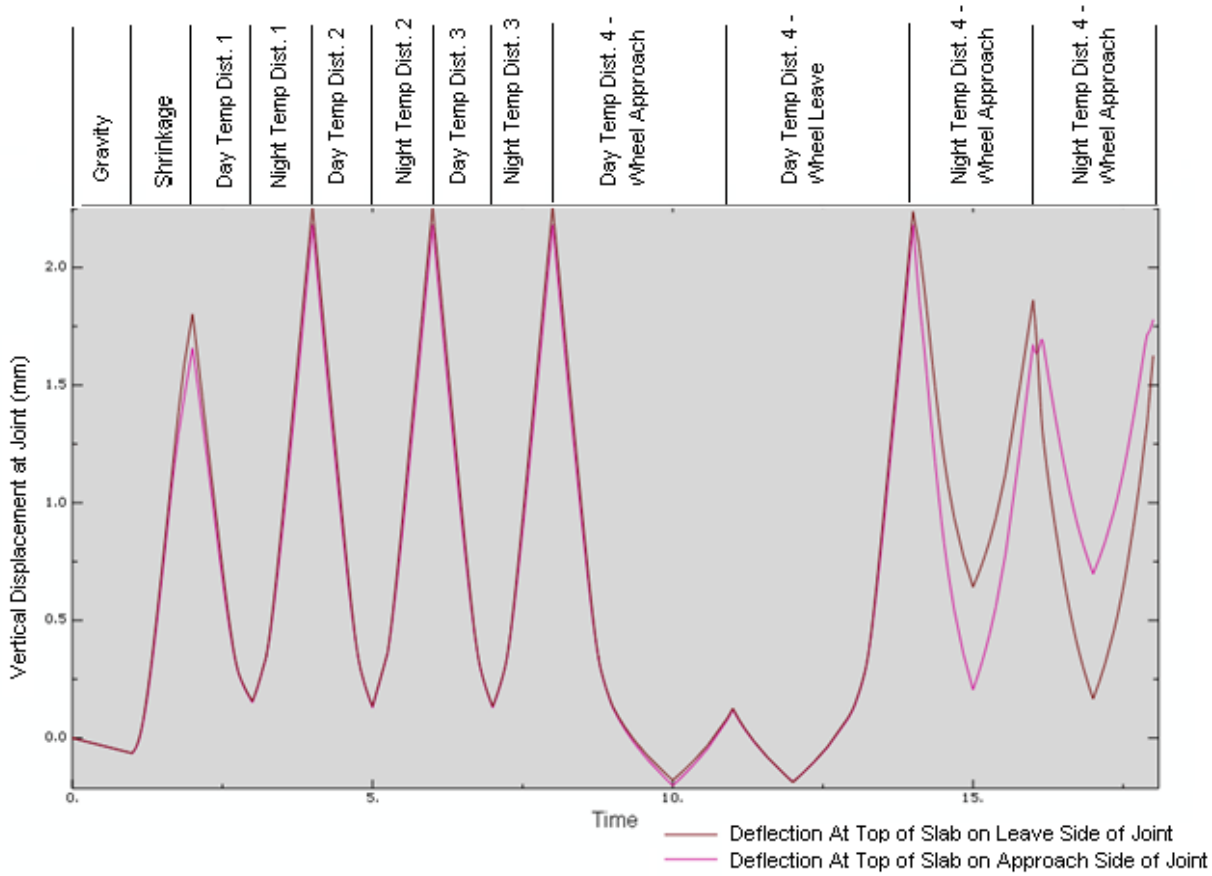

Figure 7-39 – Horizontal V Top of Slab Deflection

The Von Mises Stress distribution in the Horizontal V device after the application of the shrinkage strains is presented in Figure 7-40. The stress in the device was very low after

shrinkage straining was applied, with a maximum Von Mises stress of 0.69 MPa. This suggests that the device is not restraining the shrinkage from occurring.

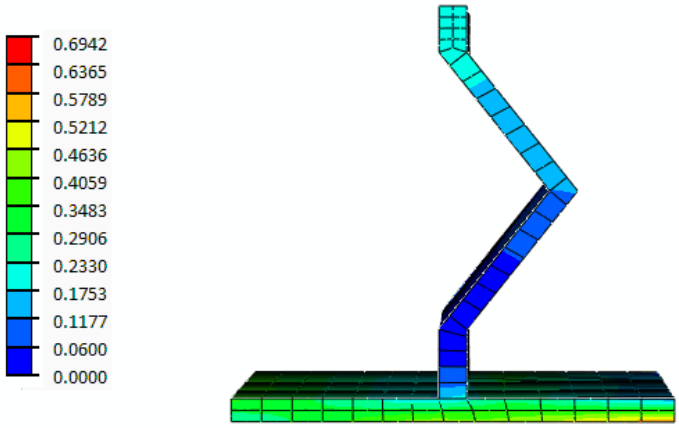

Figure 7-40 – Horizontal V Von Mises Stress Distribution after Shrinkage (MPa)

Figure 7-41 presents the vertical stress in the concrete after the application of the shrinkage loading. The maximum vertical tensile stress concentration occurred at the top of the Horizontal V leg and concrete interface. This location would be expected as the slab tries to curl upward due to shrinkage straining the inside of the V shape bears on the device directly to the other side of the slab that cause the tensile splitting stress at the top of the V. The maximum vertical tensile stress was 2.35 MPa, which is greater than the minimum tensile cracking strength of concrete of 1.98 MPa. Tensile vertical stress in the concrete ranging from 0 to 0.6 MPa was present along both sides of the Horizontal V on either side of the slab. Compressive vertical stresses concentrations developed approximately 200 mm from the joint on either side of the joint beyond the device limits. The restraint of curling caused by the V shape causes the two compressive stresses on either side of the joint.

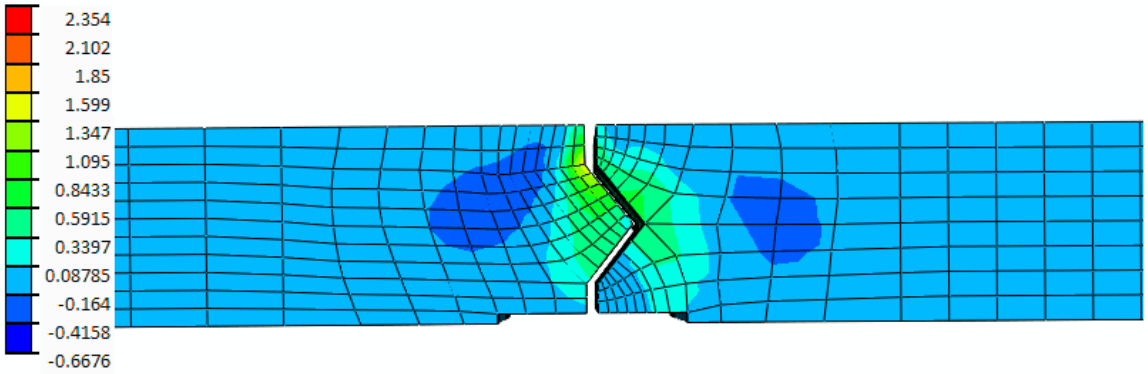

Figure 7-41 – Concrete Vertical Stress Distribution after Shrinkage (MPa)

Figure 7-42 presents the Von Mises stress distribution in the Horizontal V device after the application of the thermal daytime gradient. The maximum Von Mises stress in the Horizontal V is 3 MPa. The daytime thermal gradient is causing the slabs to curl and the bottom Horizontal V leg has the highest stress concentration due to the curling occuring. The slab geometry on the right hand side of the device, shown in Figure 7-42, is assumed to cause the device to bend towards the right as the slab tries to curl upward and bears on the device.

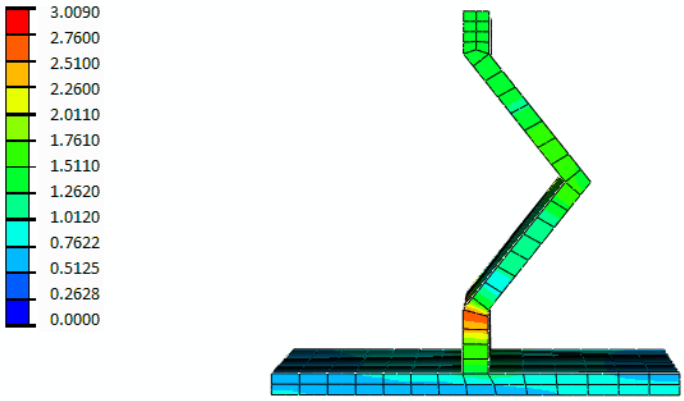

Figure 7-42 – Horizontal V Von Mises Stress Distribution after Daytime Thermal Gradient (MPa)

Figure 7-43 presents the vertical stress distribution in the concrete at the Horizontal V joint with the daytime thermal gradient applied to the model. Vertical compressive stress concentrations

occur inside the middle the V as well as below the bottom leg at the end of the bottom leg. Tensile vertical stress concentrations occur at the bottom of the V and at the top of the V above the V of the horizontal leg which can be seen in Figure 7-43. The maximum vertical tensile and compressive stresses in the concrete are 2.3MPa and 2.1 MPa respectively.

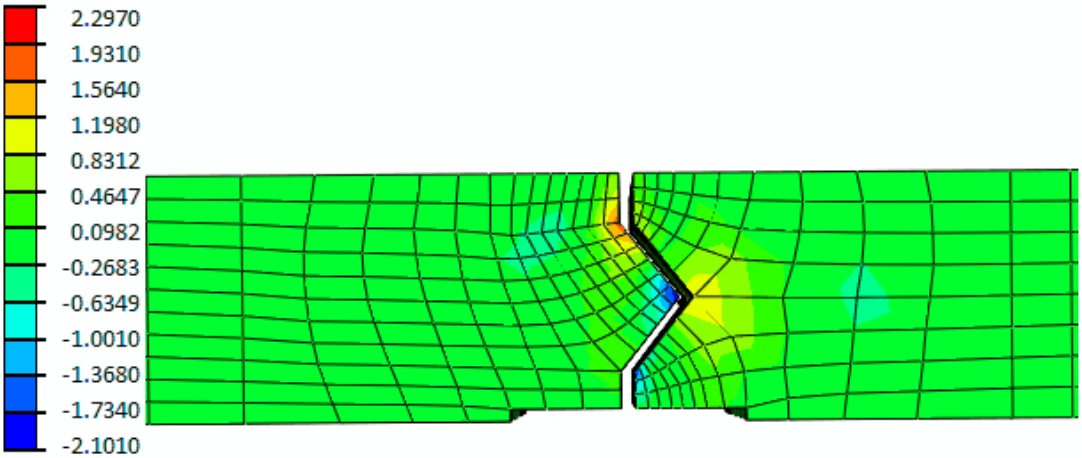

Figure 7-43 - Concrete Vertical Stress Distribution after Daytime Thermal Gradient (MPa)

The distribution of Von Mises Stress in the Horizontal V device after the application of the nighttime thermal gradient is presented in Figure 7-44. The maximum Von Mises stress in the device was still relatively low at 2.4 MPa located near the bottom of the device. The nighttime thermal gradient caused the slabs to curl upwards, compressing the device at this location while the remainder of the device would be unloaded as the top portion of the joint opens and the concrete pulls away from the device and sawcut.

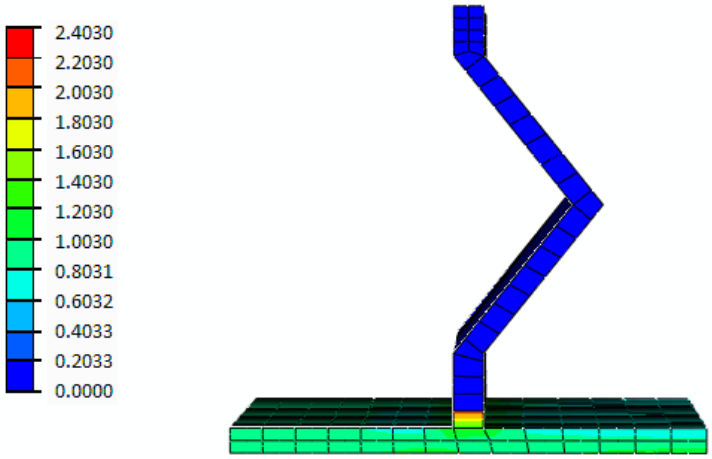

Figure 7-44 - Device Von Mises Stress Distribution after Nighttime Thermal Gradient (MPa)

Figure 7-45 presents the distribution of vertical stress in the concrete around the device after the nighttime thermal gradient was applied to the slab. The general distribution was similar to the response presented in Figure 7-41 for shrinkage as the general upward curling action was similar. The maximum tensile vertical stress in the concrete was 2.15 MPa after the application of the nighttime thermal gradient, which is slightly greater than the minimum cracking strength for 30 MPa concrete.

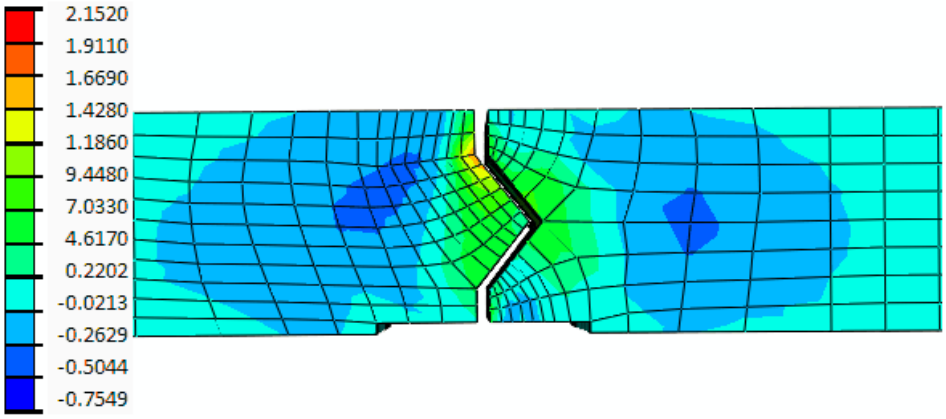

Figure 7-45 - Concrete Vertical Stress Distribution after Nighttime Thermal Gradient (MPa)

The Von Mises stress distribution in the Horizontal V device is presented after the first wheel load application in Figure 7-46. The maximum Von Mises stress in the Horizontal V device

remained low even after the first application of the wheel load with a maximum Von Mises stress of 3.79 MPa. The stress concentrated in the device around the corners of the device legs.

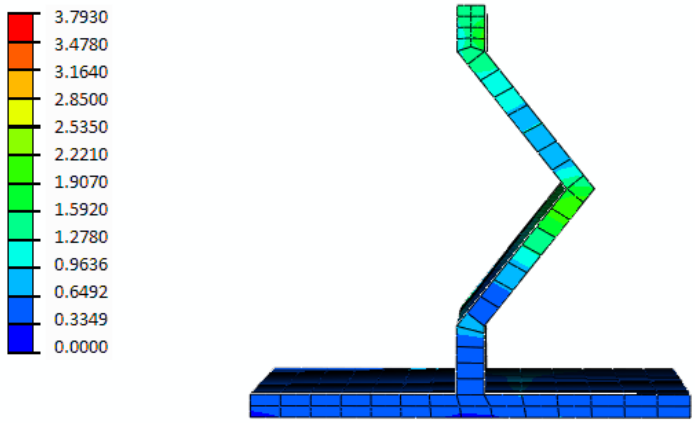

Figure 7-46 – Horizontal V Von Mises Stress Distribution after Wheel Load Application 1 (MPa)

The vertical stress distribution in the concrete around the Horizontal V device after the first wheel load application is presented in Figure 7-47. Tensile vertical stress exists in the concrete at the bottom of the V on the opposite side of the load application. The maximum tensile stress is 2.66 MPa at this location which is greater than the minimum cracking strength of 30 MPa and is approaching the mean cracking strength of 2.91 MPa. Maximum vertical compressive stress in the concrete is 2.47 MPa and is on the other side of the joint from the maximum tensile on the interior portion of the Horizontal V device.

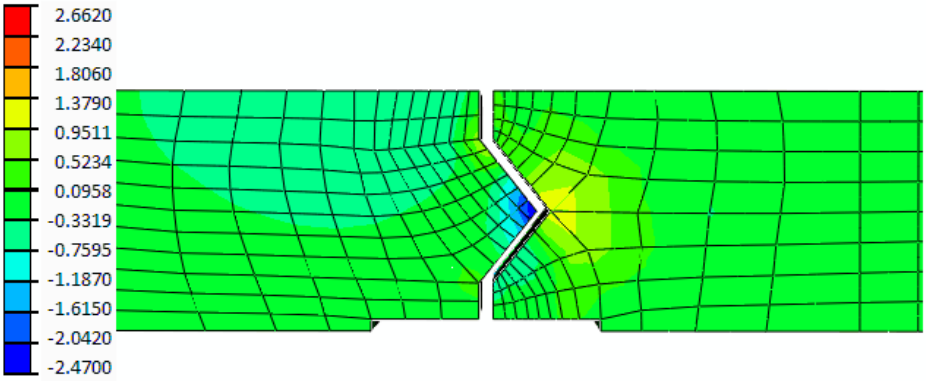

Figure 7-47 - Concrete Vertical Stress Distribution after Wheel Load Application 1 (MPa)

The distribution of the vertical stress in the base layers after the first wheel load application with the Horizontal V device is presented in Figure 7-48. The maximum vertical stress in the base layer was 186 kPa for the Horizontal V device after the first wheel load application, which is approximately 50% greater than that observed with conventional round steel dowel bars (Figure 7-10). This suggests that the device is not transferring as much load as conventional steel dowels. The device is also bearing directly on the base material which lowers the spreading to the base material through the concrete at the joint that occurs with conventional steel dowels.

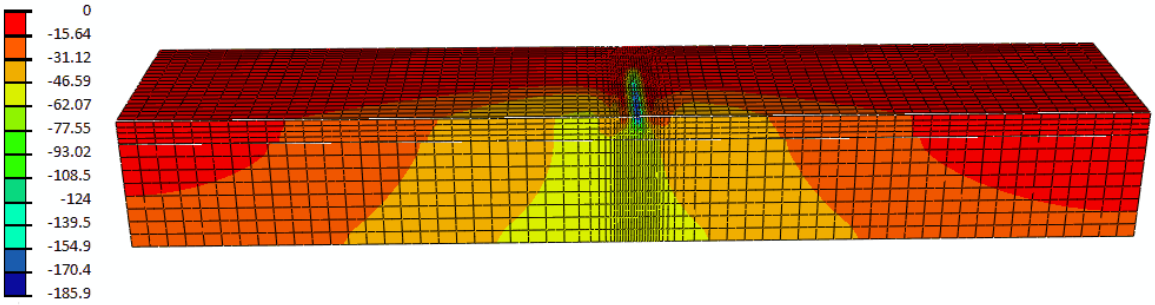

Figure 7-48 – Base Layer Vertical Stress Distribution after Wheel Load Application 1 (kPa)

Figure 7-49 presents the distribution of Von Mises Stress on the Horizontal V device after the second application of the wheel load. The maximum Von Mises stress in the Horizontal V device was 3.8 MPa. As expected, on the loaded side of the slab (on the right in Figure 7-49), the concrete above the top leg of the V bears on the device causing stress concentration in this leg of the device. The lower leg of the device does not have a bearing surface with the loaded side of the slab and hence little stress is concentrated in this flange during the wheel load application.

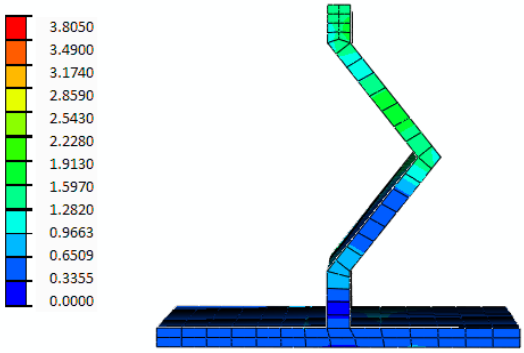

Figure 7-49 – Horizontal V Von Mises Stress Distribution after Wheel Load Application 2 (MPa)

Figure 7-50 presents the vertical stress distribution in the concrete after the second wheel load application was applied to the model. Vertical compressive stress concentration occurs under the applied wheel load and along the face of the joint. The Horizontal V surface causeed concentration of compressive vertical stress on the other side of the joint inside the middle of the V shape. The maximum tensile vertical stress in the concrete was 2.66 MPa and was concentrated on the unloaded side of the joint at the top of the top leg of the V shape as presented in Figure 7-50. The distribution of stress at either side of the point of the V shape was similar to when the load was applied to the other side of the slab; however, a tensile concentration occured at the top leg of the V on the unloaded side of the slab. There was also no clear compressive zone on the unloaded side of the joint beneath the bearing face of the V (see Figure 7-47). It appears that majority of the load transfer on the pointed side of the slab occurs directly at the point of the V shape, whereas on the indented side of the slab the transfer occurs across the top leg of the V shape.

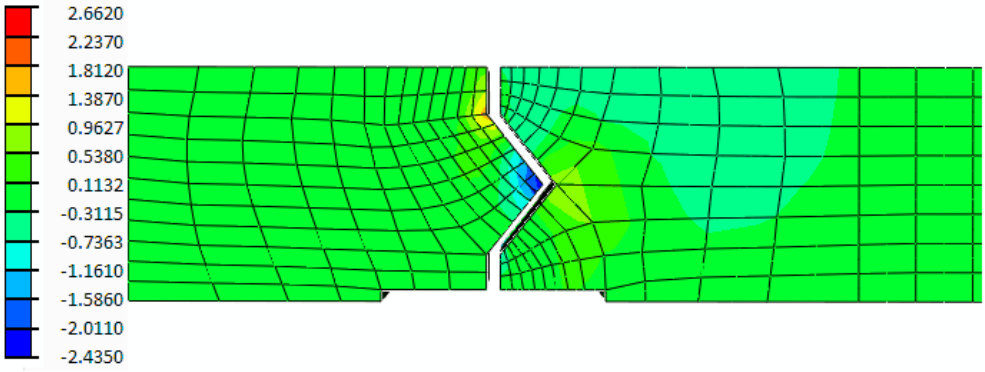

Figure 7-50 - Concrete Vertical Stress Distribution after Wheel Load Application 2 (MPa)

The vertical stress distribution in the base layer after the second wheel load application for the Horizontal V device is presented in Figure 7-51. A similar distribution and maximum stress in the base layer occurs on after the second wheel load application as the first. The maximum stress in the base layer is 185.7 kPa after the second wheel load application.

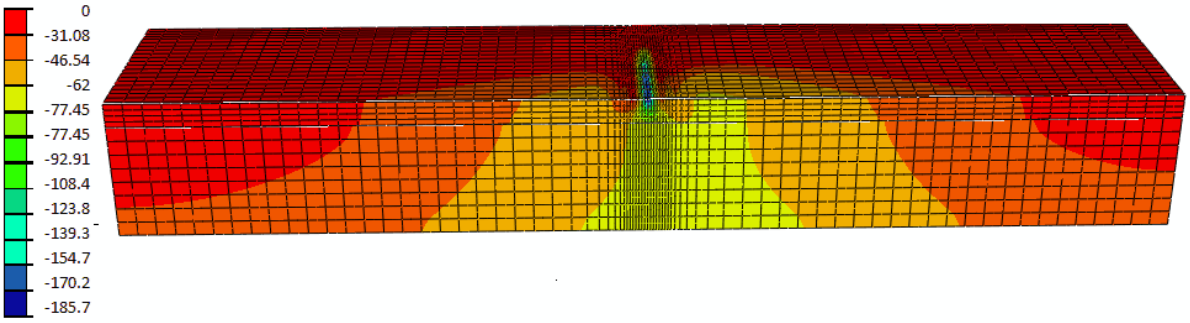

Figure 7-51 - Base Layer Vertical Stress Distribution after Wheel Load Application 2 (kPa)

Figure 7-52 presents the distribution of the Von Mises stress in the Horizontal V device after the third wheel load application along with the nighttime thermal gradient. The maximum Von Mises stress in the Horizontal V device is 2.09 MPa at the bottom of the Horizontal V leg which is lower than predicted Von Mises maximums in the device for daytime thermal gradients and wheel loading. The rest of the Horizontal V device had very low Von Mises stress (less than .17 MPa). The main portion of the device has a much lower stress distribution than when wheel loading was applied with daytime thermal gradients.

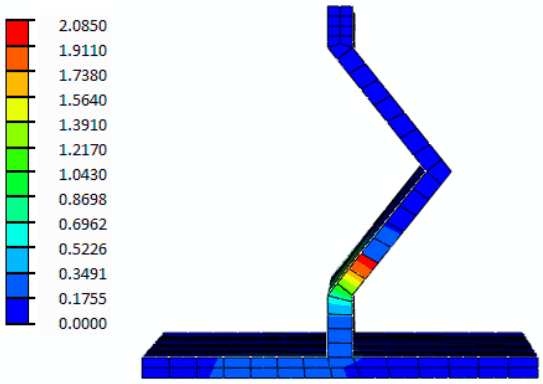

Figure 7-52 – Horizontal V Von Mises Stress Distribution after Wheel Load Application (MPa)

Figure 7-53 presents the vertical stress distribution in the concrete after the third wheel load application in the Horizontal V model. Compressive stress maximums of 1.02 MPa occurred on the unloaded side of the joint at the bottom leg of the Horizontal V concrete interface. This maximum vertical compressive, 1.02 MPa, is lower than when the load was applied to the same side of the joint with daytime thermal gradient, 2.47 MPa. Tensile vertical stresses in the

concrete developed on either side of the device during the third wheel load application. The maximum tensile vertical stress in the concrete was 2.09 MPa which is less than daytime thermal gradient applied simultaneously with the wheel load on the same side of the joint. Reduced maximum vertical concrete stresses in both tension and compression under wheel loading with the nighttime thermal gradient is expected as the slab edges curl away from the device and initial wheel loading counteracts this before contact is established at the bearing surface.

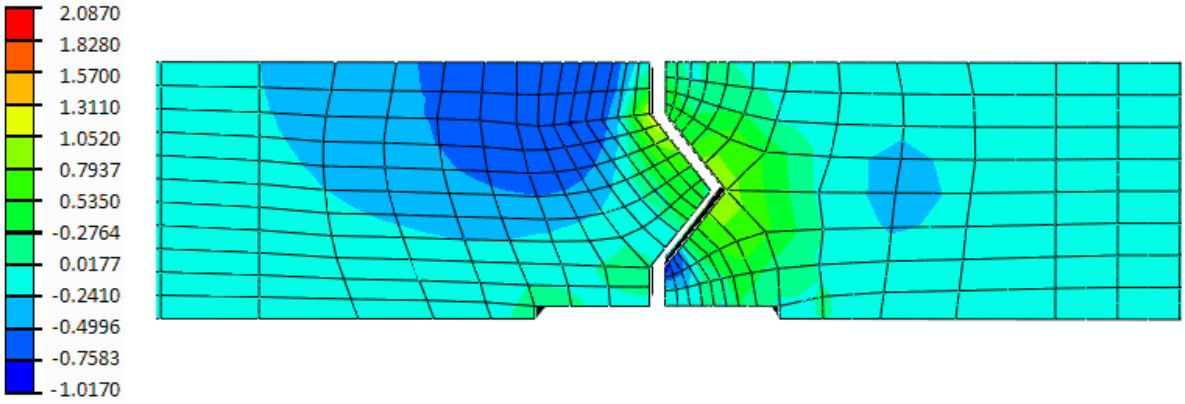

Figure 7-53 - Concrete Vertical Stress Distribution after Wheel Load Application 3 (MPa)

Figure 7-54 presents the vertical stress distribution in the base layer after the third application of the wheel load in the Horizontal V model. The vertical stress was reduced to a maximum of 77.56 kPa as the thermal gradient before the wheel load curls the slab upward which is very similar to the maximum observed in the dowel bar model for nighttime thermal gradient and wheel load applied simultaneously, 71 kPa.

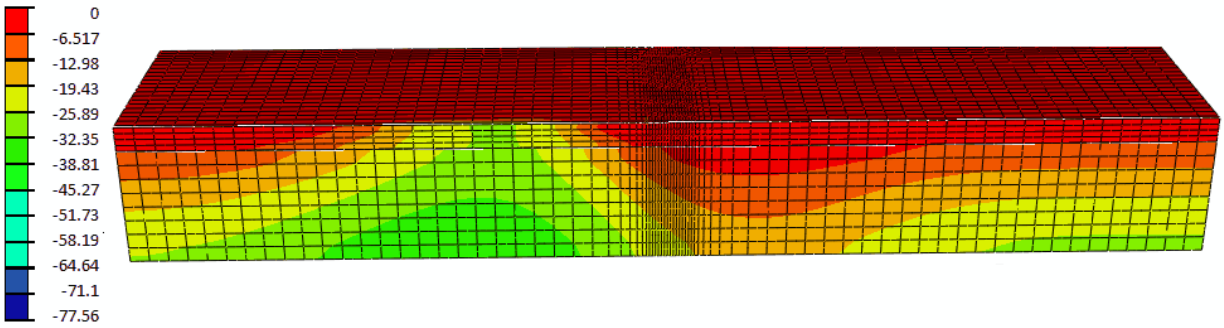

Figure 7-54 - Base Layer Vertical Stress Distribution after Wheel Load Application 3 (kPa)

Figure 7-55 presents the distribution of the Von Mises stress in the Horizontal V device after the fourth wheel load application. A maximum stress of 1.42 MPa was concentrated on the top leg of the Horizontal V near the point of the V shape. The Von Mises stresses in the remaining portion of the Horizontal V were relatively low. This stress concentration would be expected based on the wheel load transfer occurring mainly through the bottom leg of the V shape and the downward curling of the other side of the slab due to nighttime thermal gradient.

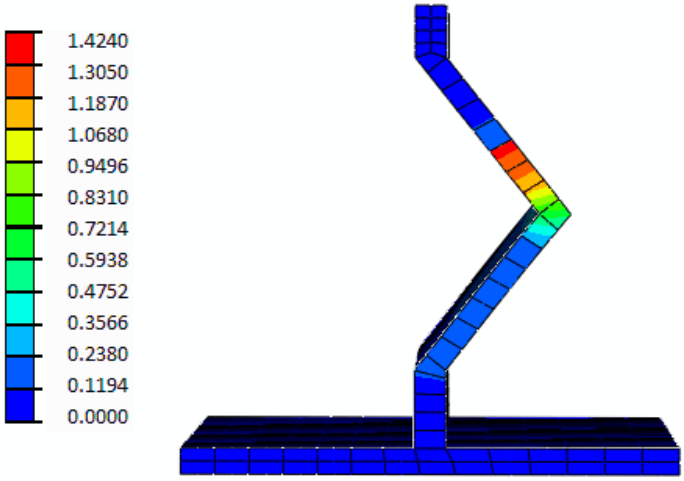

Figure 7-55 – Horizontal V Von Mises Stress Distribution after Wheel Load Application 4 (MPa)

The vertical stress distribution in the concrete around the Horizontal V device is presented in Figure 7-56. A vertical tensile stress concentration was present at the top leg of the Horizontal V device on the unloaded similar to when the load was applied to the same side of the joint with a daytime thermal gradient was applied. A small concentration of compressive vertical stress developed in the concrete inside the V, as noticeable in Figure 7-56. This concentration of compressive stress was reduced under nighttime thermal gradient when compared to daytime thermal gradient. The compressive vertical stress distribution on either side of the joint was similar just beyond the load and joint location.

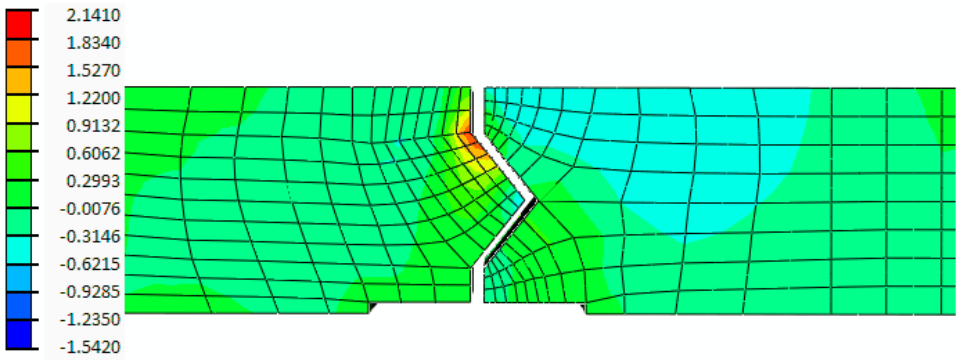

Figure 7-56 - Concrete Vertical Stress Distribution after Wheel Load Application 4 (MPa)

Figure 7-57 presents the distribution of the vertical stress in the base layers of the Horizontal V device after the fourth application of the wheel load. The maximum stress was similar to the third application and so is the distribution. The maximum vertical stress away from the joint was 78.5 kPa again similar to the maximum for dowel bar wheel loading and nighttime thermal gradient of 71 kPa.

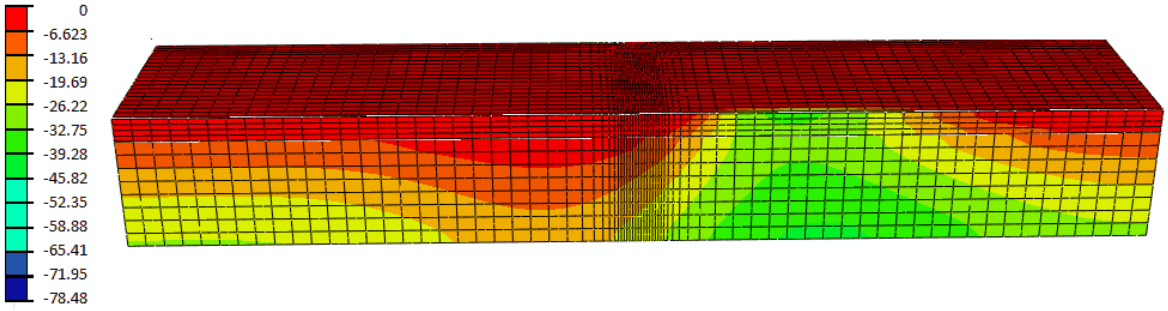

Figure 7-57 - Base Layer Vertical Stress Distribution after Wheel Load Application 4 (kPa)

The horizontal V device geometry provides little restraint to shrinkage and thermal gradients while transferring load at the joint. The device allows small differential deflection to occur under thermal and shrinkage gradients as the adjacent slab edges curl upward and downward while spreading the load along the length of slab reducing the maximum stresses in the concrete at the device concrete interface for the service strain gradients assumed. Load transfer during daytime thermal gradients that cause a downward curling of the slab is effective with the Horizontal V device and little to no differential deflection occurring. Nighttime thermal gradient applied simultaneously with wheel loading caused an increase in the differential deflection at the joint

due to the device not restraining the slab from upward curling and allowing deflection of the loaded side of the slab to occur before the device engages. The maximum differential deflection was still maintained at a maximum of approximately 0.5 mm under nighttime thermal gradient and wheel loading. Plastic straining in the concrete was minimal in the Horizontal V device model after the application of the service loading history described in Table 7-1. Reducing the plastic straining in the concrete will reduce the damage in the concrete around the device and this may improve the long term differential deflection at the joint as less softening would occur in the concrete around the device. The continuous nature of the device and the reduced number of devices would eliminate possible misalignment problems. Further experimental testing of the wheel load transfer that would take into account local weaknesses in the concrete, the actual behaviour at a concrete-concrete joint interface and with a specific compressible material chosen should be completed on the Horizontal V device.

7.7 Horizontal Pipe Service Load Finite Element Results

The horizontal pipe device was modelled in the Quarter Slab Model described in Section 7.2.2 with the service loading described in Table 7-1 applied to the model. A detailed investigation of the results around the joint for each loading step applied is presented in this Section.

Figure 7-58 presents the comparison of the deflection on either side of the joint for the horizontal pipe device as the service loading steps are applied to the slab. From Figure 7-58, the maximum deflection on either side of the slab was similar throughout the application of the service loading history. The maximum upward curling deflection was 2.2 mm after shrinkage, 0.3 mm after daytime thermal, and 2.85 mm after nighttime thermal strain gradients were applied to the slab. The differential deflection was approximately 0.15 mm after thermal daytime wheel loading was applied and 0.25 mm after nighttime wheel loading was applied. The top of slab deflection was increasing with each wheel load as the loaded slab does not return to the unloaded position upon unloading.

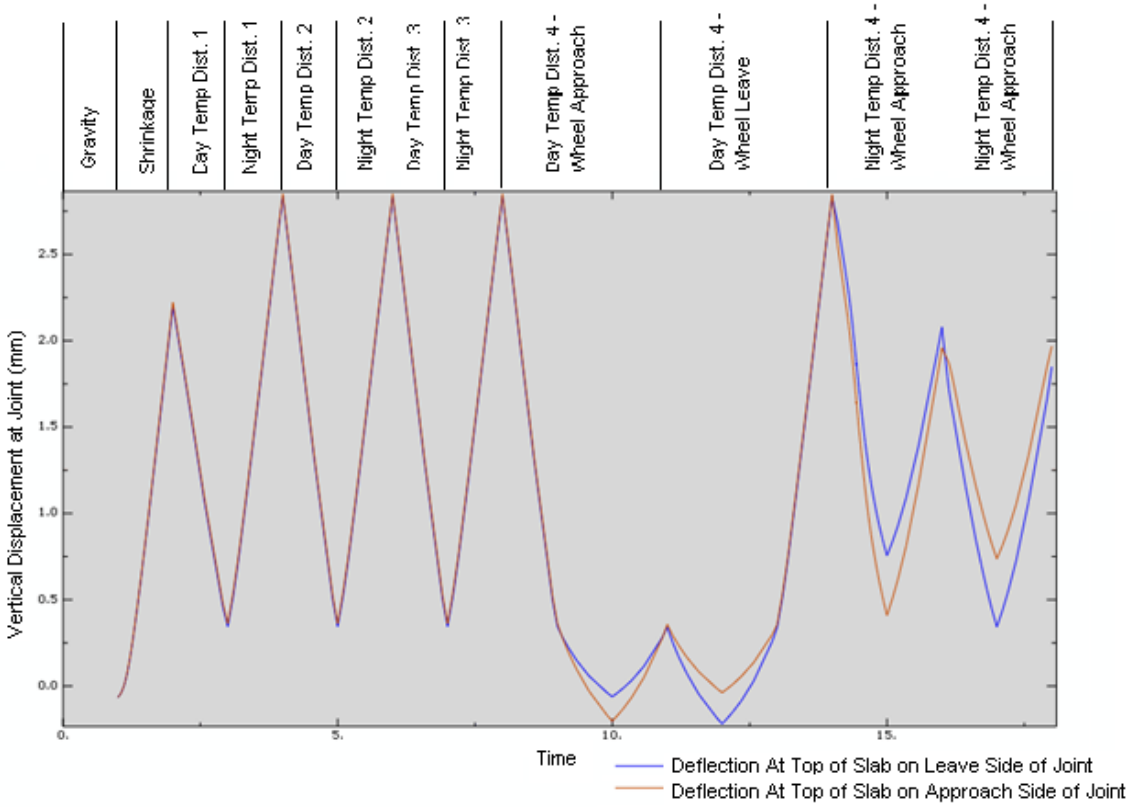

Figure 7-58 – Horizontal Pipe Device Model: Top of Slab Deflection History

The Von Mises stress distribution in the horizontal pipe device after the application of the shrinkage step is presented in Figure 7-59. The maximum Von Mises stress in the device is 0.84 MPa. Von Mises stress concentrations exist at both of the vertical legs of the device.

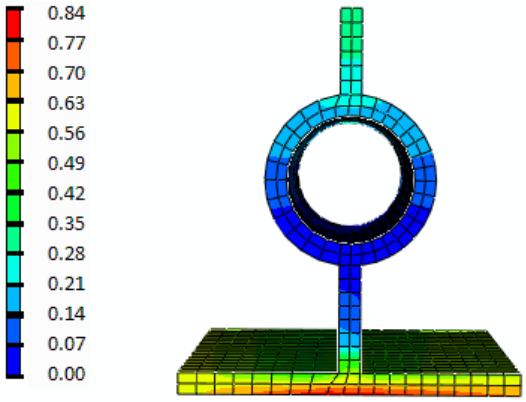

Figure 7-59 – Horizontal Pipe Device Von Mises Stress after Shrinkage Application (MPa)

Figure 7-60 presents the vertical stress distribution in the concrete around the Horizontal Pipe device after the shrinkage strain gradient was applied to the slab. Similar to the Horizontal V device, compressive vertical stress zones exist on either side of the device away from the joint as the curling edges of the slab bear on the device causing resulting compressive stress adjacent the device. At the joint location, next to the device, tensile vertical stress concentrations developed. The maximum tensile vertical stress in the concrete at this location is 2.55 MPa. This occurred because the top and bottom halves of the slab try to split away from each other where the slab was in contact with the device. The maximum stress tensile vertical stress is between the minimum and mean concrete cracking strength for 30 MPa concrete.

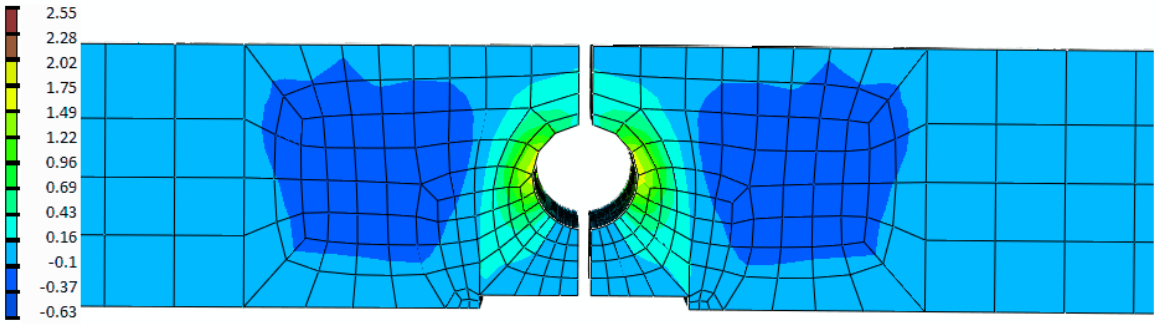

Figure 7-60 - Concrete Vertical Stress Distribution after Shrinkage Application (MPa)

Figure 7-61 presents the Von Mises stress distribution in the horizontal pipe device after the application of the daytime thermal gradient. The maximum Von Mises stress in the horizontal pipe device was 2.95 MPa in the bottom vertical leg of the device. The stress was concentrated at the top of the leg near the interface of the leg and the pipe portion of the device. A lower concentration of Von Mises stress occurred at the top of the top vertical leg as well.

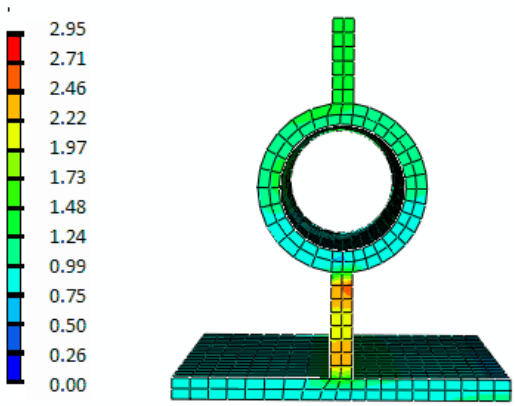

Figure 7-61 – Device Von Mises after Daytime Thermal Gradient (MPa)

Figure 7-62 presents the vertical stress distribution in the concrete around the Horizontal Pipe device after the daytime thermal gradient is applied to the model. The maximum tensile stress concentration in the concrete increases at the sides of the pipe section where the maximum vertical stress was 2.91 MPa, which is the suggested mean cracking strength of 30 MPa concrete. Compressive vertical stress zones occurred away from the device location similar to the other continuous joint device (horizontal V device). Compressive vertical stress was also occurring below the device in the concrete between the device and the base, as presented in Figure 7-62.

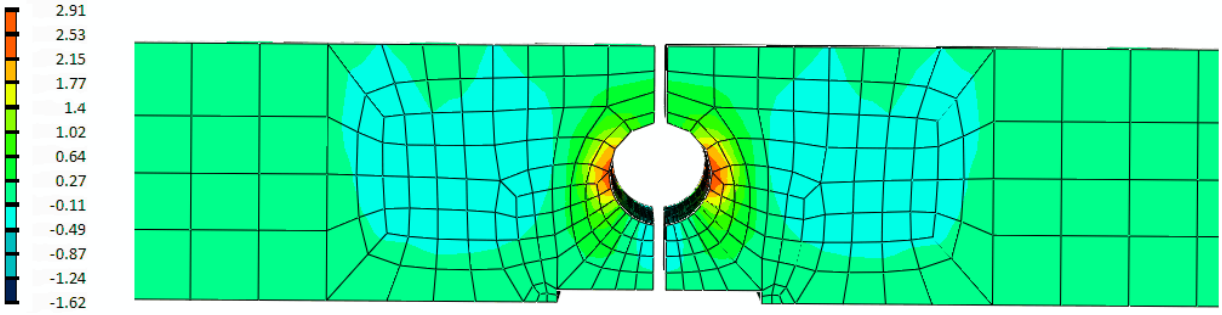

Figure 7-62 - Concrete Vertical Stress Distribution after Daytime Thermal Gradient (MPa)

Figure 7-63 presents the distribution of Von Mises stress in the Horizontal Pipe device after the nighttime thermal gradient was applied. The maximum Von Mises stress in the Horizontal Pipe device occurs at the bottom of the vertical leg of the device where the two slabs are curling upward due to the thermal nighttime and shrinkage straining applied. The maximum stress in the device is 3.31. The distribution is quite similar to the horizontal V device where little or no stress existed in the device except at the bottom under nighttime thermal gradient. This stress

distribution suggests that the slabs are curling upwards away from the device and possibly losing contact with the device. At the bottom of the device, the stress concentration occurred because of the curling of the slabs causing the device to compress locally as the slabs curled upwards.

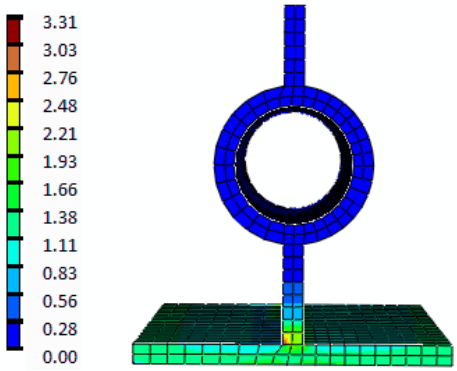

Figure 7-63 - Device Von Mises after Nighttime Thermal Gradient (MPa)

Figure 7-64 presents the vertical stress distribution in the concrete around the horizontal pipe device after the application of the nighttime thermal gradient. The maximum tensile vertical stress at the sides of the pipe portion of the device is 2.43 MPa which is less than after the daytime thermal gradient. This maximum tensile stress in the concrete is above the minimum cracking strength for concrete but less than the mean cracking strength. Similar to the stress distributions observed after the shrinkage and daytime thermal gradients, compressive vertical stress zones exist away from the device on either side of the joint. Curling of the slab and relative rotation assumed about the primary axis of the pipe device caused the vertical stresses on either side of the device.

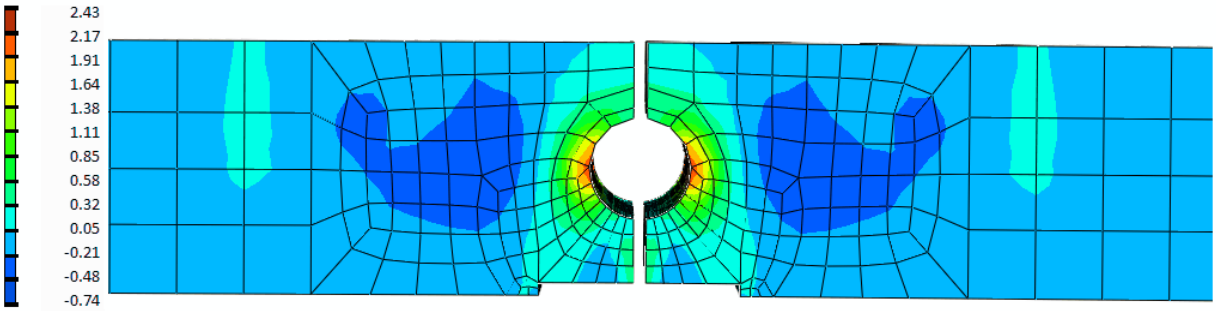

Figure 7-64 - Concrete Vertical Stress Distribution after Nighttime Thermal Gradient (MPa)

The distribution of Von Mises stress in the Horizontal Pipe device after the first wheel load application is presented in Figure 7-65. The maximum Von Mises stress in the Horizontal Pipe device occurs at the top of the bottom vertical leg near the interface with the pipe portion of the device. The maximum stress is located on the unloaded side of the vertical leg. The loaded side of the slab slips relative to the device and attempts to push the device towards the unloaded side as it slides along the pipe shape. This sliding action on the loaded side of the slab and will cause a slight opposite reaction from the otherside of the joint resulting in this high concentration of stress. The maximum Von Mises stress was 4.01 MPa which is higher than for the horizontal V device but it will be possible to select a material that can sustain this stress.

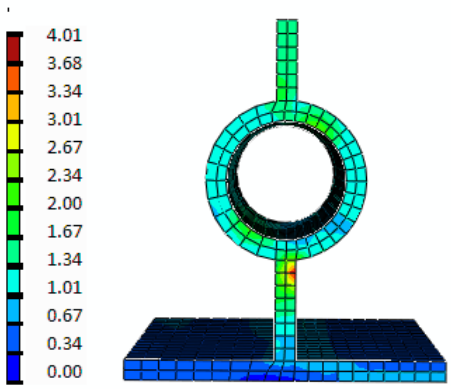

Figure 7-65 - Device Von Mises after Wheel Application 1 (MPa)

The vertical stress distribution in the concrete around the horizontal pipe device after the first application of the wheel load is presented in Figure 7-66. The highest concentration of tensile vertical stress in the concrete occurred on the unloaded side of the slab at the side of the pipe device. The maximum tensile vertical stress was 2.84 MPa on the unloaded side of the joint, which is approaching the mean tensile cracking strength of concrete of 2.91 MPa. Compressive vertical stress concentrations occurred in the concrete beneath the pipe section of the device on the unloaded side of the joint as well. The vertical stress distribution on the unloaded side of the slab suggests load transfer was occurring at the joint. The maximum vertical compressive stress in the concrete beneath the device was 2.74 MPa.

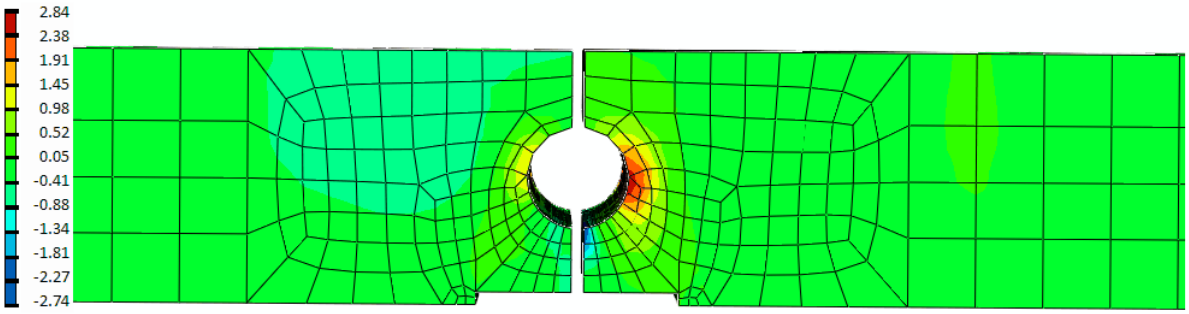

Figure 7-66 - Concrete Vertical Stress Distribution after Wheel Application 1 (MPa)

Figure 7-67 presents the vertical stress distribution in the base layers after the first application of the wheel load in the Quarter Slab horizontal pipe model. A vertical stress concentration occurred along the joint with a maximum vertical stress of 187 kPa. The maximum vertical stress is similar to the horizontal V device for the same load application and is greater than for conventional steel dowels. The vertical stress distributes gradually away from the loaded side of the slab. The concentration of vertical stress generally was located under the loaded side of the slab. This stress distribution suggests that the device is not as efficient as transferring loads at the joint as dowels.

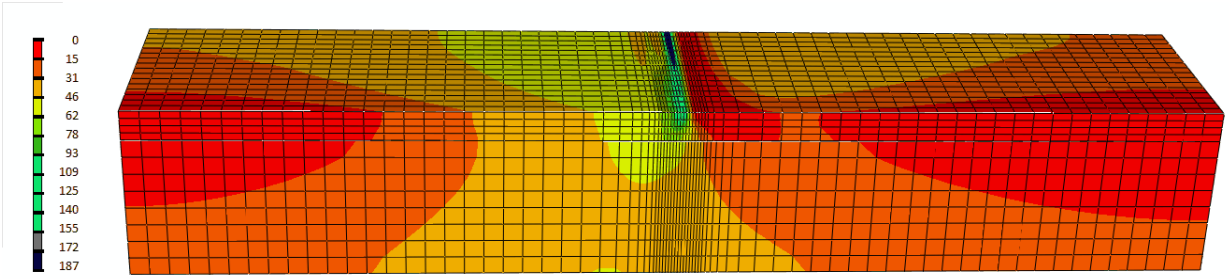

Figure 7-67 - Base Layers Vertical Stress Distribution after Wheel Load Application 1 (kPa)

Figure 7-68 presents the Von Mises stress distribution in the horizontal pipe device after the second wheel load application. The maximum Von Mises stress in the device occurred on the unloaded side of the joint at the top of the bottom horizontal leg of the device similar to the first wheel load application. The maximum Von Mises stress in the horizontal pipe device was 3.57 MPa after the second wheel load application which is lower than that observed for the first wheel load application. It is possible that minor damage occurring in the concrete between the steps could alter this maximum slightly as the behaviour would be expected to be symmetric.

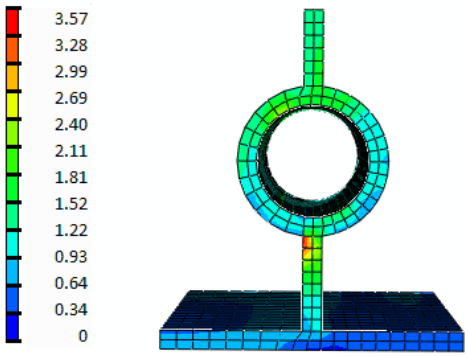

Figure 7-68 - Device Von Mises after Wheel Application 2 (MPa)

Figure 7-69 presents the vertical stress distribution in the concrete after the second application of the wheel load to the quarter slab Horizontal Pipe device model. After the application of the second wheel load, a tensile vertical stress concentration existed in the concrete on either side of the pipe portion of the device with a larger concentration occurring on the unloaded side of the joint. On the loaded side of the slab, the wheel load pushes the top half of the slab down and resists the two halves of the slab from splitting. On the unloaded side of the slab the wheel load pushes the bottom half of the slab and tries to split the two halves of the slab apart causing a higher maximum tensile stress at the side of the device in the concrete. Compressive vertical stress concentrations occur under the device on each side of the pipe portion of the device with the largest compressive stress occurring on the loaded side of the slab.

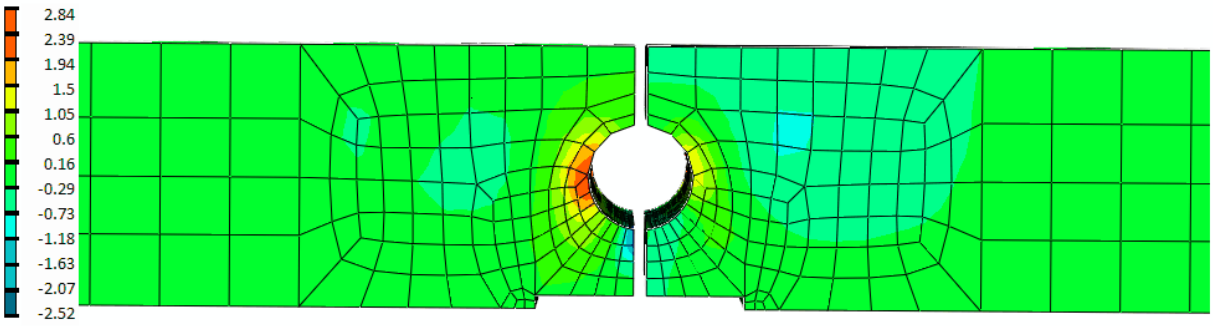

Figure 7-69 - Concrete Vertical Stress Distribution after Wheel Application 2 (MPa)

The distribution of the vertical stress in the base layers is presented after the second wheel load application in Figure 7-70. The maximum stress in the base layer after the second wheel load application was similar to that observed after the first application, with a maximum stress of 191

kPa occurring at the joint location. Similar to the first wheel load application, the concentration of vertical stress in the base was generally on the loaded side of the joint.

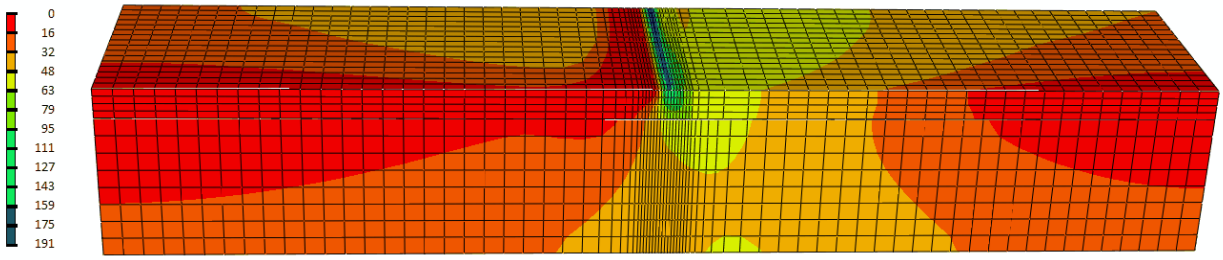

Figure 7-70 - Base Layers Vertical Stress Distribution after Wheel Load Application 2 (kPa)

Figure 7-71 presents the distribution of the Von Mises stress in the Horizontal Pipe device after the third wheel load application along with nighttime thermal gradient. The maximum Von Mises stress occurred on the loaded side of the device at the bottom of the bottom horizontal leg. The maximum Von Mises stress in the horizontal pipe device was 4.15 MPa. The upward curling from the nighttime thermal gradient and shrinkage cause the concentration of stress to occur at the bottom of the device and wheel loading will cause stress concentrations across the device as wheel load is transferred.

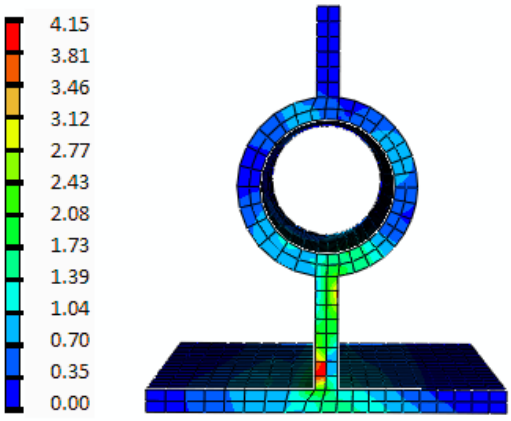

Figure 7-71- Device Von Mises after Wheel Application 3 (MPa)

Figure 7-72 presents the vertical stress in the concrete around the Horizontal Pipe device after the third application of the wheel load. After the application of the third wheel load, the

maximum tensile vertical stress in the concrete exists next to the pipe portion of the device on the unloaded side of the slab. This vertical tensile stress region extends almost the entire height of the device. The maximum vertical tensile stress located near the middle of the pipe portion is 2.42 MPa. This maximum vertical tensile stress is between the minimum and mean cracking strengths for 30 MPa concrete.

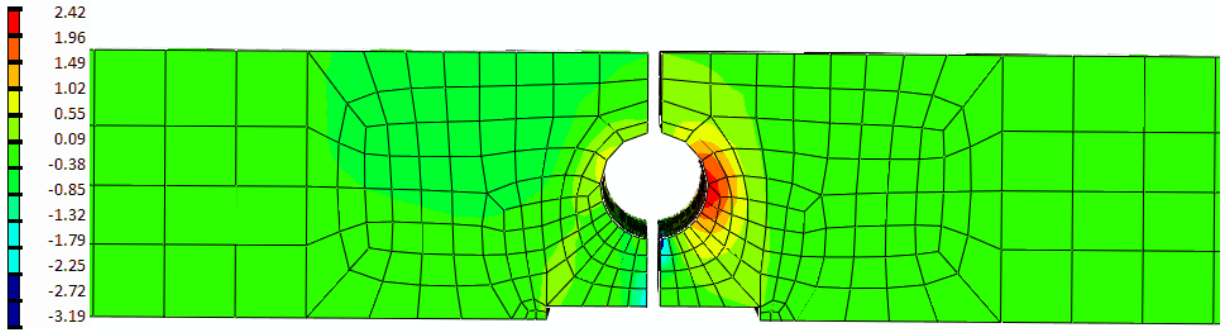

Figure 7-72 - Concrete Vertical Stress Distribution after Wheel Application 3 (MPa)

The vertical stress distribution in the base layers after the third application of the wheel load is presented in Figure 7-73. The maximum stress occurred away from the joint location as the slab was curling upward from the thermal gradient and the wheel load is pushing the slab downward. The maximum stress in the base layer is 86 kPa less than for daytime thermal gradient applied simultaneously with wheel loading. This maximum stress in the base layer is greatest away from the slab edges with a small concentration that occurred near the joint as the slab was curled upward.

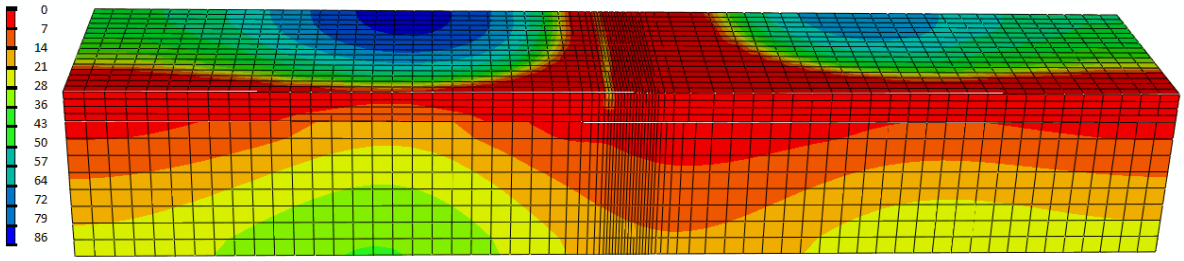

Figure 7-73 - Base Layers Vertical Stress Distribution after Wheel Load Application 3 (kPa)

The results after the fourth application of the wheel load for the Horizontal Pipe device were similar to the results after the third application with the exception of stress reversals due to the

wheel load being applied on the other side of the joint. Almost no plastic straining occurs throughout the application of the service loading in the concrete for the Horizontal Pipe device.

The horizontal pipe device was capable of transferring load at the joint with little restraint to shrinkage and thermal gradients. Higher stresses occurred in the base layer at the edge of the slab with the horizontal pipe device model than with the conventional steel dowel model indicating that joint load transfer was not as efficient when wheel loading was applied. The horizontal pipe device reduced maximum stresses in the concrete and reduces plastic straining in comparison to conventional steel dowels. Reducing the maximum plastic stress in the concrete will decrease the degradation of load transfer that occurs at the joint due to plastic concrete damage. The continuous nature of the device and geometry will also eliminate a number of the misalignment problems that are associated with conventional steel dowels. The horizontal pipe device wheel load transfer ability should be investigated in an experimental testing program. Shrinkage and thermal effects as well as the crack formation should be investigated in a field application to confirm the model results.

7.8 Comparison of Service Load Finite Element Results

The relative performance of the discrete and continuous devices when subjected to the service loading history (Table 7-1) is compared in this section. Comparisons are made in terms of maximum compressive and tensile stresses in the concrete, maximum plastic strains in the concrete (PEEQ and PEEQT), maximum Von Mises stress in the devices, and maximum stresses in the base layer. The maximum concrete stress data are shown for each of the three primary axis directions for the slab: S11 refers to the axis parallel to the joint, S22 refers to the vertical axis, and S33 refers to the direction parallel to the traffic direction (perpendicular to the joint). The joint vertical deflection and differential deflections are also compared for the different devices.

Average differential deflection at the joint for each device is presented in Figure 7-74 to compare the behaviour of the devices when service loading was applied to the models. The most deflection due to shrinkage occurred in the horizontal pipe device suggesting that it provides the least restraint to curling. Average upward deflection at the joint for the horizontal pipe was approximately 1.5 mm. Conventional dowels restrained the upward curling more than the other

proposed devices by approximately 0.25 mm and average upward deflection at the joint for these devices was very similar after shrinkage. The dowel bar model had the highest predicted average deflection at the joint after the application of the thermal daytime gradient and the horizontal V device had the lowest upward deflection at the joint.

The greatest relative downward deflection during the thermal gradient step (from the maximum average joint deflection at the end of the shrinkage step to the minimum joint deflection after the daytime thermal gradient step) occurred in the horizontal pipe device model. The relative deflection that occurred in the horizontal pipe device during the daytime thermal gradient was -1.83 mm. This suggests that the horizontal pipe device provides the least amount of restraint to daytime thermal gradients. The horizontal V device model predicted the next highest relative deflection at the joint during the daytime thermal gradient at -1.45 mm. The GFRP I-beam, dowel and GFRP tapered plate models predicted similar relative deflection during the daytime thermal gradient step of -1.08 mm, -1.01 mm, and -0.97 mm, respectively. The continuous devices appeared to provide the least restraint to daytime thermal gradients as expected based on the geometry of the devices. The FRP tapered plate device appeared to provide the most restraint to daytime thermal gradients.

Relative deflection at the joint that occurred during the nighttime thermal gradient in the horizontal pipe device was the greatest similar to the shrinkage and daytime thermal gradient. The relative deflection at the joint during the first nighttime gradient in the horizontal pipe device was approximately 2.45 mm. The remaining devices all had approximately the same relative deflection occur during the nighttime thermal gradient step with values ranging from 1.78 mm to 1.86 mm. This suggests that the restraint at the slab provided by the horizontal V to nighttime thermal gradients is similar to the discrete devices. The horizontal pipe device provided the least restraint to shrinkage and thermal daytime and nighttime gradients. Cycling of the thermal nighttime and daytime gradients did not appear to change the average joint deflection that occurred in any of the models.

The horizontal V allowed the least amount of relative deflection at the joint to occur when daytime thermal gradients and wheel loading was applied simultaneously to the slab for wheel loading applied to either side of the slab. Relative deflection of -0.29 mm and -0.28 mm occurred for the first wheel load applications for the horizontal V device. The horizontal pipe device had

the second least relative deflection occur when wheel loading was applied along with daytime thermal gradients. The relative deflections that occurred at the joint during the first and second wheel load applications for the horizontal pipe device were -0.47 mm and -0.46 mm, respectively. There was little change in the relative deflection that occurred at the joint for the first and second wheel load applications for each of the horizontal V and horizontal pipe devices. All of the continuous devices had more noticeable change in relative deflection that occurred during the first and second wheel load applications. The dowel bar model predicted the most relative deflection occurring during the first and second wheel load applications of 0.86 mm and 0.67 mm. The GFRP tapered plate had relative deflections of 0.68 mm and 0.59 mm occur during the application of the first and second wheel loads. The GFRP I-beam had relative deflections of 0.60 mm and 0.49 mm occur during the first and second wheel load applications with thermal daytime gradients applied simultaneously. The amount of relative deflection that occurred during the first and second wheel loads with daytime thermal gradients appear to be directly proportional to the amount of upward curling that occurred. This relationship makes sense as the horizontal V device had the least amount of upward deflection occur during the daytime thermal gradient and as the wheel loading was applied would have came into contact with the base layer first. It also appears that as more relative deflection occurred at the joint during the first wheel load more change in relative deflection occurred during the second applications of the wheel load, except the GFRP tapered plate had less change in relative deflection than the GFRP I-beam. This could suggest that more relative deflection at the slab was causing more damage to occur in the concrete and hence more change in the response as the load was applied to the other side of the slab.

All the devices allowed more relative deflection to occur at the joint with nighttime thermal gradients applied simultaneously with wheel loading. The GFRP I-beam allowed 1.74 mm relative deflection to occur during the third wheel load application before the model failed to converge at a loading of 74 kN and the GFRP tapered plate allowed 1.44 mm of relative deflection to occur before the model failed to converge at 49.6 kN. The horizontal pipe device had the most relative deflection occur at the joint with nighttime thermal gradients and wheel loading applied simultaneously. The first wheel load application with nighttime thermal gradients caused 2.24 mm of relative deflection to occur in the horizontal V device and reduced to 1.43 mm for the second wheel load application. The dowel bar had the second most relative

deflection occur at the joint during the third and fourth wheel load application of 2.03 mm and 1.49 mm, respectively. The horizontal V device had the least relative deflection occur at the joint for the third wheel load of 1.71 mm. The relative deflection at the joint for the horizontal V device reduced to 1.28 mm for the fourth wheel load application. The amount of relative deflection at the joint under wheel loading was proportional to the amount of average upward curling that had occurred after the nighttime thermal gradient. This is a similar result to daytime curling and wheel loading. The relative deflection that occurred at the joint after the second wheel load for the horizontal V, horizontal pipe and dowel models varied more with more relative deflection as well. This could suggest that damage is occurring at the joint with the large amount of deflection occurring during the first wheel load and changes the behaviour of the device with subsequent wheel load applications.

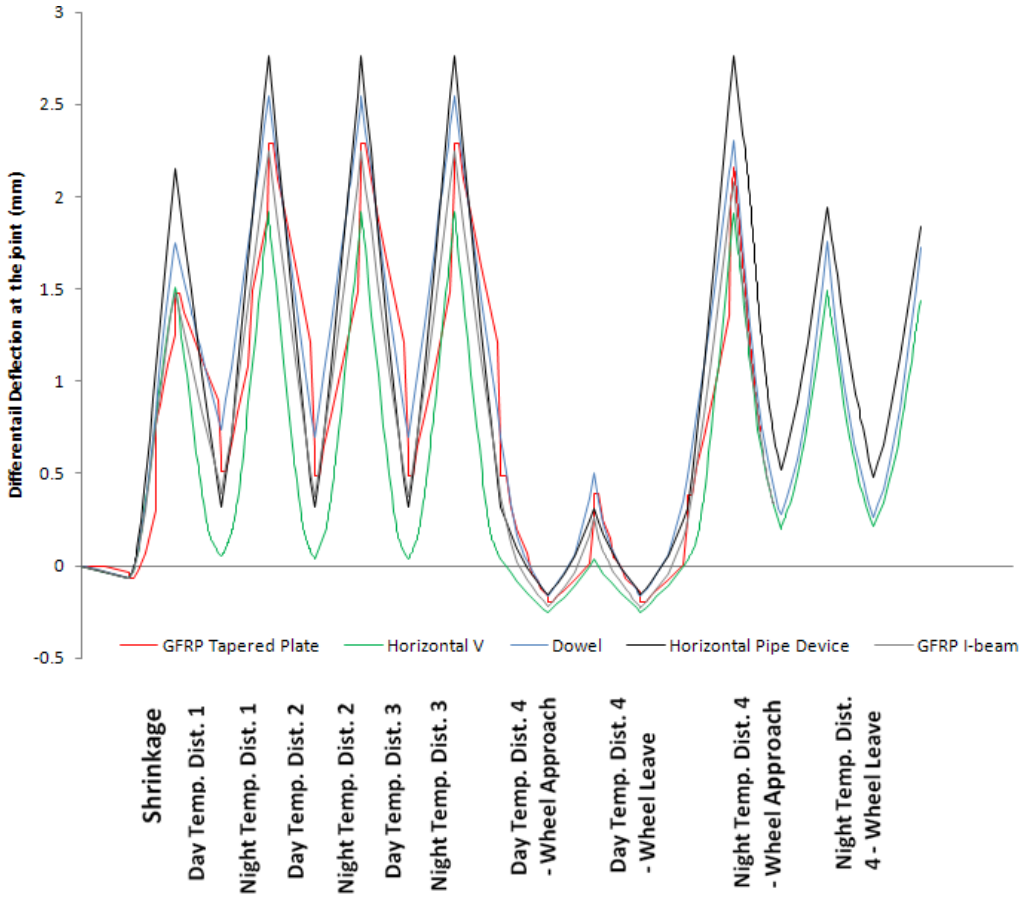

Figure 7-74 – Service Load Comparison of Average Deflection at the Joint

Figure 7-75 presents a comparison of the differential deflection that occurred at the joint all the devices. All the discrete devices had negligible differential deflection occur throughout the application of shrinkage and the thermal gradients. The discrete devices provide the most restraint to curling caused by both the shrinkage and thermal gradients at the joint and it makes sense that the differential deflection would be minimal with these devices. The horizontal V had the most differential deflection occur during the shrinkage step with a total differential deflection of -0.15 mm. The concave side of the V device deflects upward more as the top portion of the slab is not restrained by the other side of the joint and the pointed side of the V device further pries the slab upward as it curls upwards. The unsymmetrical geometry of the horizontal V device and low restraint to upward curling is assumed to cause this behaviour. With daytime thermal gradients applied to the horizontal V device, the device appears to begin to lock near the end of the curling gradient as the differential deflection of the slab reduces near the end of these steps, as can be noticed in Figure 7-75. The horizontal pipe device has minimal differential deflection occur during the shrinkage step and little change occurs through the thermal daytime and nighttime thermal gradient cycles with a differential deflection of approximately 0.02 mm. The symmetrical layout of the horizontal pipe device would suggest that no differential deflection should occur during the application of shrinkage and thermal gradients. It was assumed that either the difference in nonlinear behaviour in the concrete slabs or the behaviour of the slip surface at the rounded pipe portion of the device caused the small differential deflection to occur during thermal and shrinkage strain gradient application.

The horizontal V device had the least amount of differential deflection occur when wheel loading and daytime thermal gradients were applied to the slab simultaneously. The horizontal V device had differential deflection of approximately 0.03 mm for the first two wheel load applications. The unsymmetrical geometry did not appear to affect the differential deflection with daytime thermal gradients and wheel loading applied to the slab for the horizontal V device. The remaining devices had similar differential deflection occur for the first two wheel load applications. The second lowest differential deflection at the joint for the first and second wheel load applications was conventional steel dowels, with values of 0.13 mm for both the first two wheel load applications. The pipe device had a differential deflection of 0.16 mm and 0.18 mm for the first two wheel load applications, respectively. The GFRP I-beam allowed the most differential deflection for the first wheel load application but had less differential deflection than

the pipe device after the second wheel load application. All the devices were capable of maintaining the differential deflection at the joint with wheel loading and daytime thermal gradients applied simultaneously but only the horizontal V device reduced the differential deflection occurring at the joint when compared to conventional steel dowels.

Nighttime thermal gradients applied simultaneously with wheel loading had much different results than daytime thermal gradients with the horizontal V device having the most differential deflection occurring at the joint when wheel loading is applied. Differential deflection that occurred due to the upward curling as well as the possible loss of contact at the base-concrete interface was assumed to cause the increased differential deflection for the horizontal V model for the third and fourth wheel load applications. The differential deflection was 0.45 mm and 0.51 mm for the horizontal V device. The horizontal pipe device had the second most differential deflection occur at the joint for the third and fourth wheel load applications. Conventional steel dowels had the least amount of differential deflection occur for nighttime thermal gradient and wheel loading applied simultaneously. The differential deflection at the joint for the dowel was similar for both nighttime and daytime thermal gradients applied simultaneously with wheel loading. Overall the average deflection at the joint throughout the service loading history was the lowest with conventional steel dowels. The horizontal V device providing significantly less differential deflection at the joint with daytime thermal gradients and wheel loading applied simultaneously is worth more investigation since majority of traffic would be experienced on a pavement during these conditions than nighttime thermal gradients. Depending on the anticipated traffic distribution this may provide more rider comfort for a larger percentage of the traffic. Furthermore, the load transfer efficiency and joint efficiency for the horizontal V device with nighttime thermal gradient and wheel loading applied simultaneously were 80.1% and 90.0% which are both within the limits suggested. This also means that the LTE and joint efficiency for all the devices were within suggested limits of 78% and 85%, respectively (previously presented in Section 5.0).

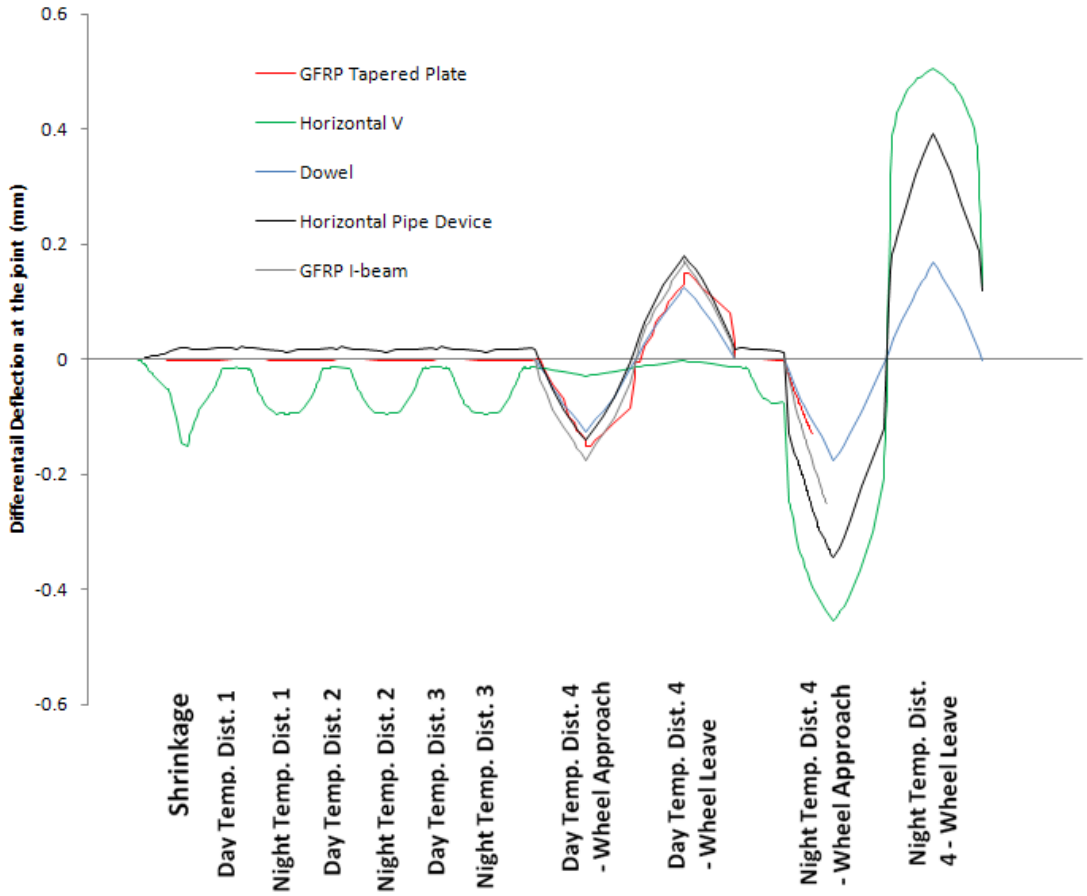

Figure 7-75 – Service Load Comparison of Differential Deflection at the Joint

The maximum compressive (negative) S11 stress in the concrete (parallel to joint) at the device to concrete interface is compared in Figure 7-76 for each device and the maximum tensile (positive) S11 stress is compared in Figure 7-77. The maximum compressive S11 stress in the two continuous devices was the lowest throughout the service loading sequence. The continuous devices should reduce the stress in this direction as these devices did not have any mechanical restraint along the joint length. The horizontal V device had the lowest maximum compressive stress along the joint length. The GFRP tapered plate dowel and GFRP I-beam behaved similar to the conventional dowel bar until the wheel loading was applied when the maximum compressive S11 stress in the concrete increased rapidly in the GFRP devices. The maximum compressive S11 stress in the concrete at the device interface was lower for the GFRP I-beam than for the conventional dowel through the shrinkage and thermal gradients; however, as wheel loading was applied the maximum S11 compressive stress in the concrete increased rapidly. The maximum tensile S11 stress for all of the devices reaches 3 MPa which was the ultimate tensile

strength input to the concrete model used (explained previously in Section 4.1.1). The maximum stress being at 3 MPa means that cracking has occurred in the model. The mechanical restraint the devices cause to shrinkage as well the curling and restraint due to the slab geometry cause this cracking to occur when shrinkage was applied. The only device that had a maximum tensile stress in the S11 direction in the concrete below 3 MPa during thermal gradient cycling was the horizontal pipe device; although, the concrete in the horizontal pipe device model reaches a maximum of 3 MPa after the wheel loading was applied.

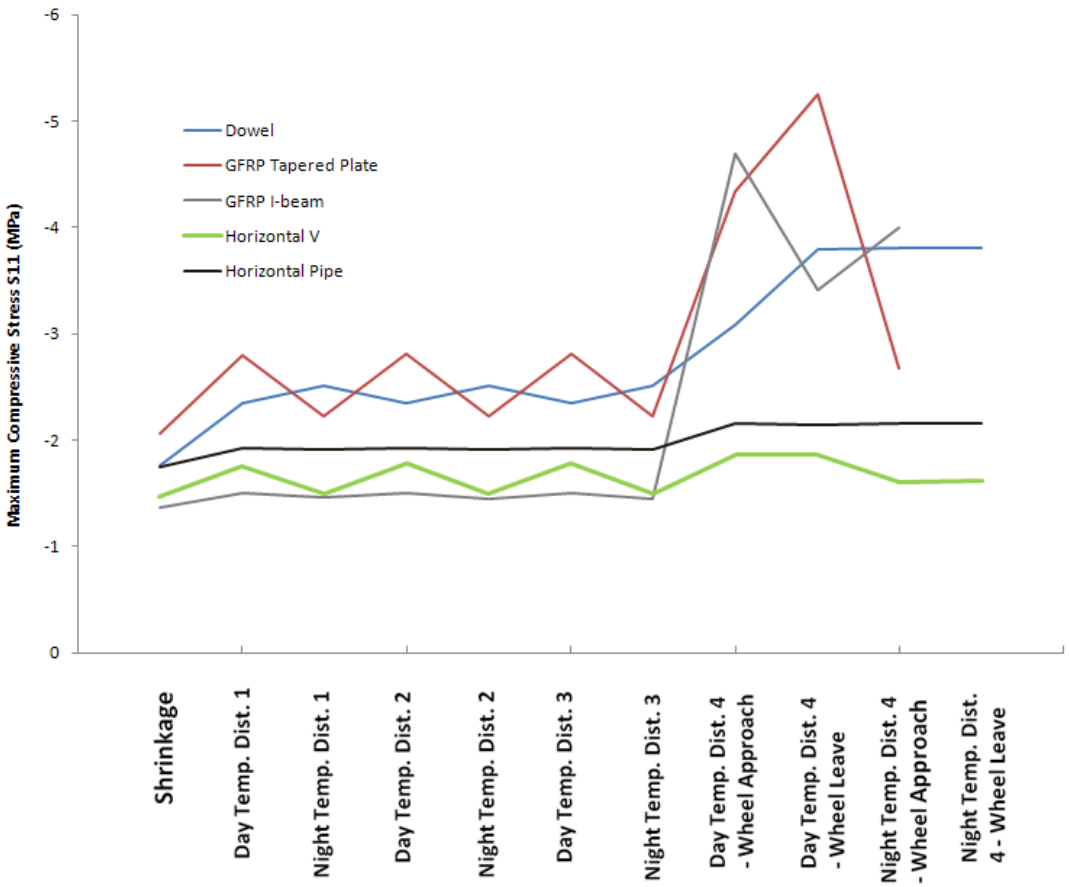

Figure 7-76 – Service Load Comparison of Maximum Concrete Compression Stress in S11 Direction (Parallel to Joint)

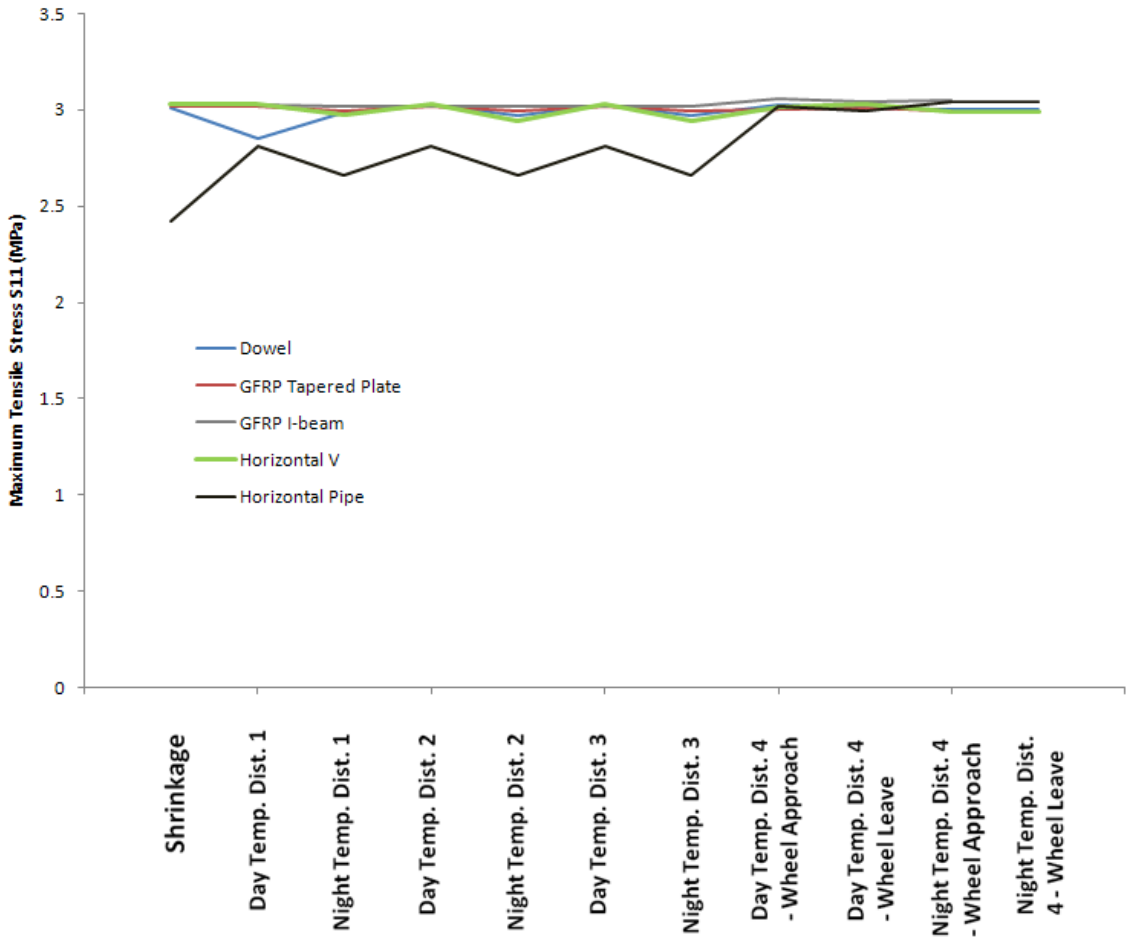

Figure 7-77 – Service Load Comparison of Maximum Concrete Tensile Stress in S11 Direction (parallel to joint)

The maximum compressive stress in the S22 (vertical) direction in the concrete at the device interface is compared for the different devices under service loading in Figure 7-78. The maximum compressive stress in the S22 direction in the concrete at the concrete device interface was lowest for the horizontal V device throughout the analysis. The maximum compressive stress in the S22 direction with the horizontal pipe device was also similarly low. The continuous nature of the horizontal V and horizontal pipe devices increases the bearing area in the vertical direction for load transfer to occur and lower maximum compressive stresses in the concrete were expected with these devices. The maximum compressive stress in the S22 direction in the concrete with the GFRP I-beam was the highest. The GFRP I-beam was stiffer than the steel dowel and as shrinkage was applied to the slab the upward curling of the slab causes the devices to bend. The higher stiffness of the GFRP I-beam requires high force to bend the device to match

the profile of the slab. Increased force transfer required at the device caused the high stress concentration even though device was lower in the slab where less bending is required in the device under shrinkage gradients. The GFRP tapered plate dowel behaved similar to steel dowels; although the maximum compression stress in the S22 direction is lower for the GFRP dowels during the wheel load applications.

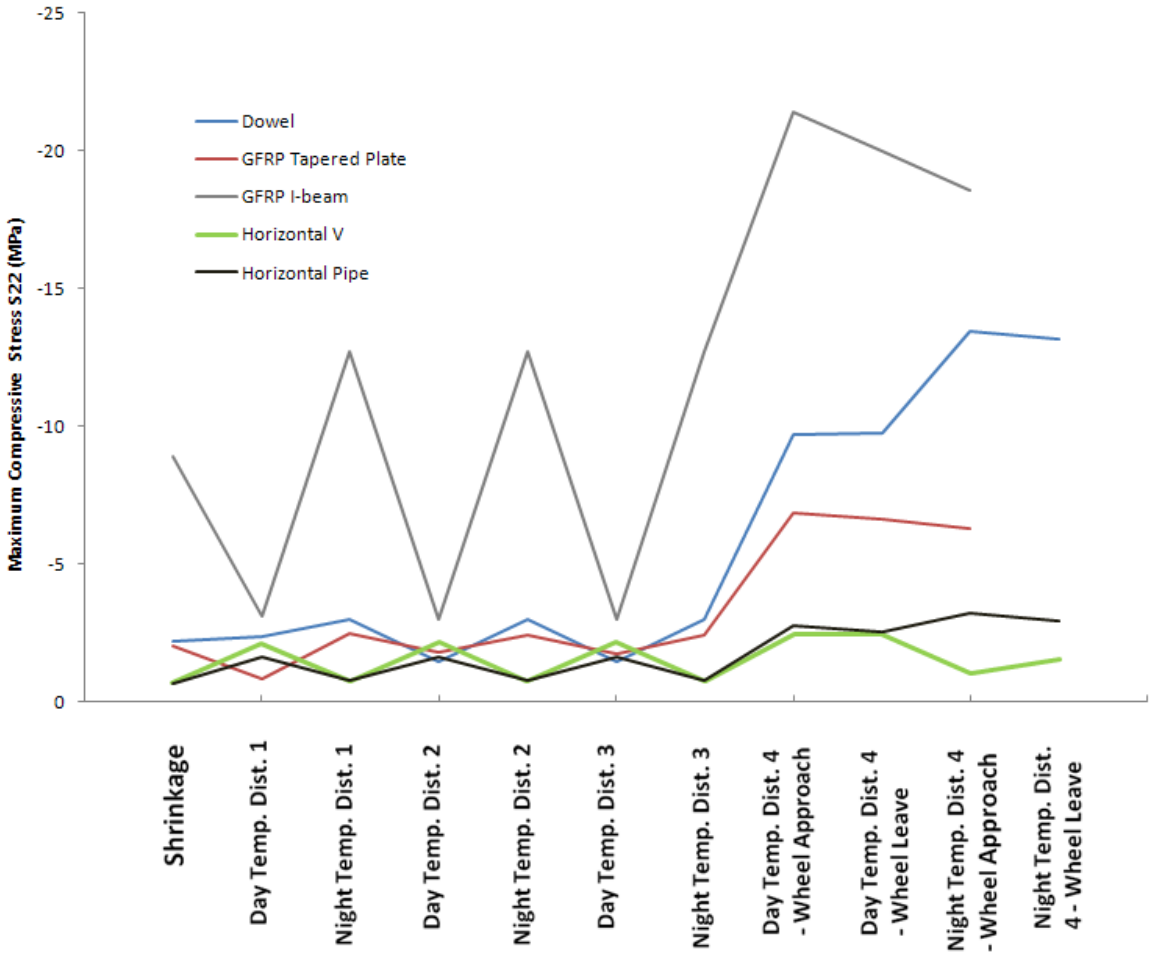

Figure 7-78 – Service Load Comparison of Maximum Concrete Compression Stress in S22 (Vertical) Direction

The maximum tensile stress in the concrete in the S22 (vertical) direction at the joint for the various devices is presented in Figure 7-79. The maximum tensile stress in the horizontal V device was the lowest through the service loading sequence. The continuous nature of the horizontal V device has a larger bearing area for load transfer that reduces stress concentrations. The geometry of the device also allows the upward curling to occur at the slip surface between

the concrete and device interface. Less restraint to upward curling in the device reduced the amount of splitting occurring in the slab. The horizontal pipe device has the second lowest maximum tensile stress in the S22 direction at the joint under wheel loading. The horizontal pipe device restrained upward curling more than the horizontal V device and vertical tensile stresses occurred at the sides of the pipe device. The maximum tensile stress in the S22 direction in the concrete with the GFRP I-beam varied the most due to the relative stiffness of the device. The maximum tensile stress in the S22 direction in the concrete with the GFRP Tapered plate is highest during the wheel loading sequence. High tensile vertical stresses were concentrated at the top edge of the tapered plate dowel. The maximum tensile stresses in the vertical direction for all the devices were below the ultimate concrete tensile cracking strength of 3 MPa. The maximum tensile stresses were all above the minimum concrete cracking strength for 30 MPa concrete.

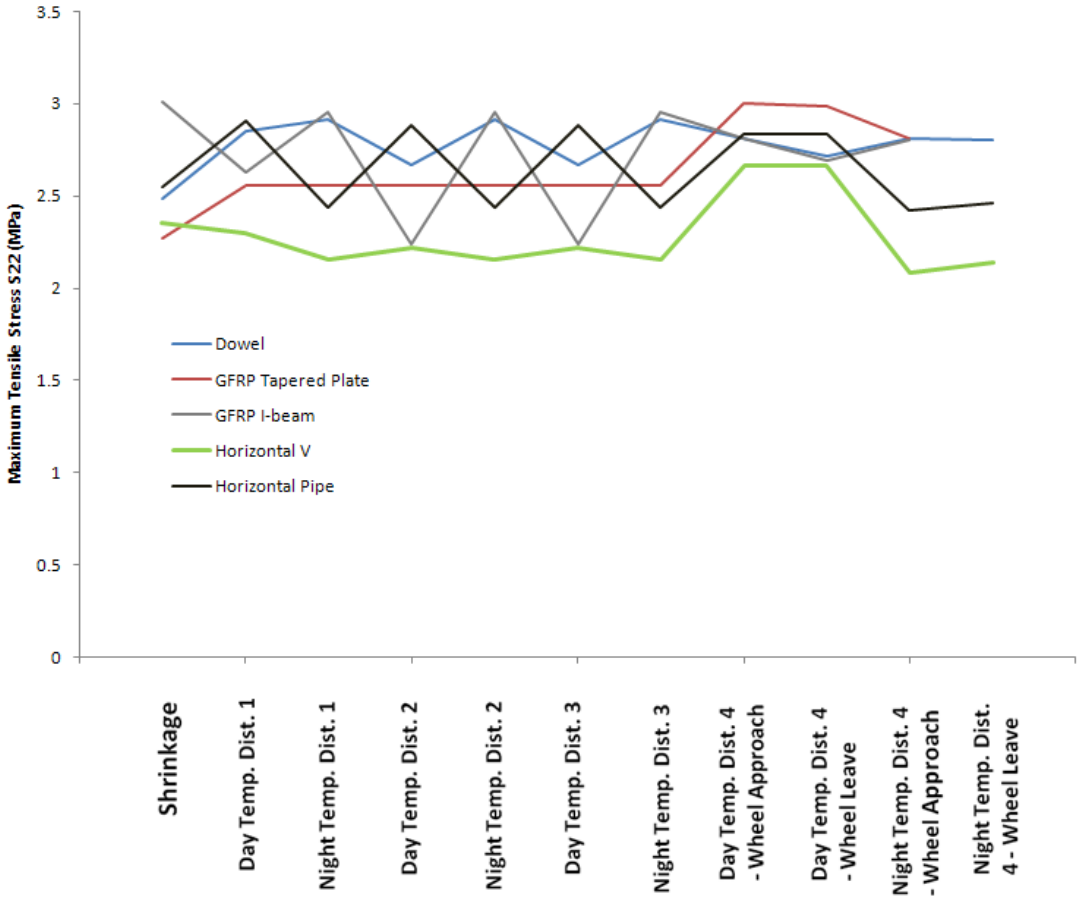

Figure 7-79 - Service Load Comparison of Maximum Concrete Tensile Stress in S22 (Vertical) Direction

Figure 7-80 presents a comparison of the maximum compressive stress in the S33 direction (perpendicular to the joint) in the concrete at the joint interface for all the devices. The GFRP tapered plate created the highest compressive stress concentrations in the S33 direction. The GFRP tapered plate section bears on concrete perpendicular to joint due to the geometry of the device as curling occurs and causes the tapered plate to move relative to the concrete causing the increased compressive stress in the longitudinal direction. With daytime thermal gradients applied the maximum compressive stress in the S33 direction in the horizontal V was the largest. This suggests that the concrete on either side of the joint was bearing on the device and the geometry of the device caused high compressive stresses perpendicular to the joint. Similarly, the horizontal pipe device geometry caused bearing perpendicular to the joint when the slab curled. The maximum compressive stress in the S33 direction in the concrete at the joint interface in the GFRP I-beam quickly increased as the wheel load is applied and before the model fails to converge. High normal force at the device concrete interface and large frictional area of the device cause the increase in compressive stress due to increased frictional force at the concrete device interface. The maximum compressive stress in the S33 direction for the dowel, horizontal pipe, and horizontal V were all in the similar range and were below compressive failure strengths.

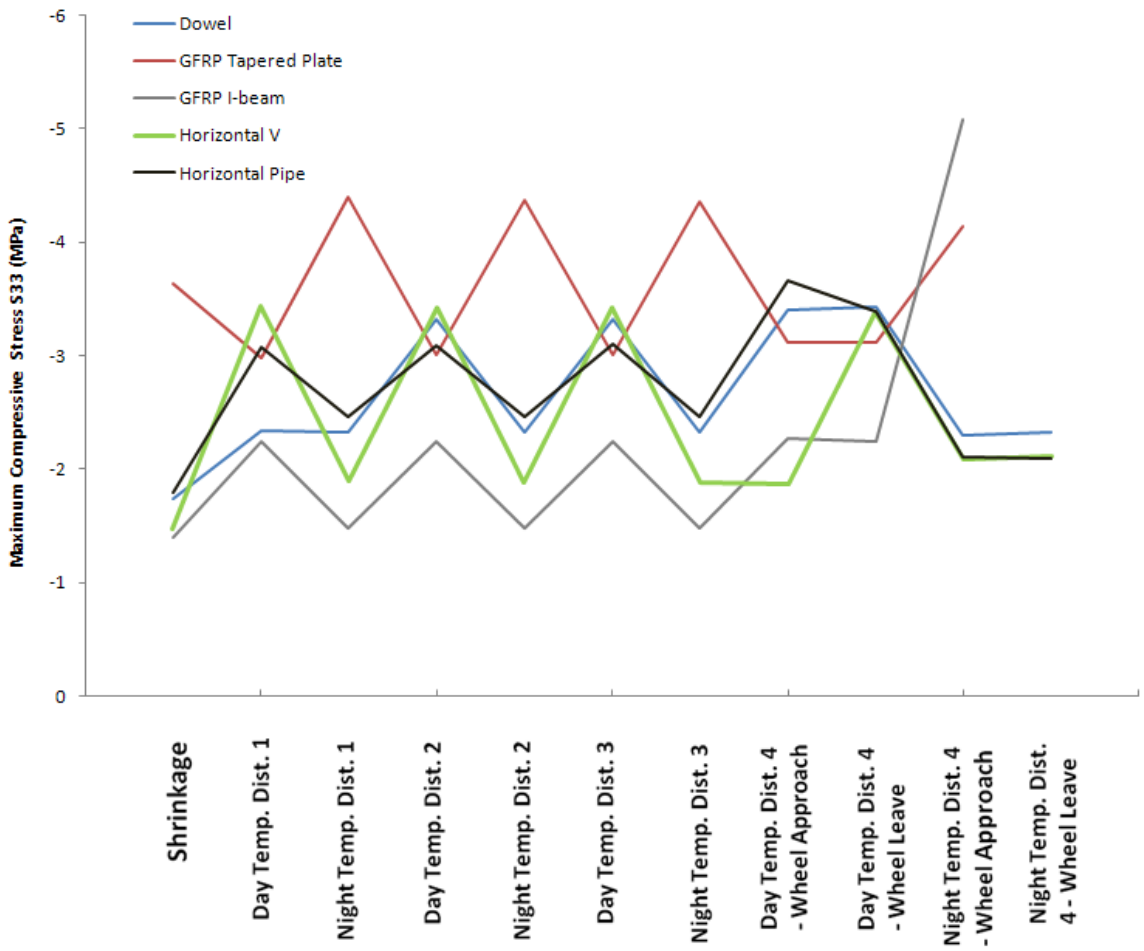

Figure 7-80 Service Load Comparison of Maximum Concrete Compressive Stress in S33 (perpendicular to joint) Direction

Figure 7-81 presents the maximum tensile stress in the concrete at the device interfaces in the S33 direction (perpendicular to the joint). All of the maximum tensile stress concentrations in the concrete at the device interface are near 3 MPa, the ultimate tensile strength of the concrete. The Horizontal Pipe and Horizontal V are the only devices that have maximum tensile stresses below noticeably below 3 MPa. The geometry of both the continuous devices reduced the length of mechanical restraint caused due to curling that causes tensile stress perpendicular to the joint. Low frictional restraint against relative movement at the device slab interface also caused the reduction in maximum tensile stresses perpendicular to the joint.

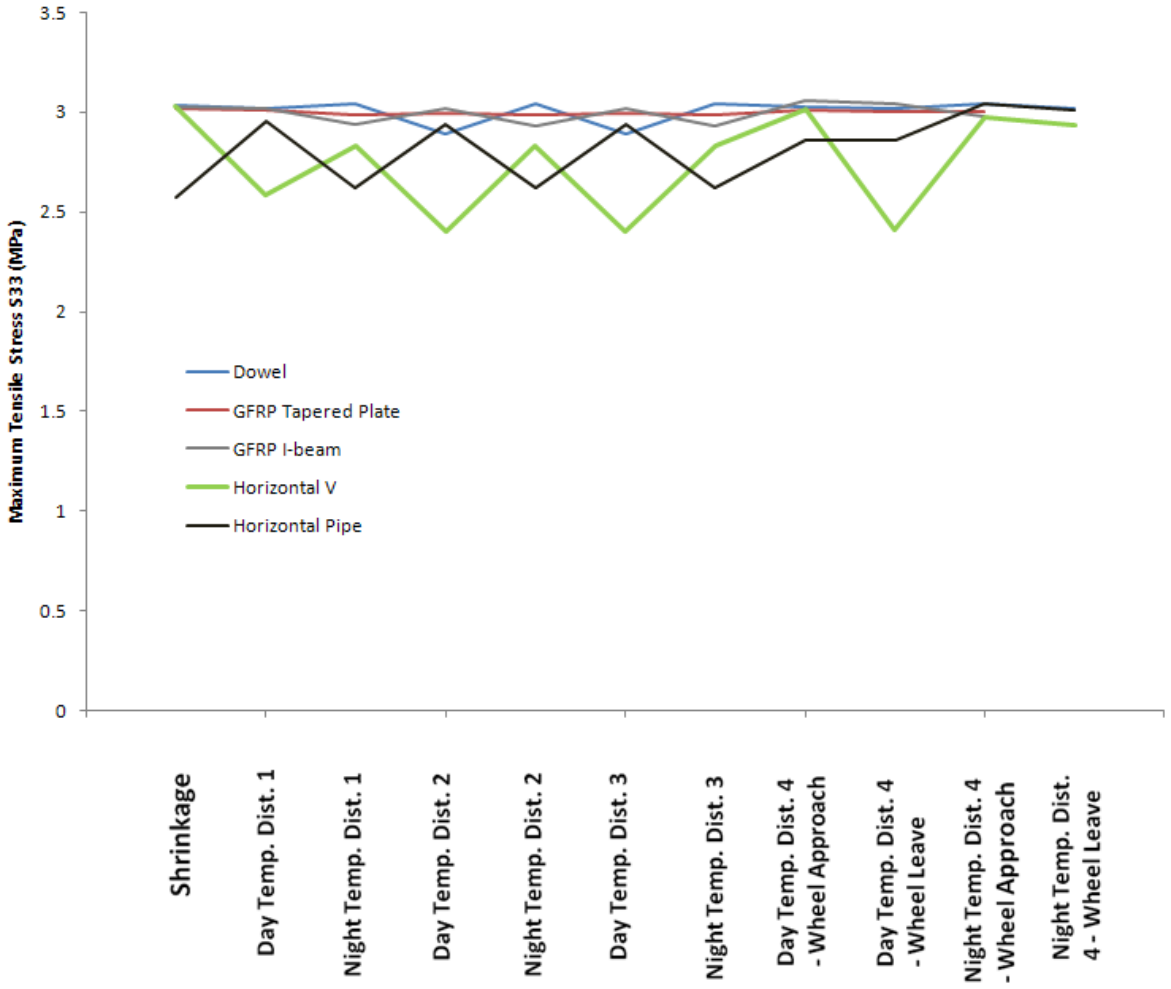

Figure 7-81 - Service Load Comparison of Concrete Maximum Tensile Stress in S33 (perpendicular to joint) Direction

The maximum plastic equivalent compression strain (PEEQ) in the concrete near the device is compared for the device with service loading applied in Figure 7-82. The maximum PEEQ in the concrete for the horizontal V and horizontal Pipe devices remain very low compared to the other devices. The continuous nature of the devices spread load transfer surfaces and eliminate local stress concentrations causing compressive damage in the slab that is the maximum under wheel loading as expected. The horizontal pipe and horizontal V device geometries also appear to reduce the amount of restraint to thermal and shrinkage gradients reducing the maximum compressive stresses causing plastic straining. The GFRP I-beam caused high PEEQ to occur in the concrete at the device as the wheel loads were applied. The stiffness of the GFRP I-beam and relatively small bearing area was assumed to cause the increase in compressive straining

occurring in the concrete. The maximum PEEQ in the concrete was highest for the GFRP tapered plate under the shrinkage and thermal gradients. This suggests that the GFRP tapered plate dowels cause the most restraint to shrinkage and thermal strain gradients. As wheel loading was applied the GFRP tapered plate has lower maximum PEEQ than the conventional dowel. Tapered plates had the highest bearing area to stiffness ratio, which could have attributed to the reduced compressive straining occurring under wheel loading. There was also a large amount of equivalent tensile plastic strain that occurred in the GFRP tapered plate under wheel load that may have reduced the compressive plastic straining at the joint. The cracking at the sides of the device occurred before the plastic compressive straining occurred in the concrete under wheel loading and these cracks formed releasing energy as the slab was able to deflect further and compressive plastic straining remained low. Conventional dowels had increased compressive damage occur under wheel loading but the reversed loading on the slabs did not increase the compressive damage occurring suggesting that the failure remains local.

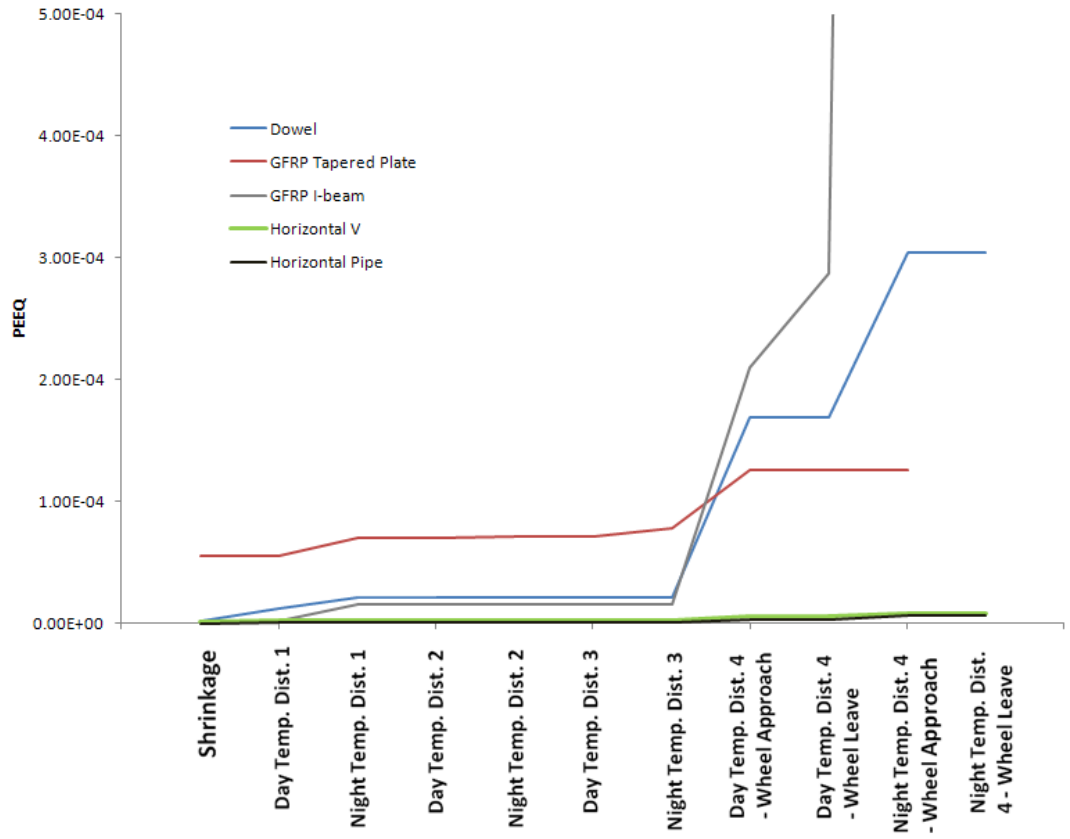

Figure 7-82 – Service Load Comparison of Maximum Concrete PEEQ

Figure 7-83 presents a comparison of the maximum plastic tensile equivalent tensile strain (PEEQT) in the concrete at the device interface as the service loads are applied to the models. The maximum PEEQT in the concrete for the GFRP tapered plate and the GFRP I-beam were well beyond the failure level assumed for significant cracking to occur. The devices both have large bearing areas with a sharp edge where tensile stress concentrations occurred. The concentrated tensile zone at the edges top of the top flange of the GFRP I-beam and GFRP tapered plate dowel caused tensile plastic straining to occur under wheel loading. The maximum PEEQT in the concrete for the dowel, Horizontal V and Horizontal Pipe devices are all below the failure level and are very similar. The rounded edges of the dowel bar reduced the tensile stress concentration adjacent the bearing area reducing the plastic tensile strain in the concrete. The horizontal V and horizontal pipe device both had increased bearing areas for load transfer to occur reducing tensile stress concentrations in the concrete and hence the plastic straining that occurred in the slab.

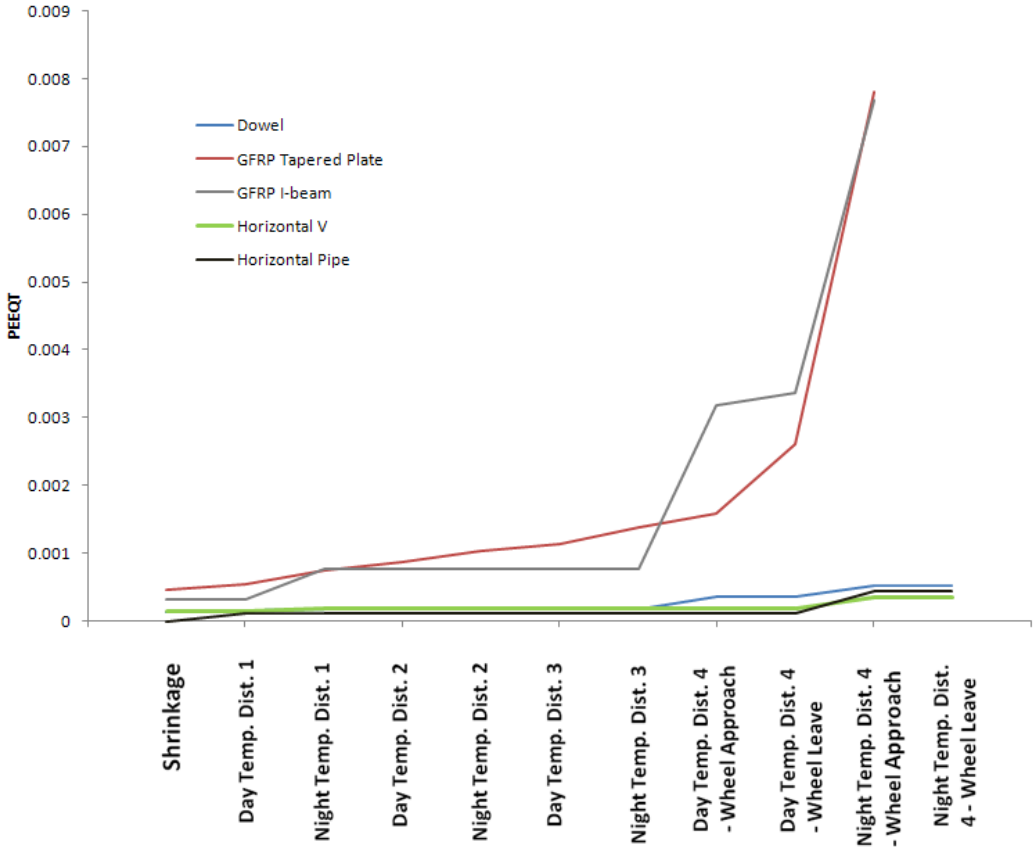

Figure 7-83 – Service Load Comparison of Maximum Concrete PEEQT

A comparison of the maximum Von Mises stresses in the devices through the service load analysis is presented in Figure 7-84. The lowest maximum Von Mises stress occurs in the horizontal pipe device and the Horizontal V device. The devices being continuous spread the load transfer for wheel load and reduce restraint causing Von Mises stress in the devices. The GFRP tapered plate and the GFRP I-beam were similar to the conventional dowel until wheel load was transferred when they increase to a larger maximum Von Mises stress in the device. Under wheel loading the GFRP I-beam top flange provides most of the restraint and the local effects cause the GFRP I-beam Von Mises stress to increase. Tensile plastic straining in the concrete will also cause more load transfer through the device and increase the maximum Von Mises stress in the device until an ultimate failure of the device occurs (not captured in the model as linear elastic material properties were used for all the devices). The reduced stress in the GFRP tapered plate under the final wheel load is prior to failure and may be reduced also due to the decreased loading at failure.

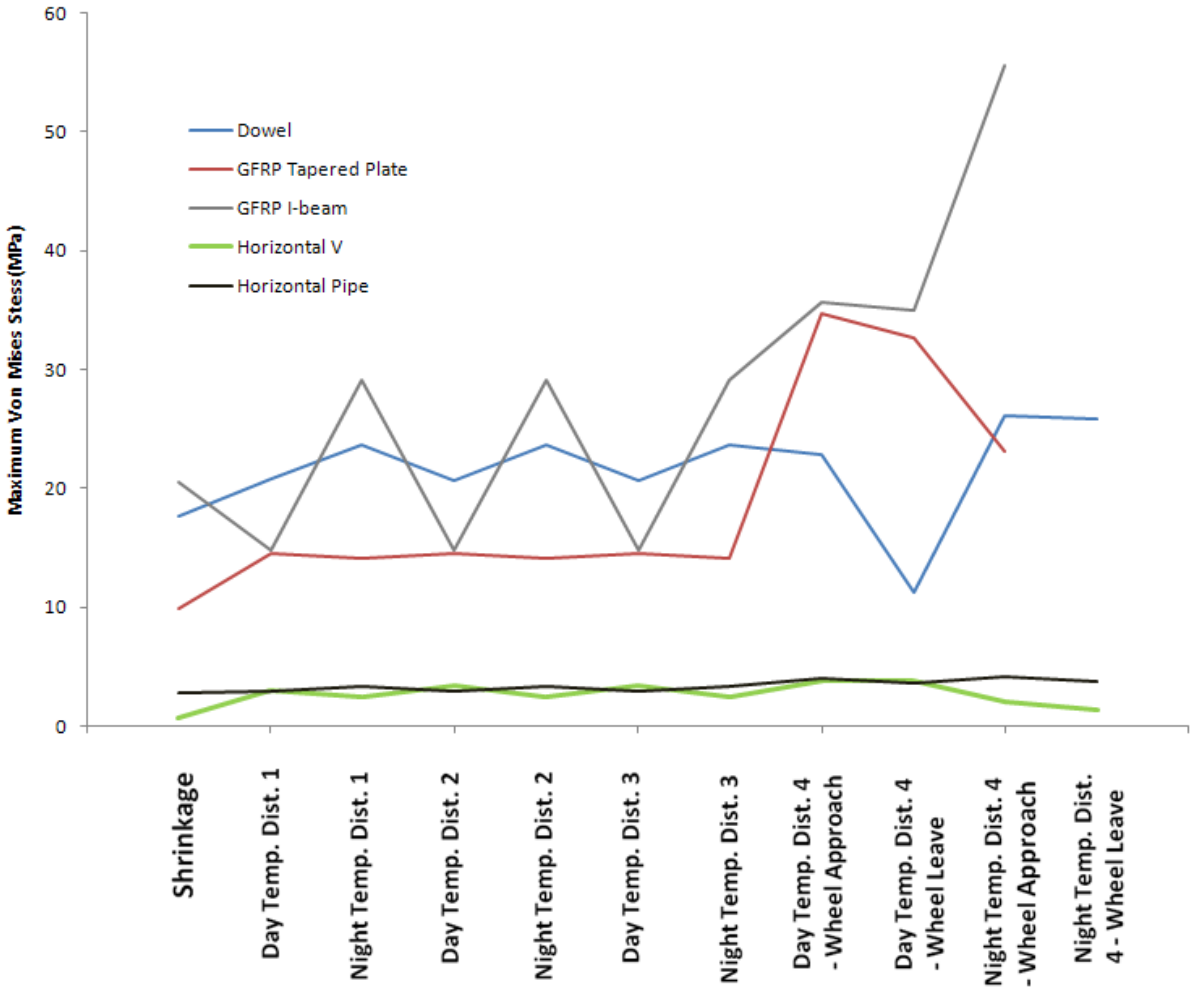

Figure 7-84 – Service Load Comparison of Maximum Device Von Mises Stress

The maximum vertical stress in the subbase occurred during the combined daytime thermal gradient and wheel loading as the slab was curling downward as the top of the slab is heated and then the wheel load curls the slab edge further downward. Table 7-2 presents the maximum vertical stress in the base layer during the wheel application on both the approach and leave sides of the slab during the daytime thermal gradient. The maximum vertical stress in the base layer occurred in the GFRP I-beam model at 221 kPa. This occurred because the end of the GFRP I-beam directly bearing on the base layer is cantilevered out of the loaded slab. The higher vertical base stress in horizontal V and pipe device may suggest that less load transfer was occurring. Less upward curling of the slabs during shrinkage and thermal gradients also occurred in the horizontal pipe and horizontal V models before the application of the wheel load meaning the slab comes into direct contact with the base layer at a lower wheel load. All of the maximum

vertical stresses are reasonable for the base layer and should not cause failure. The maximum vertical stresses in the base layer appear to be low enough that they will not cause failure. A detailed investigation into the complex behaviour of the base was not completed.

Table 7-2 - Service Wheel Load Maximum Base Layer Vertical Stress Comparison

	Day Temperature Distribution and Wheel Approach (kPa)	Day Temperature Distribution and Wheel Leave (kPa)
Dowel	-127	-130
FRP Tapered Plate	-150	-153
FRP I	-214	-221
Horizontal Vee Device	-186	-186
Pipe Device	-187	-191

The maximum stress in the base layer for each of the devices does not vary significantly between the approach and leave side of the slabs. The GFRP I-beam varied the most with a difference of 7 kPa. Conventional dowel bars reduce the maximum stress in the base layer the most under daytime wheel loading at a maximum of approximately 130 kPa. The GFRP Tapered plate behaves the second best with maximum vertical stresses of approximately 150 kPa. The maximum stress in the base layer for both the Horizontal V and the Pipe device is around 190 kPa. The GFRP I-beam has the highest maximum vertical stress in the base layer at approximately 220 kPa. Higher vertical stress concentrations in the base layer may cause more permanent deflection in the base layer at the slab edge causing more deflection at the joint similar to what was observed in the geo-foam base layer during experimental testing. The permanent deflection of the soil at the joint could also cause poorer support at the base layer for repetitive wheel load cycles. The nonlinear behaviour of the base layer was not captured in the model and cyclic wheel loading may cause permanent deflection in the base near the joint. Using a nonlinear material model could determine the effects of the high vertical base stress more adequately to assess the importance of the maximum stresses in the base layer.

7.9 Summary of Service Finite Element Analysis

After applying service loading similar to the loading that the slabs would encounter in service, generally the behaviour of the GFRP I-beam and GFRP tapered plate dowels perform poorer than conventional steel dowels. The horizontal V and the horizontal pipe device both behave similarly, with similar concrete stress distributions and peak stresses. The maximum stress

concentrations as well as plastic straining occurring in the concrete were reduced in the horizontal V and horizontal pipe devices compared to conventional dowels.

The following are conclusions made based on the service load finite element analysis:

- The horizontal pipe device provided the least restraint to shrinkage curling of the slab and the highest deflection occurred at the joint.
- The horizontal V device provided the least restraint to daytime thermal gradients causing curling of the slab since the most relative downward deflection occurred in the horizontal V device.
- The conventional dowel, GFRP I-beam and GFRP tapered plate dowels all provide similar restraint to shrinkage, daytime and night thermal gradients and had similar joint deflections throughout.
- Differential deflection at the joint after shrinkage and thermal gradients only occurred in the horizontal pipe and horizontal V device. The devices restrained the curling less which reduced stress concentrations in the concrete; however, the free movement also allowed differential deflection to occur at the joint. The differential deflection during thermal and shrinkage in the horizontal V and horizontal pipe device is within limits.
- The horizontal V had the lowest differential deflection after the application of wheel load and daytime thermal gradient simultaneously on both sides of the slab.
- The horizontal V had the most differential deflection occur at the joint with nighttime thermal gradient and wheel loading applied to the slab.
- The horizontal pipe device had more differential deflection occur at the joint than conventional steel dowels with both daytime and nighttime thermal gradients applied simultaneously with wheel loads. The differential deflection at the joint for the horizontal pipe device with daytime thermal gradients was the greatest. The differential deflection at the joint for the horizontal pipe device was greater under nighttime thermal gradients than daytime thermal gradients.
- The differential deflection at the joint for all the models throughout the service loading history was below the maximum suggested values.

- The GFRP I-beam and GFRP tapered plates caused higher maximum stress concentrations in the concrete around the device when compared to the conventional steel dowels in almost all directions.
- The sharp edges of the GFRP I-beam and GFRP tapered plates cause high tensile stress concentrations at the edges of the devices that cause cracking in the concrete.
- The maximum vertical stress in the base layer occurred in the GFRP I-beams with wheel loading and daytime thermal gradients applied to the slab simultaneously. The horizontal V and horizontal pipe devices had similar maximum vertical stress occur in the base layer but were greater than conventional steel dowels. This increased vertical stress in the base layer may cause permanent deformation in the base layer and affect the overall behaviour of the joint.

Based on the service analysis the GFRP tapered plate and GFRP I-beams do not perform better than conventional dowels. Increasing the size of the devices or reducing the spacing could be attempted to reduce stress concentrations and improve the load transfer capability of the devices. The spacing of the GFRP I-beams could also be decreased further; however, the author does not see any value in this as the relative stiffness to bearing area of the device already causes high concentrations of stress in the concrete resulting in failure and altering the spacing would not affect this. The bearing surfaces of the devices could also be rounded to reduce the concentration of tensile stress at the edges of the devices. The tapered plate geometry does not appear to provide any reduction in stress in the concrete under shrinkage and thermal gradients. A more detailed service investigation of the devices including misalignment should be completed to determine if the devices do provide advantages when compared to conventional dowels with misalignment, since the devices appear to provide no net benefit when compared to aligned conventional dowels and the material already makes the devices cost-prohibitive but this was not considered as part of this research.

Both the horizontal V and horizontal pipe device were capable of transferring load at the joint and reduced concentrations of stress in the concrete when compared to conventional steel dowels. Greater differential joint deflection under nighttime thermal gradients and wheel loading occurred for both devices when compared to conventional steel dowels. The horizontal V device had allowed less differential deflection at the joint compared to conventional dowels. Based on

the results from the service load analysis further investigation of the horizontal V and horizontal pipe devices would be suggested. Comparing the devices to misaligned dowels to further assess the benefits of the devices would be suggested as well as experimental testing of the device to confirm the model results. Full-scale testing to determine the effects of shrinkage and thermal gradients would also be suggested. A further investigation could also be completed to determine if the distribution of traffic on a typical highway would suggest that the lower differential during the daytime provided by the horizontal V would outweigh the poor nighttime differential deflection under wheel loading.

8.0 Conclusions and Recommendations

This section presents the summary of the research completed followed by conclusions and recommendations based on the research completed.

A comprehensive study of alternative joint load transfer devices was completed. Two different styles of devices were developed: discrete load transfer devices and continuous joint load transfer devices. Two alternative discrete devices were developed and evaluated, described as a GFRP I-beam device placed directly on the pavement base and tapered GFRP plate dowels. Two continuous joint devices were developed and evaluated described as the horizontal V and horizontal pipe devices. The continuous devices extend over the full width of the joint, and are intended to behave similarly to a shear keyed joint.

The discrete devices and conventional dowels were analyzed in a wheel path sized, three-dimensional finite element model for wheel loading and quasi-static reversed wheel loading. The effects of friction between the devices and the concrete under static wheel loading were also investigated. Under quasi-static reversed cyclic loading, the effects of vertical skew misalignment in the GFRP tapered plate and dowel were investigated. An experimental testing program was developed to test the discrete devices and conventional steel dowels to assess load transfer behaviour. Testing arrangement included quasi-static reversed cyclic wheel loading applied to either side of the joint.

The continuous devices, discrete devices and conventional steel dowels were also analyzed in a quarter-slab, three-dimensional finite element model with shrinkage and thermal strains, as well as wheel loading applied to the slab to simulate service conditions.

8.1 Conclusions

8.1.1 Discrete Device Finite Element Wheel Path Investigation

The following conclusions were made based on the wheel path finite element analysis completed:

- A wheel path model with a thinner base layer was capable of predicting behaviour similar to a full slab with the back edge of the slab restrained; however, the stress concentrations,

differential deflection and plastic straining occurring in the wheel path model were greater than in a full slab model but were on the same order of magnitude.

- Based on the results from the finite element load transfer study completed using the wheel path model, all of alternative devices appeared to be effective at transferring wheel load at the joint. All of the devices reduced the maximum vertical stress in the base layer and differential deflection at the joint, when compared to no load transfer devices. The mechanical transfer provided at the joint reduced differential deflection across the joint.
- Differential deflection predicted using conventional steel dowels was the lower than both the FRP I-beam and FRP tapered plate devices.
- The GFRP I-beam was the least effective at transferring load at the joint with highest plastic straining occurring in the concrete as well as the most differential deflection across the joint. The top flange of the GFRP I-beam provided most of the load transfer with the bottom flange being less effective which was assumed to occur because of the bottom flange bearing directly on the base. Altering the size the FRP I-beam thickness or possibly creating an alternative shape with an increased upper flange thickness only could improve the efficiency of the device.
- Increasing the thickness of the GFRP tapered plate could be completed to reduce the differential deflection at the joint by increasing the relative stiffness of the device to be closer to that of conventional steel dowels.
- Conventional steel dowels had the lowest plastic straining occurring in the concrete for both tension and compression. It is assumed that the sharp corners at the bearing surfaces for GFRP tapered plates and I-beams created the higher concentrations of stress when compared to round dowel bars.

8.1.2 Discrete Device Experimental Testing

The following conclusions were made based on the experimental testing program completed:

- All of the devices were observed to provide load transfer under quasi-static reversed wheel loading in experimental testing
- The conventional steel dowel bar failed at the highest load level and also maintained joint differential deflection better than the GFRP I-beam and GFRP tapered plate dowel as predicted by the wheel path finite element modeling completed.

- The GFRP I-beam supported a higher maximum load than the aligned GFRP tapered plate. Finite element modeling predicted failure with the GFRP I-beam at a lower load than the tapered plate dowel.
- Misalignment of the GFRP tapered plate increased the maximum load capacity compared to the aligned GFRP tapered plate and GFRP I-beam. The inclined orientation of the misaligned tapered plate causes that the longitudinal fibres within the GFRP to be more efficient in resisting the vertical shear loading at the joint. This effect was not captured in the finite element model due to isotropic material property assumptions.
- The differential deflection at the joint was lower with the GFRP tapered plate at the wheel load level in the experimental testing compared to the misaligned GFRP tapered plate and GFRP I-beam. The finite element modeling also predicted similar behaviour.
- Generally, the areas of damage observed and comparative differential deflection in the experimental testing were in agreement with the zones of plastic straining in the finite element model.
- Based on the testing results and failure mechanisms observed, it would be important in device design to ensure that the shear failure of the devices does not occur. The sudden failure of the device in shear caused sudden stepping to occur at the slab with poor support in the base for the GFRP devices.

8.1.3 Quarter Slab Service Load Finite Element Analysis of Discrete Devices

The following conclusions were made based on the quarter-slab service load finite element analysis completed:

- The horizontal pipe device provided the least restraint to shrinkage curling of the slab which resulted in the highest joint deflection in comparison to the other devices.
- The horizontal V device provided the least restraint to daytime thermal gradients causing curling of the slab which resulted in the largest relative downward deflection in comparison to the other devices.
- The conventional dowel, GFRP I-beam and GFRP tapered plate dowels all provide similar restraint to shrinkage, daytime and night thermal gradients and had similar joint deflections throughout.

- The horizontal V had the lowest differential deflection after the application of wheel load and daytime thermal gradient simultaneously on both sides of the slab.
- The horizontal V had the most differential deflection occur at the joint with nighttime thermal gradient and wheel loading applied to the slab.
- The horizontal pipe device had more differential deflection occur at the joint than conventional steel dowels with both daytime and nighttime thermal gradients applied simultaneously with wheel loads. The differential deflection at the joint for the horizontal pipe device with daytime thermal gradients was the greatest. The differential deflection at the joint for the horizontal pipe device was greater under nighttime thermal gradients than daytime thermal gradients.
- All the devices were capable of maintaining the differential deflection throughout the service loading history applied.
- The GFRP I-beam and GFRP tapered plates caused higher maximum stress concentrations in the concrete around the device in almost all directions when compared to the conventional steel dowels.
- The sharp edges of the GFRP I-beam and GFRP tapered plates cause high tensile stress concentrations at the edges of the devices that cause cracking in the concrete.
- The maximum vertical stress in the base layer occurred in the GFRP I-beams with wheel loading and daytime thermal gradients applied to the slab simultaneously. The horizontal V and horizontal pipe devices had similar maximum vertical stress occur in the base layer but were greater than conventional steel dowels. This increased vertical stress in the base layer may cause permanent deformation in the base layer and affect the overall behaviour of the joint.

8.2 Recommendations

Based on the research completed, the following recommendations would be made for the discrete devices:

- Increasing the size of the GFRP I-beam and tapered plate dowel and reducing the device spacing should be investigated to determine whether performance can be made similar to steel dowels.

- Further research on inclining the GFRP tapered plate could also be completed based on the wheel load experimental investigation completed, as the device had a higher load capacity compared to the aligned GFRP tapered plate.
- The effects of misalignment on the GFRP tapered plate dowel and GFRP I-beam should be compared to misaligned dowels to determine if the devices provide benefit when misalignment is considered.

Based on the research completed the following recommendations would be made for the continuous devices developed:

- Based on the results from the service load analysis a material for the horizontal V and horizontal pipe device should be chosen to provide the stiffness assumed and strength required.
- The horizontal V and horizontal pipe devices should be tested using experiment testing arrangement developed to assess the load transfer ability of the devices and general constructability.
- A full scale test section would be suggested for the horizontal V and horizontal pipe device if the devices perform well in the wheel load experimental testing.
- Misalignment of the horizontal V and horizontal pipe should be modeled to determine the effects of misalignment
- The possibility of using the horizontal pipe device as drainage should be investigated to determine if it would be advantageous and possible.

Works Cited

ABAQUS, 2008. *ABAQUS Analysis User's Manual*. Dassault Systemes.

Anon., n.d. *MATBASE*. [Online] (http://www.matbase.com/material/polymers/commodity/abs-general-purpose/properties) [Accessed 1 March 2012].

APCA, 2008. An Alternative to Traditional Round Dowel Bars. *R&T Update - Concrete Pavement Research and Technology*, 9(2).

Ardani, A., Suthahar, N. & Morian, D., 2000. *Early Evaluation of LTPP Specific Pavement Studies*. Springfield: Colorado Department of Transportation Research Branch.

Cairns, J., Du, Y. & Law, D., 2007. Influence of corrosion on the friction characteristics of the steel/concrete interface. *Construction and Building Materials 21*, pp.190-97.

Chen, W.-F. & Han, D.-J., 2007. *Plasticity for structural engineers*. For Lauderdale: J. Ross Publishing.

Chen, D.H., Won, M. & Zha, X., 2008. Performance of Dowel Bar Retorfit Projects in Texas. *Journal of Performance of Consructed Facilites*.

Comite Euro-International Du Beton, 1991. *CEB-FIP Model Code 1990*. London, England: Thomas Telford.

Davids, W.G., 2007. Foundation Modeling for Jointed Concrete Pavements. *Transportation Research Record*, (1730), pp.34-42.

Eddie, D., Shalaby, A. & Rizkalla, S., 2001. Glass Fiber-Reinforced Polymer Dowels for Concrete Pavements. *ACI Structural Journal*, 98(2), pp.201-06.

Falls, L.C., 2006. *Case Study of the Portland Cement Concrete Pavement Section of Deerfoot Trail, Calgary, Alberta*. Case Study. Cement Association of Canada.

Falls, L.C., 2006. *Case Study of the Portland Cement Concrete Pavement Section of Grant McConachie Way, Vancouver, B.C.* Case Study. Cement Association of Canada.

Fibergate Custom Structures, 2003. Dynaform Sturctural Shapes Design Guide.

Friberg, B.F., 1938. Load and Deflection Characteristics of Dowels in Transverse Joints of Concrete Pavements. In Council, N.R., ed. *Proceedings of Highways Research Board No. 18*. Washington , 1938.

Fricks, G.K. & Parkes , N.K., 2002. Innovations for Durable Floors. *Concrete Construction, The World of Concrete*.

Gulden, W. & Brown, D., 1985. Establishing Load Transfer in Existing Jointed Concrete Pavements. *Transportation Research Record*, (1043).

Kim, J.K. & Lee, C.S., 1998. Prediction of Differential Drying Shrinkage in Concrete. *Cement and Concrete Research*, 28(7), pp.985-94.

Leong, P., Tighe, S., Rothenburg, L. & Hein, D., 2006. Finite Difference Modeling of Misaligned Dowel Bars and Their Effects on Joint Performance. *Transportation Research Record*, No. 1946, pp.101-10.

Levy, C., 2010. *Numerical Investigation of the Effects of Shrinkage and Thermal Loading on the Behaviour of Misaligned Dowels in Jointed Concrete Pavements*. Waterloo: University of Waterloo.

MacGregor, J.G. & Bartlett, 2000. *Reinforced Concrete Mechanics and Design*. Toronto: Pearson Education Canada Inc.

McCracken, J., 2008. *Seasonal Analysis of the Response of Jointed Plain Concrete Pavements to FWD and Truck Loads*. University of Pittsburgh.

Murison, S., Shalaby, A. & Mufti, A., 2004. Laboratory Evaluation of Concrete-Filled GFRP Dowels in Jointed Concrete Pavements. In *2004 Annual Conference of the Transportation Associaton of Canada*. Quebec City, 2004.

Parkes, N., 2007. A Decade of Dowel Development. *L&M Concrete News*, 7(1).

Porter, M.L. et al., 2006. *Laboratory Study of Structural Behaviour of Alternative Dowel Bars*. Final Report. Ames: Center for Transportation Research and Education Iowa University.

Porter, M.L., Guinn, R.J.J. & Lundy, A.L., 2001. *Dowel Bar Optimization: Phases I and II*. Ames: Iowa State University.

Porter, M. & Pierson, N., 2007. Laboratory Evaluation of Alternative Dowel Bars for Use in Portland Cement Concrete Pavement Construction. *Transportation Research Record*, (2040), pp.80-87.

Prabhu, M., Buch, N., Varma, A. & Thandaveswara, D., 2006. Experimental Investigation of Dowel Misalignment on Joint Opening Behaviour in Rigid Pavements. (1947), pp.15-27.

Prabhu, M., Varma, A. & Buch, N., 2007. Analytical investigation of the effects of dowel misalignment on concrete pavement joint opening behaviour. *International Journal of Pavement Engineering*, 10(1), pp.49-62.

Qiao, P., Davalos, J.F. & Barbero, E.J., 1996. *Design Optimization of Fiber Reinforced Plastic Composite Shapes*. Morgantown: West Virginia University.

Reiter, M.J., Darter, M.I. & Carpenter, S.H., 1988. Restoration of Joint Load Transfer. *Transportation Research Record*, 1183.

Rufino, R. & Roesler, J., 2006. Effect of Slab-Base Interaction on Measured Concrete Pavement Responses. *Journal of Transportation Engineering*, 132(5).

Sargand, S.M. & Figueroa, J.L., 2010. *Monitoring and Modeling of Pavement Response and Performance Task A: Ohio*. Athens: Ohio University.

Schrader, E.K., 1991. A solution to cracking and stresses caused by dowels and tie bars. *Concrete International*, 13(7), pp.40-45.

Shalaby, D.A., 2005. *Case Study of the Portland Cement Concrete Pavement Section on Kanaston Boulevard from McGillvray Boulevard to Lowson Street in the City of Winnipeg*. Case Study. Cement Association of Canada.

Shalaby, D.A., 2005. *Case Study of the Portland Cement Concrete Pavement Test Sections on Provincial Trunk Highway 75 in Manitoba*. Case Study. Cement Association of Canada.

Shoukry, S.N., 2000. Backcalculation of Thermally Deformed Concrete Pavements. *Transportation Research Record*, pp.64-72.

Shoukry, S., William, G., Riad, M. & Motamarri, S.v., 2003. *Effect of Bonding Force on Stresses in Concrete Slabs*. Morgantown, West Virginia: West Virginia University - College of Engineering and Mineral Resources.

Siddique, Z.Q., Hossain, M. & Meggers, D., 2005. Temperature and Curling Measurements on Concrete Pavement. In *Proceedings of the 2005 Mid-Continent Transportation Research Symposium*. Ames, Iowa, 2005. Iowa State University.

Tayabji, S.D., 1986. Dowel Placement Tolerances for Concrete Pavements. *Transportation Research Record*, 1062, pp.47-54.

Tighe, S., 2005. *Case Study of the Portland Cement Concrete Pavement Section of Highway 427 in Toronto, Ontario*. Case Study. Cement Association of Canada.

Timoshenko, S.P. & Lessels, J.M., 1925. *Applied Elasticity*. East Pittsburgh: Westinghouse Technical School Press.

Transportation Association of Canada, 2013. *Pavement Design and Management Guide*. Ottawa, Ontario, Canada: Transportation Association of Canada.

Walker, W.W. & Holland, J.A., 1998. Plate Dowels for Slabs on Ground. 20(7).

APPENDIX A – Design Calculations for Discrete Devices using Dowel Bar Equations

STEEL DOWEL BAR

Dowel Properties:

$Ed := 29000ksi$ Modulus of Elasticity of the dowel bar (psi)

$Gd := 11154ksi$ Shear modulus for the dowel bar (psi)

$Ko := 700000 \frac{lbf}{in^3}$ Moduluis of Dowel Support (pci)

$b := 0.75in$ Device Width (in)

$I := \frac{b^4 \cdot \pi}{64}$ Moment of Inertia of the device (in^4)

$Sd := \frac{\pi \cdot b^3}{32}$ Section Modulus of device (in^3)

$fc := 4350psi$ Compressive strength of concrete

$Ad := \frac{\pi \cdot b^2}{4}$ Area of the device

$Lhalf := 9in$ Half the length of the device (in)

$Fd := \frac{10}{9}$ Shear Shape Factor

$spacing := 12in$ Dowel bar Spacing (in)

$z := 0.20in$ Joint size (in)

Calculate force per dowel:

$Wv := \frac{1}{12} \frac{kip}{in}$ Uniform shear force along joint

$Pd := Wv \cdot spacing$

Shear force per device

$Pd = 1\,kip$

Calculate deflection of dowel:

$225000MPa = 3.263 \times 10^7\,psi$

$250mm = 9.843\,in$

$\Delta flexure := \frac{Pd \cdot z^3}{24 \cdot Ed \cdot I}$ $\Delta flexure = 7.401 \times 10^{-7}\,in$

$\Delta Shear := \frac{Pd \cdot z \cdot Fd}{2 \cdot Gd \cdot Ad}$ $\Delta Shear = 2.255 \times 10^{-5}\,in$

$\Delta dowel := \Delta flexure + \Delta Shear$ $\Delta dowel = 2.329 \times 10^{-5}\,in$

Calculate deflection of concrete:

Use Timoshenko elastic foundation theory to a beam of semi-infinite length to calculate the concrete deflection:

STEEL DOWEL BAR

$$\beta := \sqrt[4]{\frac{b \cdot Ko}{4 \cdot Ed \cdot I}} \qquad \beta = 0.735 \frac{1}{in}$$

$$y_o := \frac{Pd}{4 \cdot \beta^3 \cdot Ed \cdot I} \cdot (2 + \beta \cdot z)$$

$$y_o = 3.005 \times 10^{-3}\,in$$

Calculate relative deflection across joint

$$\Delta := 2 \cdot y_o + 2\Delta dowel$$

$$\Delta = 6.056 \times 10^{-3}\,in$$

Determine max bearing stress on the concrete:

$$\sigma bear := Ko \cdot y_o \qquad \sigma_{allowable} := \left(\frac{4 - \frac{b}{in}}{3}\right) \cdot (fc)$$

$$\sigma bear = 14.501\,MPa \qquad \sigma_{allowable} = 32.492\,MPa$$

GFRP I-BEAM

Dowel Properties:

$Ed := 2.8 \cdot 10^6 psi$ Modulus of Elasticity of the dowel bar (psi)

$Gd := 0.450 \times 10^6 \cdot psi$ Shear modulus for the dowel bar (psi)

$Ko := 700000 \frac{lbf}{in^3}$ Modulus of Dowel Support (pci)

$b := 2in$ Device Width (in)

$fc := 4350psi$

$I := \frac{2in \cdot (4in)^3}{12} - \frac{\left(2in - \frac{1}{4}in\right) \cdot \left(4in - 2 \cdot \frac{1}{4}in\right)^3}{12}$ Moment of Inertia of the device (in^4)

$I = 4.414 \cdot in^4$

$Sd := \frac{I}{2in}$ Section Modulus of device (in^3)

$Sd = 2.207 \cdot in^3$

$Ad := 2 \cdot 2in \cdot \frac{1}{4}in + \left(4in - 2 \cdot \frac{1}{4}in\right) \cdot \frac{1}{4}in$ Area of the device

$Ad = 1.875 \cdot in^2$

$Lhalf := 9in$ Half the length of the device (in)

Calculate the Shear shape factor according to the formula provided in USDA Forest Service Research Note FPL-0210 1970 - Simplified method for calculating shear deflections of beams

$b_1 := \frac{1}{4}in$ Web Width

$b_2 := 2in$ Flange Width

$\rho := \frac{b_1}{b_2}$

$d_1 := 1.75in$ Half height of web (exclude flange)

$h := 4in$ Full height of member

$t := \frac{2 \cdot d_1}{h}$

$\beta_1 := 1$

GFRP I-BEAM

$$Fd := \frac{9}{2}\cdot\left[\frac{1}{\rho}\cdot(1-t)+t\right]\cdot\left[\frac{1}{\rho^2}\cdot\left(\frac{t^5}{2}-t^3+\frac{t}{2}\right)+\frac{1}{\rho}\cdot\left[-t^5\cdot\left(\frac{3}{30\cdot\beta_1}+\frac{2}{3}\right)+t^3\cdot\left(\frac{1}{3\cdot\beta_1}+\frac{2}{3}\right)-\frac{t}{2\cdot\beta_1}+\frac{8}{30\cdot\beta_1}\right]\right]$$

$Fd = 21.277$ Shear Shape Factor

$spacing := 900mm$ Dowel bar Spacing

$z := 10mm$ Joint size

Calculate force per dowel:

$Wv := \frac{1}{12}\frac{kip}{in}$ Uniform shear force along joint

$Pd := Wv\cdot spacing$

$Pd = 2.953\cdot kip$ Shear force per device

Calculate deflection of dowel:

$$\Delta flexure := \frac{Pd\cdot z^3}{24\cdot Ed\cdot I} \qquad \Delta flexure = 6.075\times 10^{-7}\cdot in$$

$$\Delta Shear := \frac{Pd\cdot z\cdot Fd}{2\cdot Gd\cdot Ad} \qquad \Delta Shear = 0.015\cdot in$$

$\Delta dowel := \Delta flexure + \Delta Shear$ $\Delta dowel = 0.372\cdot mm$

Calculate deflection of concrete:

Use Timoshenko elastic foundation theory to a beam of semi-infinite length to calculate the concrete deflection:

$$\beta := \sqrt[4]{\frac{b\cdot Ko}{4\cdot Ed\cdot I}} \qquad \beta = 0.41\cdot\frac{1}{in}$$

$$y_o := \frac{Pd}{4\cdot\beta^3\cdot Ed\cdot I}\cdot(2+\beta\cdot z)$$

$y_o = 1.87\times 10^{-3}\cdot in$

Calculate relative deflection across joint

$\Delta := 2\cdot y_o + 2\Delta dowel$

$\Delta = 0.84\cdot mm$

Determine max bearing stress on the concrete:

$\sigma bear := Ko\cdot y_o$ $\sigma_{allowable} := (0.6\cdot 0.85)\cdot(fc)$

$\sigma bear = 9.026\cdot MPa$ $\sigma_{allowable} = 15.296\cdot MPa$

GFRP TAPERED PLATE

Dowel Properties:

$Ed := 2.8 \cdot 10^{6} psi$ Modulus of Elasticity of the dowel bar

$Gd := 0.450 \times 10^{6} \cdot psi$ Shear modulus for the dowel bar

$Ko := 190 \frac{N}{mm^{3}}$ Moduluis of Dowel Support

$fc := 30MPa$

$b := 50mm$ Device Width

$t := 12.5mm$

$I := \frac{b \cdot t^{3}}{12}$ Moment of Inertia of the device (in^4)

$I = 8.138 \times 10^{3} \cdot mm^{4}$

$Sd := \frac{2 \cdot I}{t}$ Section Modulus of device (in^3)

$Sd = 1.302 \times 10^{3} \cdot mm^{3}$

$Ad := b \cdot t$ Area of the device

$Ad = 625 \cdot mm^{2}$

$Lhalf := 225mm$ Half the length of the device (in)

Calculate the Shear shape factor according to the formula provided in USDA Forest Service Research Note FPL-0210 1970 - Simplified method for calculating shear deflections of beams

$Fd := \frac{6}{5}$ Shear Shape Factor for Rectangle

$spacing := 12in = 304.8 \cdot mm$ Dowel bar Spacing (in)

$z := 10mm$ Joint size (in)

Calculate force per dowel:

$Wv := \frac{1}{12} \frac{kip}{in}$ Uniform shear force along joint

$Pd := Wv \cdot spacing$ Shear force per device

$Pd = 4.448 \cdot kN$

Calculate deflection of dowel:

$\Delta flexure := \frac{Pd \cdot z^{3}}{24 \cdot Ed \cdot I}$ $\Delta flexure = 1.18 \times 10^{-3} \cdot mm$

GFRP TAPERED PLATE

$$\Delta Shear := \frac{Pd \cdot z \cdot Fd}{2 \cdot Gd \cdot Ad} \qquad \Delta Shear = 0.014 \cdot mm$$

$$\Delta dowel := \Delta flexure + \Delta Shear \qquad \Delta dowel = 0.015 \cdot mm$$

Calculate deflection of concrete:

Use Timoshenko elastic foundation theory to a beam of semi-infinite length to calculate the concrete deflection:

$$\beta := \sqrt[4]{\frac{b \cdot Ko}{4 \cdot Ed \cdot I}} \qquad \beta = 0.062 \cdot \frac{1}{mm}$$

$$y_o := \frac{Pd}{4 \cdot \beta^3 \cdot Ed \cdot I} \cdot (2 + \beta \cdot z)$$

$$y_o = 0.077 \cdot mm$$

Calculate relative deflection across joint

$$\Delta := 2 \cdot y_o + 2\Delta dowel$$

$$\Delta = 0.183 \cdot mm$$

Determine max bearing stress on the concrete:

$$\sigma bear := Ko \cdot y_o \qquad \sigma bear = 14.554 \cdot MPa$$

$$\sigma_{allowable} := (0.6 \cdot 0.85) \cdot (fc) \qquad \sigma_{allowable} = 15.3 \cdot MPa$$